Geothermal Methods: Application of Time-Dependent Tomography to Detect Changes in Structure at Long Valley Caldera and the Coso Geothermal Area, California

MHANA, NAJWA

Geothermal Methods:
Application of Time-Dependent Tomography to Detect Changes in Structure at Long Valley Caldera and the Coso Geothermal Area, California

Najwa Mhana

A thesis submitted in partial fulfillment of the requirements for the degree of Doctoral of Philosophy

Department of Earth Sciences
University of Durham
May 2016

Abstract

Structural changes in active volcanic and producing geothermal systems are expected because of changes in the distribution of fluids, gases and cracks in the host rocks. Such changes have traditionally been studied using seismic tomography where two independent inversion results are differenced. A new tomography program *tomo4d*, inverts two epochs simultaneously, imposing constraints to minimize the structural differences calculated between different epochs. This method suppresses spurious changes not required by the data. Both methods were applied to data from Long Valley caldera and the Coso geothermal area, and the results compared.

Long Valley caldera, California, has been seismically active since 1978. In particular, a region to the south of the resurgent dome (the "south moat") and Mammoth Mountain have experienced multiple swarms involving hundreds of thousands of earthquakes. Inverting data from 1997 and 2009/10 using *tomo4d* detected changes with weaker anomaly strengths compared to those of *simul2000A*. Some changes imaged using *simul2000A* are thus not required by the data. Variable changes in V_p, V_s and V_p/V_s were detected and are interpreted as pore pressure decrease and/or drying of minerals, CO_2 depletion and flooding during the tectonically active period.

The Coso geothermal area, California, is highly seismogenic, with thousands of earthquakes occurring each year. Time-dependent seismic tomography was performed for the years 1996, 2006, 2007, 2008, 2010 and 2012 using both *simul2000A* and *tomo4d*. The epochs 1996-2006 and 2007-2012 were studied in detail. During the first epoch, V_p, V_s and V_p/V_s mostly increased in the geothermal field whereas during the second epoch changes were more varied and less extreme. It is concluded that different parts of this tripartite field have different reservoir characteristics, and that operational activities changed with time. These likely involved increasing water saturation in some areas as a result of increased water injection in recent years.

Acknowledgments

I would like to thank:

My supervisors Gill Foulger and Bruce Julian, for their invaluable guidance and support during my research.

Christine Peirce, for her support and encouragement.

Ceri Nunn, for useful discussions on seismic tomography and help with plotting scripts.

My family, for all their support, encouragement and their belief in me.

My husband for patience, understanding and invaluable help.

My son Ali for brightening my life and making me stronger for challenges.

Staff at the Earth Sciences Department, Durham University, for their support in many different ways that enabled me keep going.

Damascus University, for providing the great opportunity to continue my postgraduate studies.

Durham University, for providing an excellent place to do my research.

The Geothermal Program Office of the U.S. Navy, Andy Sabin, and David Meade for providing the Coso seismic data and helpful discussions.

Peter Rose and Phil Wannamaker for helpful information.

Dedicated to my father

List of contents

CHAPTER 3

METHODOLOGY

CHAPTER 4

TOMOGRAPHIC INVERSION: LONG VALLEY CALDERA

CHAPTER 5

TOMOGRAPHIC INVERSION : THE COSO GEOTHERMAL AREA

List of figures

CHAPTER 1

BACKGROUND : LONG VALLEY CALDERA

CHAPTER 2

BACKGROUND : THE COSO GEOTHERMAL AREA

CHAPTER 3

METHODOLOGY

CHAPTER 4

TOMOGRAPHIC INVERSION: LONG VALLEY CALDERA

CHAPTER 5

TOMOGRAPHIC INVERSION : THE COSO GEOTHERMAL AREA

CHAPTER 6

INTERPRETATION & CONCLUSIONS

CHAPTER 7
WIDER ISSUES

List of tables

List of appendices

List of additional material

Copies of the following papers and abstracts are contained in a pocket at the back of this thesis:

Julian, B.R., G.R. Foulger, A. Sabin, N. Mhana, TOMO4D: Temporal Changes in Reservoir Structure at Geothermal Areas, proceedings of the World Geothermal Congress, Melbourne, Australia, 19-25 April, 2015.

Mhana, N., G.R. Foulger, B.R., Foulger, C. Peirce, Study of structural change in volcanic and geothermal areas using seismic tomography, European Geosciences Union General Assembly, Vienna, Austria, 27 April - 2 May, Abstract EGU2014-1127, 2014.

Mhana, N., C. Nunn, B.R. Julian, G.R. Foulger, Andrew Sabin, Time-Dependent Tomography Using TOMO4D: Theoretical Advances and Early Applications, *Forty-first Workshop on Geothermal Reservoir Engineering, Stanford University*, Stanford, California, February 22-24, 2016.

Nunn, C., B.R. Julian, G.R. Foulger, and N. Mhana, No evidence from seismic tomography for time-dependent changes during the Mount Etna 2002–3 eruption, submitted to *Geophys. J. Int.*

Tezel, T., B.R. Julian, G.R. Foulger, C. Nunn, N. Mhana, Preliminary 4D Seismic Tomographic Images for the Geysers, 2008-2014, *Forty-first Workshop on Geothermal Reservoir Engineering, Stanford University*, Stanford, California, February 22-24, 2016.

Declaration

I declare that this thesis, which I submit for the degree of Doctor of Philosophy at the University of Durham, UK is my own work and is not substantially the same as any which has previously been submitted for a degree at this or any other university.

Najwa Mhana
University of Durham
May 2016

CHAPTER 1

BACKGROUND : LONG VALLEY CALDERA

1.1 Tectonic evolution

Long Valley caldera is a large silicic volcano in central eastern California (Figure 1.1). It was formed by an eruption, 760,000 years ago, when the Bishop Tuff was formed. This tuff is ~600 km^3 in volume. It evacuated the magma chamber, causing a ring fault system to form and creating a 32 km x 17 km caldera that subsided 2-3 km [*Bailey*, 1989; *Bailey et al.*, 1976; *Hill et al.*, 1985]. Subsequently a resurgent dome formed which is ~10 km in diameter and ~500 m higher than the surrounding moat. The moat's average elevation is ~2100 m above sea level.

Long Valley caldera is one of the most seismically active areas of California [*Hill et al.*, 1985]. It lies between the Sierra Nevada and the Basin and Range province, north of the Owens Valley and south of the Mono Basin (Figure 1.1). The Owens Valley and the Hilton Creek faults to the southeast of the caldera accommodate part of the relative motion between the Pacific Plate to the west and North America to the east. Most of this motion is taken up on the San Andreas fault, which is responsible for many earthquakes in California. The Owens Valley experienced the 1872 M 7.6 earthquake as well as four M 5 earthquakes and one M 6 earthquake in 1941 which are examples of historical earthquakes that ruptured the Hilton Creek fault (Figure 1.1).

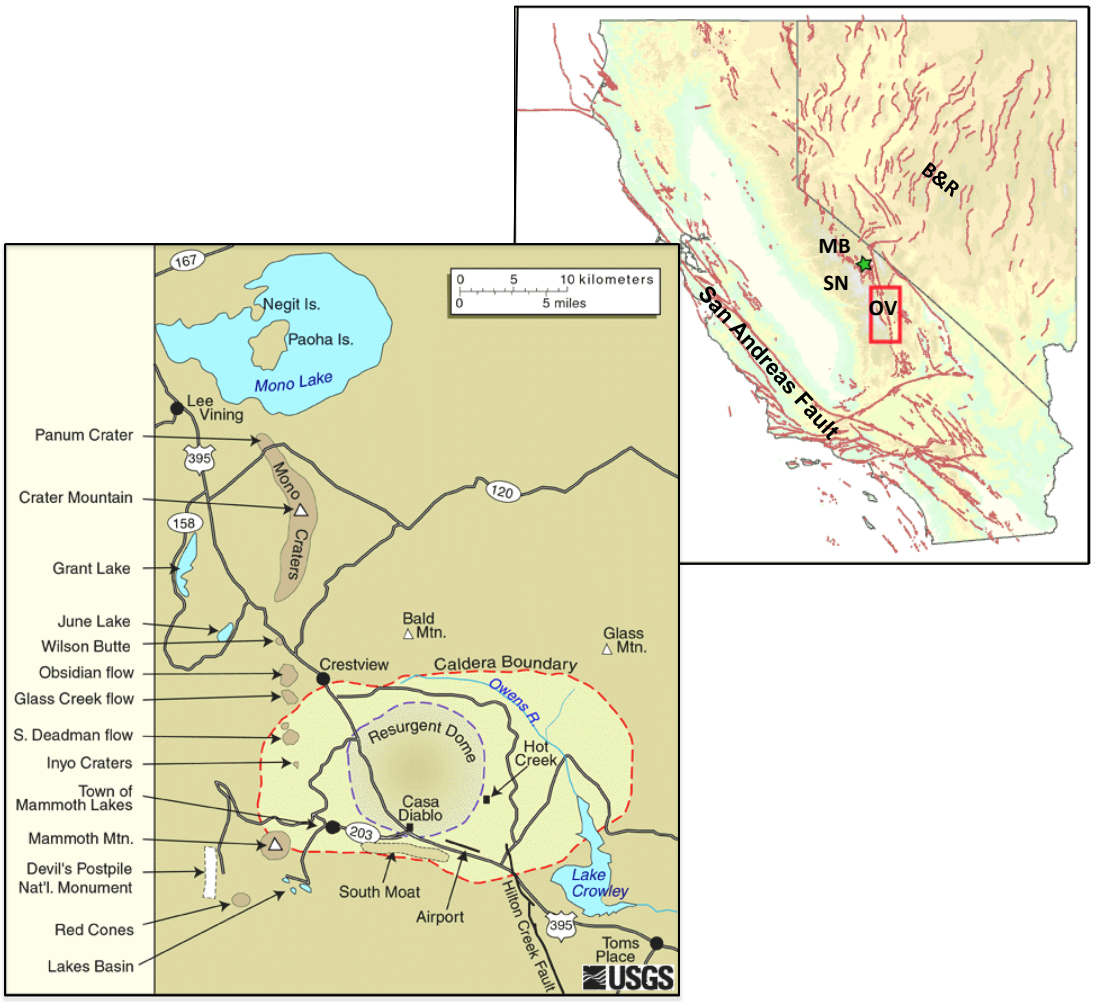

Figure 1.1: Regional map (top) showing the location of Long Valley caldera (green star), California. SN: Sierra Nevada; MB: Mono Basin; B&R: Basin and Range province; OV: Owens Valley. Red lines: faults. The caldera (bottom) is bounded by dashed red line. The resurgent dome is bounded by dashed purple line. Black squares are Hot Creek and Casa Diablo Hot Springs (from *http://volcanoes.usgs.gov/volcanoes/long_valley/long_valley_geo_hist_13.html* and *http://www.dpc.ucar.edu/earthscopeVoyager/JVV_Jr/didyouknow/lvcTect.html*).

1.2 Geology

The catastrophic eruption that formed Long Valley caldera ~760,000 years ago ejected flows of hot glowing ash, which cooled to form the Bishop Tuff (Figure 1.2). Since that time the caldera has experienced many smaller eruptions [See, *Bailey*, 1989, for summary]. Rhyolitic to basaltic postcaldera flows filled the moat, along with glacial till, lake sediments and landslide debris. Eruptions along the Mono-Inyo

Craters volcanic chain, which extends from Mammoth Mountain on the southwest rim of the caldera northward ~40 km to Mono lake, occurred 400,000 years ago. Repeated eruptions from vents on the southwest rim of the caldera 220,000 – 50,000 years ago formed Mammoth Mountain, a 3380-m-high dacite volcano. The north-south trending zone comprising Mammoth Mountain, the Inyo domes, the Mono craters, and Mono Lake, is still active as eruptions in both the Inyo and Mono craters occurred as recently as 600 years ago [*Miller*, 1985]. Small eruptions occurred in Mono Lake sometime between the mid-1700's and mid-1800's. The Inyo Domes-Mono Craters-Mono Lake Zone is thought to overlie and to be fed by a dyke-like system underneath [*Fink*, 1985; *Miller*, 1985]. A speculative cross-section of the structure of Long Valley is shown in Figure 1.3.

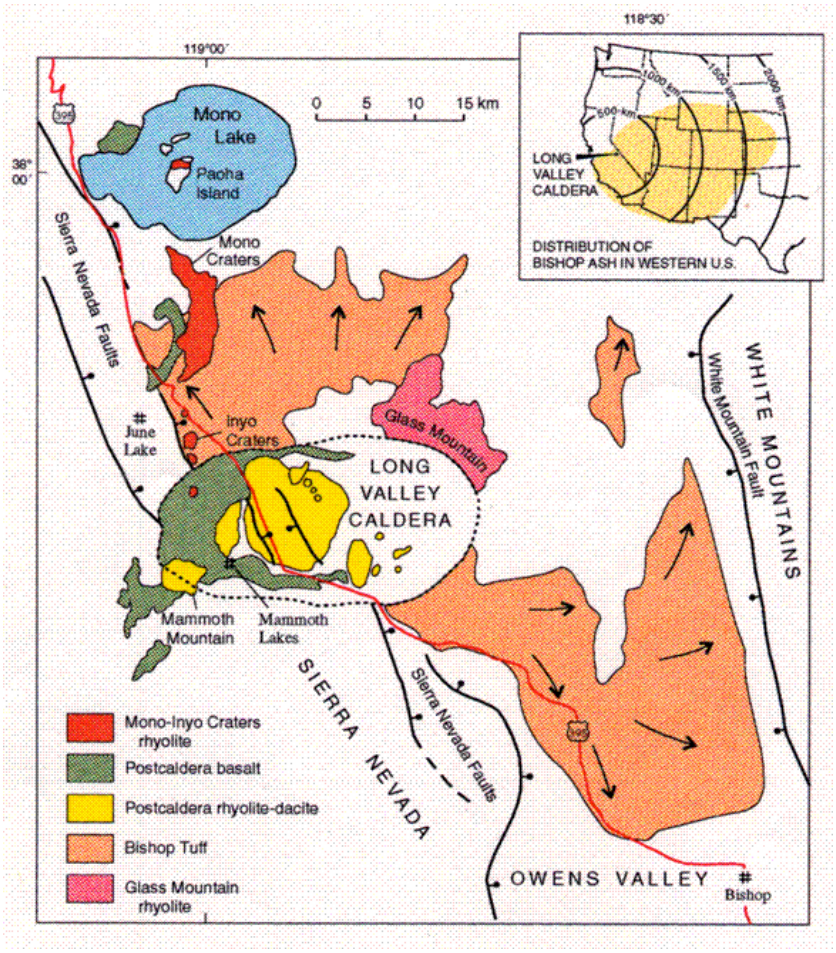

Figure 1.2: Simplified geologic map of Long Valley caldera at the northern end of Owens Valley with inset map showing ash distribution across western U.S. (from *http://volcanoes.usgs.gov/volcanoes/long_valley/long_valley_geo_hist_13.html*).

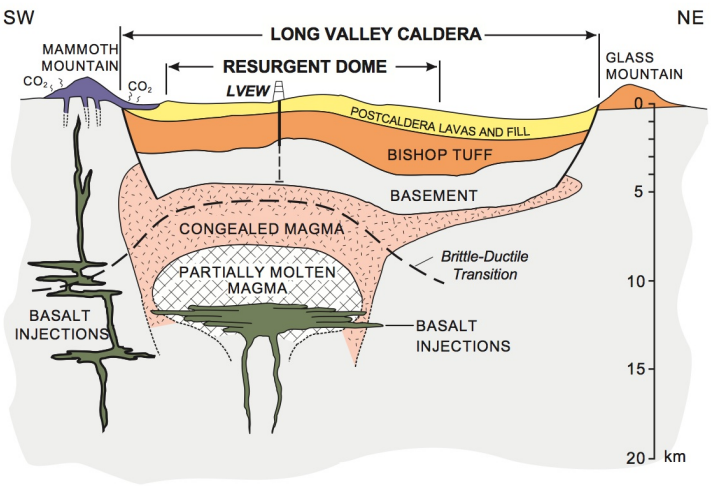

Figure 1.3: A southwest-northeast cross-section of Long Valley caldera showing the postulated sub-surface structure of the area [from *Sackett et al.*, 1999].

1.3 Seismicity

1.3.1 Distribution of seismicity

The seismicity in Long Valley caldera mostly occurs in the south moat and beneath Mammoth Mountain. Seismicity in 1997 and 2010 is shown in Figure 1.4. Appendix 1 shows the seismicity in Long Valley caldera over the period 1983-2014 as a series of maps.

1.3.2 Seismic networks

The first installation of instruments for recording earthquakes at Long Valley caldera was done in 1974. Additional instruments were added throughout the 1980s and 1990s. Since the 1980 earthquake swarm, earthquakes at Long Valley caldera have been monitored by the Northern California Seismic Network (NCSN) which has approximately 50 stations within 50 km of the caldera. After adding more stations and updating others between 2000 and 2003, the total number of stations in 2005 was 61 short-period seismic stations. Currently there are 25 short-period seismic stations. Of these, there are eleven 3-component stations and fourteen single-component stations (Figure 1.5).

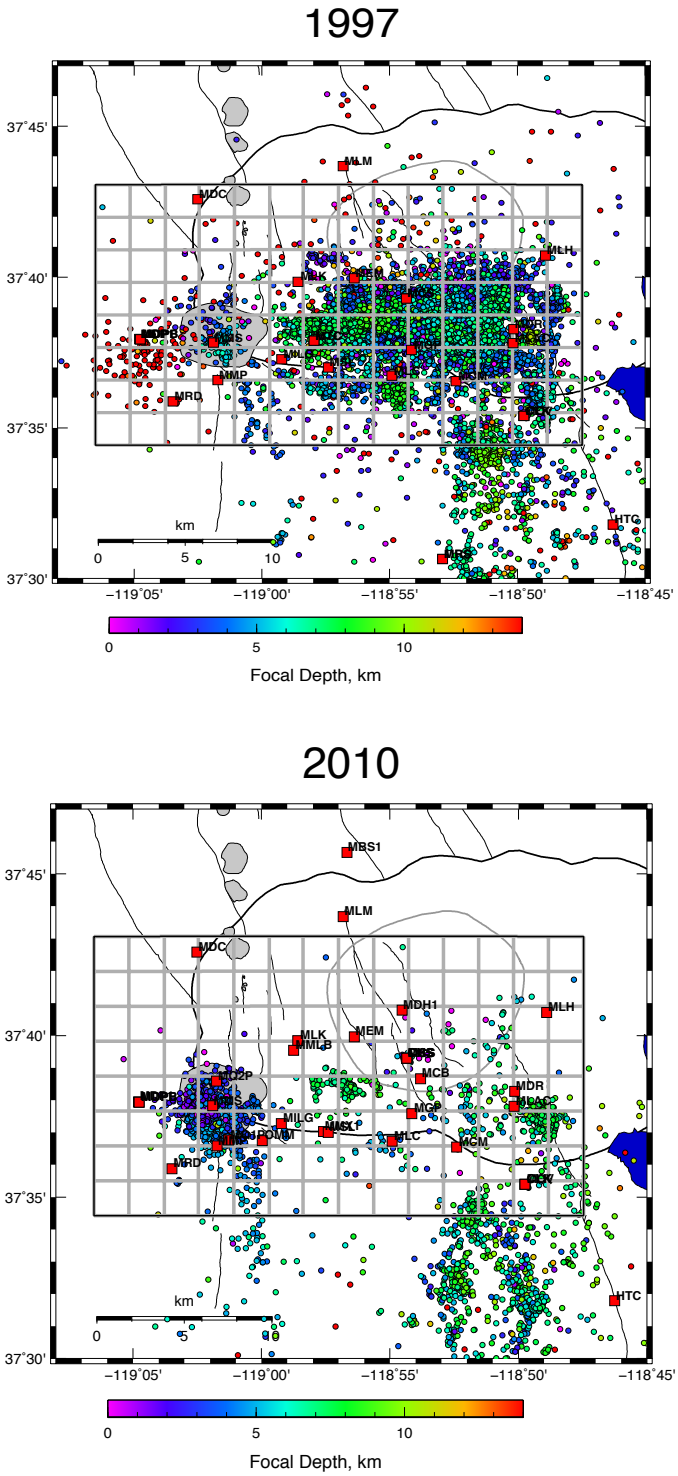

Figure 1.4: Seismicity maps of Long Valley caldera and vicinity for 1997 (top) and 2010 (bottom). Mammoth Mountain is shown in light grey. Resurgent dome is bounded by thin grey line. Thick line is topographic margin of caldera; thin grey lines are faults; and coloured dots are epicenters of the earthquakes. The grid is the tomography inversion grid used by *Foulger et al.* [2003] and in this thesis. Red squares are the seismometer stations. Blue region at right is Crowley Lake.

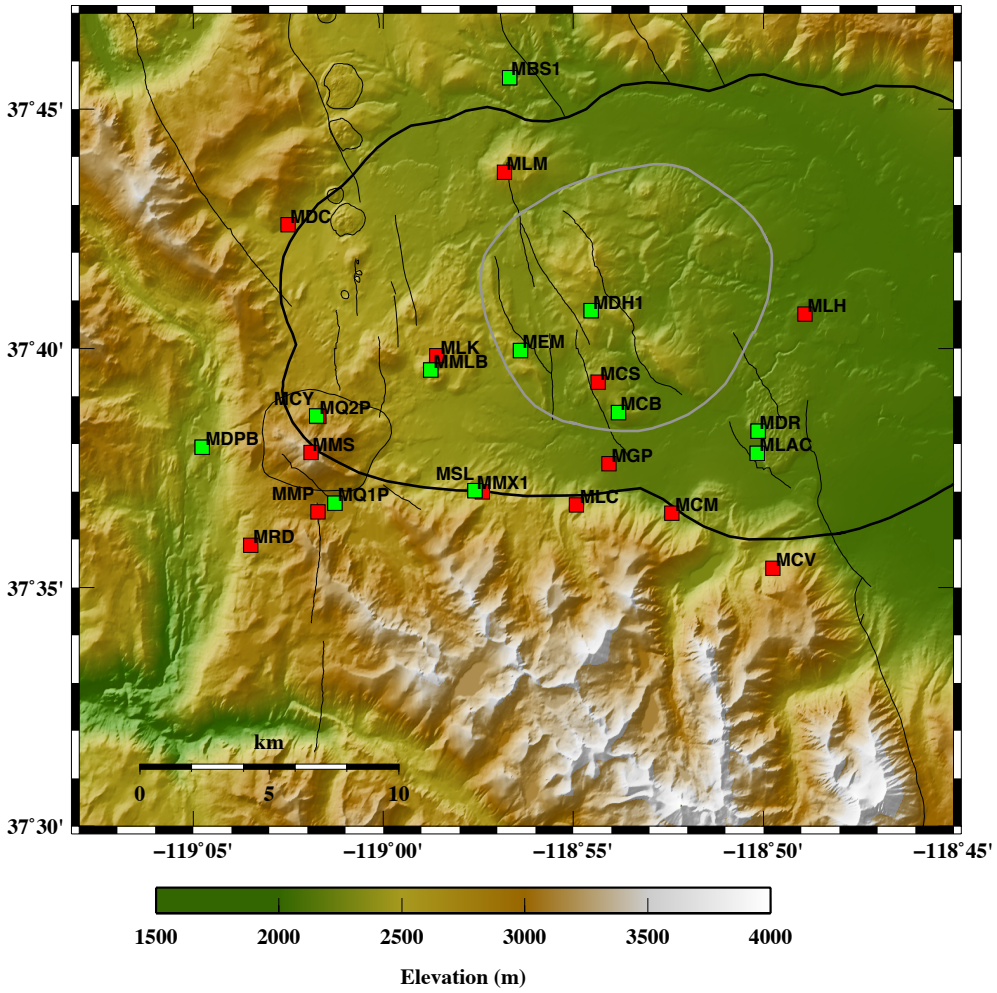

Figure 1.5: Topographic map of central and western Long Valley caldera and vicinity showing the current permanent seismic stations. Red squares: one-component stations; Green squares: three-component stations. Thick black and grey lines bound the caldera and the resurgent dome respectively and thin black lines show faults. Mammoth Mountain in the southwest of the caldera is bounded by thin black line.

1.3.3 History of seismic monitoring

After a long period of quiescence, Long Valley caldera has been in a state of seismic unrest since 1978 when a magnitude 5.7 earthquake occurred 20 km south of the caldera beneath Wheeler Crest (Figure 1.6 and Figure 1.7). This was followed by an intense earthquake sequence in May 1980 that involved four M~6 earthquakes, three of them located in the Sierra Nevada block south of the caldera and one beneath the southern caldera rim [*Hill et al.*, 1985]. Non double-couple components were

significant in two of the May 1980 earthquakes and the 1978 earthquake (Figure 1.7) and are consistent with magma intrusion [*Julian*, 1983]. The resurgent dome experienced 25 cm of uplift between 1979 and 1980 [*Savage and Clark*, 1982]. This activity subsequently slowed but earthquakes continued in the Sierra Nevada to the south of the caldera including a M~6 earthquake in 1981. A swarm including M 3 to 4 earthquakes occurred in the South Moat of the caldera in 1982, and a more intense earthquake swarm started in January 1983 involving two M~5 earthquakes [*Savage and Cockerham*, 1984]. Following an earthquake swarm in 1984, activity within the caldera slowed and declined to low level through 1988 (Figure 1.6).

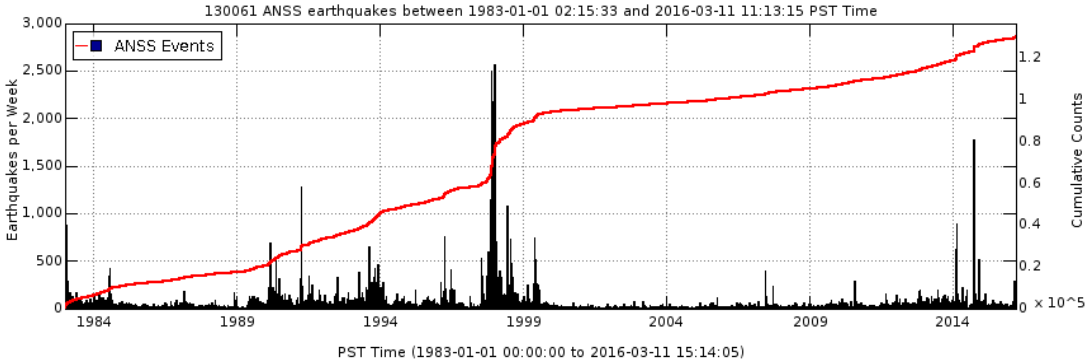

Figure 1.6: Graph showing seismicity at Long Valley caldera since 1983 (from *http://volcanoes.usgs.gov/volcanoes/long_valley/long_valley_monitoring_57.html*). The vertical bars correspond to the left y-axis and represent the number of earthquakes per week. The red line corresponds to the right y-axis and indicates the cumulative number of earthquakes.

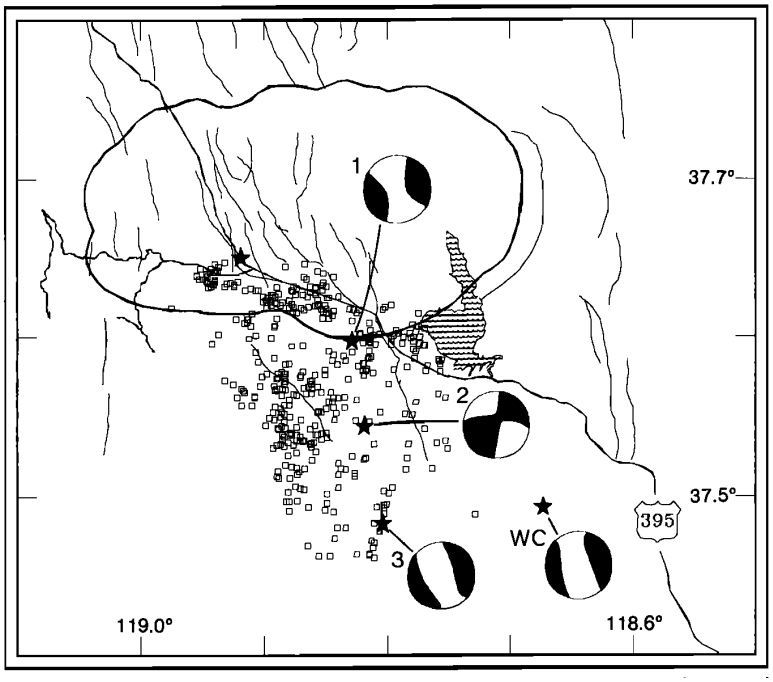

Figure 1.7: Long Valley caldera and vicinity [from *Julian and Sipkin*, 1985]. Squares: locations of earthquakes larger than M 3 in 1980; stars: M~6 earthquakes in 1980 and Wheeler Crest earthquake (WC) in 1978; numbered focal spheres: mechanisms obtained for 1980 earthquakes by *Julian and Sipkin* [1985] and for Wheeler Crest earthquake in 1978 by *Ekström and Dziewonski* [1983]. Heavy lines: caldera boundary and highways; light lines: normal faults.

In 1989, a 6-month-long earthquake swarm occurred beneath Mammoth Mountain. This swarm included long-period earthquakes centered at depths of 7-20 km southwest of Mammoth Mountain [*Pitt and Hill*, 1994] and diffuse emission of up to 500 tonnes of CO_2 per day in areas around the flanks of Mammoth Mountain [*Farrar et al.*, 1995; *Hill*, 1996; *Hill et al.*, 1990; *Sorey et al.*, 1993] (Figure 1.8). This CO_2 killed thousands of trees. Both long-period earthquakes and CO_2 emissions were interpreted as consistent with the presence of an activated basaltic magma body at depths of 10-25 km beneath the southwest flank of Mammoth Mountain [*Sorey et al.*, 1998].

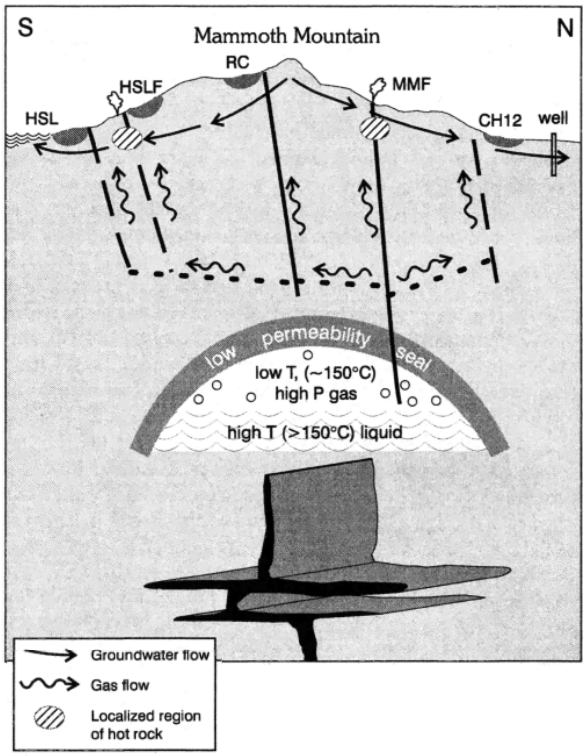

Figure 1.8: Schematic cross-section across Mammoth Mountain [from *Sorey et al.*, 1998] showing hypothesized magmatic source and derived gas reservoir from which gas leaks along faults (black lines) toward the surface in sites that include HSL (Horseshoe Lake tree kill), HSLF (Horseshoe Lake fault tree kill), RC (Reds Creek tree kill), MMF (Mammoth Mountain fumarole), and CH12 (Chair 12 tree kill). The dyke breaching the low-permeability seal was emplaced in 1989 and is assumed to have increased the rate of upward gas leakage.

Renewed swarm activity began in early 1990 and continued through 1995 (Figure 1.6). It occupied the entire South Moat and the southern section of the resurgent dome with the strongest activity in March 1991. Another earthquake swarm in the caldera occurred in 1996 but there was no significant change in ground deformation. Uplift of the resurgent dome continued to slow. In spring 1997 the seismicity and the rate of uplift of the resurgent dome began to increase again. It peaked in late November, with earthquakes as large as M_w 4.9, then declined to background levels through March 1998 with the resurgent dome standing roughly 10 cm higher than in the spring of 1997 (Figure 1.9).

The Northern California Seismic Network (NCSN) of the U.S. Geological Survey located more than 20,000 events in this entire episode. The unrest in the caldera then declined and uplift of the resurgent dome essentially stopped in mid-spring 1998 with no additional deformation in the caldera through 1999.

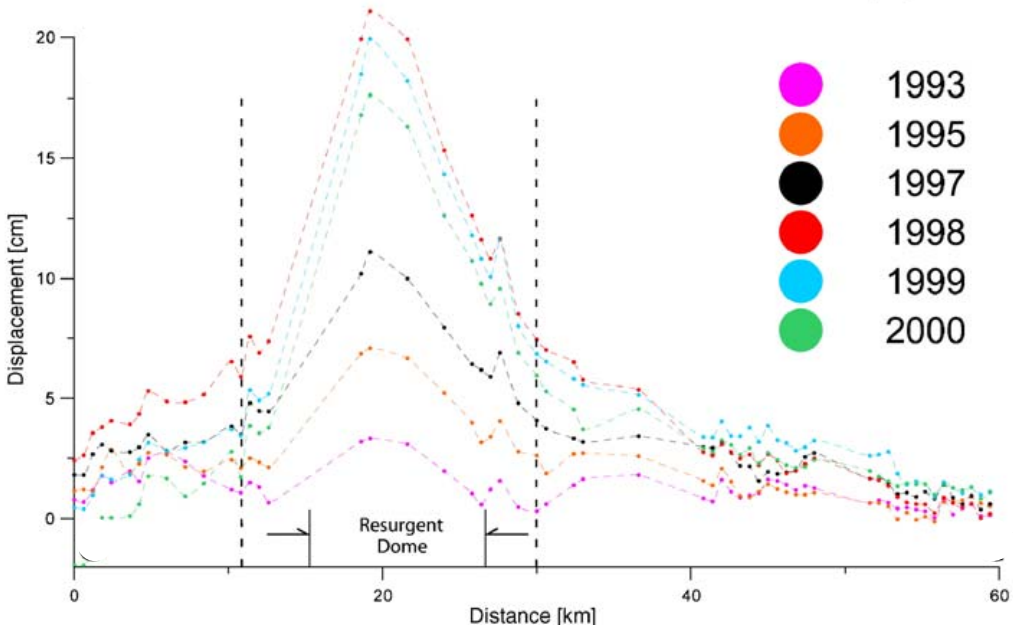

Figure 1.9: Plots of surface deformation at Long Valley caldera measured using Synthetic Aperture Radar (SAR) [from *Tizzani et al.*, 2007]. Evaluation with respect to June 1992 along a northeast-southwest cross-section traversing Long Valley caldera is shown for the years 1993, 1995, 1997, 1998, 1999 and 2000. The vertical dashed and solid lines indicate the caldera and the resurgent dome boundaries respectively.

The seismicity in Long Valley caldera over the period of monitoring mostly occurred in the swarms of earthquakes in 1978-1983, 1989, 1990-1995, 1996, and 1997-1998 (Figure 1.10). The seismic rate since the end of the 1997 swarm has been relatively low, occasionally punctuated by brief swarms. The U.S. Geological Survey recorded more than 1500 earthquakes in the period 22 September through 3 October 2014 with magnitudes M 0.1 - 3.5.

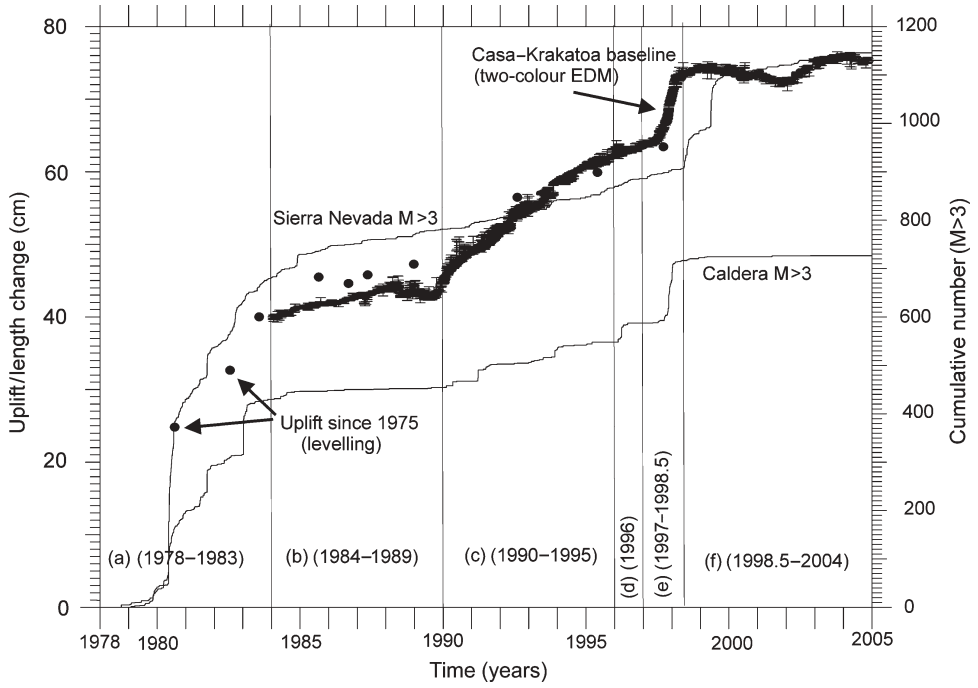

Figure 1.10: Graph showing the cumulative number of M ≥ 3 earthquakes in Long Valley caldera and the adjacent Sierra Nevada block for 1978-2004, together with the uplift history for the centre of the resurgent dome [from *Hill*, 2006], based on leveling surveys (solid circles) and extension of the Casa-Krakatoa baseline measured using an electronic distance meter (black band of measurements with error bars).

1.3.4 Previous tomography studies

- **Local earthquake tomography study by *Sanders et al.* [1995]**

Sanders et al. [1995] compared previous seismic tomography inversion results in Long Valley caldera that inverted the amplitudes and arrival times of local earthquakes to calculate three-dimensional seismic structure: (1) a study of *SV*-phase attenuation using the *S*- to *P*-phase amplitude-ratio technique [*Sanders*, 1993], (2) a study of *SV*- and *SH*-phase attenuation ratios using an *S*- to *P*-phase amplitude ratio technique [*Nixon*, 1992; *Sanders and Nixon*, 1995], (3) a study of *P*- and *S*-phase attenuation using a spectral ratio technique [*Ponko and Sanders*, 1994], and (4) a study of the V_p/V_s ratio [*Schwartz*, 1993].

Sanders et al. [1995] presented the results of all these studies with the data inverted using the same LSQR algorithm (a conjugate-gradient type method for solving sparse

linear equations and sparse least-squares problems [*Paige and Saunders*, 1982]). They found some consistencies among these studies where relatively low *P*-phase attenuation and relatively low V_p/V_s dominated to the east of Mammoth Mountain. They interpreted this as an indication of hydrothermal fluids. A relatively low-*S*-phase-attenuation region beneath the resurgent dome was interpreted as a possible magma body (Figure 1.11).

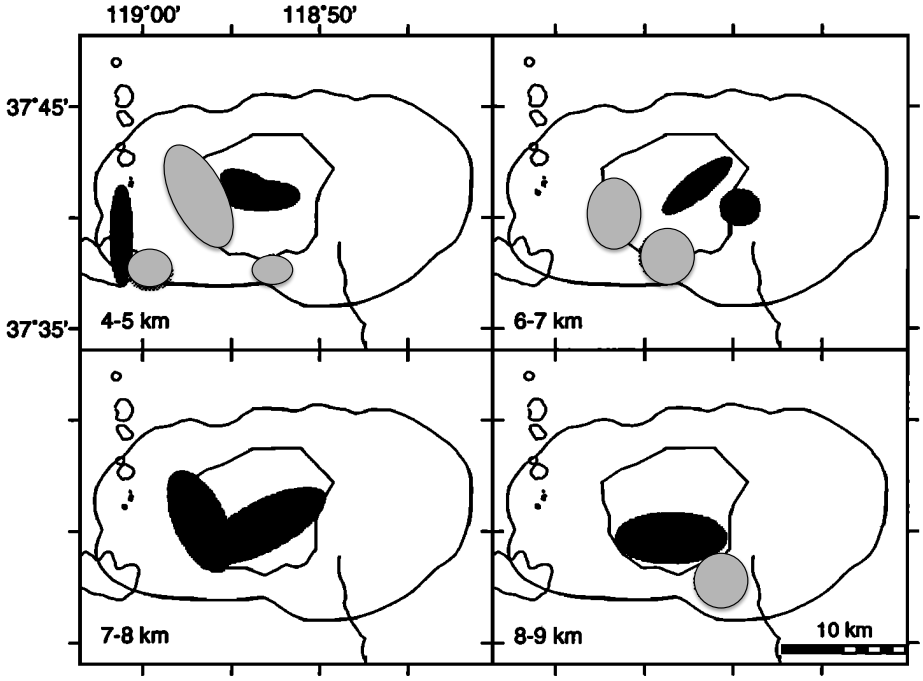

Figure 1.11: Map summarizing the results of the comparison study done by *Sanders et al.* [1995] showing anomalies at four depth intervals. Black: high temperature and perhaps magma; grey: supercritical compressible hydrothermal fluids [from *Sanders et al.*, 1995].

- **Non-linear teleseismic tomography study by *Weiland et al.* [1995]**

Teleseismic *P*-phase arrival times recorded on 1-component sensors were inverted using a three-dimensional ray tracing method. The study revealed two regions to the northwest of the caldera and beneath the resurgent dome at depths of 11.5 km and 24.5 km respectively with velocity anomalies of about 25-30% and 15%, lower than the surroundings (Figure 1.12). They interpreted the shallower anomaly to be the caldera magma chamber and the deeper one as basaltic magmas. This is consistent with a previous teleseismic study by *Dawson et al*. [1990] that inverted travel-time

residuals measured from teleseismic *P*-phases to obtain a three-dimensional structural image. That study implied the presence of a low-V_p feature at about 5-28 km depth beneath the resurgent dome with a decrease in V_p of about 7-9%.

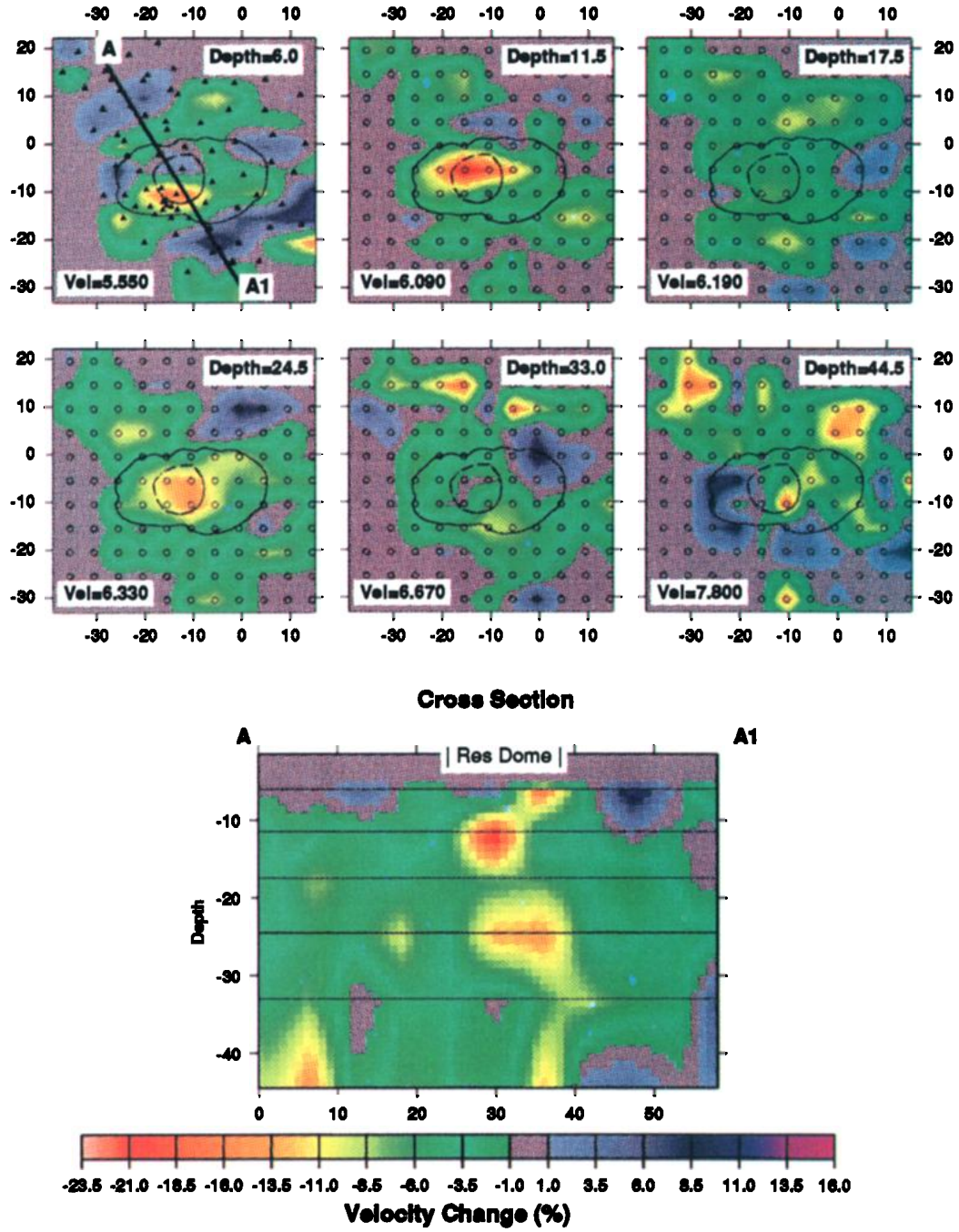

Figure 1.12: Crustal velocity (V_p) perturbation beneath Long Valley caldera [from *Weiland et al.*, 1995]. Background velocity is given in the lower left of each map. Triangles show the stations in the depth=6 km map, and the tomography grid nodes are shown as open circles. Solid black lines bound the caldera and the resurgent dome.

The cross section A-A1 is also shown. Horizontal lines in cross-section indicate depths of nodal layers.

- **Local-earthquake tomography by *Julian et al.* [1998]**

Julian et al. [1998] obtained a tomographic image of the upper 4 km beneath Mammoth Mountain using data from local earthquakes collected in 1989. *P* and *S-P* times were inverted for compressional-wave-speed (V_p) and compressional-to-shear wave-speed ratio (V_p/V_s) fields using the tomography program *simulps12* [*Evans et al.*, 1994; *Thurber*, 1983]. This inverts arrival-times for earthquake locations and three-dimensional V_p and V_p/V_s fields using an iterative, damped least squares method. The V_p images agree well with the known geological structure of the area. The V_p/V_s ratio showed a strong negative anomaly beneath Mammoth Mountain in the upper 2 km (Figure 1.13). *Julian et al*. [1998] interpreted the anomaly as a CO_2 reservoir. This is consistent with a recent study of Kilauea caldera in Hawaii [*Lin et al.*, 2015] that detected low-V_p/V_s ratios which were interpreted as CO_2-filled cracks.

- **Local-earthquake tomography by *Foulger et al.* [2003]**

A similar experiment to that of the 1989 work was carried out using data collected in 1997 [*Foulger et al.*, 1998a; *Foulger et al.,* 1998b]. This work enabled comparison of the results with those from 1989 and study of structural change in the period 1989-1997. *Foulger et al.* [2003] obtained a seismic crustal structure (Figure 1.14) using the same tomography program *simulps12*. A low-V_p/V_s anomaly extending from near the surface to 1 km b.s.l. beneath Mammoth Mountain was imaged. This anomaly increased in strength by up to 3% between 1989 and 1997. The study suggested that CO_2 migrated into the top 2.5 km beneath the centre of Mammoth Mountain between 1989 and 1997 and became depleted in the flanks of the mountain. The source of the CO_2 venting was thought to be a reservoir extending from the surface to at least 1 km depth [*Foulger et al.*, 2003].

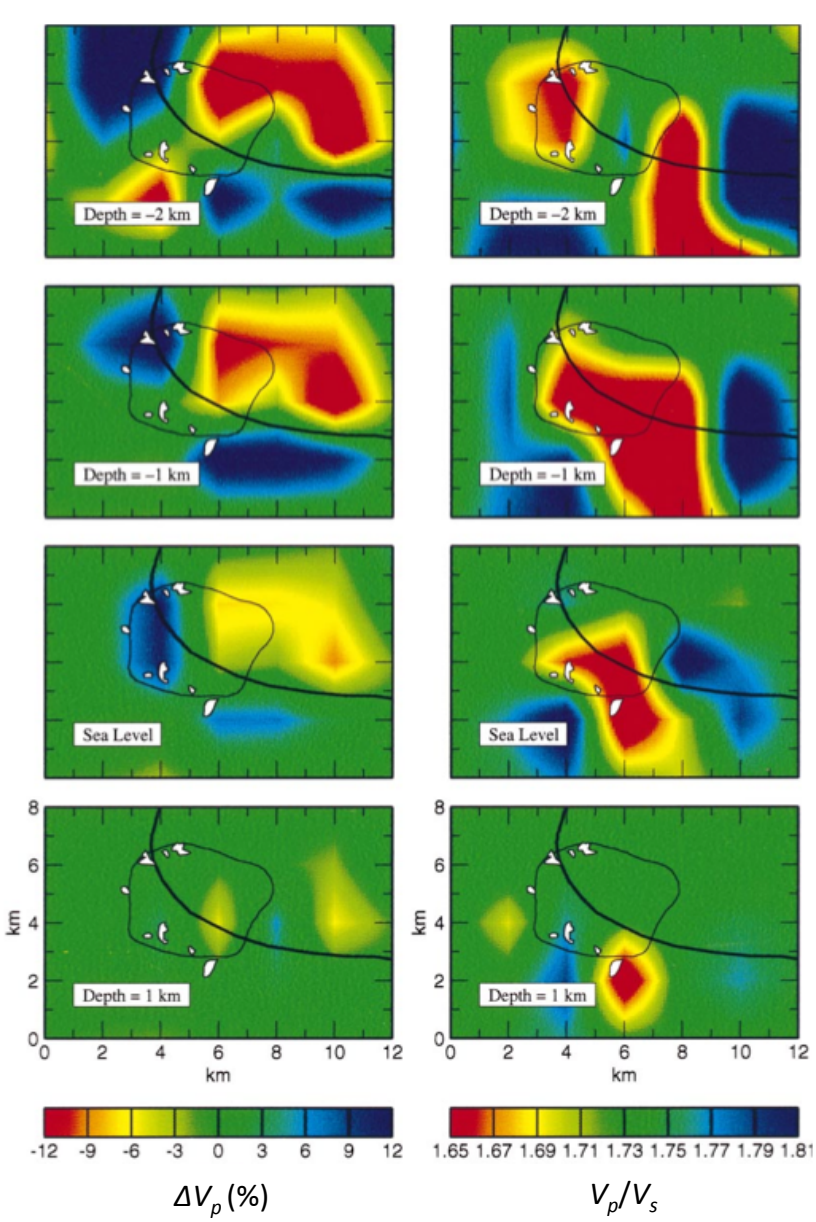

Figure 1.13: The crustal structure beneath Mammoth Mountain to the southwest of Long Valley caldera at depths of -2, -1, 0 and 1 km b.s.l. [from *Julian et al.*, 1998]. Thick black line bounds the caldera; thin black line bounds Mammoth Mountain; white areas: tree-kill areas.

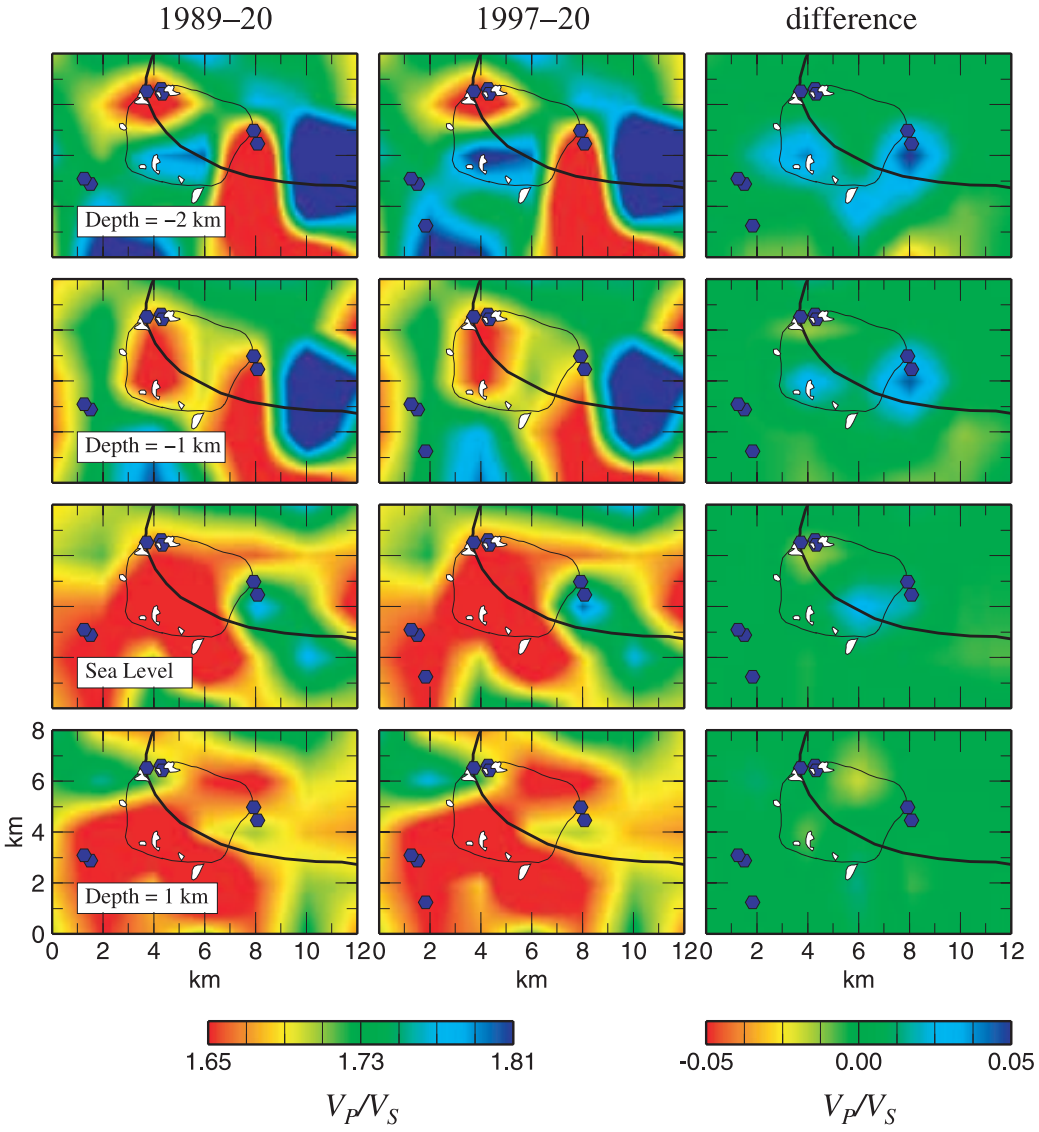

Figure 1.14: V_p/V_s structure at depths of -2, -1, 0 and 1 km b.s.l. for the Mammoth Mountain area [from *Foulger et al.*, 2003]. Map features are as shown in Figure 1.13. (left) and (middle) horizontal slices show structure obtained from inverting the 1989/1990 and 1997 data respectively using a starting model obtained using a combined data set; (right) difference between the middle and the left panels.

- **Local-earthquake tomography by *Seccia et al.* [2011]**

A recent local earthquake tomography and teleseismic receiver function analysis [*Seccia et al.*, 2011] using the same tomography algorithm as used by *Foulger et al.* [2003] and *Julian et al.* [1998] yielded a crustal structure for Long Valley caldera characterized by low-V_p anomalies at depths of 4-5 km b.s.l. beneath the resurgent

dome and > 6 km b.s.l. beneath the southern margin of the caldera (Figure 1.15). These were interpreted as a partial-melt volume for the first anomaly and a larger mid-crustal magma body for the other anomaly in agreement with that suggested by previous teleseismic studies [*Dawson et al.*, 1990; *Weiland et al.*, 1995]. This supports the view that this deeper magma body feeds the shallower one in a complex magmatic system underlying the caldera. At shallower depths (upper 3 km) a high-V_p body above the low-V_p anomalies at the centre of the resurgent dome was attributed to the structural uplift of the resurgent dome.

- **Local-earthquake tomography by *Lin* [2015]**

New three-dimensional V_p and V_p/V_s models for Long Valley caldera and its adjacent fault zones were obtained by *Lin* [2015] using the same tomography algorithm as used by *Seccia et al.* [2011]. Data from 1984-2014 from the Northern California Earthquake Data Center (NCEDC) were used. The resulting V_p models agreed well with those of *Seccia et al.* [2011]. However, low V_p/V_s values were detected beneath the south moat at depths > 1 km b.s.l. (Figure 1.16) which are inconsistent with the presence of partial melt suggested by previous studies [*Seccia et al.*, 2011; *Weiland et al.*, 1995].

Low V_p and high V_p/V_s values were resolved between ~2-4 km b.s.l. beneath the resurgent dome and above 1 km b.s.l. beneath the south moat. This can be attributed to the existence of partial melt for the first and hydrous magmatic fluids for the second anomaly [*Lin*, 2015]. Below 1 km b.s.l. under the south moat and adjacent Sierra Nevada, low V_p/V_s is generally dominant corresponding to the fault zones in these areas [*Lin*, 2015].

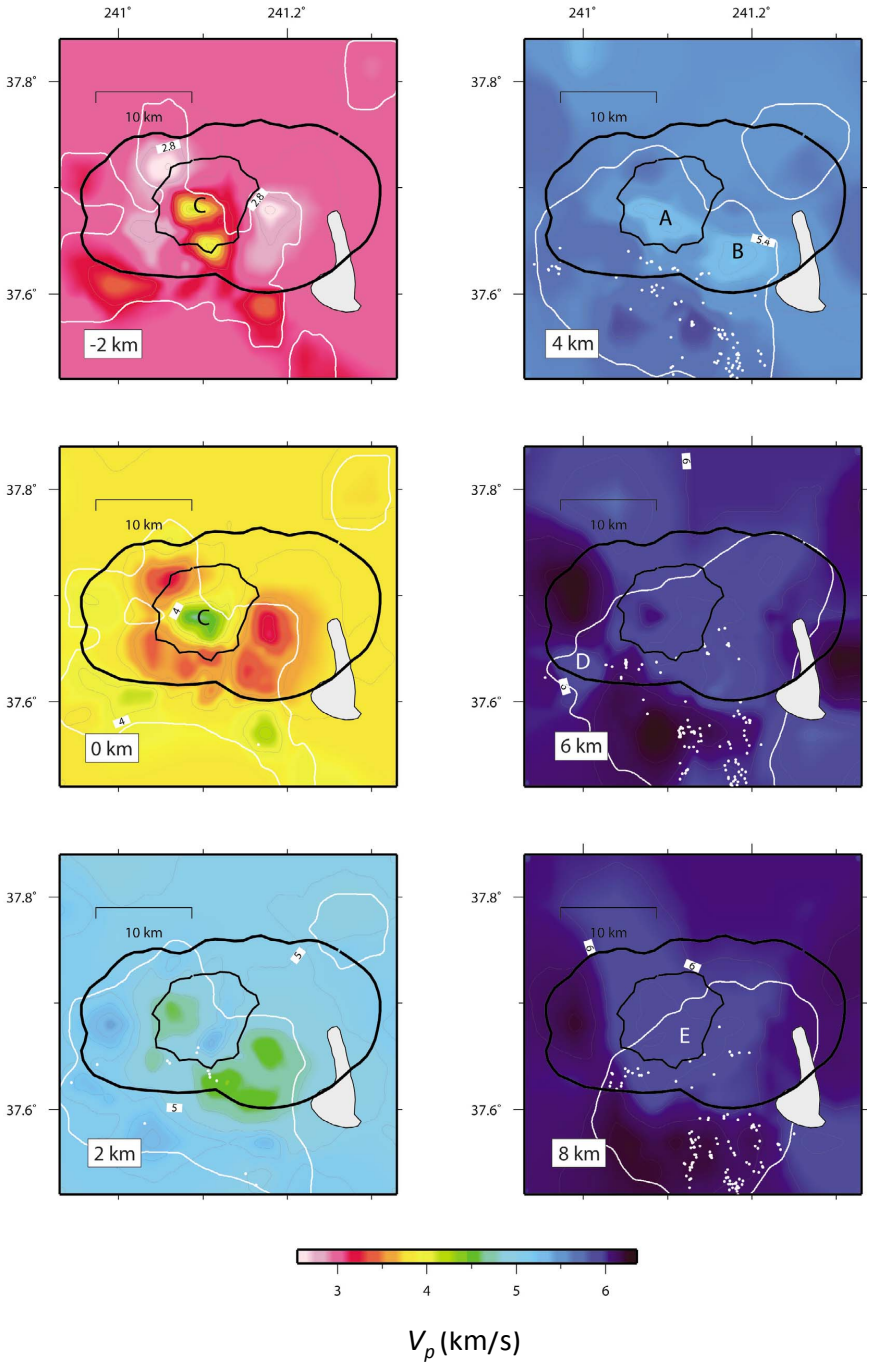

Figure 1.15: Velocity variations at depths of -2, 0, 2, 4, 6 and 8 km b.s.l. beneath Long Valley caldera [from *Seccia et al.*, 2011]. The white line outlines the limits of the resolved regions where the spread function (Section 3.2.7) is ≤ 3.0. White circles are locations of seismicity at depths within 1 km above and below each layer. A, B and D, low-V_p bodies beneath the resurgent dome, Hot Creek and Mammoth Mountain respectively; C, high-V_p body beneath the resurgent dome; E, low-V_p anomaly beneath the Long Valley caldera.

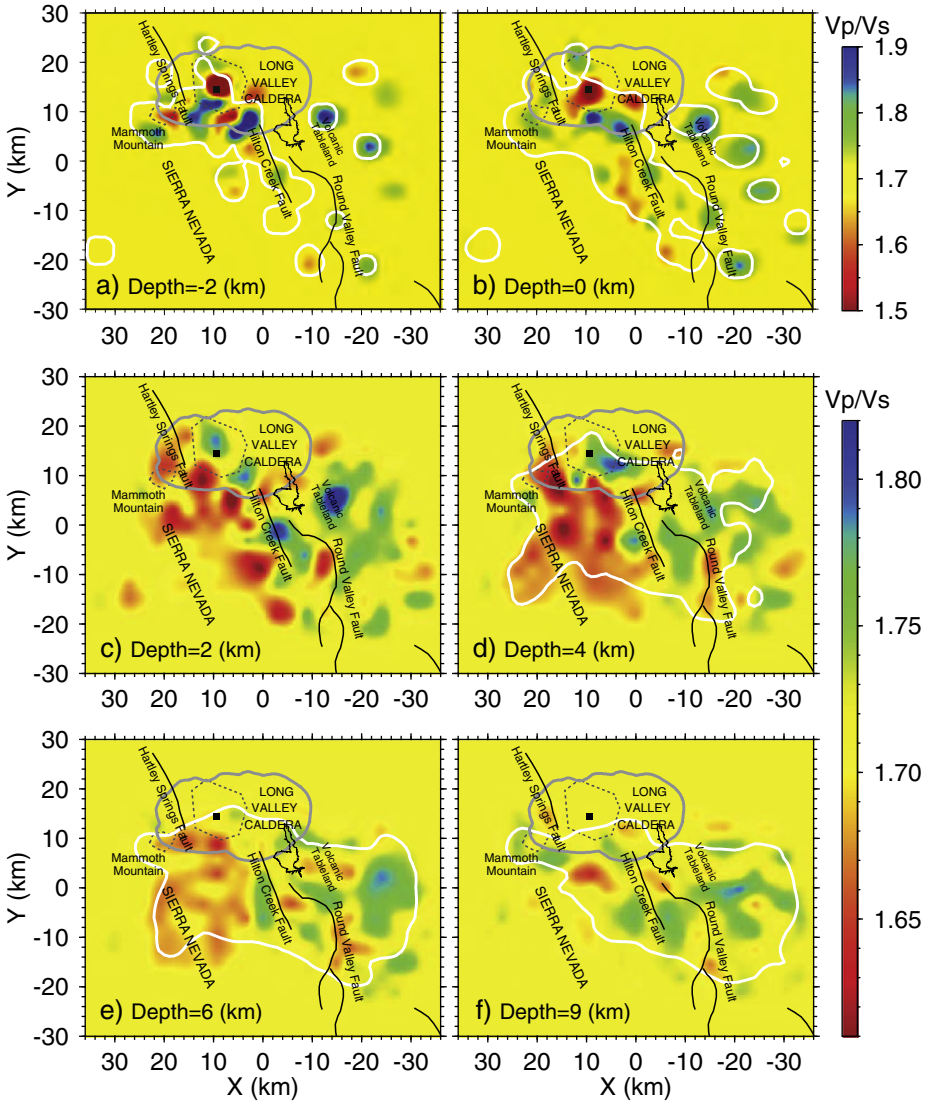

Figure 1.16: V_p/V_s model at different depths [from *Lin*, 2015]. White contours enclose the well-resolved areas. Black lines are the surface traces of mapped faults and Crowley Lake. Dotted lines bound Mammoth Mountain and the resurgent dome. Black square shows the location of the 3-km deep Long Valley Exploratory Well (LVEW).

- **Summary of tomography studies**

Low-V_p/V_s anomalies were detected beneath Mammoth Mountain at variable depths in different studies. These were at depths of 4-5 km b.s.l. interpreted as hydrothermal fluids [*Sanders*, 1993], and in the upper 2 km, interpreted as a CO_2 reservoir [*Foulger et al.*, 2003; *Julian et al.*, 1998].

Low-V_p anomalies were detected beneath the resurgent dome at variable depths, more than 4 km, 5-28 km, 4-5 km and 2-4 km, by different studies [*Dawson et al.*, 1990; *Sanders*, 1993; *Seccia et al.*, 2011; *Weiland et al.*, 1995]. All were interpreted as magma bodies.

A low-V_p anomaly at depths > 6 km b.s.l. beneath the southern margin of the caldera was interpreted as magma body [*Seccia et al.*, 2011]. This observation was not confirmed by another study by *Lin* [2015] that detected low-V_p/V_s at depths > 1 km beneath the south moat. Tomography results for Long Valley caldera are thus somewhat variable from study to study.

1.4 Other geophysical studies

Many geophysical studies have been performed in the Long Valley caldera region. *Savage and Cockerham* [1984] studied 19 earthquakes of the swarm of January 1983 and determined fault-plane solutions. These reflect a mixture of right-lateral strike-slip and normal faulting beneath the Casa Diablo Hot springs area (Figure 1.17), and pure right-lateral strike-slip faulting further east on the South Moat fault (Figure 1.17).

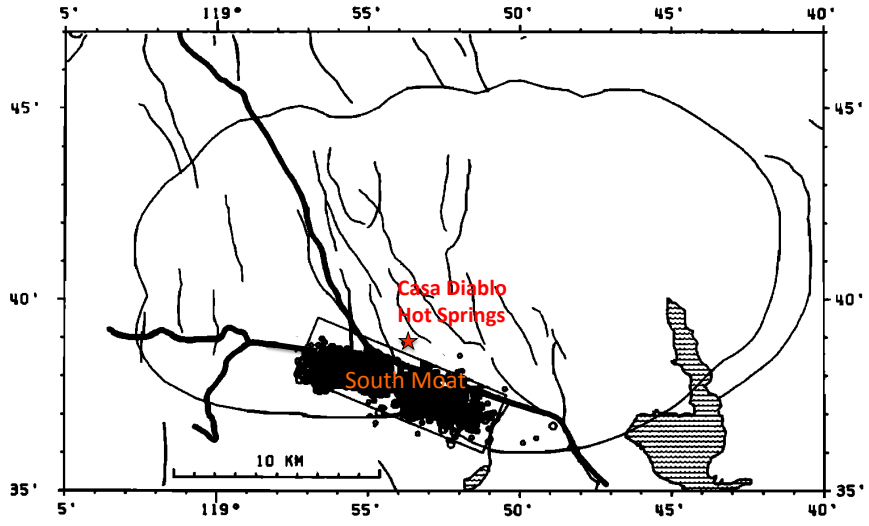

Figure 1.17: Map showing the epicentres of the earthquake swarm of January 7 through January 31, 1983 enclosed in the box along the south moat. Long Valley caldera boundary and faults are shown by thin solid lines and highways by thick lines [from *Savage and Cockerham*, 1984].

Several attempts have been made to locate the source of the inflation of the resurgent dome. *Rundle and Hill* [1988] determined the inflation to be associated with the filling of magma body centered at a depth of 6-10 km beneath the resurgent dome. *Hill et al.* [1990] and *Langbein et al.* [1993] suggested a magmatic intrusion into the crust underneath Mammoth Mountain as a trigger for the intense swarm in 1989. Using seismic and continuous deformation networks, *Hill et al.* [1995] studied Long Valley caldera response to the M=7.3 Landers earthquake in June 1992. Their findings were more consistent with a model that suggests a transient pressurization of magma bodies beneath the resurgent dome and Mammoth Mountain. This is compatible with previous studies that found that the seismic activity and ground deformation in Long Valley caldera are consistent with pressure increase in two small magma bodies in the upper crust located beneath the central part of the resurgent dome at depths of 7-8 km [*Langbein et al.*, 1993] and beneath Mammoth Mountain at a shallow but poorly constrained depth [*Pitt and Hill*, 1994; *Sorey et al.*, 1993]. *Langbein et al.* [1995] studied the inflation of Long Valley caldera near Mammoth Mountain using both line measurements using a two-color geodimeter network, and leveling data. These provided evidence for dyke intrusion beneath Mammoth Mountain in the period 1988-1992, likely associated with a swarm of small earthquakes in the summer of 1989. Figure 1.18 shows deformation and seismicity in Long Valley caldera for the period 1983-1991.

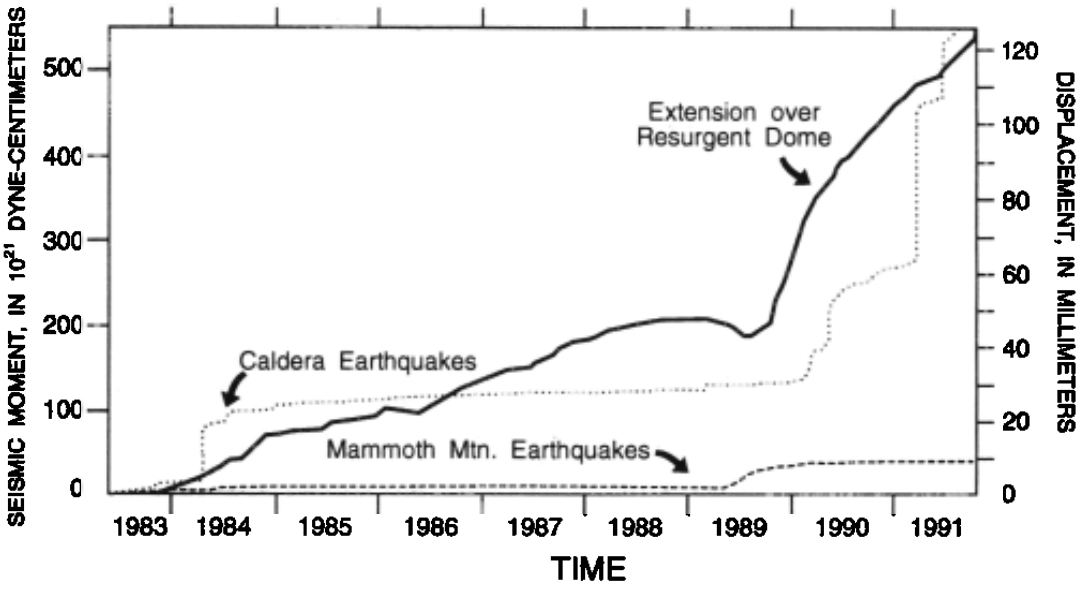

Figure 1.18: Extension over the resurgent dome in Long Valley caldera (solid black line corresponding to the right y-axis), determined using a two-color geodimeter network, and cumulative seismic moment for earthquakes under Mammoth Mountain and in the south central part of the caldera [from *Sorey et al.*, 1993].

Following the earthquake swarm in 1989, which was thought to be associated with a shallow intrusion [*Farrar et al.*, 1995; *Hill et al.*, 1990; *Rahn et al.*, 1996], areas of tree kill began to appear on the flanks of Mammoth Mountain in 1990 (Figure 1.19). They occupy > 500 km^2 with high CO_2 concentrations in the soil (20-90%) and CO_2 flux rates of ~500 tonnes per day. *Farrar et al.* [1995] carried out a soil-gas survey in 1994 in the tree-kill area (Figure 1.20) and estimated a CO_2 flux of ≥ 1,200 tonnes per day. Considering the magnitude and duration of the CO_2 flux, *Farrar et al.* [1995] and *Rahn et al.* [1996] suggested the emissions came from a large reservoir of high-pressure gas, and indicated magmatic unrest.

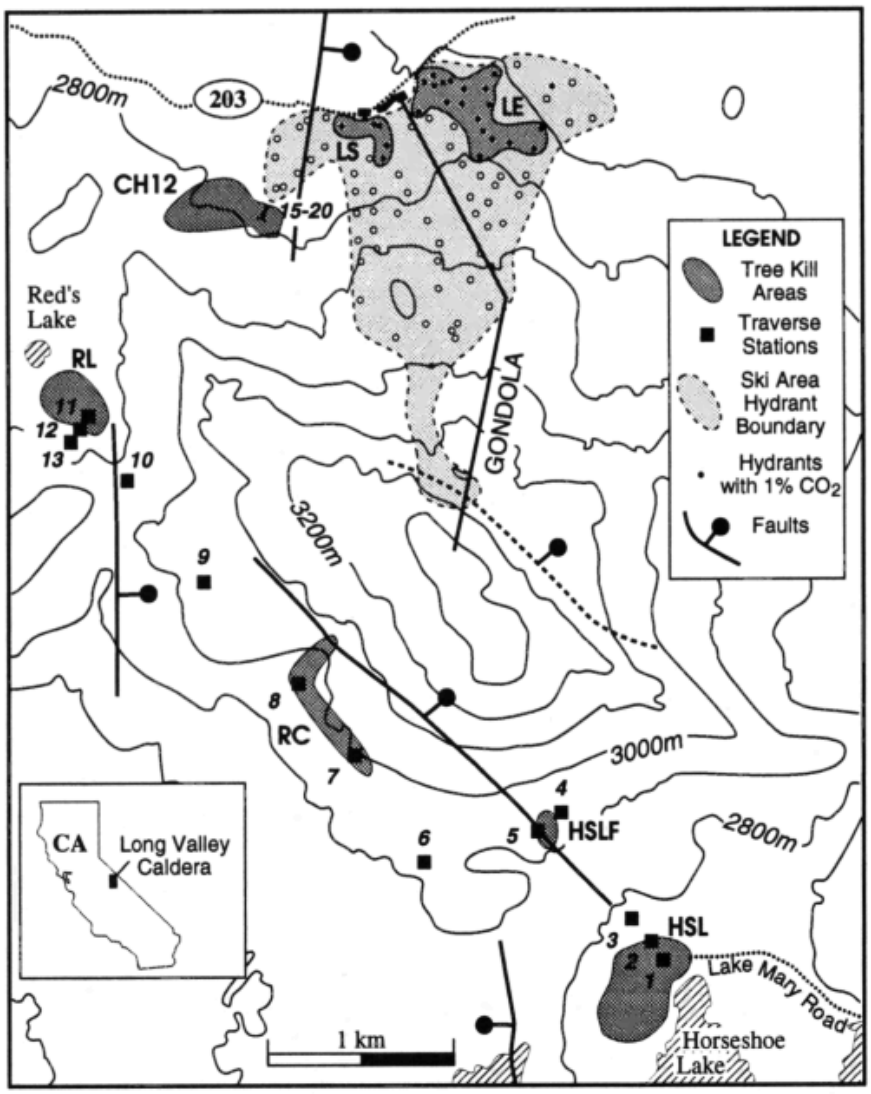

Figure 1.19: Map of Mammoth Mountain area. Dark grey indicates the tree kill areas of Horseshoe Lake (HSL), Horseshoe Lake Fumarole (HSLF), Lodge East (LE), Lodge South (LS), Red's Lake (RL), Chair12 (CH12), and Red's Creek (RC) [*Rahn et al.*, 1996].

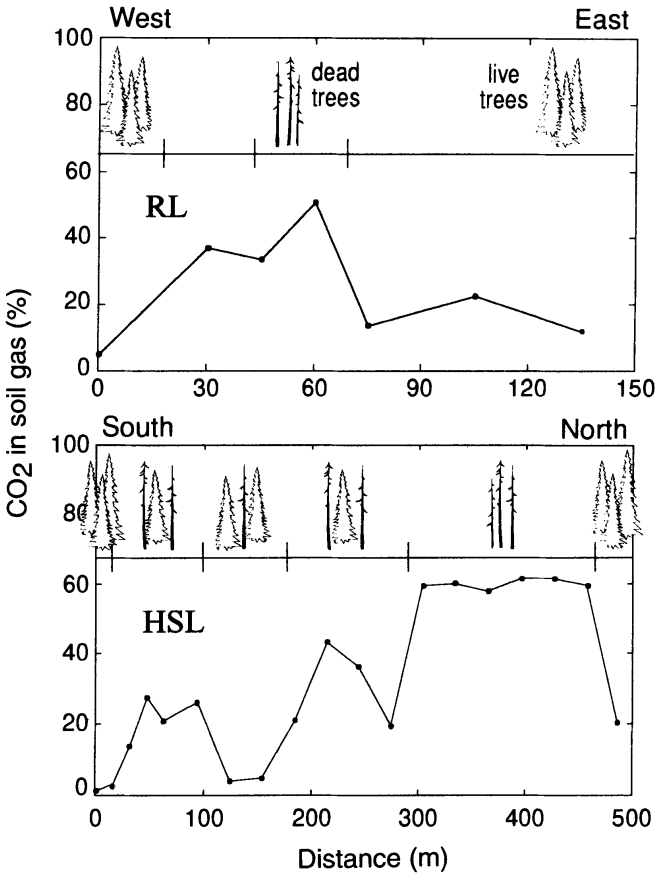

Figure 1.20: Carbon dioxide concentrations along transects in both the RL and HSL areas (Figure 1.19) where top panel represent measurements along transect RL and bottom panel measurements along transect HSL. Both were taken in September 1994 at 0.6 m depth. Symbols at the top denote relative degree of tree mortality along the transect [from *Farrar et al.*, 1995].

Gerlach et al. [1998] confirmed a decline in CO_2 emissions between 1995 and 1997, followed by another onset of degassing in late in 1997. They concluded that direct degassing from a shallow magma intrusion could not be the cause of the degassing events in 1997, since the gas continued to be cold and devoid of other magmatic gases except for helium. They suggested that accumulated CO_2 in a reservoir at depth was released to the surface by a fault.

Werner et al. [2014] measured CO_2 emission rates yearly from 1995 to 2013 at Horseshoe Lake (HSL), the largest tree kill area on Mammoth Mountain, and intermittently at four smaller degassing areas around Mammoth Mountain from 2006 to 2013. The measurements at HSL show decadal-scale variations in diffuse CO_2

degassing with peaks in 2000–2001 and 2011–2012 following peaks in seismicity (Figure 1.21). The seismic activity was thought to result from the addition of deep fluids to a shallow reservoir causing pressurization events.

The delayed transport to the surface results from the time it takes for the pressure front to move CO_2-rich fluids along fault pathways, something that has been observed at other volcanoes such as Solfatara in Campi Flegrei, Teide and Vesuvius [*Werner et al.*, 2014]. This was discussed by *Lewicki et al.* [2014] who reported a pattern of elevated deep, then shallow seismicity beneath Mammoth Mountain from 2006-2012. They suggested this was triggered by upward immigration of CO_2-rich magmatic fluids from basaltic intrusions in the middle to lower crust. The magmatic fluids increased the pore pressure in an existing CO_2-charged reservoir and fractured the reservoir cap rock allowing CO_2 to be released to the surface. Between the diffuse degassing events, pore fluid pressure probably decreased in the reservoir, along with CO_2 emissions, but some fractures likely remained open allowing for continuous CO_2 emissions to the surface at moderate levels [*Lewicki et al.*, 2014].

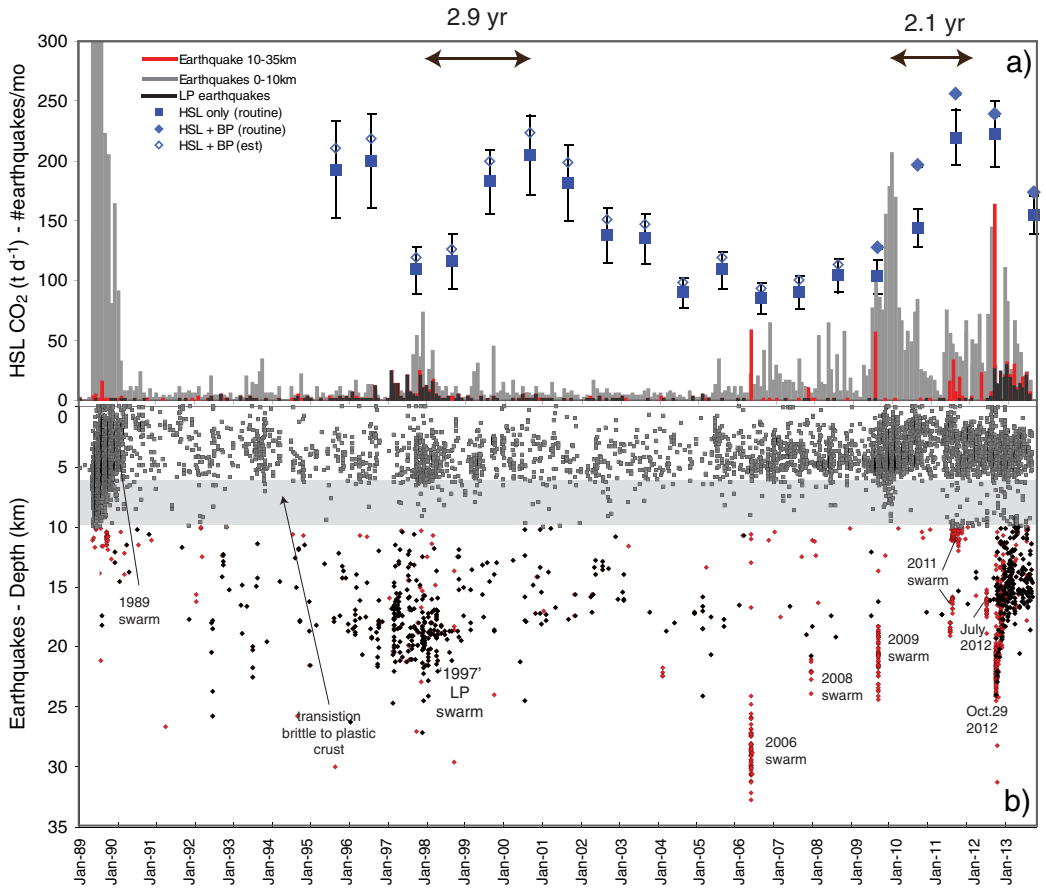

Figure 1.21: Emission rates from HSL and Borrow Pit (BP) for 1995–2013 and monthly counts of earthquakes below Mammoth Mountain [from *Werner et al.*, 2014]. Earthquake data from the NCEDC (*http://www.ncedc.org/ncedc/catalog-search.htm*).

A gravity study by *Battaglia et al.* [1999] showed that gravity within the caldera decreased between 1982-1998 with the largest gravity decease in the resurgent dome (Figure 1.22). The study suggested that basaltic magma intruded at ~11.6 km depth beneath the resurgent dome. They excluded thermo-elastic deformation or hydrothermal fluids as sources for the change in gravity.

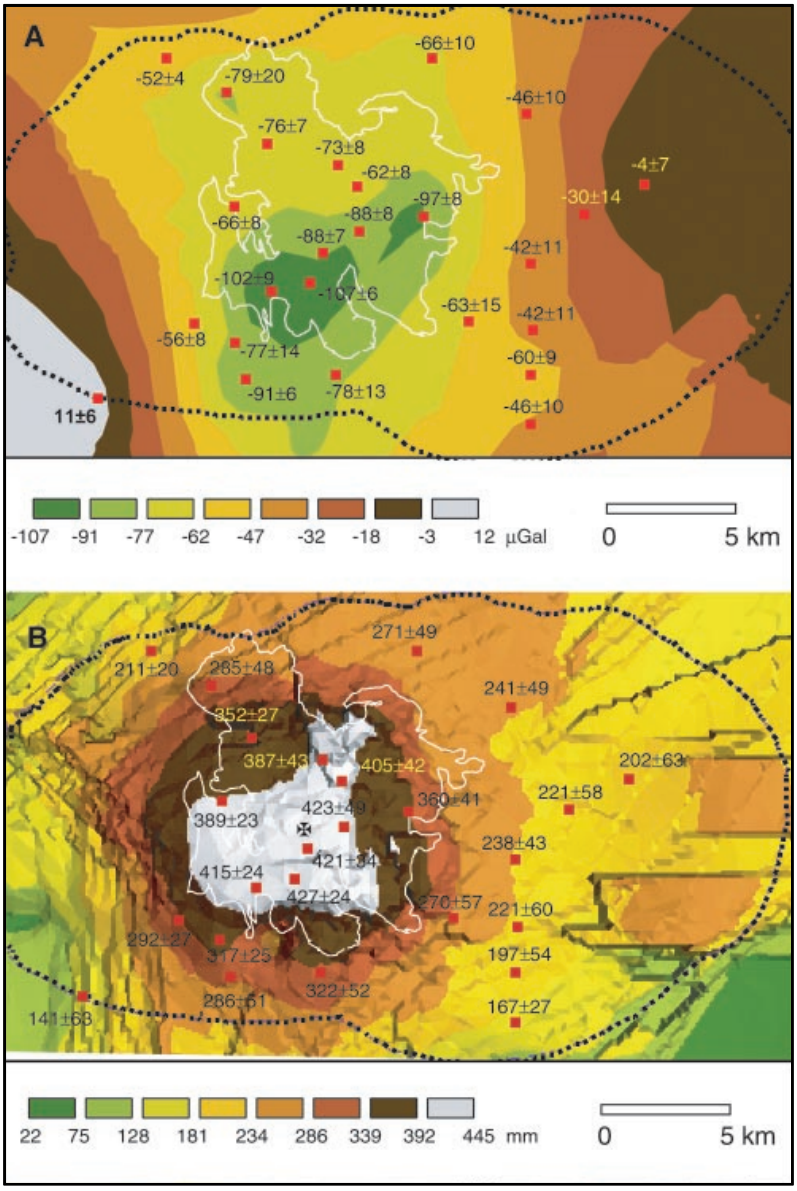

Figure 1.22: (A) Map showing gravity changes (in microgals) in Long Valley caldera for the period July 1982 – July 1998. The resurgent dome is bounded by a white line. (B) Uplift at Long Valley caldera during the same period as (A). [from *Battaglia et al.*, 1999].

Dreger et al. [2000] obtained moment tensors for six M 4.6 - 4.9 earthquakes near Casa Diablo Hot springs in the swarm in November 1997. Four of the events were found to have non-double-couple moment tensors. This was interpreted as indicating that a hydrothermal or magmatic fluid injection caused the earthquakes. *Foulger et al.* [2004] found non-double-couple mechanisms and volume increase components for many smaller earthquakes (0.4 < M <3.1) in the summer of 1997 by inverting *P*- and

S-wave polarities and amplitude ratios (Figure 1.23). They interpreted these observations as indicating that cracks with fluid flow caused the earthquakes. Such focal mechanisms have also been observed in geothermal areas, *e.g.*, The Geysers and the Coso geothermal area [*Ross et al.*, 1999].

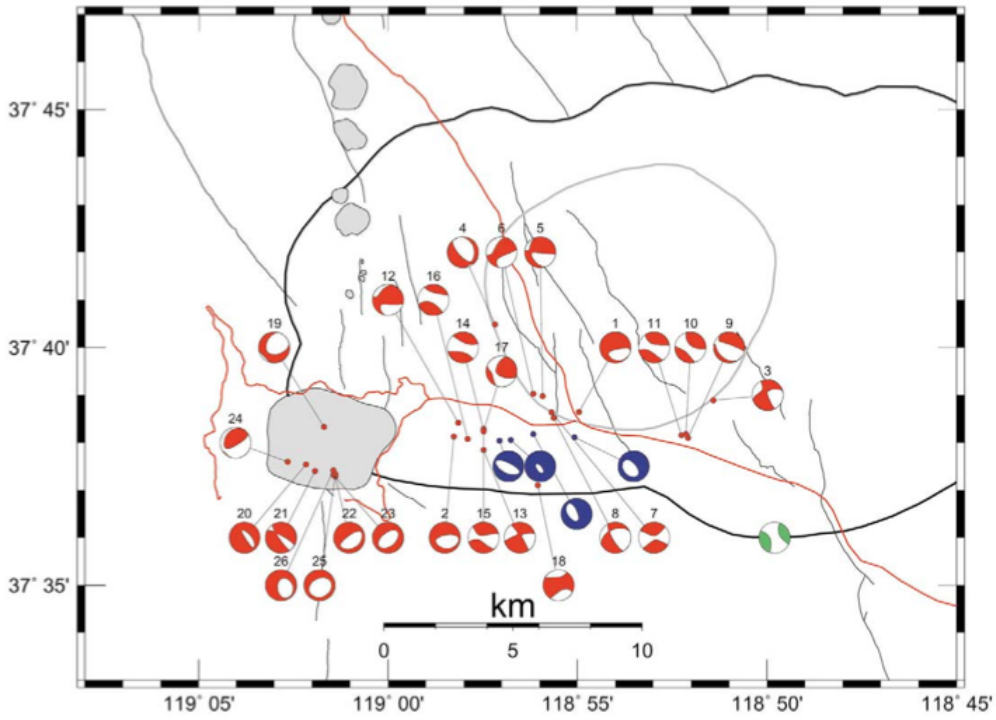

Figure 1.23: Map showing Long Valley caldera and earthquake focal mechanisms. Thick black line: the caldera boundary; thin grey lines: faults; grey line: the resurgent dome boundary; red lines: highways. Mammoth Mountain is shown in grey to the southwest of the caldera and the Inyo domes are shown in grey to the northwest. Coloured circles show focal mechanisms as reported by *Foulger et al.* [2004] in red, *Dreger et al.* [2000] in blue, and *Julian and Sipkin* [1985] in green. Each circle shows the far-field *P*-phase polarity pattern on an equal-area projection of the upper focal hemisphere, with the compressional field filled [from *Foulger et al.*, 2004].

Hill [2006] suggested that 'leaky' strike-slip fault zones in the south moat provide pathways for magmatic fluids to migrate from the mid-lower crust into the upper 10 km (Figure 1.24). He also proposed that three magmatic sources were associated with the unrest in the caldera, an inflation source 6 to 7 km beneath the resurgent dome, another beneath the western part of the south moat, and basaltic dykes at depths of 10-

25 km beneath the southwest flank of Mammoth Mountain. The latter was consistent with the long-period volcanic earthquakes that occur there.

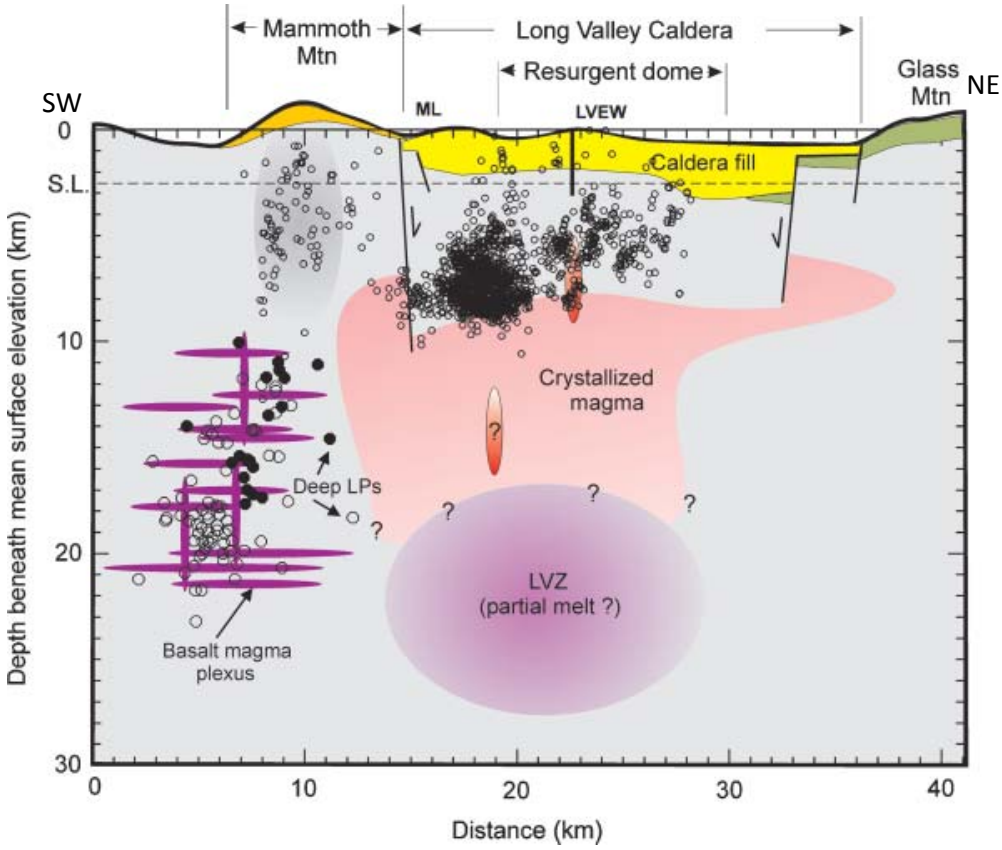

Figure 1.24: Schematic northeast-southwest cross-section through Long Valley caldera and Mammoth Mountain illustrating the structural and magmatic elements [from *Hill*, 2006]. LVEW is the 3-km-deep Long Valley Exploratory Well in the centre of the resurgent dome. Small circles are hypocenters for earthquakes ($M \geq 2$) for 1978-2004. Large circles are hypocenters for mid-crustal long-period earthquakes with filled circles indicating hypocenters constrained by a dense, temporary seismic network deployed in 1997 [*Foulger et al.*, 1998a]. Orange ellipsoids indicate inflation sources. Deep structure (>10 km) is less certain, but teleseismic tomographic studies [e.g., *Dawson et al.*, 1990; *Weiland et al.*, 1995] provide evidence for a volume of low-V_p in the 15-30 km depth range.

CHAPTER 2

BACKGROUND : THE COSO GEOTHERMAL AREA

2.1 Tectonic evolution

The Coso geothermal area (Figure 2.1) is located in central eastern California between the southern Sierra Nevada to the west and the Basin and Range province to the east. Tectonically, this area is controlled by the interaction between the western margin of the North American plate and the Pacific plate, resulting in shear along a strike-slip fault zone [*Miller et al.*, 2001]. This corresponds to the transition between the strike-slip San Andreas fault in the west and the extensional Basin and Range province to the east [*Roquemore*, 1980; *Walter and Weaver*, 1980].

A considerable number of roughly north-trending normal faults reflect tectonics dominated by east-west lithospheric extension in the area [*Duffield et al.*, 1980], between two northwest-striking dextral faults: the Little Lake and Airport Lake fault zones to the south, and the Owens Valley fault to the north [*Hauksson and Unruh*, 2007] (Figure 2.1 and Figure 2.2). Two major groups of faults fracture the area. One group consists of west-northwest trending faults with right-lateral strike-slip motion in the southern and northwestern parts of the geothermal field and minor northeast trending left-lateral strike-slip faults in the northeast part of the field. The other group consists of north-northeast trending normal faults dipping both east and west with a small component of strike-slip in the north-east and north-west parts of the geothermal field [*Davatzes and Hickman*, 2006; 2010; *Duffield et al.*, 1980; *Feng and Lees*, 1998; *Roquemore*, 1980] (Figure 2.3). The central part of the geothermal area is considered to be a transtensional regime surrounded by a transpressional area [*Bhattacharyya and Lees*, 2002; *Feng and Lees*, 1998].

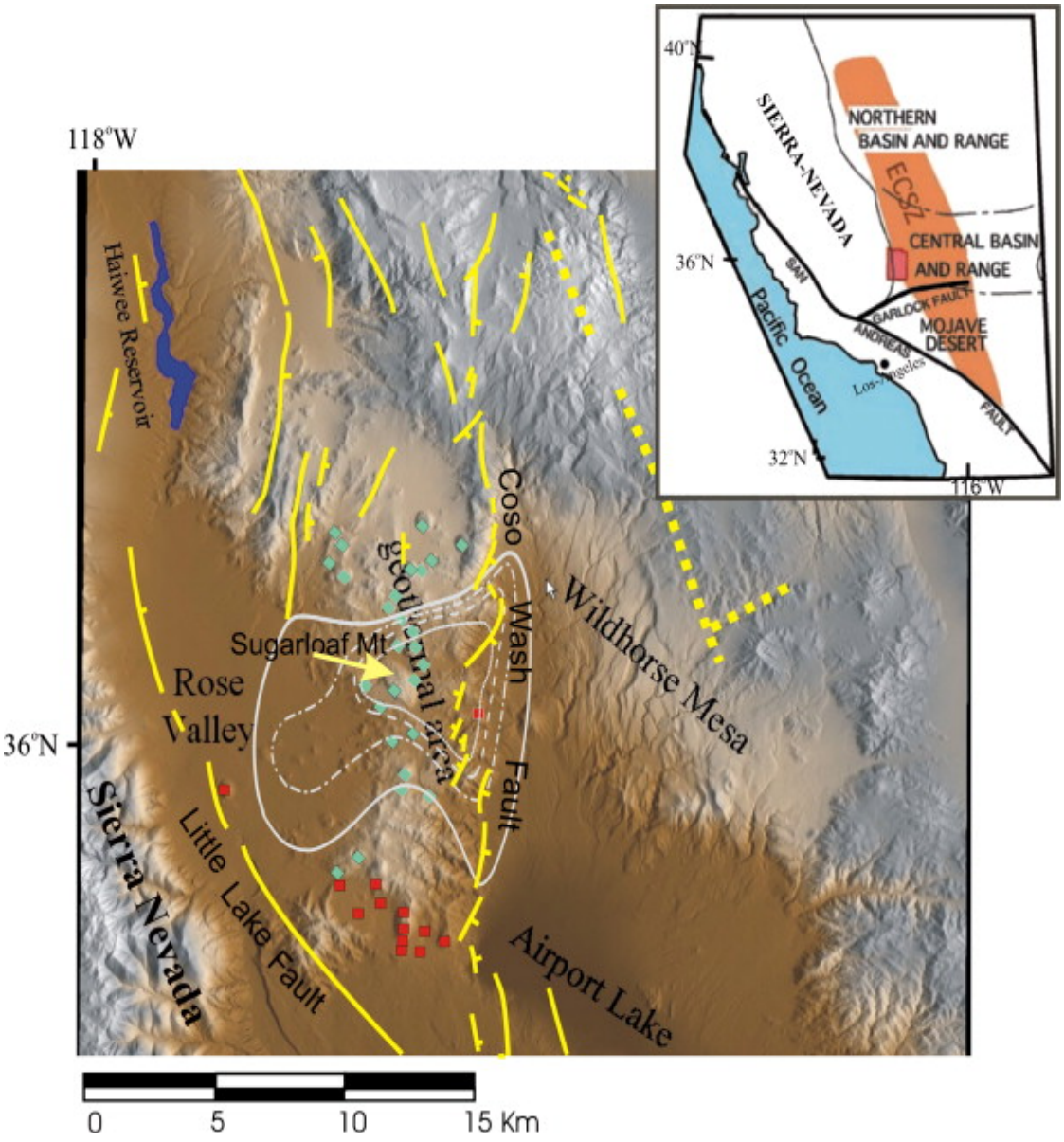

Figure 2.1: Schematic geologic map of the Coso area [from *Simakin and Ghassemi*, 2007]. Yellow lines show the positions of faults dashed where uncertain [*Unruh et al.*, 2003]. Red squares indicate basaltic vents younger than 0.3 Ma [*Wicks et al.*, 2001]; blue diamonds indicate rhyolitic vents younger than 3 Ma. Gray lines are the 3-, 5-, 10-, and 15-heat flow unit (HFU) contours [*Combs*, 1980] where 1 HFU=41.87 mW/m^2. The red rectangle in the inset indicates the position of the Coso geothermal area in the east California shear zone.

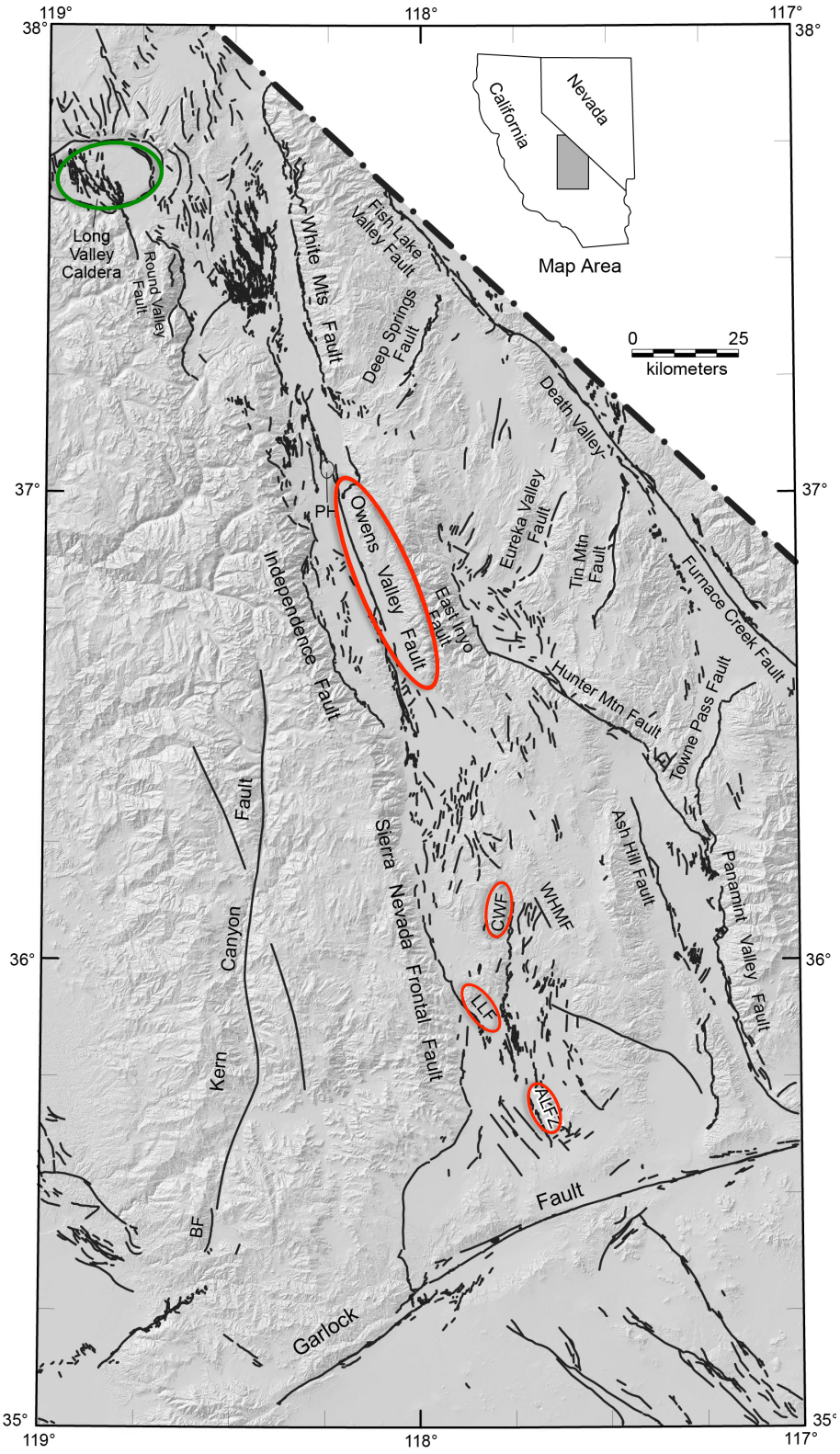

Figure 2.2: Map showing faults in east-central California [from *Stevens et al.*, 2013]. Highlighted fault names are Airport Lake Fault Zone (ALFZ), Coso Wash Fault (CWF), Little Lake Fault (LLF) and Owens Valley Fault. The location of Long Valley caldera is also indicated in green.

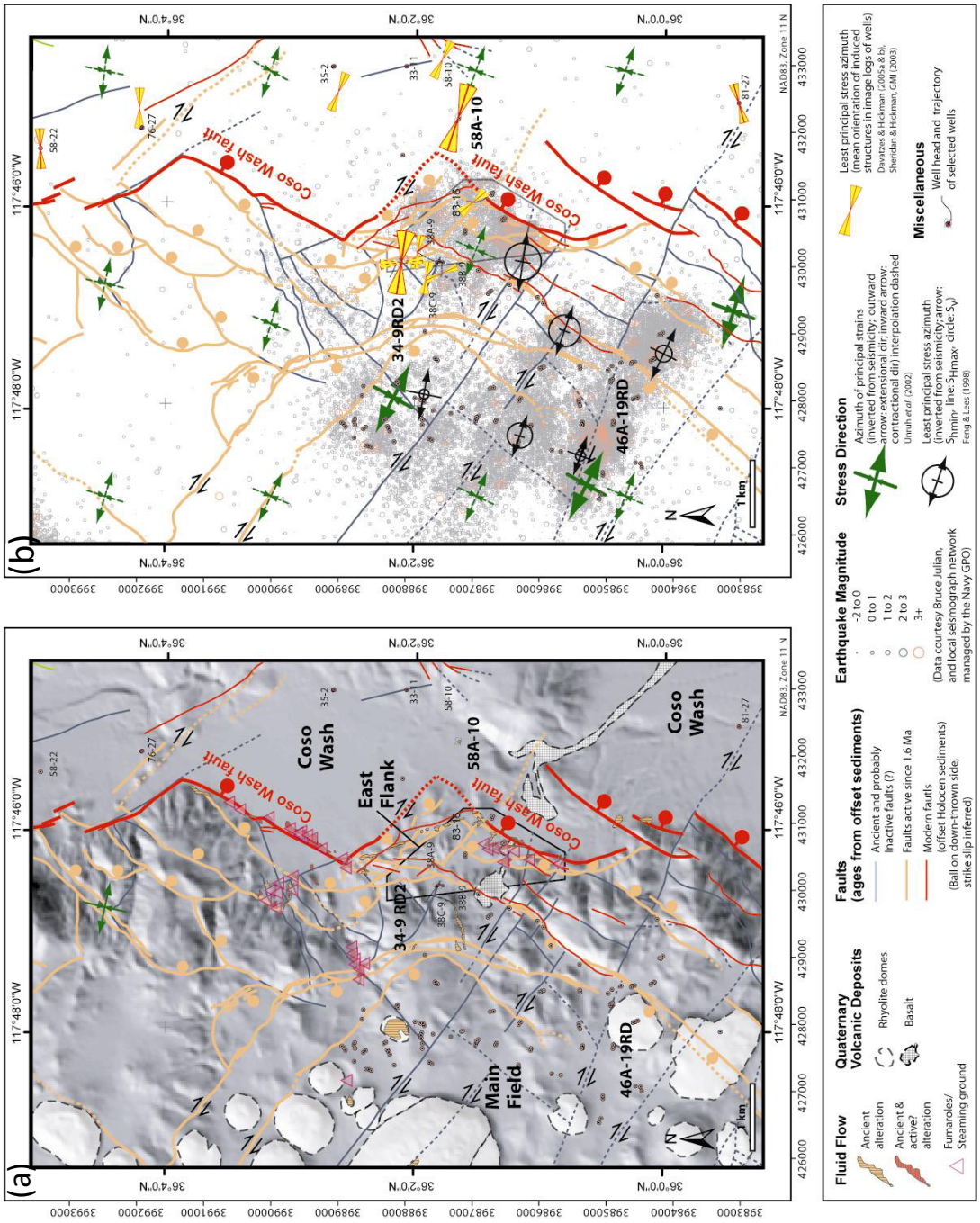

Figure 2.3: Tectonic and stress orientation maps of the east flank of the Coso geothermal field [from *Davatzes and Hickman*, 2006]. (a) Tectonic map based on mapping and results from *Hulen* [1978], *Duffield et al.* [1980], *Whitmarsh* [1998], and *Unruh and Streig* [2004]. (b) Minimum horizontal stress orientations inferred from borehole image logs from *Sheridan et al.* [2003], *Sheridan and Hickman* [2004], and *Davatzes and Hickman* [2005].

2.2 Geology

Mesozoic granitic and metamorphic rocks similar to those found in the adjacent Sierra Nevada underlie the Coso geothermal area [*Duffield*, 1975], most of which is covered by Cenozoic rocks [*Duffield et al.*, 1980]. Numerous igneous rocks ranging from rhyolitic domes to basaltic lava flows of Pleistocene age characterize the geology of the area (Figure 2.4). Surface geothermal features, including the Coso Hot Springs and the Devil's Kitchen [*Adams et al.*, 2000] lie in a northeast-trending belt and coincide with the northern edge of the reservoir. Sinter and travertine deposits occur along a north-trending fault zone on the east flank with travertine to the east side of the field and sinter at the Wheeler prospect. This suggests two different earlier geothermal systems formed these deposits, a low-to-moderate temperature system 307,000 years ago and a high-temperature geothermal system 238,000 years ago [*Adams et al.*, 2000].

The geothermal system is thought to consist of several weakly connected reservoirs heated by and related to a magma body underneath at depths of 5-20 km [*Bacon*, 1982; *Bacon and Metz*, 1984; *Combs*, 1980; *Duffield*, 1975; *Duffield et al.*, 1980; *Walck*, 1988; *Walter and Weaver*, 1980; *Wilson et al.*, 2003]. These are thought to be formed by mantle-derived magma intruded into the crust in response to lithospheric extension [*Bacon*, 1982; *Duffield et al.*, 1980]. *Mordick and Glazner* [2006] proposed that basaltic magma provides the heat source to generate and sustain the rhyolitic magma body beneath the geothermal area. *Monastero et al.* [2005] observed crustal thinning accomplished by high- and low-angle brittle faulting in the upper 4 km of the crust, underlain by the brittle-ductile transition, and suggested a nascent metamorphic core complex beneath the Coso geothermal area.

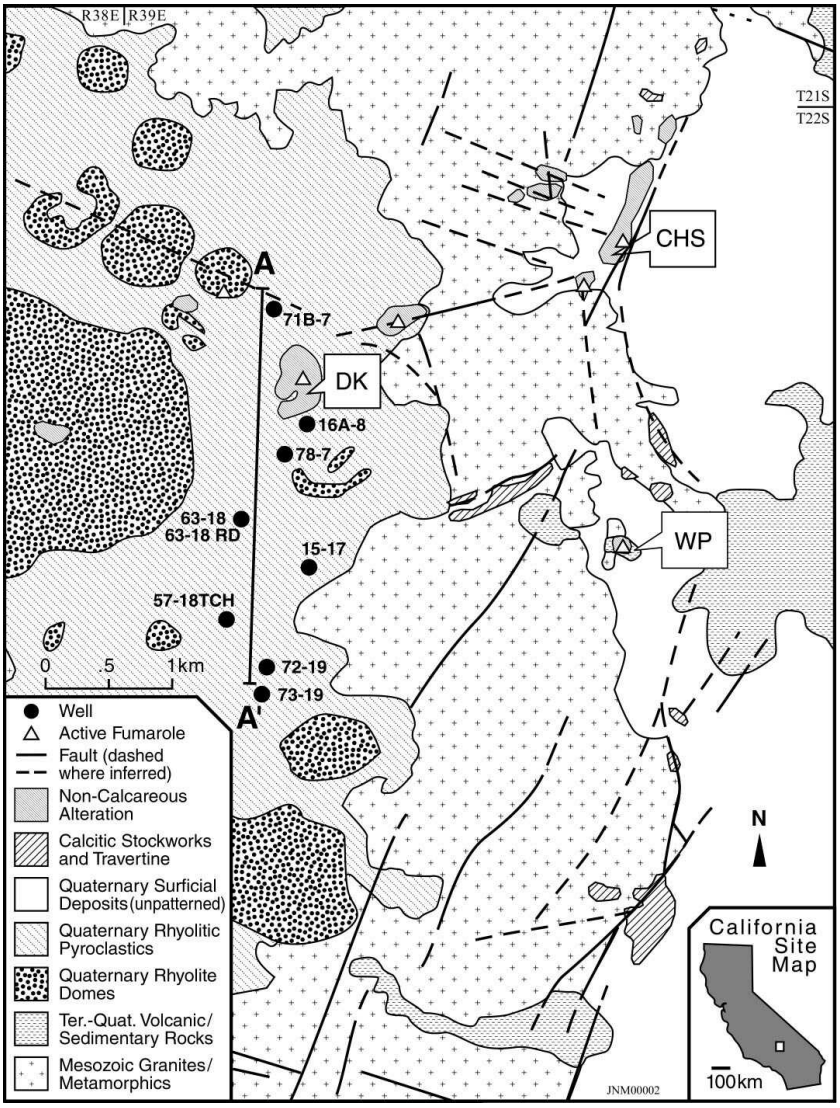

Figure 2.4: Map showing the geology of the Coso geothermal field from *Adams et al.* [2000]. CHS: Coso Hot springs; DK: Devil's Kitchen; WP: Wheeler prospect.

2.3 Commercial exploitation

The Coso geothermal field has been producing geothermal power since 1987. Production began with a 90 MW power plant. Over the following three years additional power plants were installed. At the time of writing, there are over 170 production and injection wells (Figure 2.5) and four geothermal power plants with a total capacity of about 300 MW. The produced electricity is fed into the national grid and used for industrial and domestic consumption.

Seismic monitoring began in 1975 with 16 stations operated by the U.S. Geological Survey. The U.S. Navy has a permanent seismometer network that has been operating since the 1980s. Over 600,000 microseismic events had been recorded by 2011.

The most serious problem facing commercial exploitation of the field is the availability of water for reinjection. The reservoir is rapidly becoming depleted and the water table is reported to have dropped by 1-2km since exploitation began. The US Navy injects as much condensate and other water as possible, but there is still a significant net loss. Since this is a desert area, there is very little available surface run-off water in streams and the situation is made worse because most stream water is piped to Los Angeles for consumption in the city. In The Geysers geothermal area in northern California, grey water is piped to the field from neighbouring towns, but this solution is not available for Coso because there are few settlements of any size nearby.

The present study, to assess bulk change in the seismic structure of the reservoir using time-dependent tomography, is thus important to monitor depletion of the field. At the same time, much operational data is proprietary and the possibility to calibrate the seismic results using extraction and reinjection data is limited at the present time.

2.4 Seismicity

2.4.1 Seismic networks

Seismicity within the Coso geothermal field is recorded by the Navy Geothermal Program Office using both surface and down-hole seismometers, most of which are three-component. Since the early 1990s, the U.S. Navy has operated a network of 18 three-component digital borehole seismometers in the area, 13 of them within or near the producing field and providing high-quality microearthquake data (Figure 2.5).

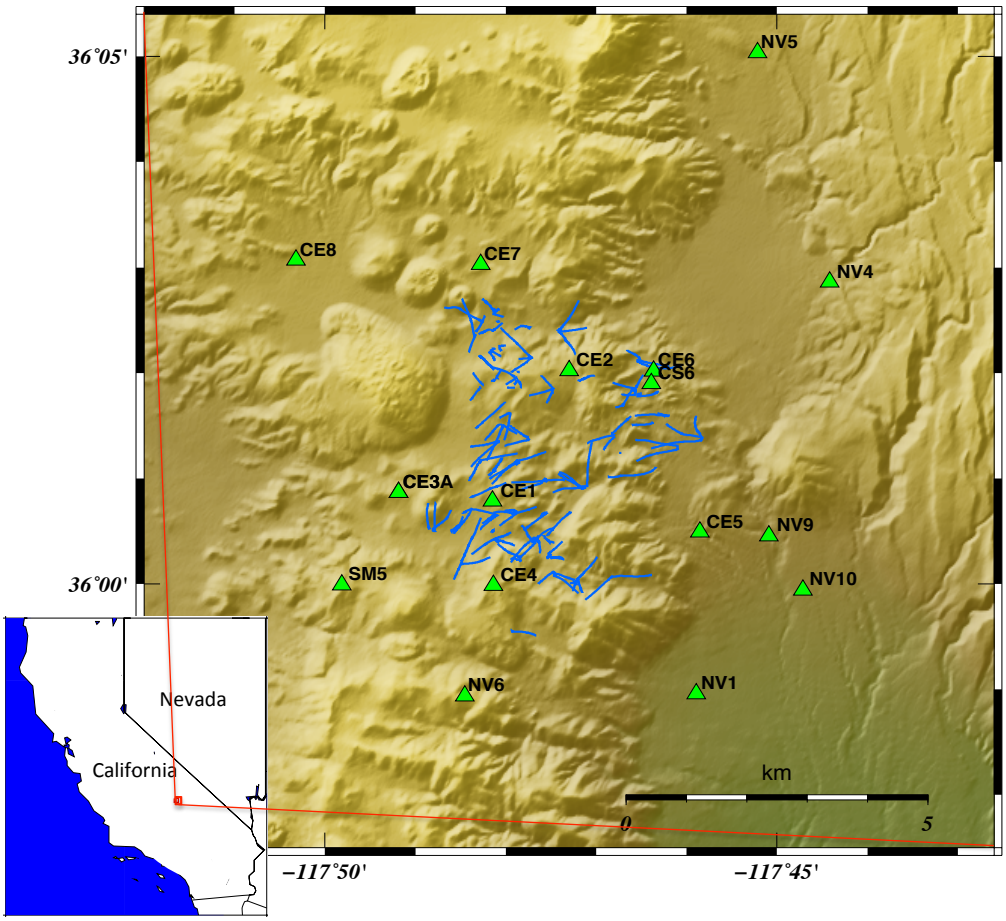

Figure 2.5: Map of the Coso geothermal area showing shaded topographic relief. Green triangles are seismic station locations. Blue lines are the surface projections of geothermal wells marking the location of the geothermal field. Inset map shows the location in California of the main map.

2.4.2 History of seismic monitoring

The Coso geothermal area is one of the most active seismic areas of southern California with typically more than 20 earthquakes per day. Most occur at depths of 1-8 km in a zone striking approximately north-south [*Walter and Weaver*, 1980]. Most events are less than 3 km deep and are surrounded by regional seismicity that extends down to 12 km depth [*Vlahovic et al.*, 2002]. Examples of those regional earthquakes are the M 5.8 Ridgecrest earthquake in 1995 [*Hauksson et al.*, 1995] and the M 5.0 earthquake which occurred ~10 km northeast of Coso in 1998 (Figure 2.6). *Kaven et al.* [2013] showed that seismicity in the area is concentrated in the main field

to the southwest and the east flank to the northeast with aseismic areas in between (Figure 2.7).

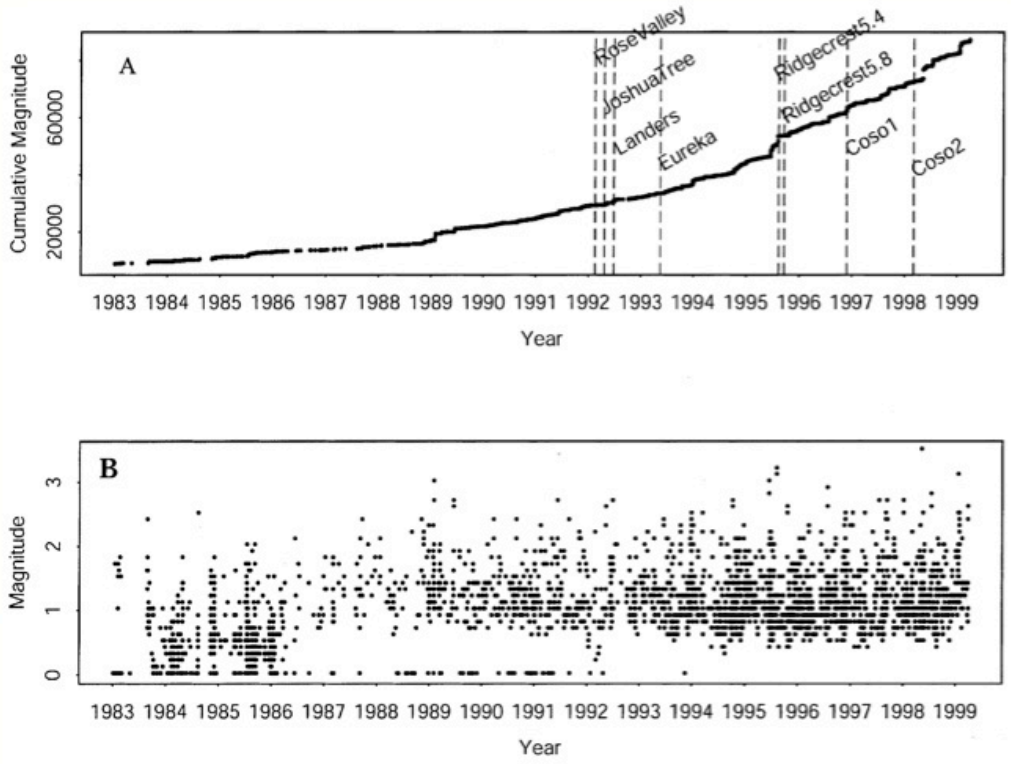

Figure 2.6: Seismicity distribution in the Coso geothermal field [from *Bhattacharyya and Lees*, 2002]. (A) Cumulative magnitude for 1983-1999. Increase in seismic moment release occurred following the Ridgecrest and the Coso Range (Coso1 and Coso2) events. The small increase in 1989 coincides with a relatively large earthquake (M~3.0) inside the geothermal field. (B) Distribution of earthquake magnitudes.

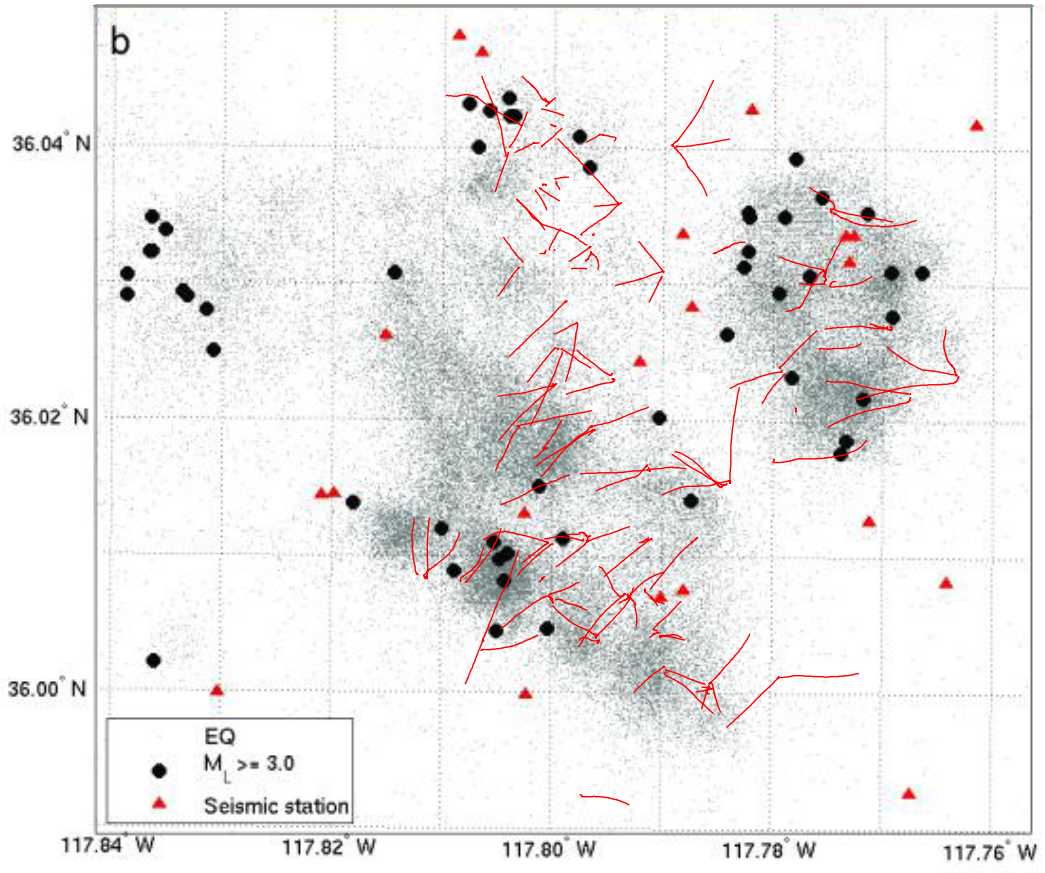

Figure 2.7: Map of the Coso geothermal field [modified from *Kaven et al.*, 2013] showing seismicity over the period April 1996 - May 2012. Grey dots are locations of earthquakes smaller than M_L 3.0. Black dots are locations of events with $M_L \geq 3.0$. Red triangles are stations. Red lines are the surface projections of wells. The cluster of seismicity in the northeast corresponds to the east flank and the more diffuse seismicity to the west corresponds to the main production field.

2.4.3 Previous tomography studies

Several early tomography studies were performed for Coso. Local earthquake seismic tomography applying a back-projection technique to *P*-phase arrival times to obtain an upper crustal seismic wave speed image was done by *Walck and Clayton* [1987]. This showed a low-V_p block (7% perturbation anomaly) beneath the Coso geothermal area, about 10 km southeast of Devil's Kitchen at 5-10 km depth. It was suggested to be an extension of a deep magma chamber consistent with a previous teleseismic study that identified a low-V_p body below 5 km depth southeast of Devil's Kitchen

[*Reasenberg et al.*, 1980]. This was thought to be associated with partial melt in the middle crust.

Walck [1988] performed a second iterative back-projection tomographic inversion for three-dimensional variations of the ratio of compressional to shear velocity V_p/V_s. This work showed very low values of V_p/V_s near the surface near Devil's Kitchen. Other parts of the region had high V_p/V_s values and low V_p and V_s suggestive of small shallow magmatic bodies. The low V_p/V_s corresponding to the geothermal area may result from depressed V_p but normal V_s as the water-steam transition reduces the bulk modulus.

- **Microearthquake tomography by *Wu and Lees* [1999]**

Three-dimensional compressional and shear velocity structures in the upper 5 km of the Coso geothermal area were derived using local earthquake tomography for *P*- and *S*-phases [*Wu and Lees*, 1999]. 2104 microearthquakes from a two-year period (July 1993 - June 1995), recorded on 29 seismic stations, were selected and *P*- and *S*-phase arrival times were measured on vertical and horizontal components. The chosen events had hypocentral depths less than 6 km. The inversion block size was 0.2 km horizontally and 0.5 km vertically and the initial reference wave-speed model was a one-dimensional model derived from seismic inversion and geological constraints.

The inversion results (Figure 2.8 and Figure 2.9) show low-V_p and low-V_s zones at geothermal production depths of 1-3 km, and a very high-V_p zone under Coso Hot Springs accompanied by normal V_s. This was interpreted as fluid accumulation. A high-V_s zone east of Sugarloaf Mountain surrounded by a thick low-V_s zone was interpreted as a fossil fracture caused by magmatic intrusion.

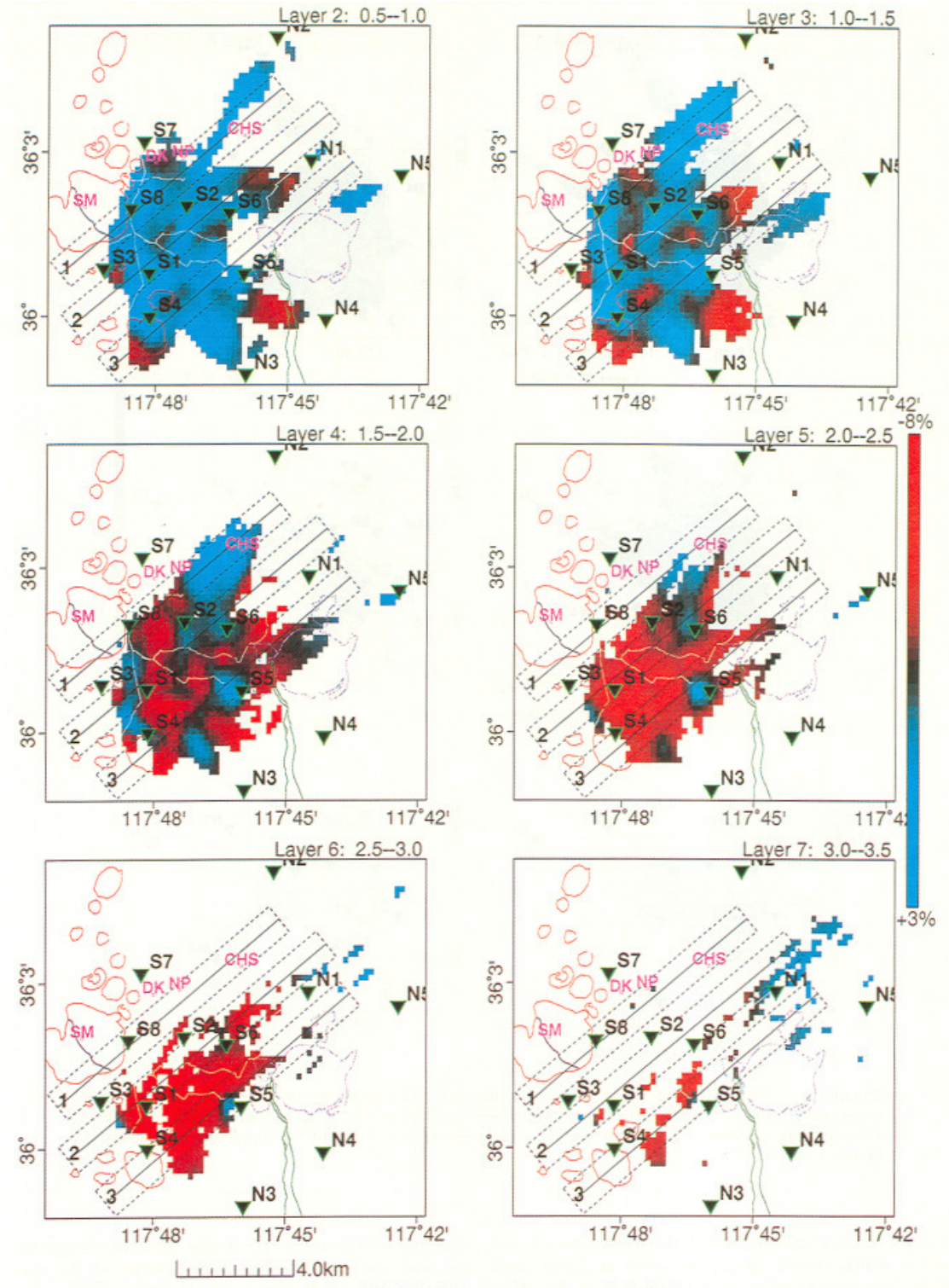

Figure 2.8: Percent perturbation in V_p [from *Wu and Lees*, 1999]. Blue: positive wave-speed perturbations (high-wave-speed zones); red: negative wave-speed perturbations (low-wave-speed zones). Triangles: seismic stations. DK: Devil's Kitchen; NP: Nicol Prospects; CHS Coso Hot springs; SM: Sugarloaf Mountain. Hash-marked regions 1, 2, and 3 represent lines of sections.

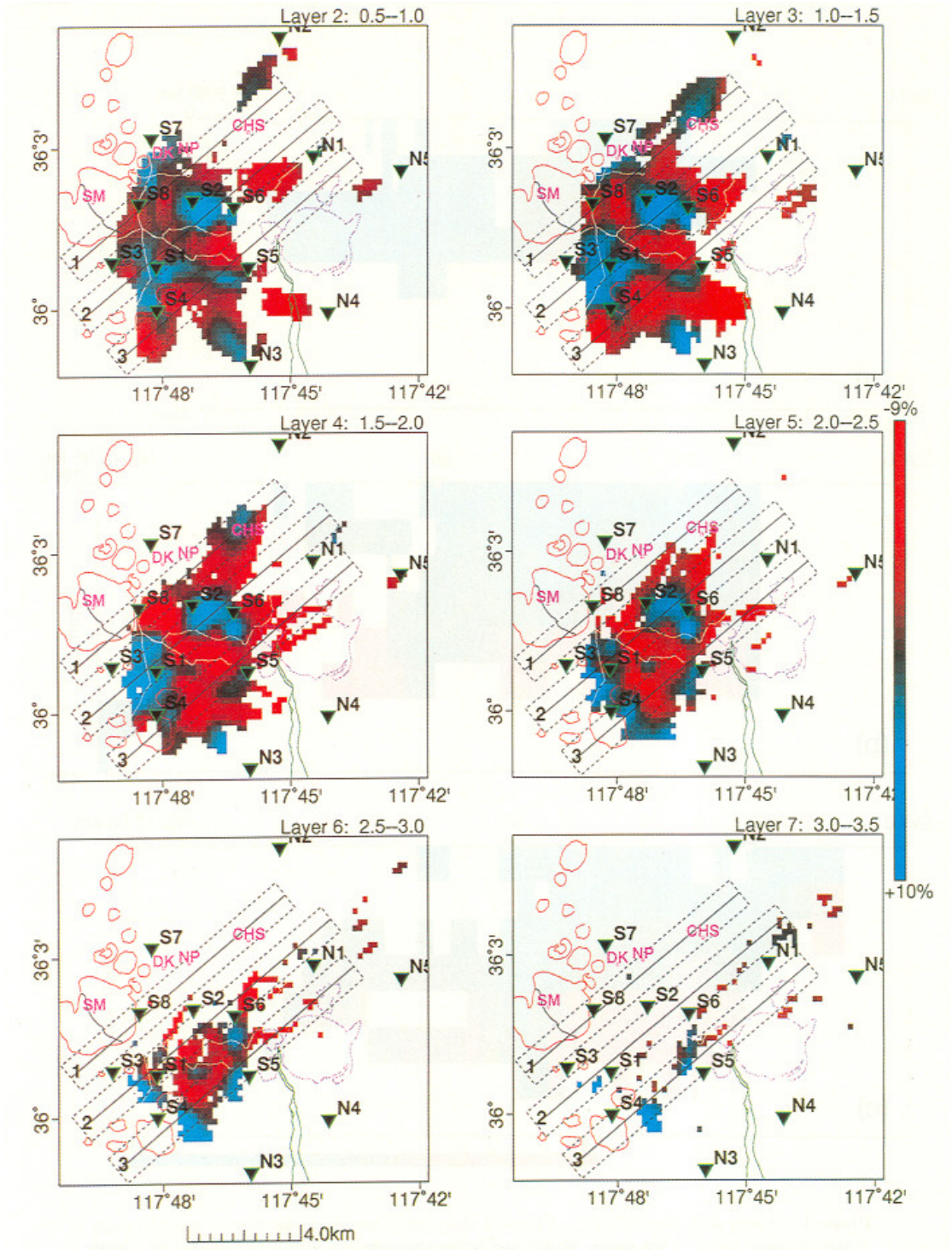

Figure 2.9: Same as Figure 2.8 but for V_s showing the high-V_s region east of Sugarloaf Mountain between stations S2 and S6 surrounded by a low-V_s belt [from *Wu and Lees*, 1999].

- **Local-earthquake tomography by *Foulger* [2007]**

Foulger [2007] obtained tomographic images for each of the years 1996-2006 using arrival times recorded on the U.S. Navy network (Section 2.3.1.; Figure 2.5). 4811 microearthquakes were selected from the Navy catalogue. This catalogue comprises locations calculated by the Geothermal Program Office (GPO) using hand-measured *P*- and *S*-wave arrival times. The best 10 events in each 1x1x1 km block of the volume of interest were detected. The events were ranked in terms of the number of readings available and the goodness-of-fit to the arrival times for each event. The tomographic inversions were performed in three steps. First, the entire data set was inverted for a one-dimensional wave speed structure using the program *velest* [*Kissling et al.*, 1994]. Second, the model obtained in step one was used as a starting model to run the inversion using *simul2000A* [*Evans et al.*, 1994; *Thurber*, 1993]. This yielded an average three-dimensional model. Finally, the data for each of the years 1996-2006 were inverted independently (Figure 2.10) using *simul2000A*.

In the upper two kilometers, these inversions consistently show shallow, low-V_p and V_s beneath Coso Wash, and a low-V_p/V_s anomaly under the northern part of the production zone. The low-V_p/V_s anomaly resulted from high V_p but even higher V_s (Figure 2.10). *Foulger* [2007] postulated that this anomaly resulted from exploitation of the geothermal reservoir so whether or not it expanded with time was of interest. It was not clear from the results, however, whether this was the case or not and this problem was the impetus for development of the *tomo4d* program.

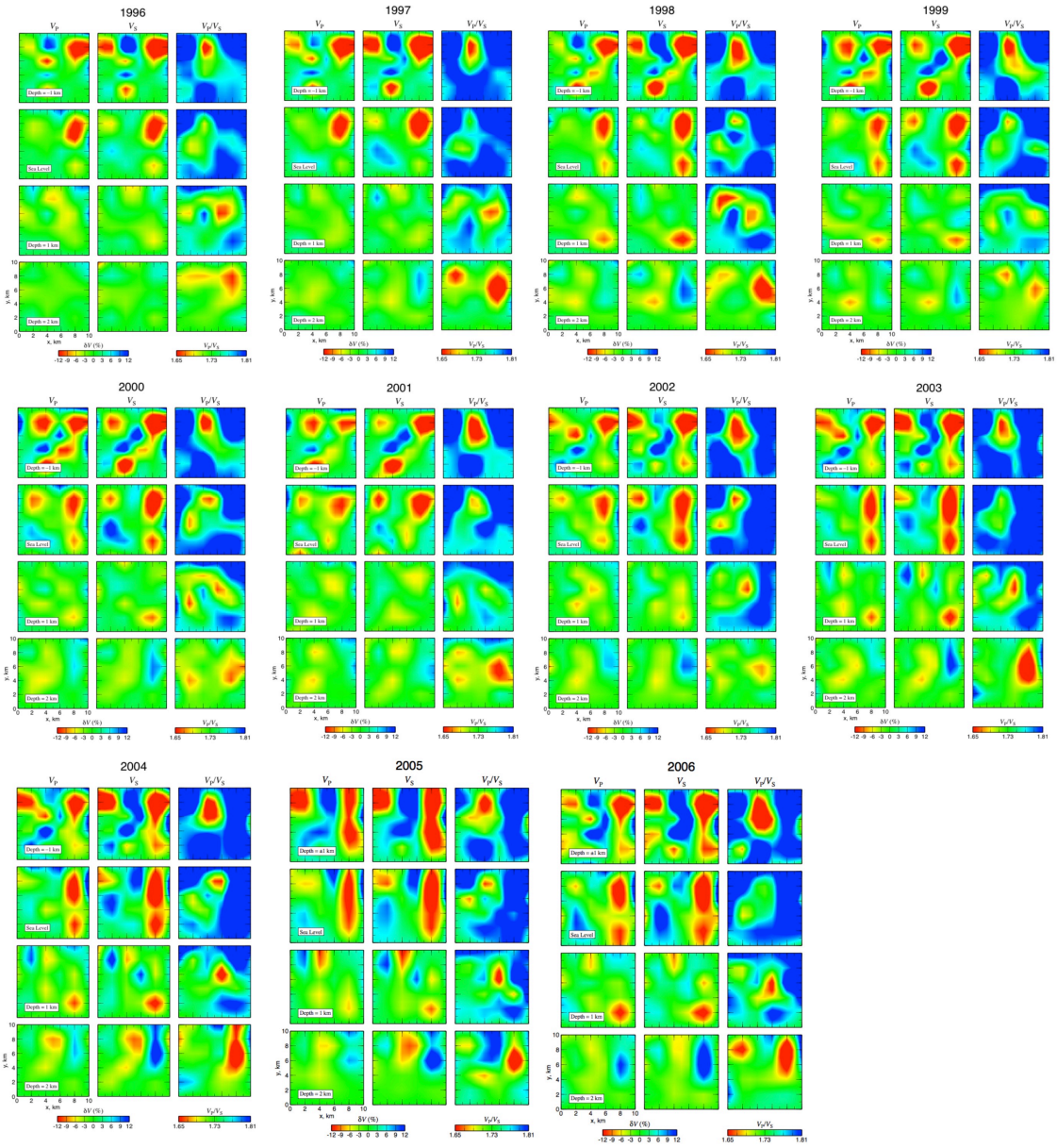

Figure 2.10: Maps of V_p, V_s, and V_p/V_s at different depths for the years 1996-2006 [from *Foulger*, 2007].

- **Local-earthquake tomography by *Kaven et al.* [2011]**

Kaven et al. [2011] used *P*- and *S*-phase arrival times recorded on the Navy Geothermal Program Office network between April 1996 and October 2008. They selected only earthquakes with magnitudes ≥ 0.5 for inversion and used a "double-difference" technique for locating the seismicity. This technique is based on the assumption that two earthquakes close to each other recorded at the same stations have rays that travel through essentially the same subsurface structure [*Waldhauser and Ellsworth*, 2000].

The three-dimensional wave-speed structure derived (Figure 2.11) revealed that at shallow depths, V_p in the main field and east flank of the geothermal area is higher than in adjacent parts of the field, while at depths of 1.5-3 km V_p is only high beneath the east flank. Relatively high V_s at depths of 0-1.5 km within both the east flank and the main field may reflect decrease in fluid pressure due to production [*Kaven et al.*, 2011]. This is consistent with the findings of *Foulger* [2007].

Kaven et al. [2011] compared their V_p/V_s model with subsurface temperature and reported good correlations between low-V_p/V_s anomalies and high temperatures at depths of 0.5 km and 1.0km but poor correlations at depths ≤ 0 km, in spite of high subsurface temperatures (Figure 2.12). While low-V_p/V_s anomalies corresponded to the main field and east flank at depth of 1 km, this correlation diminishes at shallower depths and disappears at depths above 0 km. *Kaven et al.* [2011] interpreted these V_p/V_s anomalies as a result of decrease in water saturation or fluid pressure rather than elevated temperatures.

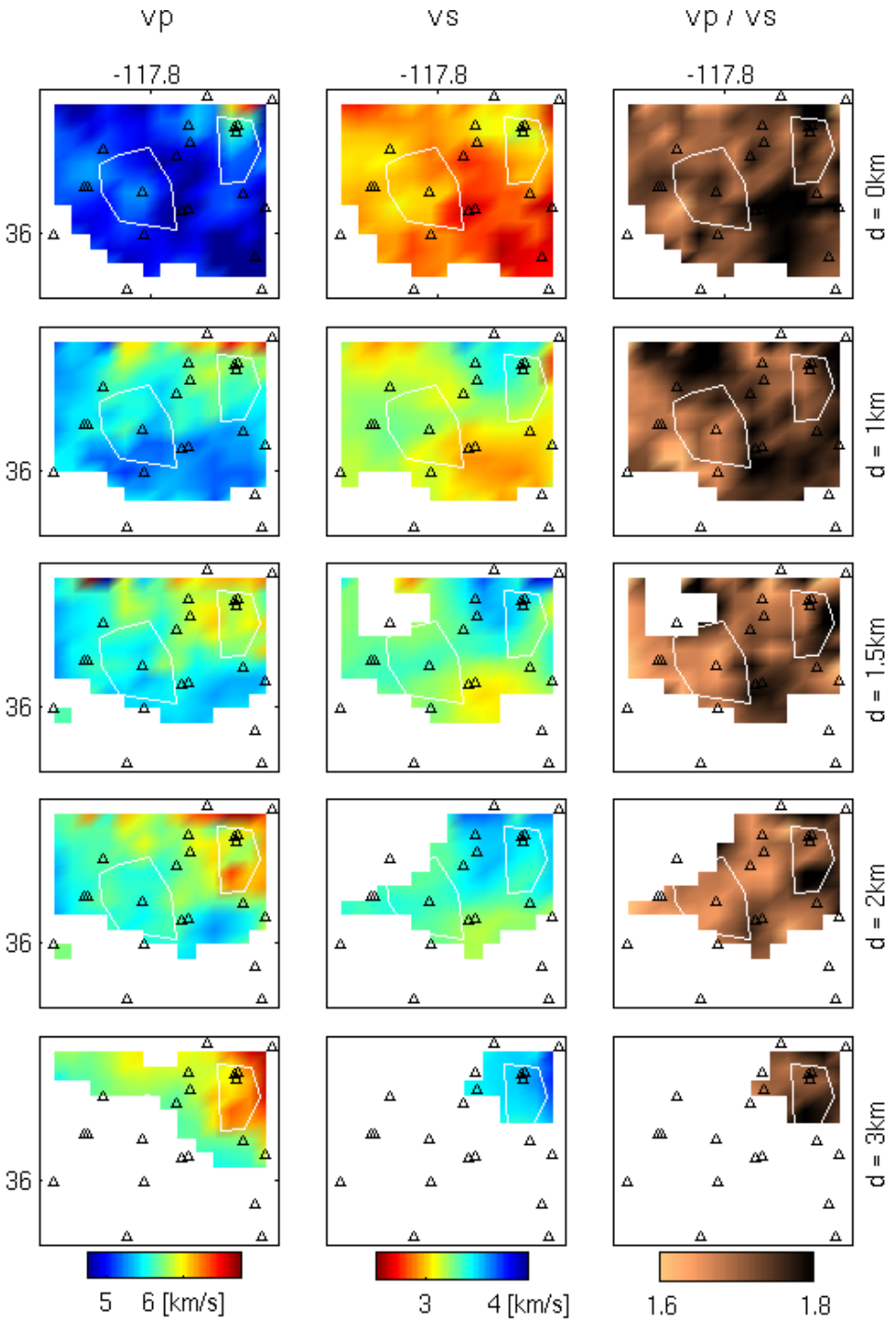

Figure 2.11: V_p (left column), V_s (middle column), and V_p/V_s (right column) models at various depths [from *Kaven et al.*, 2011]. White polygons indicate the approximate extents of the main field to the west and the east flank to the east. Black triangles are US Navy seismic stations.

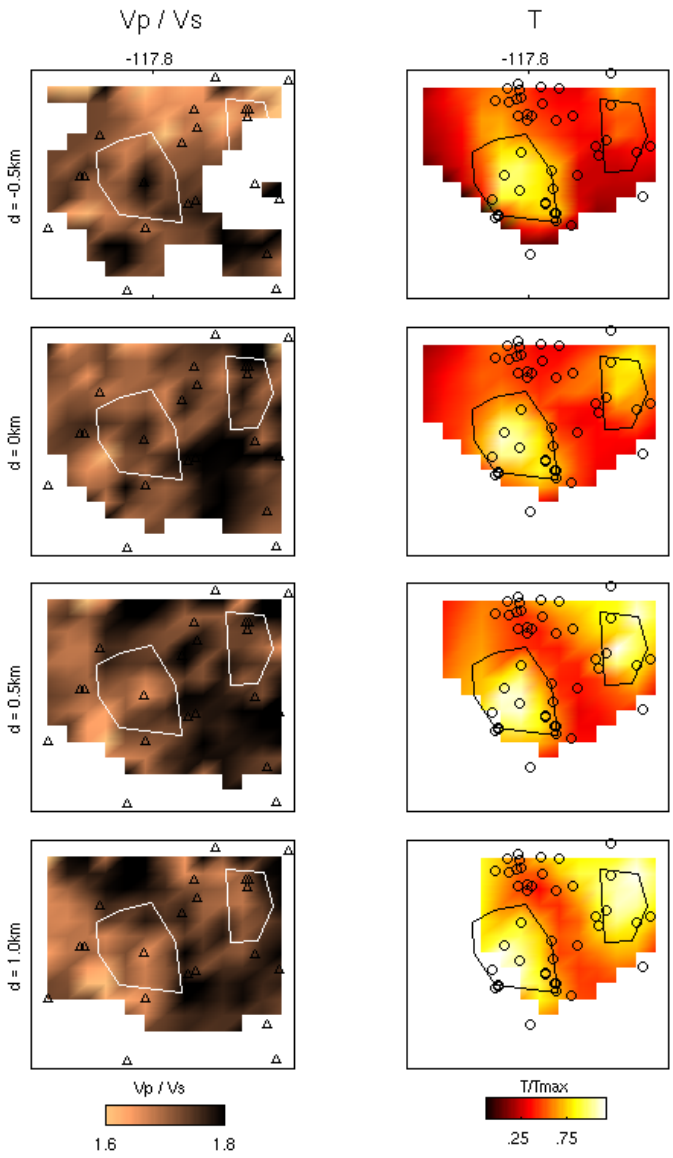

Figure 2.12: Comparison between V_p/V_s (left column) and temperature (right column) from well log data [from *Kaven et al.*, 2011].

- **Ambient noise tomography by *Yang et al.* [2011]**

Yang et al. [2011] obtained a three-dimensional V_s image of the region around the Coso geothermal field using seismic ambient noise tomography. Daily cross-correlations of ambient noise were calculated between all pairs of stations from both the Southern California Seismic Network and a temporary stations deployed between 1998 and 2000. These were stacked over the duration of the deployment. Phase velocities of Rayleigh waves between 3 and 10 s periods were measured from the cross-correlations. 300-600 reliable phase velocity measurements were then inverted

for phase velocity maps (Figure 2.13) on a 0.25° by 0.25° grid using the method of *Barmin et al*. [2001].

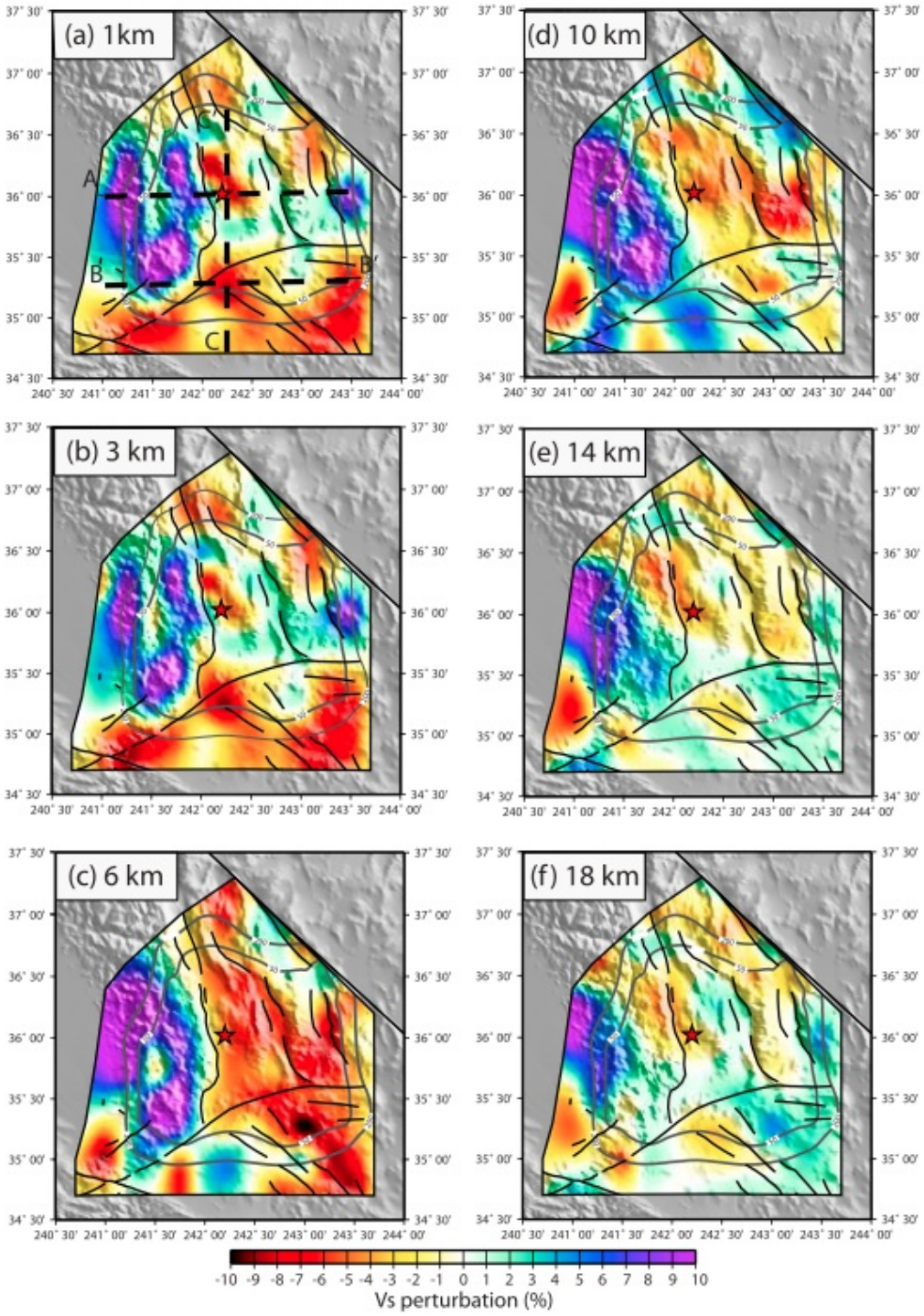

Figure 2.13: Maps of three-dimensional V_s at depths of 1, 3, 6, 10, 14, and 18 km. These are plotted as perturbations relative to the average values across the maps at each depth in the region encompassing the stations, as outlined by the polygons. The two grey contours indicate resolutions of 50 and 200 km. The red star marks the location of the Coso geothermal area. Black lines are faults [from *Yang et al.*, 2011].

This three-dimensional model revealed a low-V_s anomaly within the top 2 km in the Coso geothermal area, interpreted as resulting from geothermal alteration in the shallow layers. In the upper crust (< 10 km), low shear velocities may be attributed to high temperatures and perhaps the presence of partial melt.

- **Summary of tomography studies**

Low-V_p/V_s anomalies were imaged beneath the geothermal field at shallow depths. This results from low V_p and normal V_s [*Walck*, 1988] or, alternatively, relatively high V_s in respect to V_p [*Julian et al.*, 2006; *Kaven et al.*, 2011]. This has been interpreted as a result of decrease in fluid pressure and drying of minerals because of production. However, low-V_s anomalies were detected beneath the geothermal field at depths of 1-3 km b.s.l. [*Wu and Lees*, 1999] and in the upper 2 km [*Yang et al.*, 2011]. This was interpreted as a result of geothermal alteration. Like Long Valley, the results are thus somewhat variable from study to study.

2.5 Other geophysical studies

Geophysical and geological investigations have been conducted in the Coso geothermal area and surroundings to characterize the geothermal resource. Heat flow was studied by *Combs* [1980]. Temperature measurements in 25 shallow- and intermediate-depth boreholes and thermal conductivity measurements on 312 samples form cores and drill cuttings were made. This study found high conductive heat flow values in the rhyolite dome field (>10 HFU compared to the background value of 1.6 – 2.4 HFU) (Figure 2.1). This was interpreted as a result of thermal convection that requires heat energy supplied from depth and implies that a crustal magma body exists at depths between 5 and 20 km.

A geochemical study of geothermal fluids by *Fournier and Thompson* [1980] collected and analyzed wellhead and downhole water samples from two wells (a 114.3 m well at Coso Hot springs and a 1477 m well 3.2 km to the west). They found that the hot waters entering both wells have the same chloride concentrations suggesting that a chloride-rich, hot-water-dominated geothermal system is present with a temperature of about 200-250°C.

The lithospheric structure of the Coso geothermal area (Figure 2.14) was studied using receiver functions calculated from seismograms recorded by high-density seismic arrays [*Wilson et al.*, 2003]. The results were consistent with the presence of an upper crustal magma reservoir between 2 and 15 km thick with ≥ ~5% rhyolitic melt, situated 5 km below the centre of the Coso geothermal field. An upper mantle reservoir at about 35 km depth was also interpreted, which may feed the crustal magma body with continuous flow in dykes (< 1 km width). Using move-out analysis combined with receiver function modeling, *Wilson et al.* [2003] determined that a lower magma reservoir is unlikely to underlie the field.

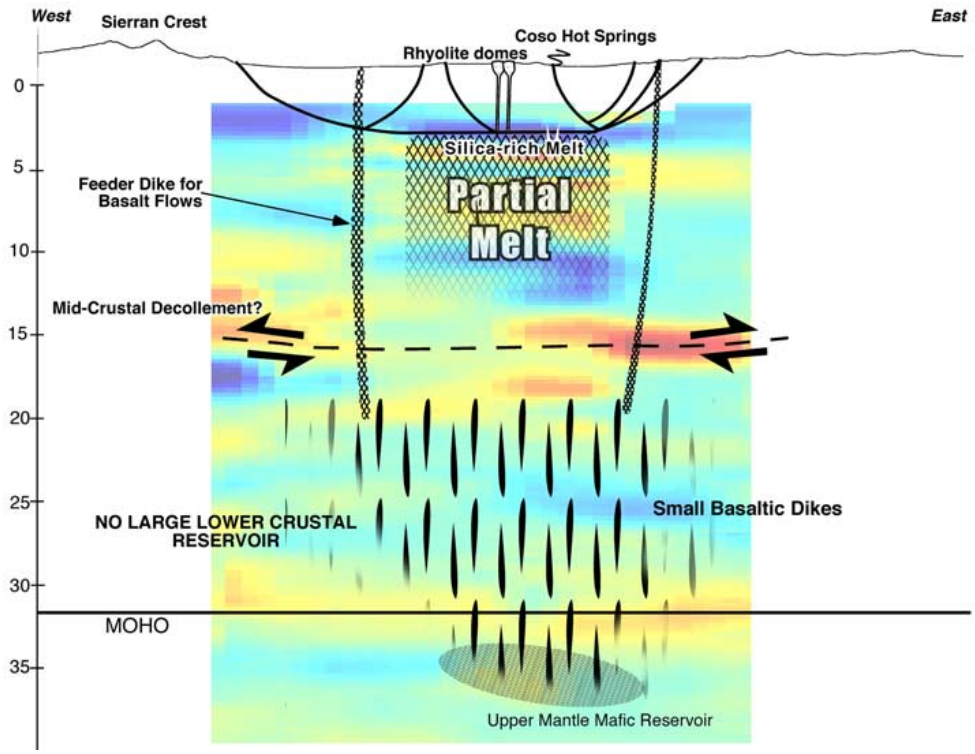

Figure 2.14: Structure of the Coso geothermal area from receiver function analysis. The inferred upper crustal reservoir (2-15 km thick) is situated at about 5 km depth. There is no lower crustal magma reservoir and the upper mantle reservoir probably feeds the upper reservoir through dykes [from *Wilson et al.*, 2003].

Julian et al. [2007] performed a microearthquake moment-tensor study inverting *P*- and *S*-phase first-motion polarities jointly with amplitude ratios using linear programming methods [*Julian*, 1986; *Julian and Foulger*, 1996]. They combined the results with high-resolution relative hypocentre locations. They studied the moment-

tensor mechanisms for eight microearthquakes from a March 2005 swarm that accompanied rapid fluid loss during an injection into well 34-9RD2. The eight moment-tensor mechanisms derived all had volume increases (Figure 2.15). *Julian et al.* [2007] suggested that tensile faulting and probably a crack opening caused the swarm in March 2005. The inferred fault plane shown in Figure 2.15 was confirmed by surface geological observations and a televiewer borehole log of well 34-9RD2 that provides evidence of a fault intersecting the well near its bottom (Figure 2.16).

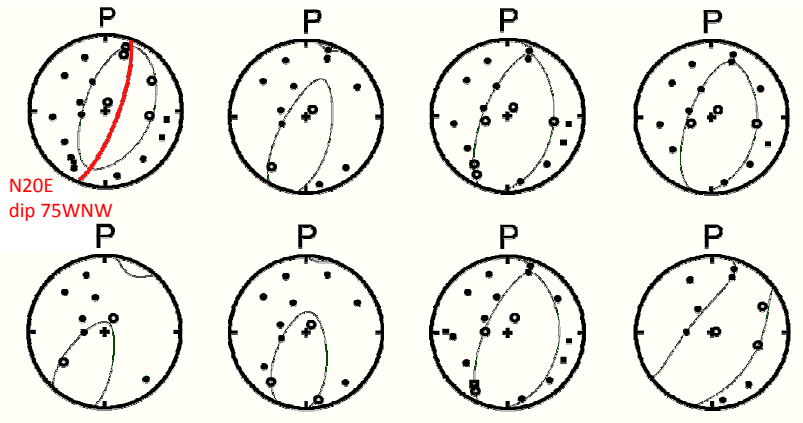

Figure 2.15: Moment-tensor earthquake source mechanisms represented by upper-hemisphere focal sphere plots [from *Julian et al.*, 2007]. Black dots and open circles indicate compressional and dilatational *P*-phase arrivals respectively. The mechanisms resemble normal-faulting mechanisms but with reduced dilatational fields, and are consistent with fluid flow into an opening crack. The red line on the top left focal sphere is the fault plane defined by accurate relatively located earthquakes.

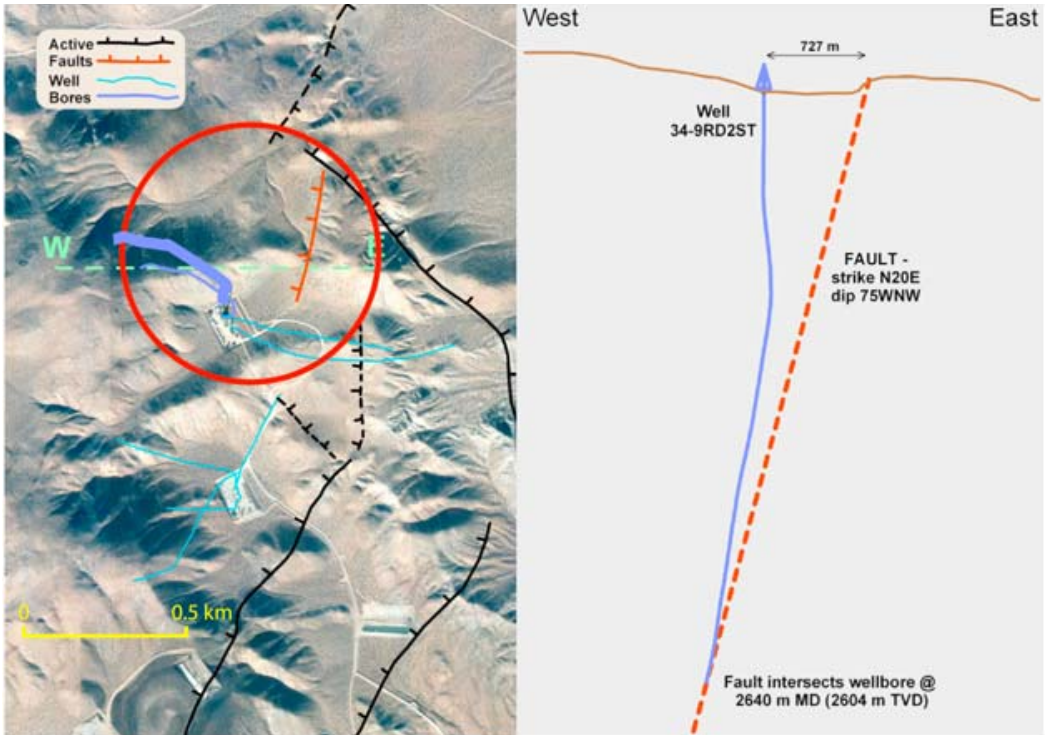

Figure 2.16: Geological confirmation of the fault inferred from microearthquake relative hypocenter locations [from *Julian et al.*, 2010]. (left) Map shows the surface projection of well 34-9RD2 (violet); blue: other wells; black: the surface traces of Quaternary faults; red: the fault activated by the earthquake swarm. (right) West-east cross section shows well 34-9RD2. Dashed red line shows activated fault. It intersects the well bore where a fault was imaged on a televiewer log.

New and improved software used by *Julian et al.* [2009] combined waveform cross-correlation measurements of arrival times and relative hypocenter location methods. They studied injection experiments in well 34A-9 in 2004 and well 34-9RD2 in 2005 in the northern part of the east flank of the Coso geothermal area (Figure 2.17) using data from the US Navy's permanent network. They calculated full moment tensors and high-resolution relative locations for microearthquakes that occurred before, during, and after the injection. They concluded that both injections activated the same fault structure (Figure 2.18). They jointly interpreted the obtained earthquake locations and moment tensors to suggest that the activated structures were opening cracks with right-lateral shear and normal motions.

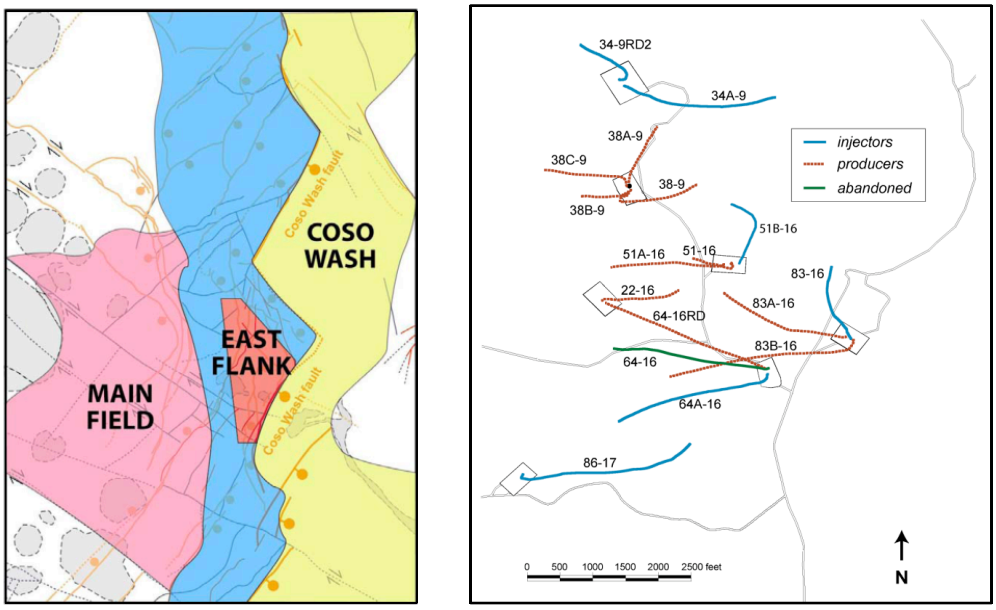

Figure 2.17: (left) Map showing fault-controlled sub-divisions of the Coso geothermal area [from *Julian et al.*, 2009]. These are distinct as regards temperature and seismicity. The main field and the east flank are the primary producing and seismically active regions. (right) locations of wells in the east flank [from *Rose et al.*, 2005].

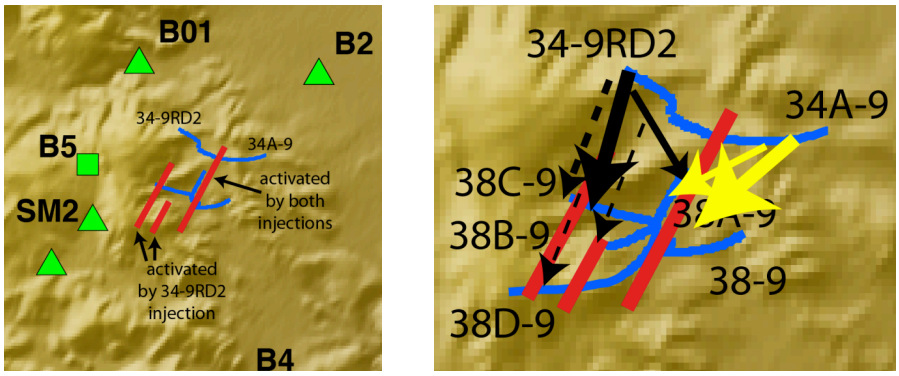

Figure 2.18: (left) Faults activated by injection experiments in well 34A-9 and 34-9RD2, deduced from earthquake relative locations. (right) Schematic diagram shows the fates of tracers injected into the same well. Blue: boreholes; red: faults seismically activated by injections; solid arrows: liquid tracers; dashed arrows: vapor tracers; black: 34-9RD2; yellow: 34A-9. Width of arrows indicates strength of returns, not to scale [from *Julian et al.*, 2009].

A recent study by *Wamalwa et al.* [2013] correlated density models derived from gravity data and a resistivity model derived from magnetotelluric data to determined the source region of the geothermal field. Both low resistivity and density at and below 6 km depth were detected in the Devil's Kitchen and the Coso Hot Springs areas. These were interpreted as a result of cooling magmatic material that provides the heat for the shallower geothermal system. That is characterized by high resistivity and low density and capped by a low resistivity clay zone.

2.6 Comparison of Long Valley caldera and the Coso geothermal area

Seismicity in Long Valley caldera is mainly related to regional tectonics such as oblique slip on fault planes [*Given et al.*, 1982] and tensile failure and opening of cracks [*Julian*, 1983; *Julian and Sipkin*, 1985]. Focal depths are <10 km for local earthquakes and >10 km for long-period earthquakes. In contrast, the vast majority of the seismicity in the Coso geothermal area is thought to be induced by injection and production activities [*Feng and Lees*, 1998; *Fialko and Simons*, 2000; *Schoenball et al.*, 2015]. Focal depths are <3 km for most earthquakes. Regional earthquakes also occur and these are caused by the tectonic activity of the southern Owens Valley [*Julian et al.*, 2004].

The Coso geothermal system shows evidence for episodes of thermal activity for more than 300,000 years [*Adams et al.*, 2000] with a heat source in the deep crust and thermal fluids flowing laterally and upwards. The present geothermal system in Long Valley caldera, represented by the Casa Diablo Hot Springs area, appears to be restricted to depths less than 1 km and is dominated by hot water (~170 °C, but decreasing with depth). This water flows from west to east [*Sorey*, 1985] and shows no evidence for heat upwelling directly beneath Casa Diablo.

Seismic tomography in both areas has revealed good correlation between the seismic wave speeds and the known geologic structure in the areas, though there is considerable variation in detail between studies.

2.7 Geothermal potential of Syria

At present, although significant geothermal resources are thought to exist in Syria, exploitation is limited to recreational bathing. This situation is likely to change in future as the need for renewable and non-polluting energy increases.

Areas where there are surface geothermal features such as hot springs and fumaroles have been identified as offering scope for power generation in Syria. The full geothermal potential has not yet been assessed. The areas are in the same zone as the most seismically active part of Syria. When exploration commences it will be important to monitor the projects seismically both for seismic hazard and to gather data that may be used to study the geothermal prospects.

Geothermal exploration has been conducted in countries neighbouring Syria such as Turkey to the north of Syria, the seventh richest country in the world in geothermal energy potential, Lebanon, and Jordan where one of the richest geothermal potential low enthalpy resources has been discovered near the border with Syria and Iraq. This is discussed in more detail in Chapter 7.

CHAPTER 3

METHODOLOGY

3.1 Background

Local earthquake tomography yields three-dimensional seismic wave-speed structures for the crust using compressional and shear wave arrival-time data measured from seismograms. Initial estimates of the seismic wave-speed structure and the earthquake hypocentral coordinates and origin times are used to calculate arrival times. Local earthquake tomography minimizes the misfit between the observed and calculated arrival times by perturbing both the hypocentres and the wave-speed model using iterative damped least squares. Ray-tracing approaches vary from a very simple approach using straight-line rays, that would be appropriate for an homogeneous medium, to approximate methods using circular arc rays *e.g.,* [*Thurber*, 1983], to more accurate ray "bending" [*Julian and Gubbins*, 1977].

In order to observe temporal variations in the wave speeds, conventional three-dimensional tomographic methods (*e.g.,* program *simul2000A*, used in this thesis) can be applied to two epochs (data sets) independently and the results can be differenced *e.g.,* [*Gunasekera et al.*, 2003]. However, changes in the models are expected even if the structure itself does not change, due to the variation in the seismic ray distribution and to observational errors. Such changes might be misinterpreted as real change in the structure when in reality they are due to experimental limitations. A new tomography program, *tomo4d*, was developed by *Julian and Foulger* [2010] to deal with this problem by inverting data from two epochs simultaneously, minimizing the structural differences allowed between the two epochs. The structural differences detected are thus likely to reflect real temporal changes and not spurious factors, *e.g.*, variations in earthquake locations between epochs. *tomo4d* is applied to real data for the first time in this thesis.

3.2 Local earthquake tomography theory

3.2.1 Introduction

Local earthquake wave-speed tomography is typically applied to regions of the order of a few kilometres to a few tens of kilometres across. Seismometers may be located on the surface or in boreholes in the study volume. The only knowns in the local earthquake tomography problem are the receiver locations and the observed arrival times. Both of these suffer some uncertainty. The earthquake source coordinates, origin times, ray paths, and slowness field (reciprocal of wave speed) are unknown. Higher resolution is achieved with denser and more uniform seismometer and source coverage. Then, the structure can be parameterised on a smaller scale, *i.e.,* a finer model grid can be used. This allows the inversion to image smaller-scale structures and can enable more realistic, complex structures to be imaged.

The body-wave travel time T_{ij} from an earthquake *i* to a seismometer *j* is expressed as a time integral along the ray path

$$T_{ij} = \int_{S}^{R} u \, dl \tag{3.1}$$

where *u* is the slowness field, *dl* is an element of path length, *R* denotes the receiver and *S* the source. The actual observations are the arrival times

$$t_{ij} = \tau_i + T_{ij} \tag{3.2}$$

where τ_i is the earthquake origin time.

The travel times from equation (3.1) are calculated using an initial model of the seismic wave-speed structure and trial hypocentral coordinates and origin times. Local-earthquake tomography uses an iterative method to improve the estimate of these model parameters by perturbing them in order to minimize the magnitude of the misfit between the observed and calculated arrival times (the residuals *r*):

$$r_{ij} = t_{ij}^{obs} - t_{ij}^{cal} \tag{3.3}$$

The change in a residual caused by small change in the hypocentre and wave speed structure parameters is, to first order

$$\Delta r_{ij} = \sum_{k=1}^{3} \frac{\partial T_{ij}}{\partial x_k} \Delta x_k + \Delta \tau_i + \int_S^R \delta u \, dl \tag{3.4}$$

where $\frac{\partial T_{ij}}{\partial x_k}$ are the hypocentral partial derivatives, Δx_k is the kth hypocentral coordinate, and $\Delta \tau_i$ is the perturbation in the origin time. For a parameterised wave-speed structure, equation 3.4 becomes

$$\Delta r_{ij} = \sum_{k=1}^{3} \frac{\partial T_{ij}}{\partial x_k} \Delta x_k + \Delta \tau_i + \sum_{l=1}^{L} \frac{\partial T_{ij}}{\partial m_l} \Delta m_l \tag{3.5}$$

where m_l is the lth parameter of the wave-speed model, L is the number of model parameters, $\frac{\delta T_{ij}}{\delta m_l}$ are the wave-speed model partial derivatives, and Δm_l is the perturbation in m_l. To improve estimates of the model parameters, local-earthquake tomography perturbs both the hypocentral and wave-speed model parameters in an attempt to minimize the residuals.

3.2.2 Least squares solution

Seismic tomography is a non-linear inverse problem because the ray paths change with changes in both earthquake locations and structure. With more equations than unknowns, the problem is over-determined but it is invariably also under-constrained and there is a range of possible solutions. This is solved by damping (Sections 3.3.4.2 and 3.3.5.2). The use of the least squares solution that minimizes the sum of the squares of the residuals is used to find an optimal solution (the principle of maximum likelihood).

In the linear forward problem, the relation between data d and model m vectors is linear and may be written in the form

$$d = Am + e \tag{3.6}$$

where A is a matrix of coefficients that are independent of both data and model, and e is the error vector. For the i^{th} datum d_i, this may be written in full as

$$d_i = \sum_{j=1}^{L} A_{ij}\, m_j + e_i \tag{3.7}$$

where the i^{th} row of A is called the *data kernel*. It describes how the i^{th} datum depends on the model.

The least squares solution minimizes the sum of the squares of the errors. From (3.7):

$$e_i = d_i - \sum_{j=1}^{L} A_{ij}\, m_j \tag{3.8}$$

and the sum of the squares, over a number D of data , is

$$E^2 = \sum_{i=1}^{D} e_i^2 = \sum_{i=1}^{D} \left(d_i - \sum_{j=1}^{P} A_{ij}\, m_j \right)^2 \tag{3.9}$$

this is minimized by choosing the unknowns $\{m_k\}$ so that

$$\frac{\partial (E^2)}{\partial m_k} = 0$$

$$2 \sum_{i=1}^{D} \left[d_i - \sum_{j=1}^{P} A_{ij}\, m_j \right] \; (-A_{ik}) = 0 \tag{3.10}$$

which may be rearranged as

$$\sum_{j=1}^{P}\sum_{i=1}^{D} A_{ik}A_{ij}\,m_j = \sum_{i=1}^{D} A_{ik}d_i \qquad (3.11)$$

in matrix notation this may be written as

$$A^T A\, m = A^T d\,. \qquad (3.12)$$

These are called the normal equations and may be solved for m by Gaussian elimination for example.

3.2.3 Wave-speed structure representation

The Earth's crust and upper mantle are heterogeneous and also display anisotropy. This heterogeneity cannot be represented well using constant wave-speed blocks such as used by *Aki*, *Christoffersson* and *Husebye* [1976] and *Aki and Lee* [1976] who modeled the Earth as a stack of boxes with constant seismic wave-speed within each. The constant wave-speed layer approach of *Crosson* [1976] also suffers from inability to represent laterally heterogeneous structure. This problem can be mitigated using an extension of the approach of *Aki and Lee* [1976], where thousands of small blocks are used and gradual or rapid wave-speed changes from block to block are allowed [*Lees and Crosson*, 1989; *Nakanishi*, 1985; *Walck and Clayton*, 1987]. However, with large numbers of blocks the inversion suffers computational difficulties and the problem is highly under-determined (many more unknowns than independent data).

Thurber [1983] used a three-dimensional grid approach, in which wave-speed values are defined at the nodes of a grid and linear interpolation is used in all directions to define wave-speed values between nodes. A program in this family, *simul2000A* [*Evans et al.*, 1994; *Um and Thurber*, 1987], is used in this thesis.

3.2.4 Ray-path and travel-time calculation

For the ray tracing used here the end points are specified by the source- and receiver positions. Both the propagation path of the seismic ray between source and receiver and the travel time along that path must be determined. The path is needed to calculate hypocentre- and wave-speed-model partial derivatives, travel times, and

arrival-time residuals. Because of the dependence of the seismic ray paths on the three-dimensional wave speed structure that is being sought, seismic tomography is a non-linear inverse problem and the only practical solution methods, including the variant described here, involve iterative refinement of initial estimated models. These might sometimes not converge or might converge to different solutions depending on the initial model chosen.

The main methods of computing rays are shooting and bending. The shooting method involves solving the initial-value problem and perturbing the starting direction to try to find a ray that arrives at the desired point (Figure 3.1, top). The bending method involves perturbing an initial source-receiver path until the travel time becomes stationary (Figure 3.1, bottom).

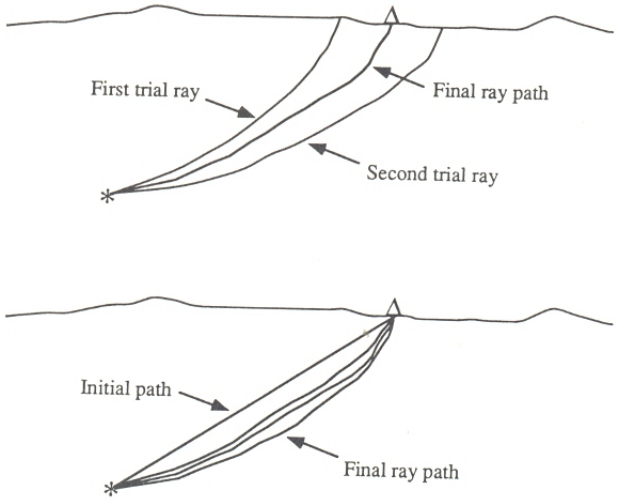

Figure 3.1: Schematic representation of two general methods of solving two-point ray-tracing problems: (top) shooting, where the starting direction of the ray at the source is perturbed until it emerges at the receiver, and (bottom) bending, where the initial path between fixed receiver and source points is perturbed until a stationary time ray-path is obtained [from *Thurber*, 1993].

Different ray-tracing approaches have been used by *Wesson* [1971], *Julian and Gubbins* [1977], *Thurber and Ellsworth* [1980], and *Thurber* [1983]. These approaches include very simplistic ray tracing using straight-line rays through an homogeneous medium [*Aki and Lee*, 1976], an approximate method using circular arc

rays, approximate for a constant-wave-speed-gradient medium [*Thurber*, 1983], and "bending" [*Julian and Gubbins*, 1977], which computes true ray paths.

3.2.5 Hypocentre and wave-speed model coupling

The inversion method used in local earthquake tomography seeks both hypocentres and wave-speed models. As a result the size of the matrix that must be inverted is large. The simultaneous inversion equations can be expressed as

$$r_i = H_i \ \Delta h_i + M_i \, \Delta m \tag{3.14}$$

where r_i is the residual vector for the ith event, H_i represents the matrix of hypocentral partial derivatives, Δh_i is a vector of hypocentre adjustments, M_i represents the matrix of wave-speed partial derivatives, and Δm is the vector of wave-speed perturbations. In order to simplify the equations, hypocentre-wave-speed separation is carried out. A matrix Q_0 is constructed such that

$$Q_0 \, H_i = 0 \, . \tag{3.15}$$

When equation (3.14) is multiplied by Q_0

$$Q_0 r_i = Q_0 H_i \ \Delta h_i + Q_0 M_i \, \Delta m = M_i' \Delta m \, . \tag{3.16}$$

This equation simplifies to

$$r_i' = M_i' \Delta m \, , \tag{3.17}$$

a system of equations containing only the wave-speed model parameters, and many systems for the earthquake origins. Normal equations can also be used to reduce the matrix size even further [*Spencer and Gubbins*, 1980; *Thurber*, 1983]. The direct solution of a very large tomography problem is often too large for the computational resources typically available.

Equation (3.17) is solved using the following normal equations for the least-squares solution:

$$(M'^{T}\, r') = (M'^{T}\, M')\, \Delta m\,. \tag{3.18}$$

Equation 3.18 is solved using Cholesky decomposition, *e.g.,* [*Press et al.*, 2007], which is an efficient method for solving systems of linear equations. The earthquakes are then relocated using the updated wave-speed model. Through several iterations, improvements are progressively made to both the wave-speed model and the hypocentre locations.

3.2.6 The inclusion of *S* phases

The use of *S*-phase data in local earthquake tomography improves constraints on earthquake hypocentral depths and provides information that helps to decouple hypocentres and wave speeds in the inversion. *S* observations are generally fewer in number and lower in quality than *P* observations, typically because of the lack of three-component data.

The developers of *simul* found that inversion for the V_p/V_s ratio stabilised the inversion compared with inverting for V_s independently. If V_p/V_s is constant, the ray-paths are identical for *P* and *S* and an *S*-*P* time difference, dt_{ij}, can be expressed as

$$dt_{ij} = \int [(V_p/V_s) - 1]/V_p\, ds\,. \tag{3.19}$$

Predicted *S*-*P* times can be calculated using the V_p model and the V_p/V_s value. The residuals ($dt_{ij}^{obs} - dt_{ij}^{cal}$) are then related to perturbations in V_p/V_s at the grid nodes and V_p/V_s is inverted for keeping the V_p values and hypocentres fixed. A V_s model is then generated using the V_p/V_s and V_p models.

3.2.7 Quality of the solution

The quality of the three-dimensional structure derived can be assessed by inspecting the variance reduction, model resolution and model covariance [*Menke*, 1989]. Variance reduction is a measure of the improvement in fit between the observed and

calculated arrival times. Resolution describes the uncertainty in the model as function of data uncertainty and resolution information. Data uncertainty is estimated from the data variance after inversion. Resolution is restricted by incomplete and inhomogeneous sampling of the study volume. For that, resolution is sharper near the centre of the model and poorer near the periphery [*Evans and Achauer*, 1993].

Other measures of solution quality are the derivative weight sum [*Foulger and Toomey*, 1989; *Toomey and Foulger*, 1989] and the spread function. The derivative weight sum measures the ray density near the grid nodes. It is defined as

$$DWS\ (\alpha_n) = N \sum_i \sum_j [\int_{P_{ij}} w_n\ (x) ds\ )] \tag{3.20}$$

for the *n*th wave-speed model parameter α_n where w_n is the weighting of the *n*th model parameter in the interpolation, P_{ij} is the ray path from event *i* to station *j*, and *N* is a normalization factor that accounts for the volume influenced by the *n*th model parameter [*Toomey and Foulger*, 1989].

The spread function measures the reliability of the wave speed obtained by expressing the extent of local averaging involved in determining the wave-speed for each node. It is defined as

$$spread = \left[\left|R_j\right|^{-2} \sum_k D_{jk}^2\ R_{jk}^2 \right]^{-\frac{1}{2}} \tag{3.21}$$

where $\left|R_j\right|^{-2}$ is the norm of the *j*th row of the resolution matrix, D_{jk} is the distance between the *j*th and the *k*th nodes, and R_{jk} is the element (*j,k*) of the resolution matrix.

3.3 The inversion method

Two tomographic inversion programs, *simul2000A* [*Evans et al.*, 1994; *Um and Thurber*, 1987] and *tomo4d* [*Julian and Foulger*, 2010], are used in this thesis. They are both applied to two field areas – Long Valley caldera and the Coso geothermal

area, both in California. In both cases the model is parameterized by values at the nodes of three-dimensional rectangular grid with spacings of 2 km horizontally and 1 km vertically. The spacings between nodes must be large enough to ensure that each is constrained by sufficient rays, but small enough to maximize the structural detail retrieved. To allow rays to pass a little outside of the grid, nodes on planes at distances of 50 km from all the faces of the imaged volumes were included [*Foulger et al.*, 2003].

3.3.1 Data requirements

A set of well-distributed earthquakes is required. The programs *qselect* and *qvalues* (Bruce Julian, personal communication) were used to select earthquakes. *qselect* is a filter that reads earthquake catalogue data and selects those earthquakes whose locations, magnitudes, or other characteristics satisfy specified criteria. *qvalues* reads the same kind of data, extracts particular values (specified by the user), and writes these values to the standard output. After selecting the events, list files in the format required by the arrival-time picking program *epick* (Bruce Julian, unpublished computer program) are generated in order to enable measurement of the arrival times.

3.3.2 Use of program *epick* for measuring arrival times

epick is an interactive seismogram-analysis program for measuring phase arrival times, amplitudes, and other information from digital seismograms. It operates within the X11 window environment. The seismogram files to be analyzed must be listed in a "list file" (Appendix 2), whose name is given via the –list command-line option. Each line of this file specifies one seismogram (trace). The *epick* display consists of a principal window and smaller "squash", "display", "pick", and "reading" sub-windows (Figure 3.2 and Figure 3.3). All user input is directed to the window in which the cursor is positioned. Each window has its own pop-up menu. Most user interaction takes place within the pick window (Figure 3.3). For this thesis *P*- and *S*-phase arrival times were measured for earthquakes using program *epick*. These arrival-time measurements were used to calculate initial locations and travel-times prior to tomographic inversion.

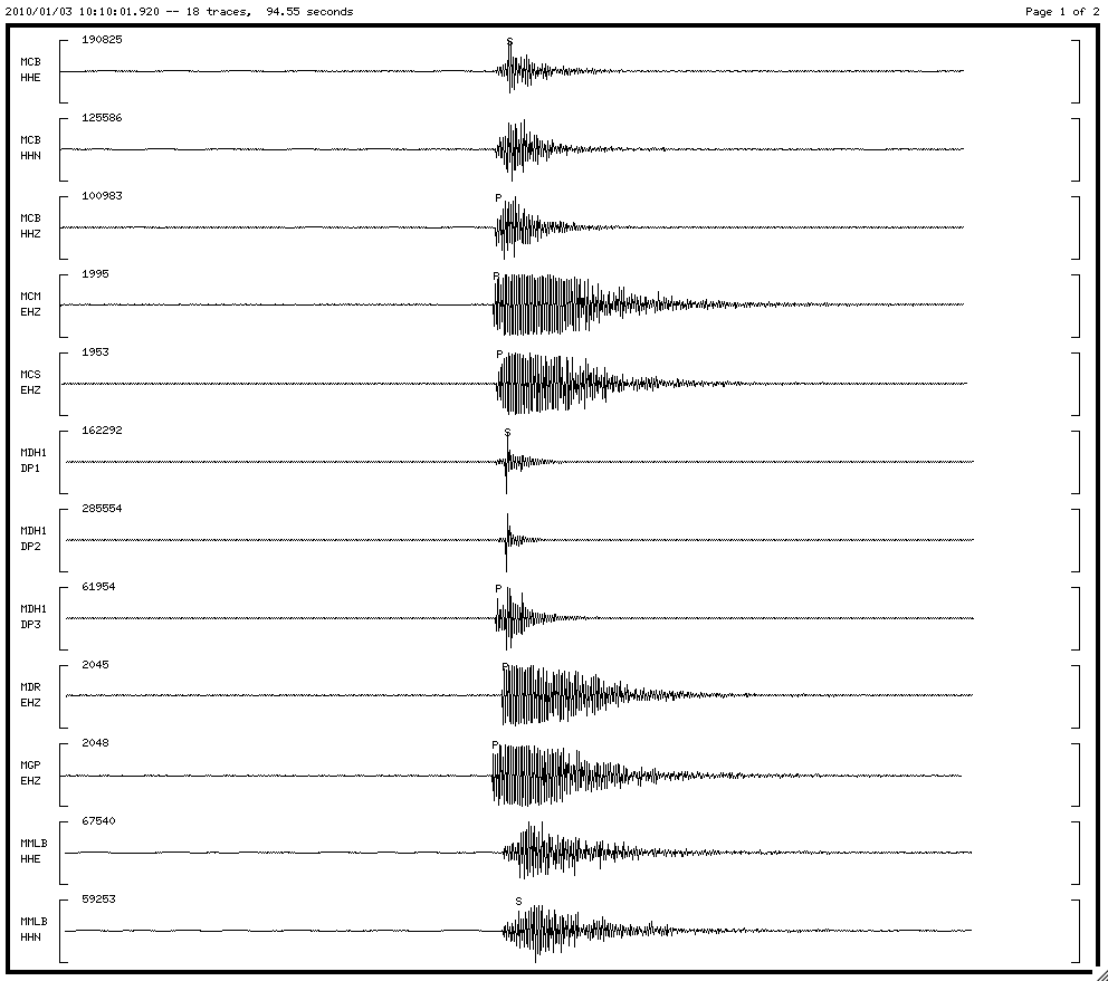

Figure 3.2: The *epick* "squash window". The top margin contains a header line giving the start time of the earliest trace, the number of traces, the total duration spanned by all the traces, and the number of pages of the squash window.

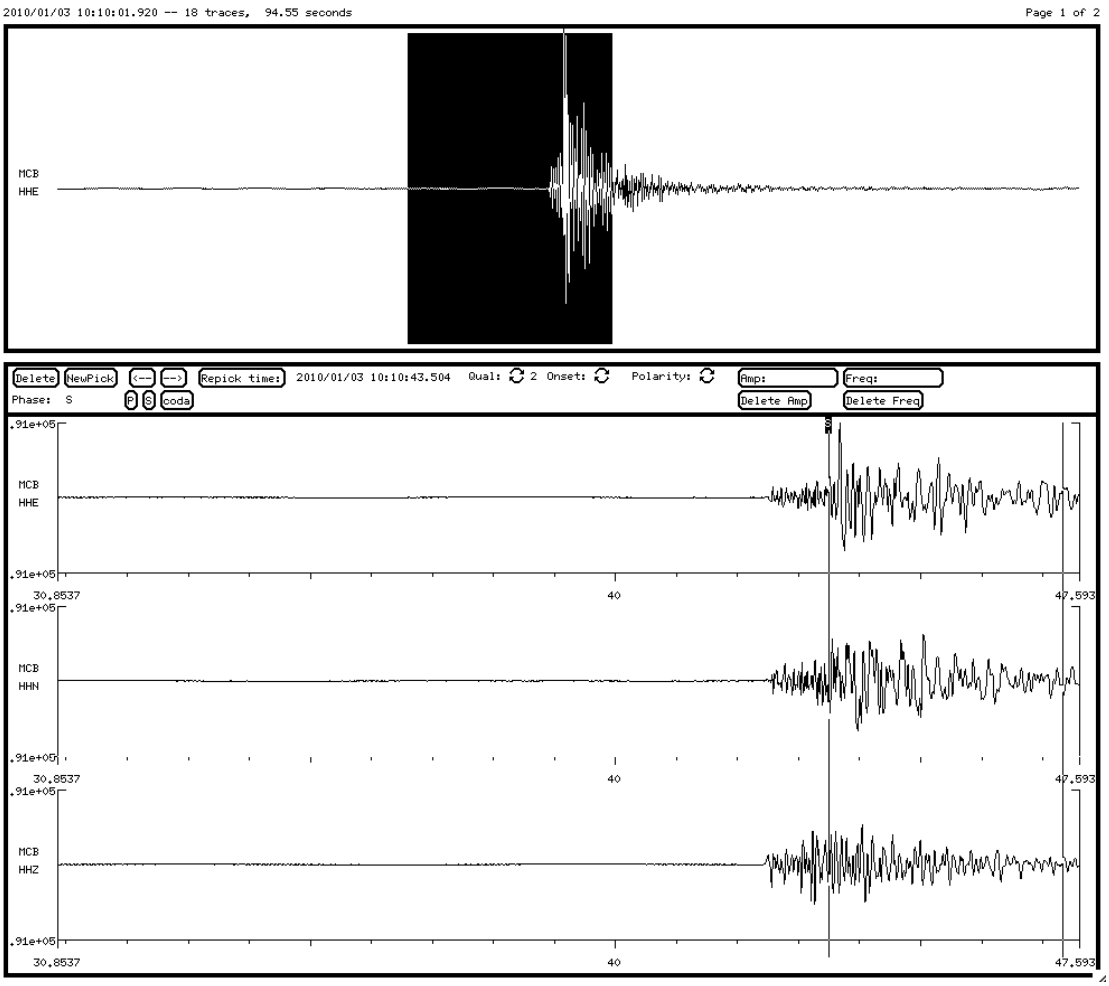

Figure 3.3: The "display" (top) and "pick" (bottom) windows appear simultaneously on the screen. The display window shows the trace selected from the squash window. The pick window shows the selected portion of the active trace (black in display window).

3.3.3 Program *qloc*

Program *qloc* was used to locate the earthquakes prior to tomographic inversion. This program reads arrival-time measurements such as those made using *epick* and station locations from a user-supplied table. It can use a crustal model with homogeneous plane layers or three-dimensional model. It performs an iterative least-squares damped inversion to minimize the root mean square (RMS) arrival-time residual of the *P* and *S* arrival times.

3.3.4 *simul2000A*

simul2000A is a descendant of the program *simul3* developed by *Thurber* [1981; 1983]. It includes modifications by *Um and Thurber* [1987] who introduced "pseudo-bending" three-dimensional ray-tracing, and *Eberhart-Phillips* [1993] who added the ability to invert *S*-*P* times to determine a V_p/V_s model [*Evans et al.*, 1994].

The program uses *P*- and *S*-phase arrival times from local earthquakes to invert for hypocentres and wave-speed models. *simul2000A* first relocates the earthquakes using the initial wave-speed model. It then performs a series of iterations to calculate changes to the model that reduce the data variance. It applies these changes to the model and then relocates the earthquakes using the new model. The wave speed is defined continuously within the volume using linear interpolation between adjacent nodes. The solution is obtained using damped least squares. The damping value is chosen to balance reducing the data misfit and increasing model complexity. The procedure is repeated until the program exit criteria are fulfilled.

3.3.4.1 Program parameters

simul2000A uses a control file that defines numerous parameters such as the number of earthquakes to be used in the inversion, the damping values, the number of iterations, the amount of inversion-summary output required, and program exit criteria (Appendix 3). Other required input files are as follows:

- **Station file**. Gives the seismometer locations.
- **Grid file**. Contains information about the geometry of the wave-speed grid, a list of which nodes are allowed to vary during the inversion and which are held fixed, and the initial V_p and V_p/V_s values at each node [*Evans et al.*, 1994]. This file was constructed by hand with help of some auxiliary scripts. In general, any node can be allowed to vary in the inversion except the "distant" nodes, which are always fixed to prevent the inversion from changing structure outside the local volume of interest. In this study the uppermost- and the lowermost-layers of the grid at depths -4 and 10 km bsl were held fixed for both Long Valley caldera and the Coso geothermal area.

- **Arrival-time measurement file**. Contains the arrival-time data that were obtained either from catalogues or from the .ep files output by *epick* for the events used. Using the script *eloc* (Appendix 2), events were located and the arrival-time measurement file output in the format required by *simul2000A*.

The main files output by *simul2000A* contain:

- The final wave-speed model;
- Final event locations and travel times;
- Summary information for each iteration;
- Changes in the model and earthquake locations at each iteration;
- Travel-time residuals for each iteration; and
- The resolution matrix.

3.3.4.2 Damping parameters

The damping parameter ε^2 balances the two factors that the damped least squares inversion minimizes [*Eberhart-Phillips*, 1993]:

$$\min \left(\sum r^2 + \varepsilon^2 \, |\Delta m|^2\right) \tag{3.22}$$

where r represents the arrival-time residuals and Δm the changes to the model parameters.

Damping values chosen aimed to balance data variance reduction with increasing model complexity [*e.g.*, *Foulger and Toomey*, 1989; *Foulger et al.*, 2003; *Julian et al.*, 1996; *Miller et al.*, 1998].

3.3.4.3 Terminating the inversion

simul2000A terminates when any of the following criteria are reached:

- The maximum number of iterations specified in the control file is reached;
- The weighted RMS residual falls below a threshold defined in the control file;

- The change in the model solution norm falls below a user-defined value; or
- The variance reduction becomes insignificant with further iterations, as judged by an F-test (*i.e.,* a statistical test to detect how well the model fits the data) defined by the user.

3.3.5 *tomo4d*

Conventional three-dimensional tomographic methods generally invert one epoch of data at a time. If temporal variations in structures are sought, two independent inversion results can be differenced. *Julian and Foulger* [2010] developed a new tomography program *tomo4d*, which treats two epochs simultaneously, minimizing the structural differences between models for the different epochs. With this approach, differences in structure detected are more likely to reflect real temporal changes.

Solving for two epochs simultaneously requires the determination of twice as many parameters as solving for one epoch, and thus might require much more than twice the computational labour. *tomo4d* takes advantage of the fact that the system of normal equations for the two-epoch problem is sparse, and the solution can be obtained with little more labour than for solving for each epoch independently [*Julian and Foulger*, 2010].

tomo4d uses the following:

- The azimuthal-equidistant Earth-flattening approximation of *Julian et al.* [2000]. This contrasts with some other programs that simply treat longitude and latitude as a local Cartesian coordinate system;
- The bending method of *Julian and Gubbins* [1977] for ray-path computation that allows "real" ray-tracing in three-directions;
- The parameter-separation method of *Spencer and Gubbins* [1980] to solve the hypocentre and wave-speed coupling problem;
- Three-dimensional tricubic interpolation [*Press et al.*, 2007, Section 3.6] which is a more effective method to compute slowness values and their spatial derivatives between grid nodes;
- Varying damping parameters to adjust the strength of the "damping" constraint on perturbations to many different parameters including the seismic-wave speed, seismic-event origin parameters, wave-speed ratio, wave-speed roughness, wave-speed steepness, the direction of incoming wavefronts from distant events and the differences in the seismic-wave speeds at different epochs. It works to minimize the differences between models for different epochs and the misfit as well. Thus the remaining variations are truly required by the data and more likely reflect real changes between the two epochs.

Prior to this thesis work, *tomo4d* had been tested using synthetic data and shown to not only suppress artificial temporal variations in seismic-wave speed but also to be able to reveal true temporal variations [*Julian and Foulger*, 2010]. Applying *tomo4d* to data from both Long Valley caldera and the Coso geothermal area in this thesis was the first use of the program with real data.

3.3.5.1 Program parameters

tomo4d reads data from input files specified by the command-line options *-blasts*, *-qdistant*, *-qlocal*, and *-shots*. Local earthquakes were used for the present studies. Because *tomo4d* reads files in the same format as *simul2000A* [*Evans et al.*, 1994], the same arrival-time measurement files were used. Other essential input files are:

- **V_p starting model**, called by the option *-pmodel*. This file contains information about the number of wave-speed nodes in the study volume, and the initial V_p values at each node;
- **V_s starting model**, called by the option *-smodel*. This file contains the same information as the V_p starting model but for V_s;
- **Station file**, called by the option *-station*. This file gives, on each line, the station code, latitude, longitude, and elevation.

tomo4d uses command-line options to control ray-tracing computations and damping parameters (Appendix 3).

3.3.5.2 Damping parameters

tomo4d uses damping to limit the magnitudes of changes made to the hypocentre parameters and wave-speed models at each iteration during the inversion. The values of these parameters can be controlled via command-line options (Bruce Julian, personal communication). *tomo4d* attempts to minimize the sum:

$$\frac{1}{n_{data}}\,\chi^2 + \varepsilon^2_{Origin}\,\frac{1}{2}\sum_{epochs}\frac{1}{n_{ev\_local}}\sum_{\substack{local\\events}}\frac{1}{4}\left[\frac{(\Delta x)^2+(\Delta y)^2}{\sigma_h^2}+\left(\frac{\Delta z}{\sigma_z}\right)^2+\left(\frac{\Delta t}{\sigma_t}\right)^2\right]$$

$$+\,\varepsilon^2_{Velocity}\,\frac{1}{2}\sum_{epochs}\frac{1}{n_{nodes}}\sum_{nodes}\frac{1}{2}\left[\left(\frac{\Delta V_p}{\sigma_{V_p}}\right)^2+\left(\frac{\Delta V_s}{\sigma_{V_s}}\right)^2\right]$$

$$+\,\varepsilon^2_{Epoch}\,\frac{1}{n_{nodes}}\sum_{nodes}\frac{1}{2}\left[\left(\frac{\Delta\delta V_p}{\sigma_{\delta V_p}}\right)^2+\left(\frac{\Delta\delta V_s}{\sigma_{\delta V_s}}\right)^2\right]$$

where Δ refers to changes from iteration to iteration and δ refers to temporal changes from epoch to epoch.

The first term is proportional to the conventional measure of the goodness of fit to data,

$$\chi^2 = \sum_{data} \left(\frac{t^{(O)} - t^{(c)}}{\sigma} \right)^2$$

where $t^{(O)}$ and $t^{(C)}$ are the observed and computed arrival times of a particular signal, and σ is its standard error.

The second term applies to local events only, and constrains changes in their hypocentral parameters. The parameter ε_{Origin} is set using the *-dorigin* option. Δx, Δy, Δz, and Δt are the per-iteration changes to the hypocentre coordinates and origin time, and σ_h, σ_z, and σ_t are *a priori* standard errors that control the changes to the horizontal positions, vertical positions, and origin times of the events. They can be set using the *-seorigin* option.

The third term constrains changes in the seismic wave-speeds in the model. The parameter $\varepsilon_{Velocity}$ is set using the *-dspeed* option. The quantities σ_{V_p} and σ_{V_s} are *a priori* standard errors that control the sensitivities to V_p and V_s. They are set using the *-sevel* option.

The fourth term constrains iteration-to-iteration changes in the difference between the seismic wave-speeds at different epochs. The parameter ε_{Epoch} adjusts the strength of the constraint and is set using the *-depoch* option. The superscripts (0) and (1) refer to the two epochs and the standard errors $\sigma_{\delta V_p}$ and $\sigma_{\delta V_s}$ are *a priori* standard errors that control the changes to wave-speed changes with time. They are set using the *-sedvel* option.

3.3.5.3 Terminating the inversion

tomo4d does not terminate the inversion automatically. It stops after running the number of iterations specified by the user.

CHAPTER 4

TOMOGRAPHIC INVERSION: LONG VALLEY CALDERA

4.1 Background

Julian et al. [1998] used local earthquake tomography with data collected in 1989-1990 on the Northern California Seismic Network (NCSN) to obtain a tomographic image of the upper 4 km of Mammoth Mountain in Long Valley caldera. They detected a negative-V_p/V_s anomaly directly beneath Mammoth Mountain at depths of 0-2 km below sea level (b.s.l.). The outer boundary of the imaged body correlates with areas of killed trees at the surface. They suggested that the body was a CO_2 reservoir.

Foulger et al. [2003] performed a tomographic inversion for crustal structure beneath a 28 km x 16 km area of Long Valley caldera encompassing part of the resurgent dome, the south moat, and Mammoth Mountain. An earthquake data set collected in 1997 during an intense swarm in the Casa Diablo Hot Springs south moat area [*Foulger et al.*, 1998a; *Foulger et al.*, 1998b] was used. A negative-V_p/V_s anomaly beneath Mammoth Mountain was detected and confirmed the observation of *Julian et al*. [1998].

Foulger et al. [2003] investigated temporal variations in structure by differencing the 1997 results with those from 1989/1990. They found significant changes in V_p and V_s consistent with the migration of CO_2 into the upper 2 km beneath Mammoth Mountain. The results suggested that repeat tomography has the potential to provide a valuable tool for monitoring gas migration beneath active silicic volcanoes.

A similar experiment to those of 1989-1990 and 1997 was performed in this thesis using data from 2009-2010, with a view to difference 2009-2010 with 1997 results and look for structural changes in the interim period. This project investigated further whether repeat tomography can provide a useful volcano-monitoring tool. The initial

earthquake locations were obtained from the United States Geological Survey (USGS) catalogues and the seismograms for the selected events were downloaded from the NCEDC. Arrival times were measured by hand using program *epick.*

A combined dataset including the 1989 and 1997 data (originally assembled and inverted by *Foulger et al*. [2003]) and the 2009-2010 data measured as part of this thesis project was first inverted using *simul2000A*. This yielded an average wave speed model, which then was used as a starting model for separate inversions for the years 1997 and 2009-2010.

The new program *tomo4d* was tested against *simul2000A* using the 1997 and 2009-2010 data. This was its first application to real data.

4.2 The dataset

A 28 x 16 km^2 area was studied throughout a depth range of -4 to 10 km b.s.l. The nodes of the grid defining the study volume were spaced by 2 km horizontally and 1 km vertically. Locations of earthquakes used for the years 2009 and 2010 are shown in Figure 4.1 and Figure 4.2. Subsets for analysis were selected (Appendix 4), comprised of events that were well distributed and recorded by the largest number of stations. The scripts *qselect* and *qvalues* (Bruce Julian, personal communication) were used for this purpose.

The seismograms for the selected events were reformatted and list files constructed in the format required by *epick* (Bruce Julian, unpublished computer program), The arrival times were then measured by hand.

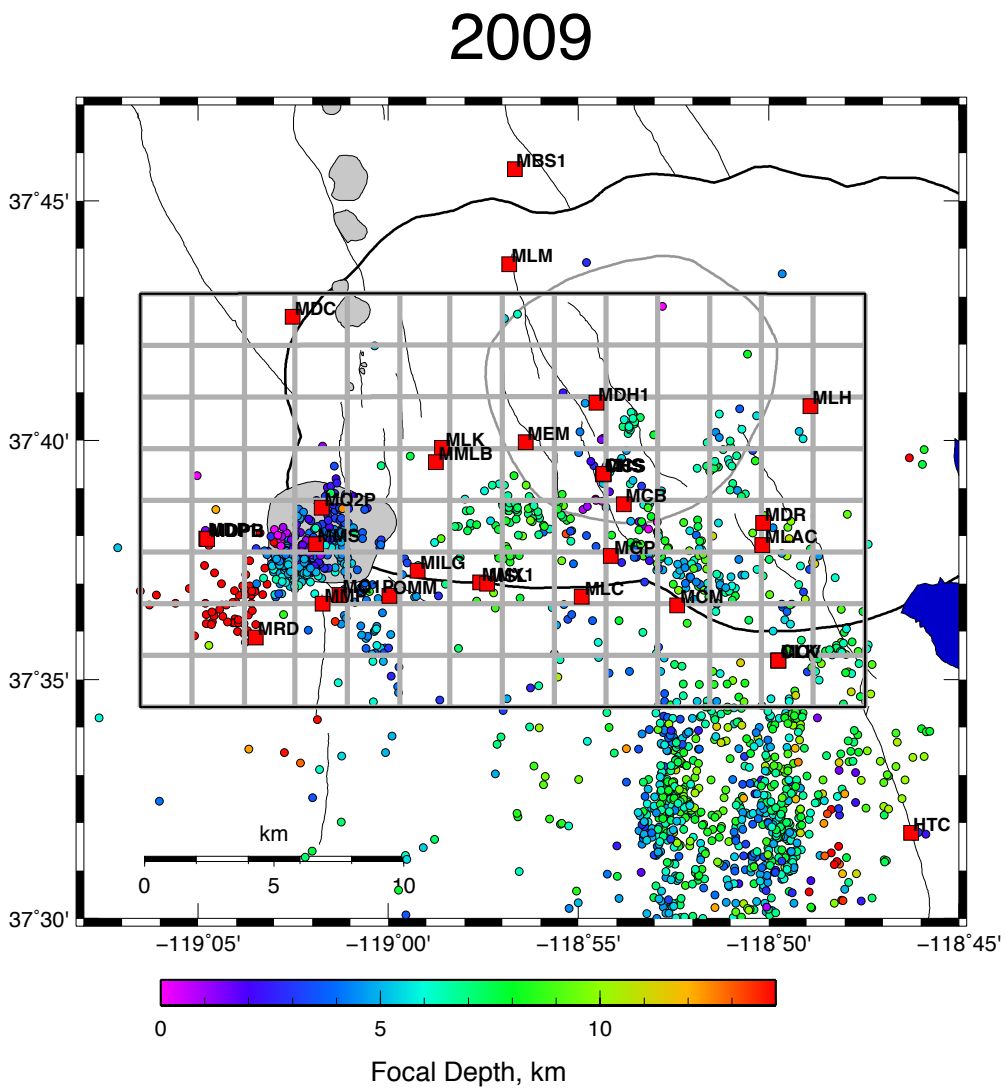

Figure 4.1: Map of central and western Long Valley caldera and vicinity, showing earthquakes in 2009 from the USGS catalogue. Mammoth Mountain in the southwestern corner of the caldera is shown in light gray. The resurgent dome is bounded by a thin gray line. Black line is the topographic margin of the caldera; thin gray lines are faults; and coloured dots are epicentres of the earthquakes. The grid is the tomography inversion grid. Red squares are the seismometer stations. Blue area at right is Crowley Lake.

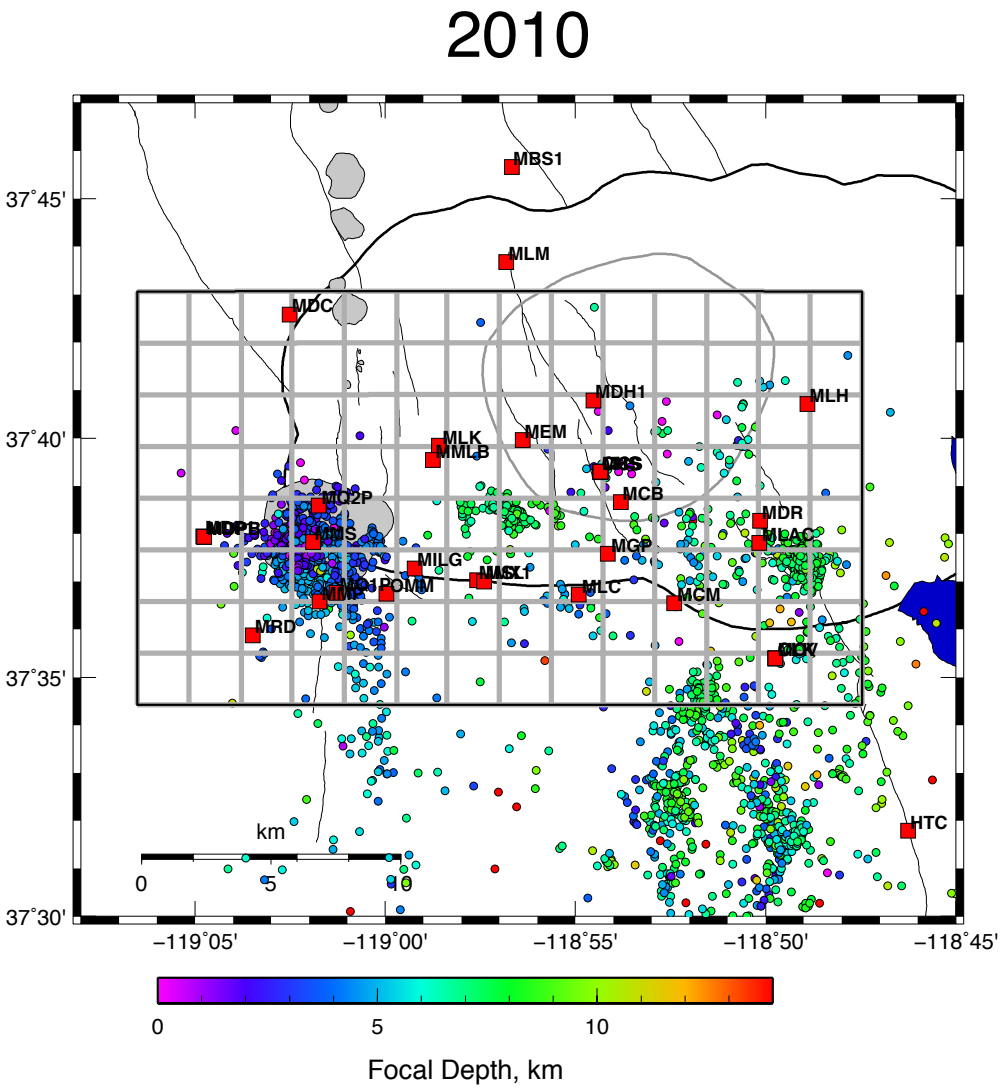

Figure 4.2: Same as Figure 4.1, for the year 2010.

4.3 Arrival time measurements

P- and *S*-phase arrival times for 267 earthquakes (Figure 4.3) were measured using program *epick*. Among these events, 3727 *P* and 1170 *S* arrival times were measured with variable qualities (Figure 4.4 - Figure 4.7). Arrivals could be measured to ~0.01 s for *P* and ~0.03 s for *S*.

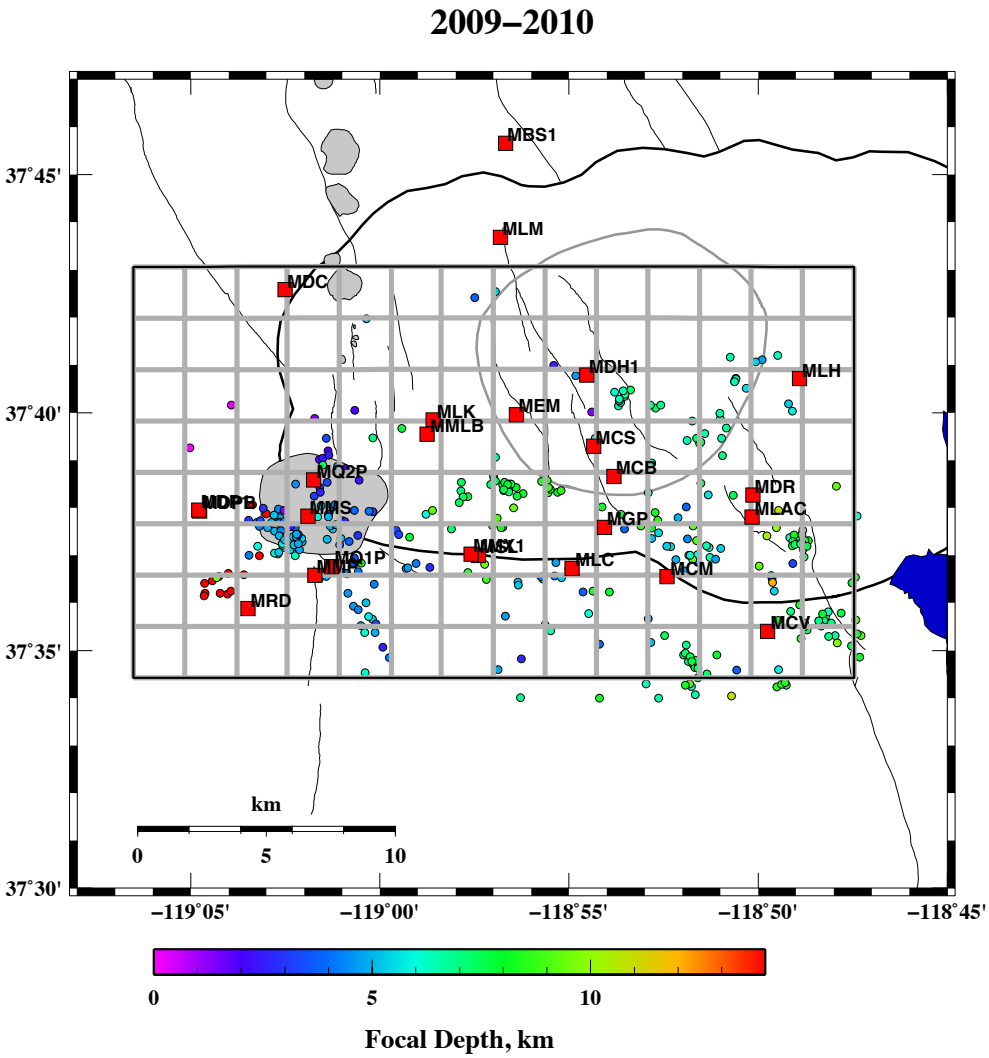

Figure 4.3: Map of central and western Long Valley caldera, showing 267 events selected for arrival-time measurement for the period 2009-2010. Symbols as for Figure 4.1.

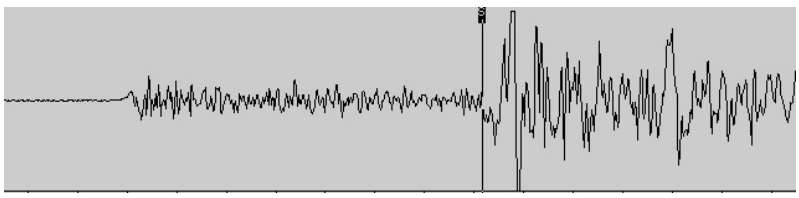

Figure 4.4: A well-recorded *S* phase on the horizontal channel EHE of the three-component seismic station MQ2P from the network shown in Figure 4.1.

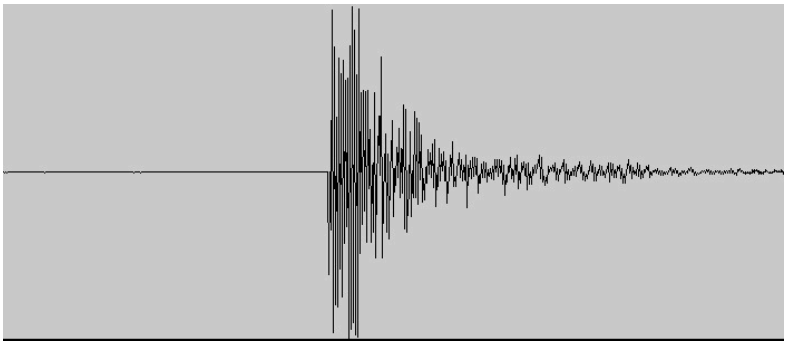

Figure 4.5: A well-recorded *P* phase from the vertical-component seismic station MRD.

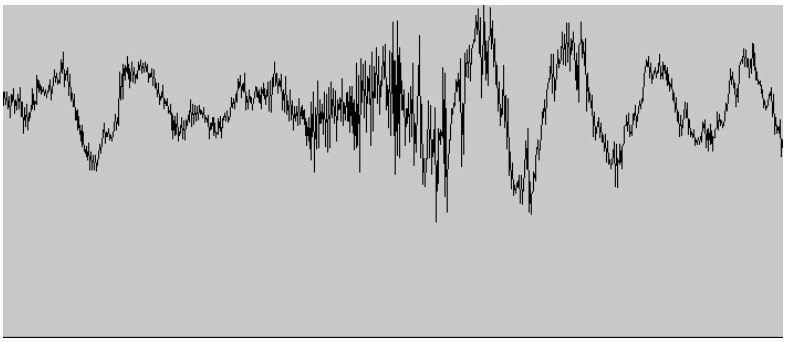

Figure 4.6: A poorly recorded *S* phase from the horizontal channel HHE of the three-component seismic station MMLB.

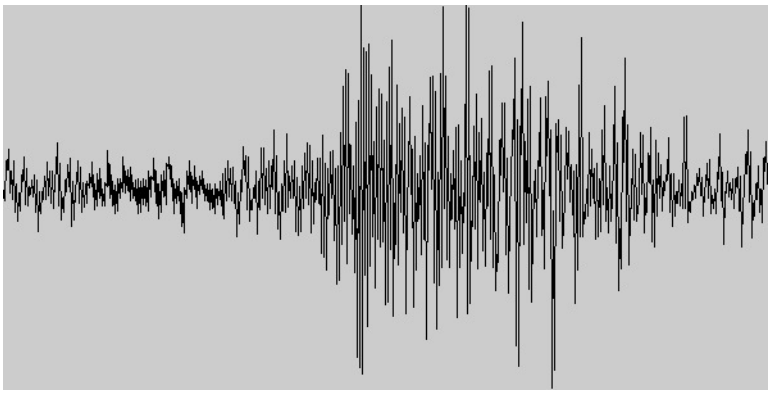

Figure 4.7: A poorly recorded *P* phase from the vertical channel HHZ of the three-component seismic station MCB.

4.4 Inversion using *simul2000A*

4.4.1 The inversion procedure

Tomographic inversion for 2009-2010 data was performed using *simul2000A* in order to compare the results with models obtained previously for the year 1997 by *Foulger et al*. [2003]. The data were first inverted using the same starting model and tomography grid used for the 1997 data by *Foulger et al*. [2003]. They first used a one-dimensional starting model derived by inverting data from 1989/1990 using the program *velest* [*Julian et al.*, 1998; *Kissling et al.*, 1994]. They then used a graded inversion method (a series of inversions with progressively smaller nodal spacing where the output of the coarser inversions is used as input for the finer-scale inversions) to invert the combined 1989/1990 and 1997 data. This step provided an average wave speed model that I used as a starting model. One-dimensional starting models were not used as the inversion proceeded smoothly with three-dimensional starting models.

After the first inversion of the 2009-2010 data, outliers were identified that might be caused by incorrect phase measurements or timing errors. As the arrival times for the 2009-2010 dataset had been measured as part of this project, these outliers could be checked on the original seismograms and either corrected or eliminated as appropriate.

A combined dataset including the 1989, 1997 and 2009-2010 data was inverted for the present project, first using large damping values of 20 s^2 km^{-1} for V_p and 20 s for V_p/V_s to obtain an average wave speed model (COMB-20), and then using smaller damping values of 5 s^2 km^{-1} for V_p and 5 s for V_p/V_s (COMB-5) to obtain a more detailed picture. A total of 606 earthquakes were used for this inversion, including 10,961 *P*-phase and 5,446 *S*-phase arrival times. The same starting model as used by *Foulger et al*. [2003] was used.

The wave speed model (Appendix 5) obtained using the combined data (COMB-5) was then used as a starting model for separate inversions for the years 1997 and 2009-2010. The input files and the executable script used to run the inversions are given in

Appendix 6 – Appendix 9. Number of data for the tomographic inversions are shown in Figure 4.8, Figure 4.9 and Table 4.1.

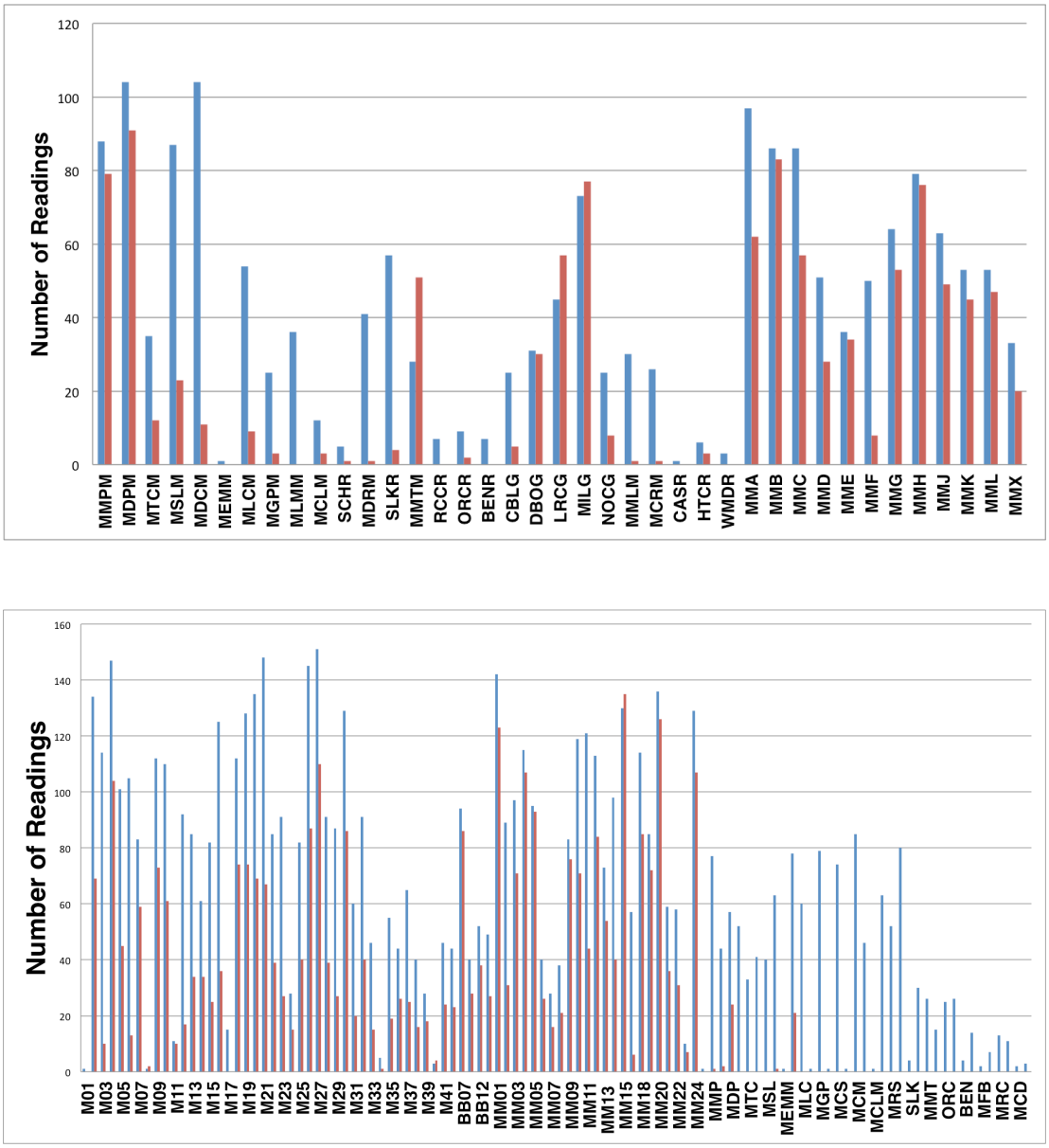

Figure 4.8: Histograms showing numbers of *P*- (blue) and *S*-phase arrival-times (red) measured at each station and used in the tomographic inversions. (top) 1989 (measured by *Julian et al.* [1998]). (bottom) 1997 (measured by *Foulger et al.* [2003]).

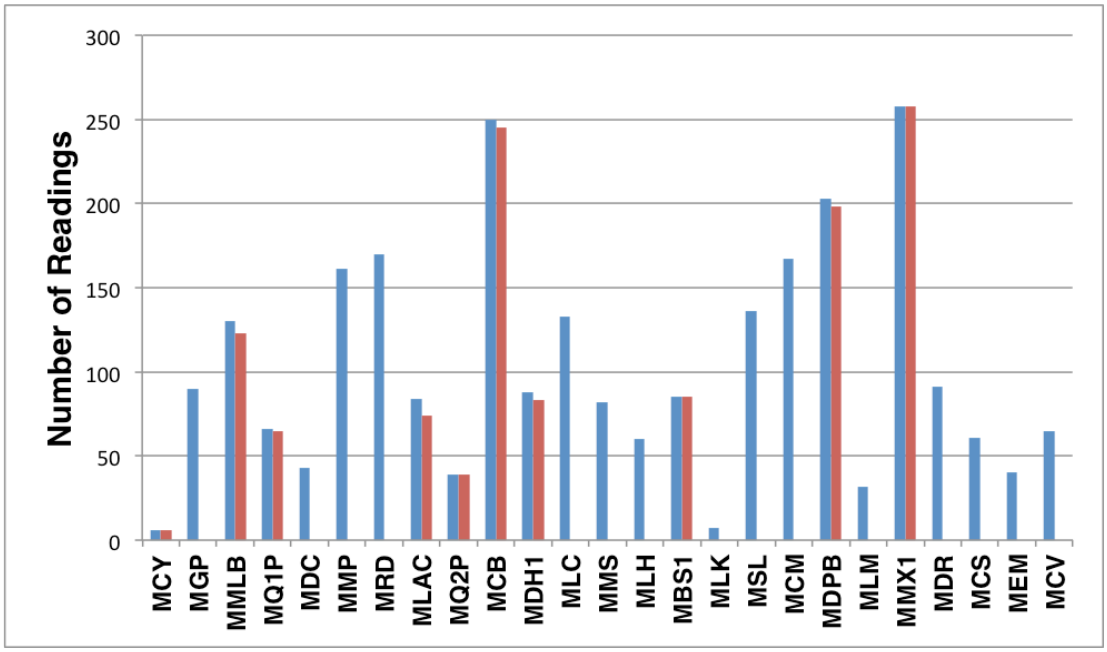

Figure 4.9: Same as Figure 4.10, for the year 2009-2010 (measured in this study).

Table 4.1: Details of tomographic inversions performed using program *simul2000A* for the years 1997 and 2009-2010 and for a combined dataset (1989, 1997 and 2009-2010) first using large damping values of 20 s^2 km^{-1} for V_p and 20 s for V_p/V_s (COMB-20) and second using small damping values of 5 s^2 km^{-1} for V_p and 5 s for V_p/V_s (COMB-5).

Model	COMB-20	COMB-5	1997	2009-2010
No. of events	606	606	233	267
No. of *P*-wave arrivals	10961	10961	6789	2456
No. of *S*-wave arrivals	5446	5446	3246	1148
V_p damping, s^2/km	20	5	20	20
V_p/V_s damping, s	20	5	20	20
Final RMS residuals, s	0.09	0.09	0.09	0.09
Variance reduction, %				
P	36	38	21	37
S-P	23	29	10	14

The final total RMS was 0.09 s for all inversions. The variance reduction achieved for the 2009-2010 inversion was 37% for *P* and 14% for *S*. This is stronger than that achieved for the 1997 inversion but is still smaller than the variance reduction in the inversion COMB-5 since low dampings were used for that inversion.

4.4.2 Damping parameters

The wave speed model obtained using high damping values (COMB-20) shows the most significant structures. For a starting model for the present inversions, the inversion COMB-5 (Table 4.1) was used. With this starting model, each yearly or bi-yearly set was inverted separately using higher damping values of 20 s^2 km^{-1} for V_p and 20 s for V_p/V_s. This strategy was extensively investigated and used by *Foulger et al*. [2003] and ensures that the inversion results contain only the most significant model changes necessary to fit the data.

4.5 Inversion using *tomo4d*

4.5.1 The inversion procedure

First, an inversion was conducted with *tomo4d* of data from the years 1997 and 2009-2010 combined (COMB). Another inversion then was performed for the data from 1997 and 2009-2010 as two separate epochs. The three-dimensional model derived using *simul2000A* was used as a starting model. This resulted in many rays not converging. This initial test showed that the bending ray tracing method of Julian and Gubbins [1977] requires a more realistic crustal model than generated by *simul2000A*.

As a result of this test, I changed the inversion strategy and used a one-dimensional starting model for *tomo4d*. The one-dimensional V_p and V_s starting models and the input station file are given in Appendix 10. Table 4.2 shows details of the inversions using *tomo4d*.

Table 4.2: Details of the *tomo4d* tomographic inversions.

Model		COMB	1997	2009-2010
No. of events		479	233	264
No. of *P*-wave arrivals		9038	6634	2404
No. of *S*- wave arrivals		4305	3199	1106
$\varepsilon_{Velocity}$, σ_{V_P} and σ_{Vs}		0.1, 0.1, 0.05	0.1, 0.1, 0.05	0.1, 0.1, 0.05
Final RMS residuals, s		0.10	0.11	0.09
χ^2reduction, %				
	P	23	20	41
	S	26	26	20

Chi-squared (the weighted variance) decreased by 20% for *P*-wave arrival times, and by 26% for *S*-wave arrival times for the 1997 epoch. For the 2009-2010 epoch, the reductions were 41% for *P* and 20% for *S*. The Final RMS was 0.11 s for the 1997 data and 0.09 s for the 2009-2010 data.

4.5.2 Damping parameters

During inversion, *tomo4d* uses a modified objective function to control the magnitudes of perturbations made to event origins, seismic wave speeds and inter-epoch wave-speed differences, as explained in Section 3.3.5.2. To choose values for the parameters ε_{Origin}, $\varepsilon_{Velocity}$, and ε_{Epoch} that control this "damping" process, single-iteration inversions were performed using a variety of values and the resulting changes in goodness of fit and in origin and model perturbations were examined.

Figure 4.10 through Figure 4.12 show typical results of such tests, conducted using data from Long Valley caldera for the two epochs 1997 and 2009-2010 and inverting for structural change. As damping parameters decrease from their largest values (left sides of figures), perturbations to the origins/models increase and the fit to the data improves. However, at some point the linearized approximation is no longer adequate and the improvement in data fit ceases. Optimal damping occurs for the smallest values that do not cause problems with nonlinearity. Thus, for example we chose $\varepsilon_{Velocity} = 0.1$, $\varepsilon_{Origin} = 50$ and $\varepsilon_{Epoch} = 0.05$ as optimal values. To ensure the optimal damping values were selected, I studied the changes in wave speed model and event origin time and location throughout five-iteration inversion using the selected damping values. These changes are supposed to get smaller over iterations and not to cause problems with nonlinearity (Appendix 11).

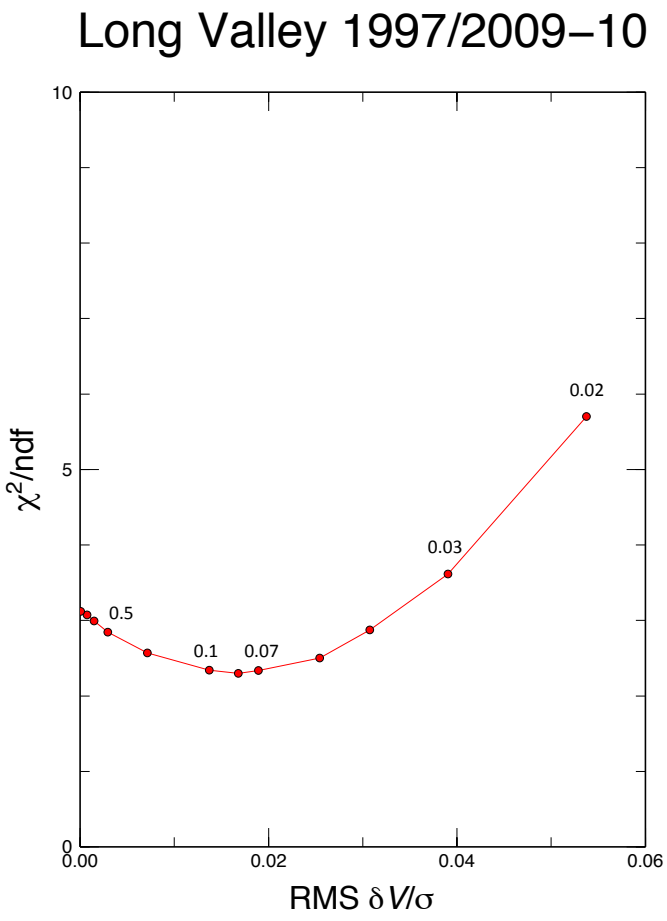

Figure 4.10: The effect of wave-speed damping $\varepsilon_{Velocity}$ on models of structure and structural change for Long Valley caldera derived from data for epochs 1997 and 2009-10. The abscissa gives the sum of the root-mean-square (RMS) scaled changes in V_P and V_S at all grid nodes for the two epochs during one iteration of the inversion process. The ordinate gives a measure of the lack of fit to the arrival-time data. The dots correspond to values of the damping parameter $\varepsilon_{Velocity}$ of 0.02 (rightmost), 0.03, 0.04, 0.05, 0.07 0.08, 0.1, 0.2, 0.5, 1, 2, and 20 (leftmost), with $\sigma_{V_P} = 0.1$ km/s, and $\sigma_{V_S} = 0.05$ km/s. As the damping parameter $\varepsilon_{Velocity}$ is decreased, the fit at first becomes better, and then becomes worse as nonlinear effects become more important. In this example, all other types of damping are disabled.

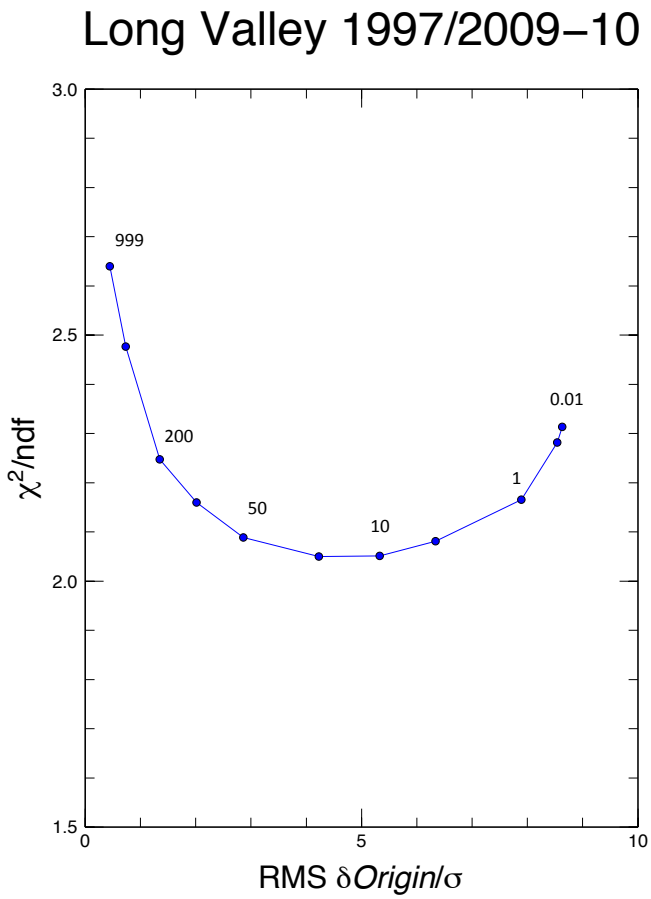

Figure 4.11: The effect of event-origin damping ε_{Origin} on models of Long Valley caldera derived from data for epochs 1997 and 2009-10. The abscissa gives the sum of the root-mean-square (RMS) scaled changes in the origin components (four per event) for all events in both epochs during one iteration of the inversion process. The ordinate gives a measure of the lack of fit to the arrival-time data. The dots correspond to values of the damping parameter ε_{Origin} of 0.01 (rightmost), 0.1, 1, 5, 10, 20, 50, 100, 200, 500 and 999 (leftmost), with $\sigma_h = \sigma_z = 0.2$ km, and $\sigma_t = 0.1$ s. As the damping parameter ε_{Origin} is decreased, the fit at first becomes better, and then becomes worse as nonlinear effects become more important. In this example, all other types of damping were disabled, except for wave-speed damping with $\varepsilon_{Velocity} = 0.08$, $\sigma_{V_P} = 0.1$ km/s, and $\sigma_{V_S} = 0.05$ km/s.

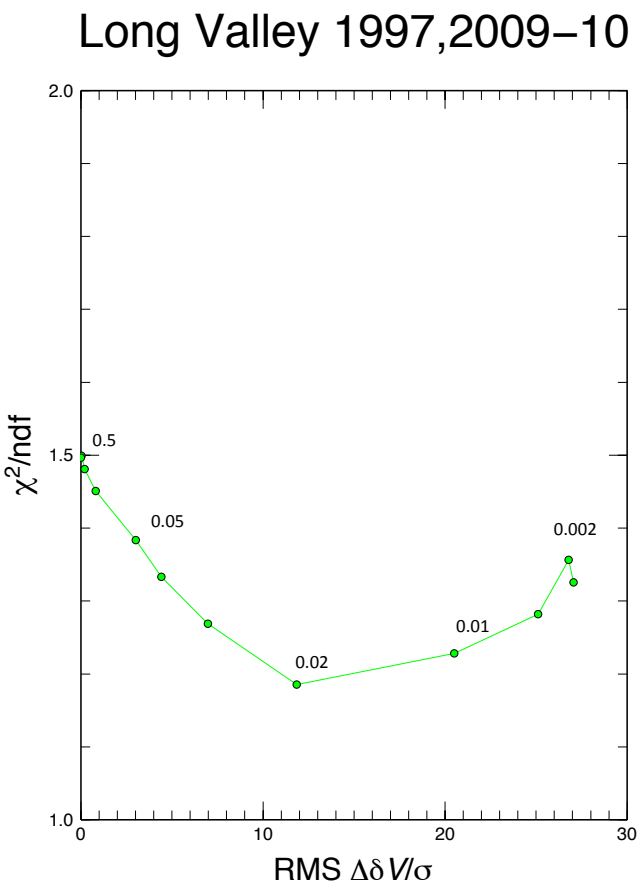

Figure 4.12: The effect of inter-epoch damping ε_{Epoch} on models of structure and structural change for Long Valley caldera derived from data for epochs 1997 and 2009-10. The abscissa gives the sum of the root-mean-square (RMS) scaled inter-epoch differences δV_P and δV_S at all grid nodes after one iteration of the inversion process. The ordinate gives a measure of the lack of fit of the model predictions to the arrival-time data. The dots correspond to values of the damping parameter ε_{Epoch} of 0.001 (rightmost), 0.002, 0.005, 0.010, 0.020, 0.030, 0.040, 0.050, 0.1, 0.2, 0.5, 1, and 10 (leftmost), with $\sigma_{\delta V_P} = 0.01$ km/s, and $\sigma_{\delta V_S} = 0.005$ km/s. As the damping parameter ε_{Epoch} is decreased, the fit becomes better, and then becomes worse as nonlinear effects become more important. In this example, all other types of damping are disabled, except for wave-speed damping with $\varepsilon_{Velocity} = 0.08$, $\sigma_{V_P} = 0.1$ km/s, $\sigma_{V_S} = 0.05$ km/s and $\varepsilon_{Origin} = 50, \sigma_h = \sigma_z = 0.2\ km,$ and $\sigma_t = 0.1\ s$.

4.6 Hit counts and quality of the results

The quality of the inversion results is assessed similarly for both *simul2000A* and *tomo4d* and illustrated using the number of rays passing through or near the nodes of the inversion grid. Thus the best-sampled areas are the ones with higher number of rays, i.e., higher number of data involved (Figure 4.13 and Figure 4.14). The sampling within the caldera is limited to the southwest and south region because the seismicity was in the south moat and beneath Mammoth Mountain. The top two layers have limited sampling especially for the V_s model with the 2009-2010 data. Ray-path density for the V_s model is generally poorer than for V_p model. This is largely because 14 out of the 25 stations used only had vertical components, and no *S*-wave measurements were made from vertical components. The best-sampled area will be interpreted in this thesis.

Figure 4.15 shows histograms of the arrival-time residuals for the inversions of 1997 and 2009-2010 data using *simul2000A*. For 2009-2010 data, the improvement to *P* residuals was greater than for *S* residuals. A slight improvement to both *P* and *S* residuals was achieved for 1997 data compared to 2009-2010 data. The final RMS travel-time residual for 1997 data was 0.05 s for *P*-waves and 0.13 s for *S*-waves. For 2009-2010 data, this was 0.06 s for *P*-waves and 0.14 s for *S*-waves. The higher final RMS for *S* residuals shows that the V_p/V_s model is not resolved as well as the V_p model.

The inversion of 1997 and 2009-2010 data using *tomo4d*, as shown in Figure 4.16, shows a stronger improvement to the data residuals than that achieved using *simul2000A*. The initial residuals are larger than those from using *simul2000A*. This is because *tomo4d* was run using a one-dimensional starting model compared to the three-dimensional starting model used for *simul2000A*. In other words, the large improvement in the data residuals for *tomo4d* results partly from the one-dimensional starting model being further from the final model. Despite this, the final RMS residual achieved using *tomo4d* is similar to that achieved using *simul2000A*. For the 2009-2010 data, the final total RMS residuals were 0.09 for both inversions. Again, as for the *simul2000A* results, the final RMS of the *S* residuals is higher than that of the *P* residuals showing that the V_p/V_s model is not resolved as well as the V_p model.

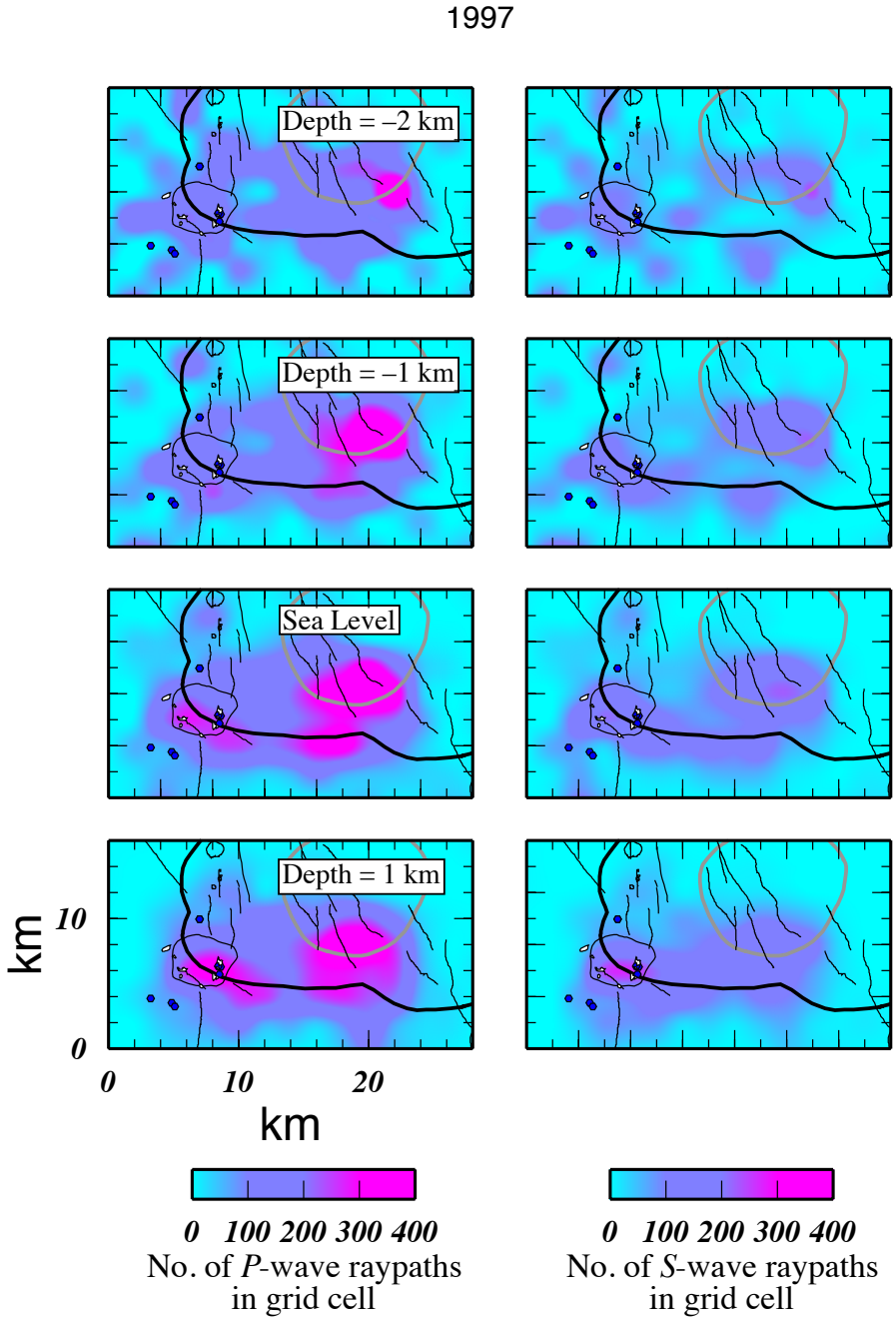

Figure 4.13: Hit count map showing the best-sampled areas in the study volume at different depths for the year 1997. Geological features are the same as for Figure 4.1.

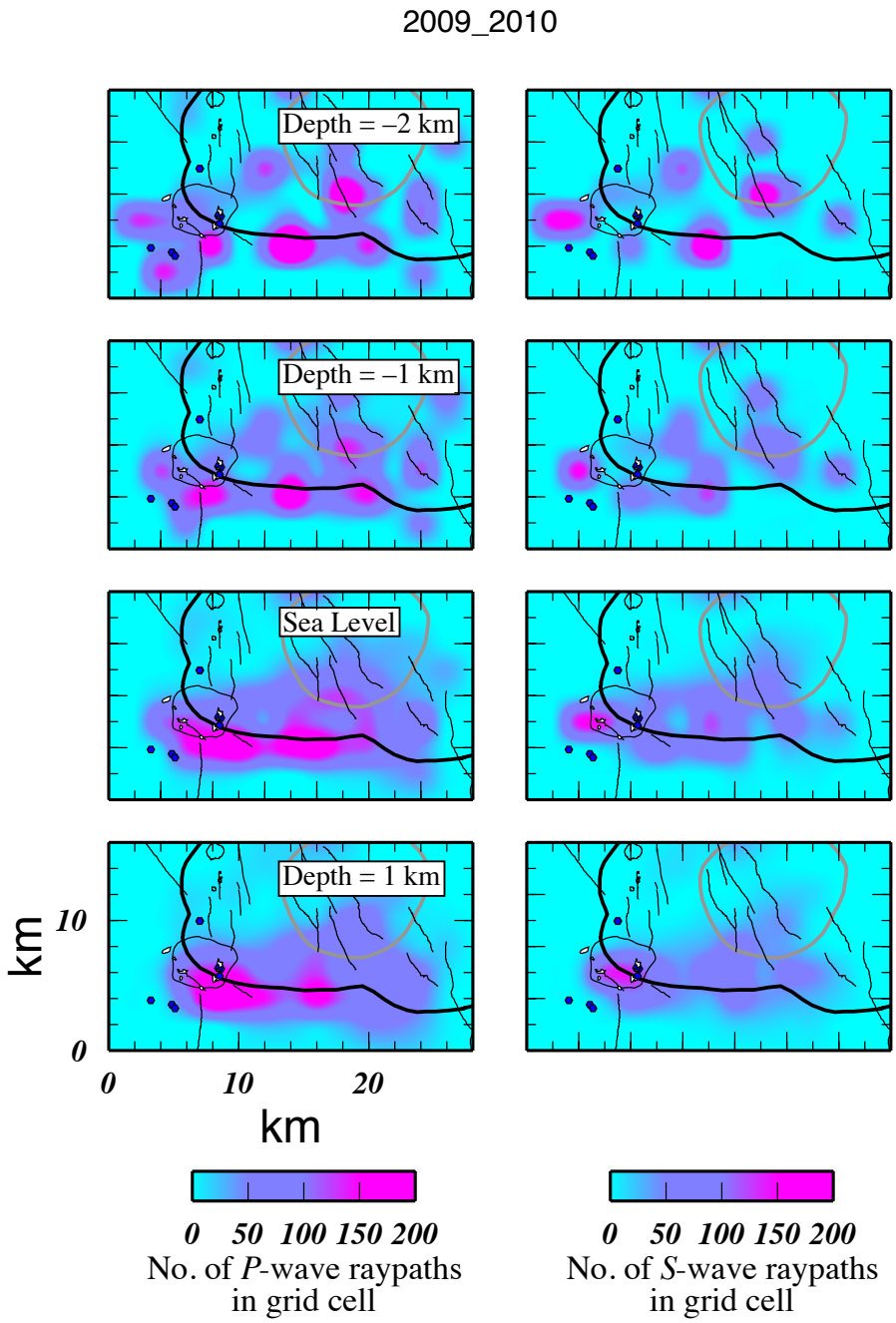

Figure 4.14: Same as Figure 4.13, for the year 2009-2010.

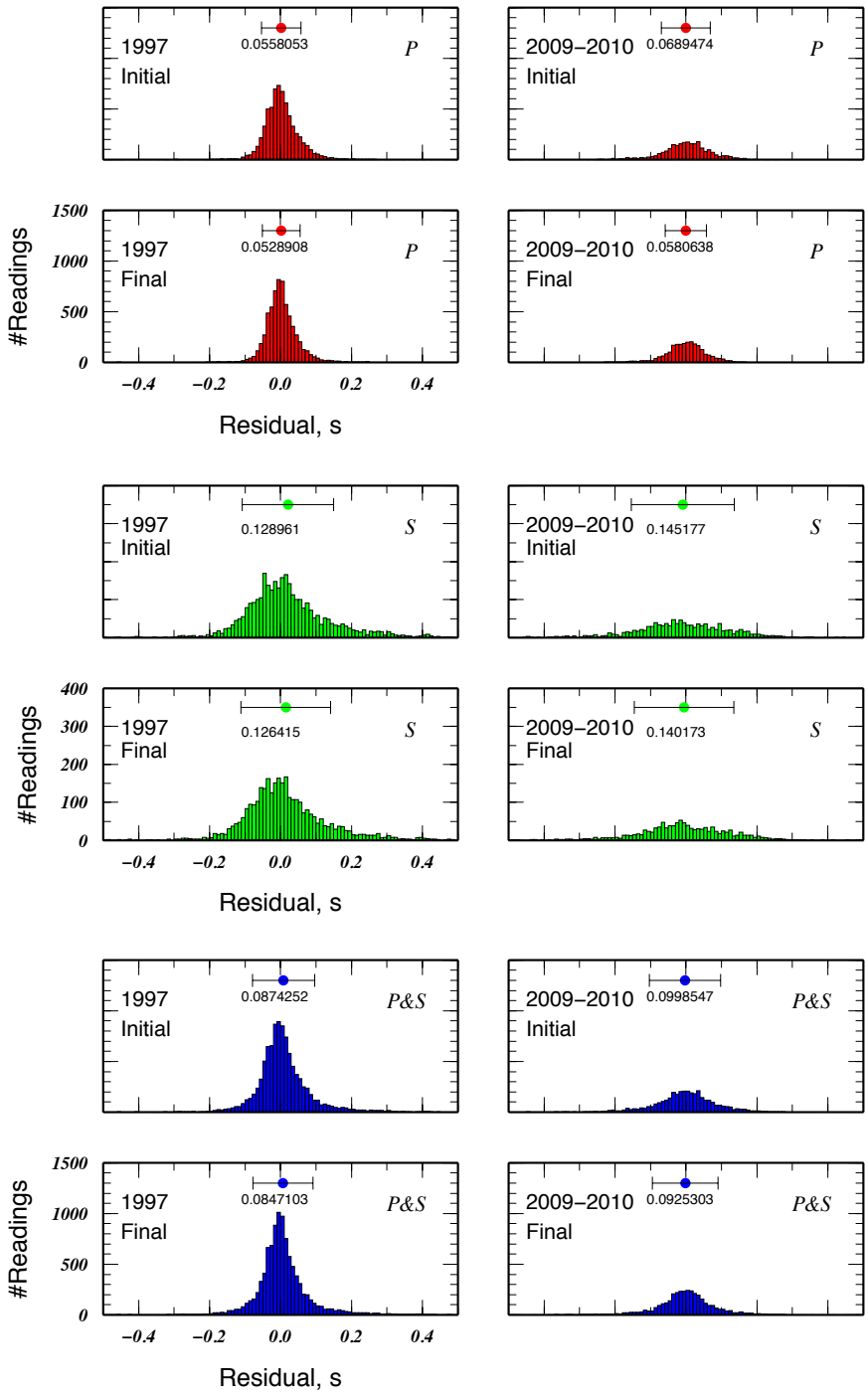

Figure 4.15: Histograms of the initial and final arrival-time residuals for (red) *P*-wave observations, (green) *S*-wave observations and (blue) both *P*- and *S*-wave observations, for the inversions of 1997 and 2009-2010 data using program *simul2000A*. The coloured circle at the top of each histogram indicates the mean residual and the error bar refers to the spread around the mean value. The number below the circle is the RMS residual.

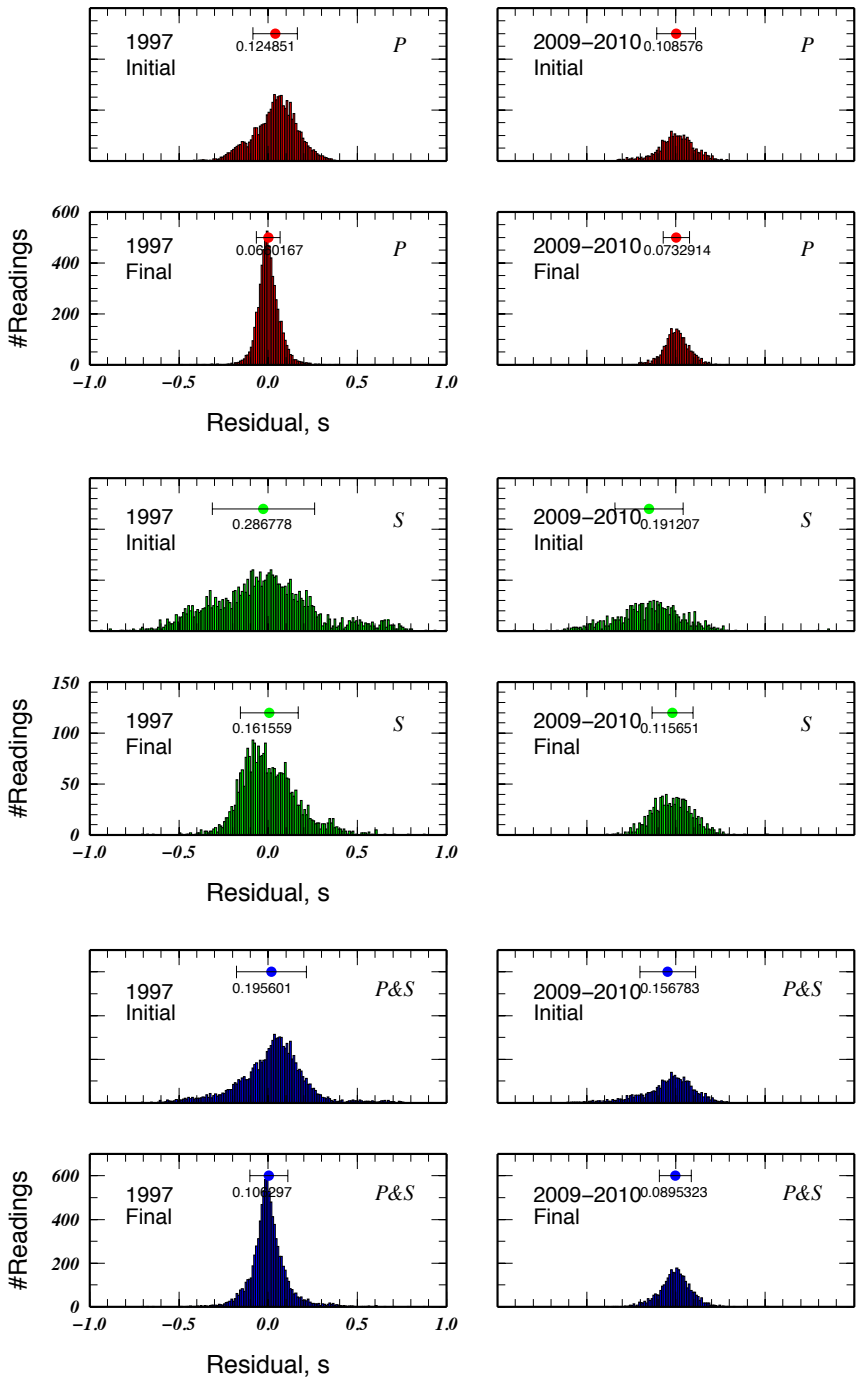

Figure 4.16: Same as Figure 4.15, for the inversion of 1997 and 2009-2010 data using program *tomo4d*. Note difference in scale of abscissa.

4.7 Results from *simul2000A*

4.7.1 V_p, V_s, and V_p/V_s structure and temporal variations

The results of combined and independent inversions of the 1997 and 2009-2010 data, along with the apparent temporal differences, are shown in Figure 4.17 to Figure 4.19. The imaged structures obtained for the two epochs are similar. Wave speeds are low inside the caldera and high outside the caldera and in the resurgent dome. Small differences can be seen in the south moat down to 1 km b.s.l. and in the eastern and western parts of Mammoth Mountain in the upper 2 km.

Both the V_p and the V_s fields in model COMB-20 (Figure 4.17) correlate with the caldera boundary and the edge of the resurgent dome. Low wave speeds dominate in the western part of the resurgent dome at 1 km a.s.l. and below. At sea level and above, high wave speeds characterize the Sierra Nevada outside the caldera except near Mammoth Mountain.

The V_p/V_s field is dominated by negative anomalies beneath the south moat and Mammoth Mountain at depth 2 km a.s.l. down to 1 km b.s.l. A small volume with high V_p/V_s dominates the southern part of Mammoth Mountain at 2 km a.s.l..

The apparent temporal change in V_p and V_s in the south moat from 1997 to 2009-2010 (Figure 4.18, right panels) resembles two volumes that progressively shrink and became more separated with depth with the strongest increase of >10% in V_p and V_s at the surface. The northeast part of Mammoth Mountain also shows an increase in V_p and V_s in the top three grid layers, with the strongest increase of ~10%, at 2 km a.s.l., disappearing at 1 km b.s.l. The western part of Mammoth Mountain shows an apparent decrease in wave speed. Overall, the patterns of change in V_p and V_s are similar, but the changes in V_s are stronger.

The apparent temporal change in V_p/V_s (Figure 4.19, right panel) is generally a decrease within the south moat to the south-east of the resurgent dome and to the east of Mammoth Mountain down to 1 km b.s.l., with the strongest decrease of ~3% in the top grid layer, resulting from an increase in V_p and a greater increase in V_s. Beneath Mammoth Mountain, another apparent decrease in V_p/V_s is seen above sea level,

consistent with a decrease in V_p and a smaller decrease in V_s. This is surrounded by areas of increased V_p/V_s (~2%) to the southeast and to the west.

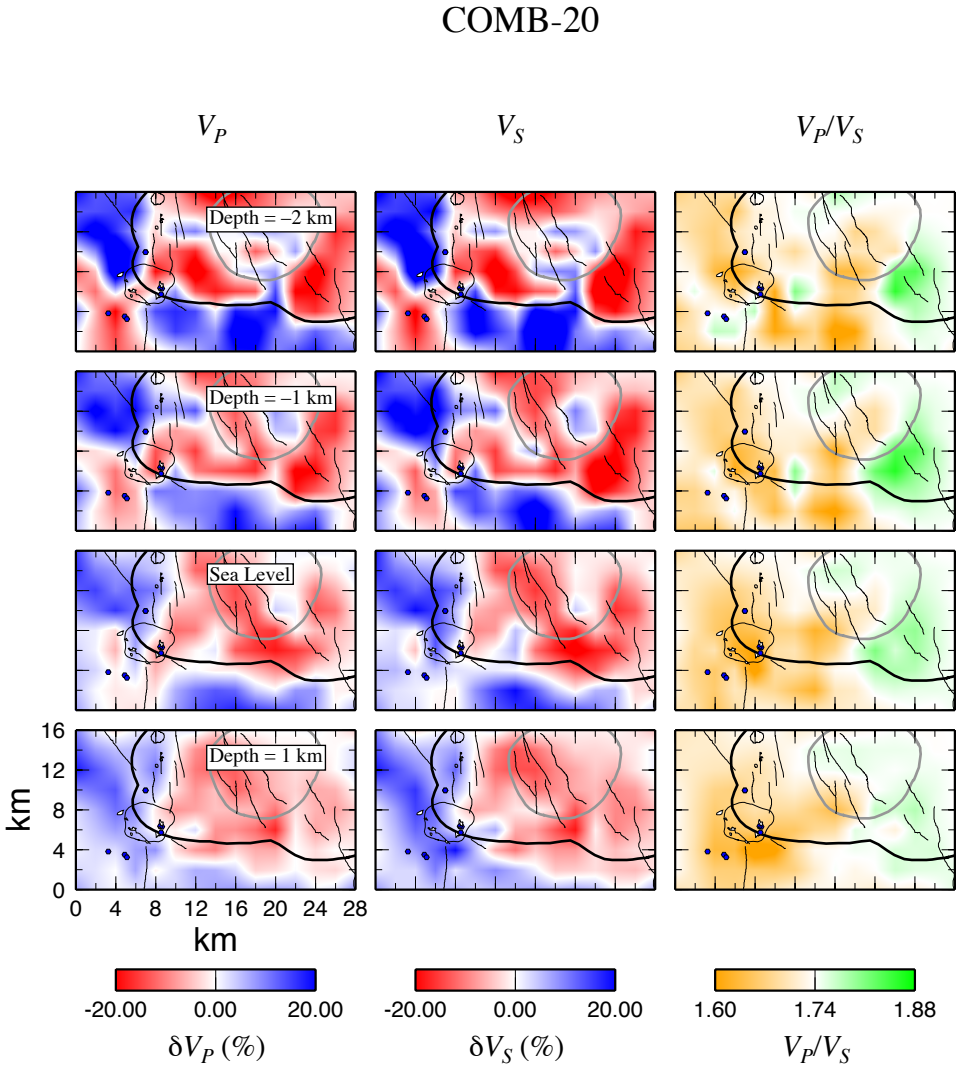

Figure 4.17: Maps showing (left) V_p (middle) V_s and (right) V_p/V_s at four depths (-2, -1, 0, 1 b.s.l.), obtained from inverting the combined 1989, 1997 and 2009-2010 data (model COMB-20). Anomalies in the V_p and V_s fields are represented by the percentage variation from mean values at each depth and V_p/V_s is displayed as the absolute values at depths. Map features are as shown in Figure 4.1. On the flanks of Mammoth Mountain dark blue circles are springs and small white patches are tree-kill areas.

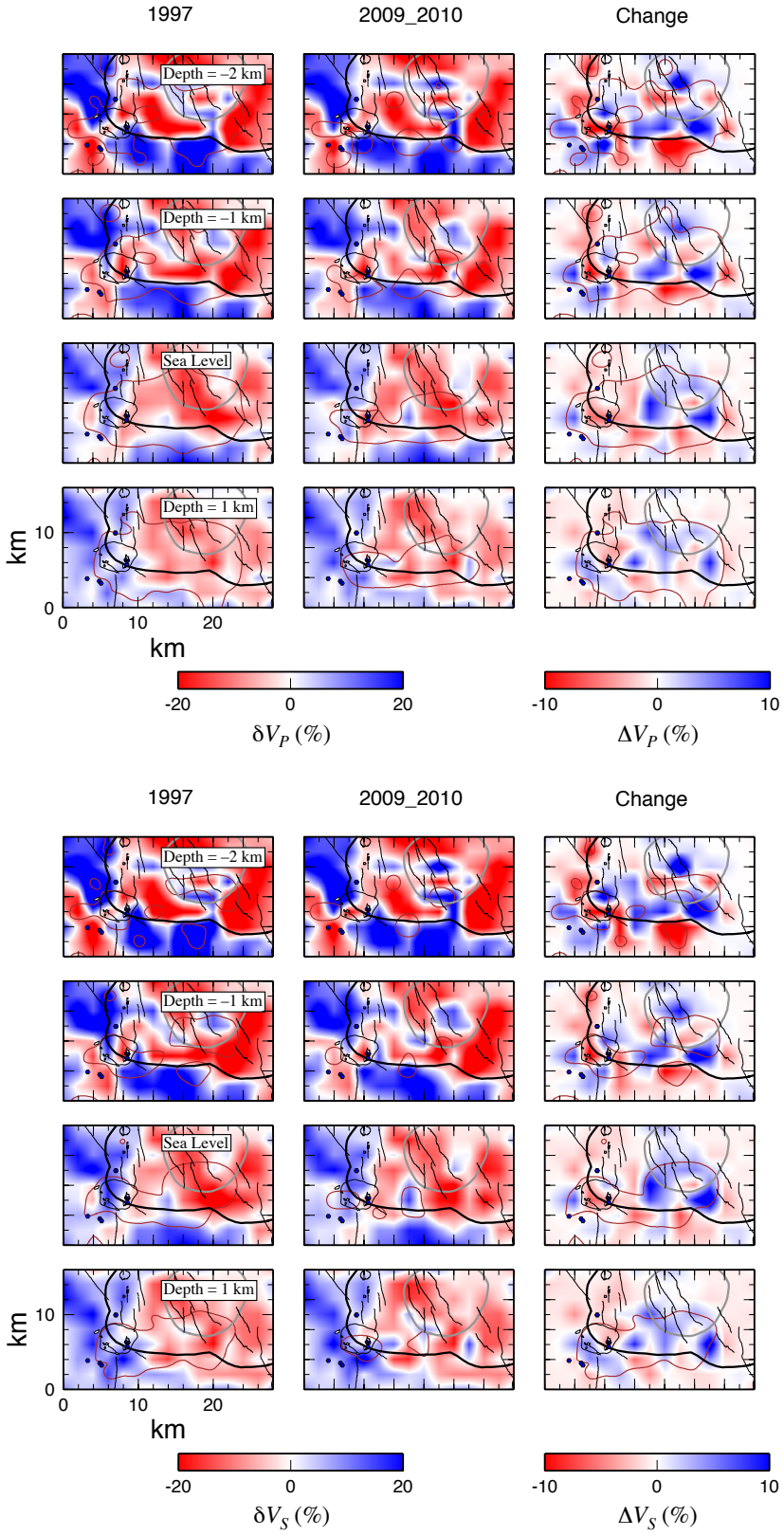

Figure 4.18: Comparison of models for 1997 and 2009-2010, showing the structure for 1997 (left panels), 2009-2010 (middle panels) and the change between the two epochs (right panels) for (top) V_p and (bottom) V_s. Geological features are the same as for Figure 4.1. Brown line is the 75 hit-count contour.

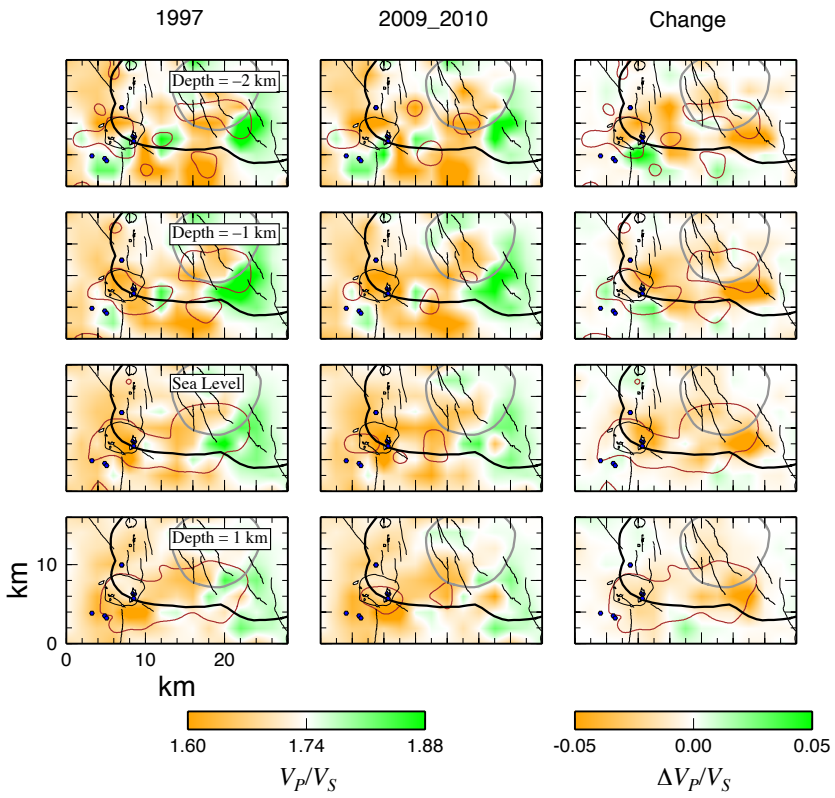

Figure 4.19: Same as Figure 4.18, for V_p/V_s.

4.7.2 Earthquake locations

The earthquakes used were relocated as part of the tomographic inversion (Figure 4.20 and Figure 4.21). In both 1997 and 2009-2010, a cluster to the south of Mammoth Mountain trending north-northwest was identified. Another cluster to the southeast of the resurgent dome trends north-northwest in the 2009-2010 data. Events are distributed in the depth range 2 km above sea level (a.s.l.) down to 10 km b.s.l. Most of the events lie at depths of 1-7 km b.s.l. with very few events located above sea level. After inversion, the locations of the events cluster more tightly. Nevertheless, the changes are small because the three-dimensional starting model was already very close to the final model.

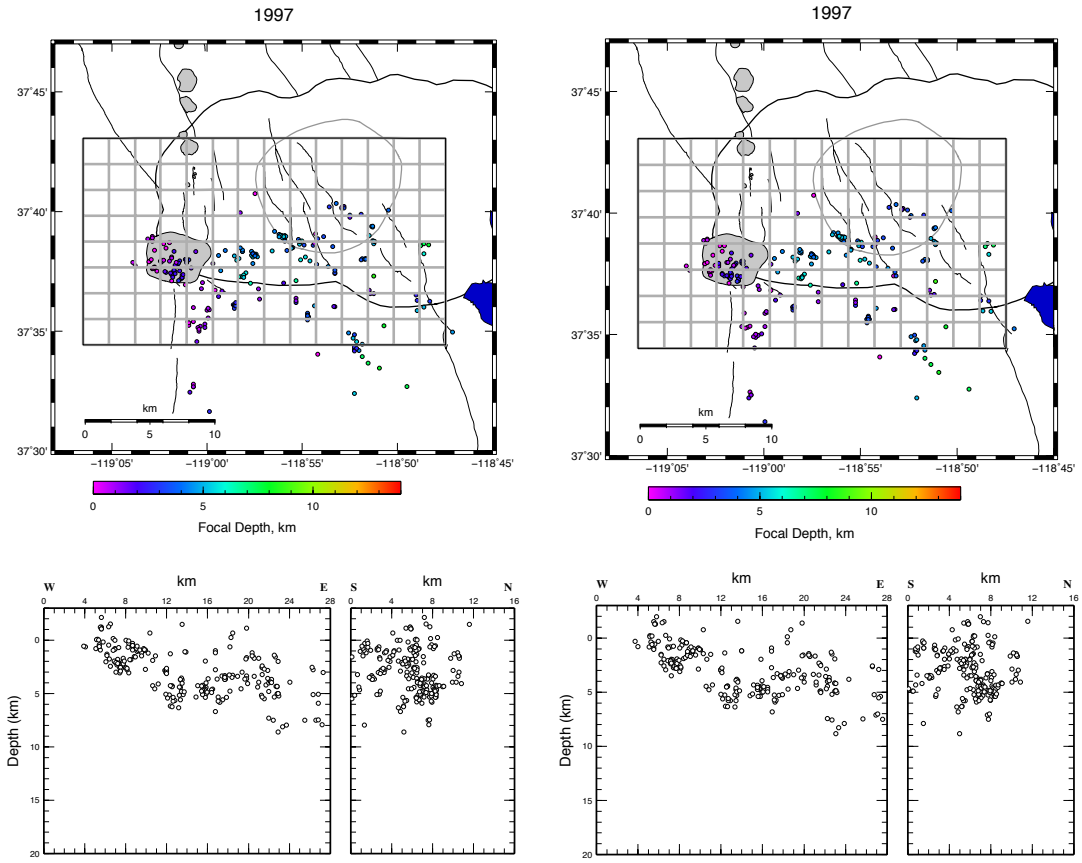

Figure 4.20: Maps and W-E and S-N cross-sections, showing the locations of earthquakes used in the 1997 data inversion, (left) before inversion and (right) after inversion.

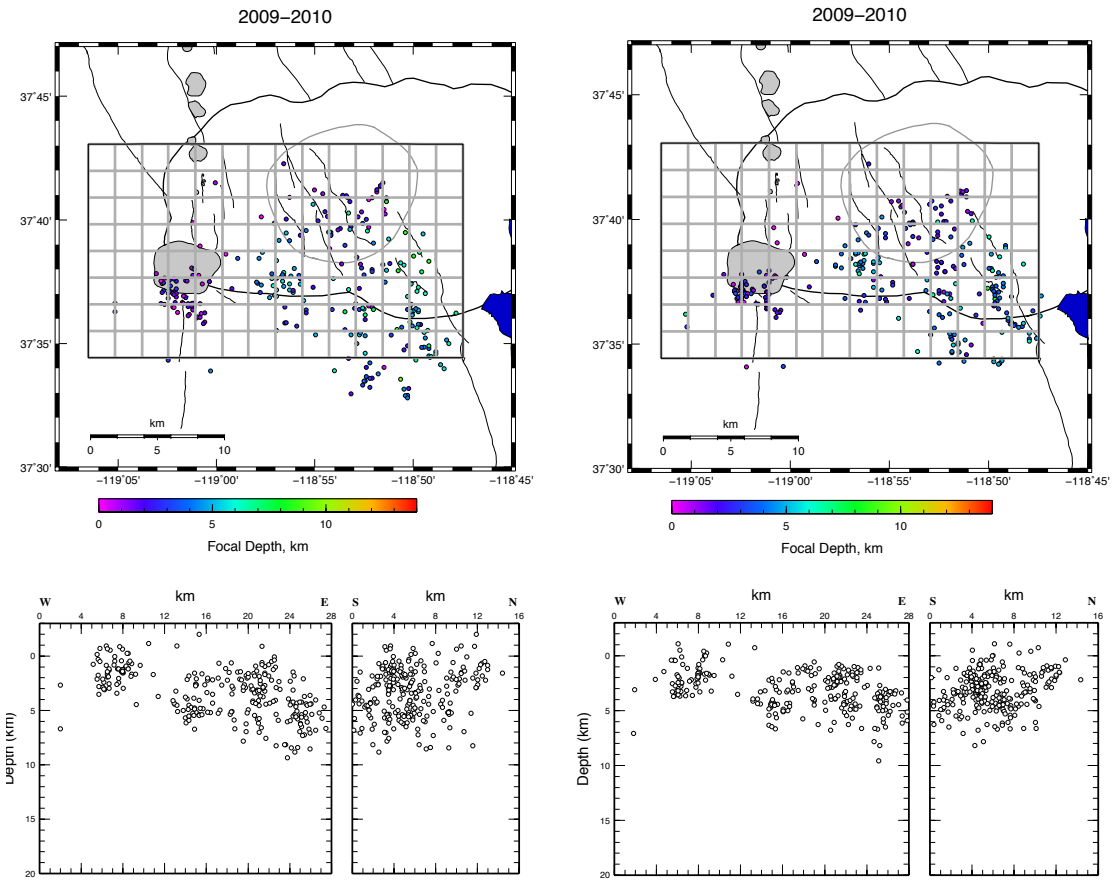

Figure 4.21: Same as Figure 4.20, for 2009-2010 data.

4.8 Results from *tomo4d*

4.8.1 V_p, V_s, and V_p/V_s structure and temporal variations

The results obtained for V_p, V_s and V_p/V_s using the tomography program *tomo4d* for the combined data are shown in Figure 4.22. The agreement between the V_p field and the known geological structure of the area is similar to the results of inversion using *simul2000A*, with a better correlation with the caldera boundary down to 1 km b.s.l. Low V_p is dominant inside the caldera and in the west part of the resurgent dome. High V_p characterizes the Sierra Nevada just south and southwest of the caldera except near Mammoth Mountain down to 1 km b.s.l. However, for the V_s field, this is not clear. The Sierra Nevada further away is poorly sampled.

The V_p/V_s field, similar to *simul2000A* results, is dominated by negative anomalies beneath the south moat and Mammoth Mountain at depths of 1 km a.s.l. down to 1 km b.s.l. The anomaly spreads and gets stronger with depth.

Weaker V_p and V_s structural changes between 1997 and 2009-2010 are obtained, compared with the results from *simul2000A*. There are increases in wave speed in the south moat down to 1 km b.s.l., with the strongest (~6%) to the south of the resurgent dome (Figure 4.23, right panels). At 1 km a.s.l., there is decreased wave speed to the south of the caldera with the decrease in V_p stronger than in V_s.

The change in the V_p/V_s field shows a decrease in the south moat at sea level and 1 km a.s.l., because of the increase in V_p and the stronger increase in V_s. Small volumes where V_p/V_s decreased also occur beneath Mammoth Mountain at sea level and above (Figure 4.24), with the strongest anomaly change up to 2%. This resulted from decreased V_p and increased V_s. In the northwestern part of Mammoth Mountain at sea level however, V_p/V_s increased because of a decrease in V_p and a stronger decrease in V_s.

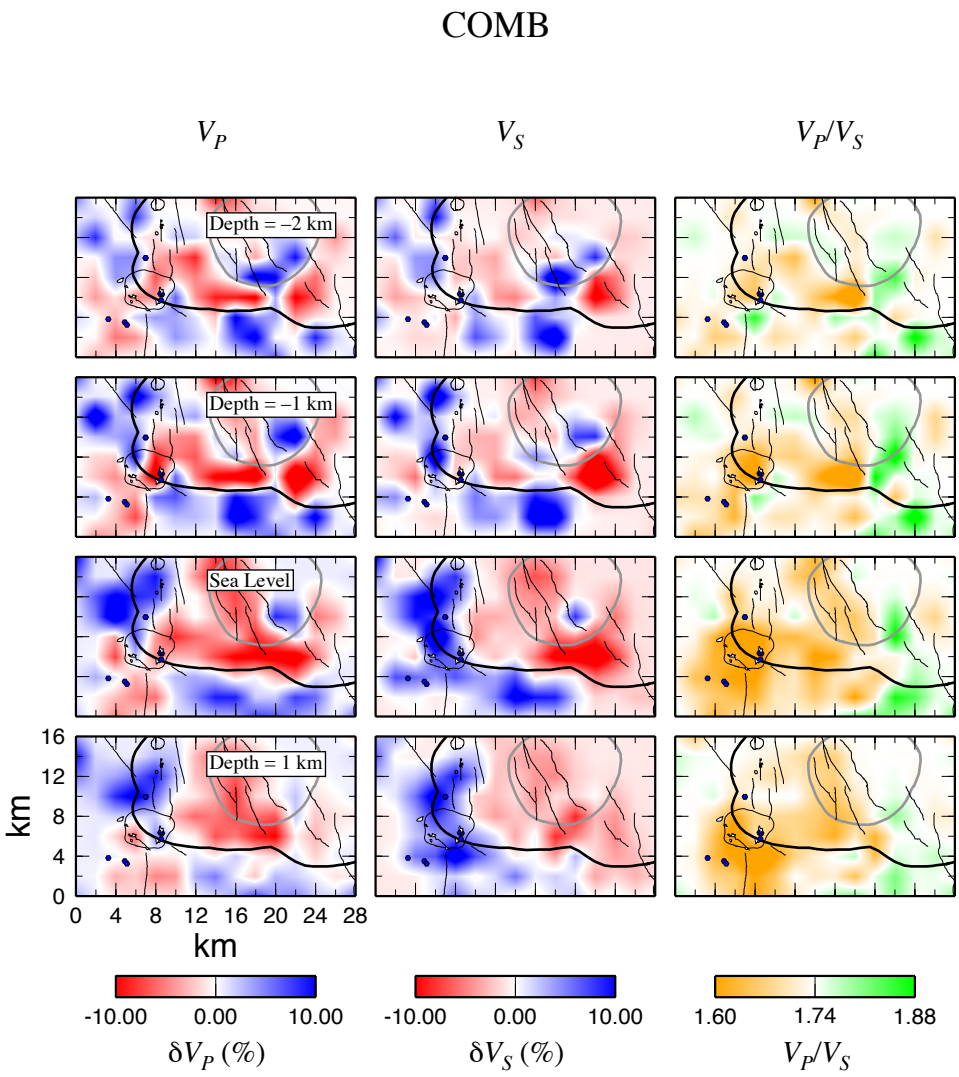

Figure 4.22: Same as Figure 4.17 but for the inversion using *tomo4d*. Note different colour scales used.

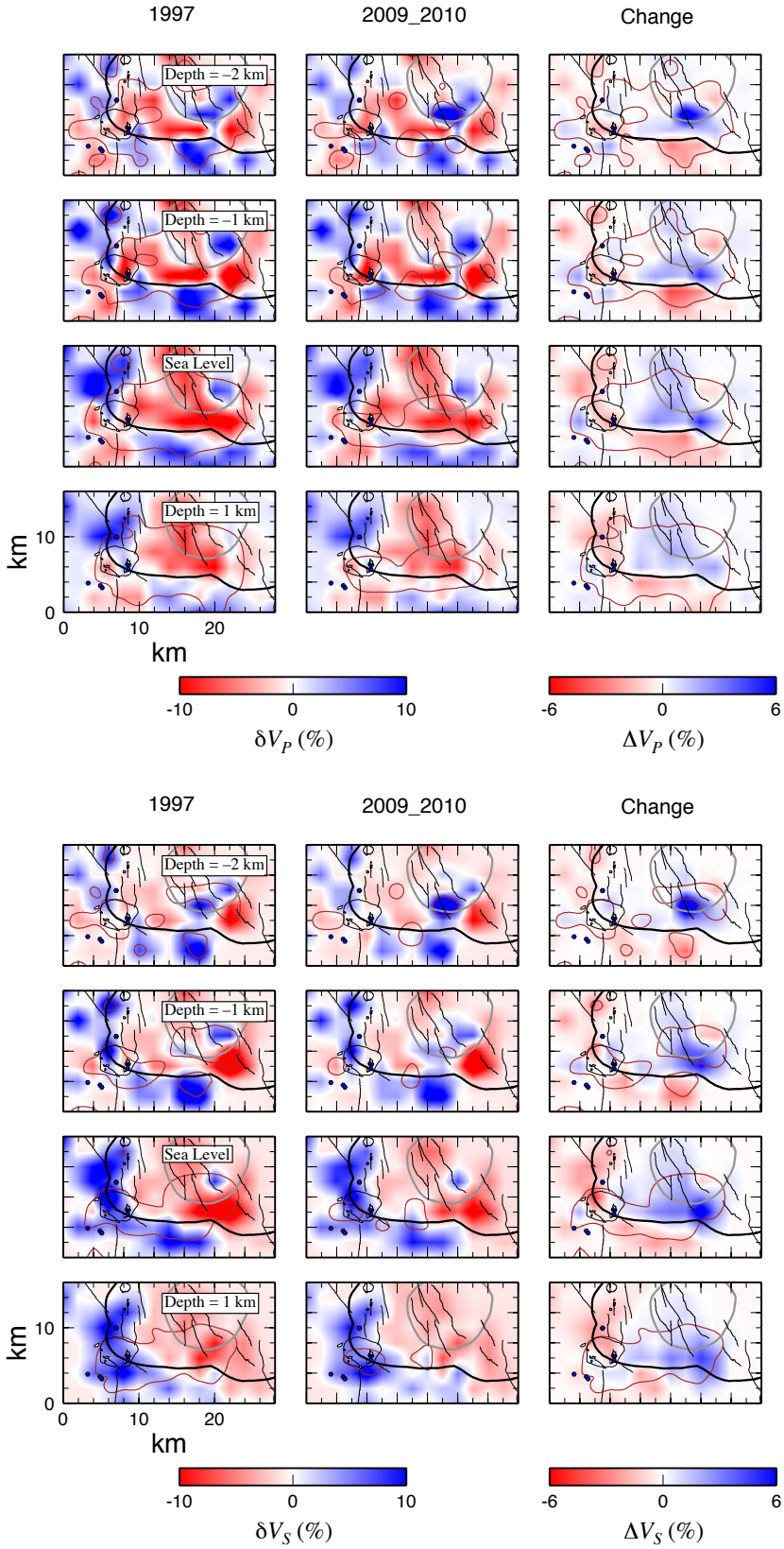

Figure 4.23: Same as Figure 4.18 but for the inversion using *tomo4d*. Note different colour scales used.

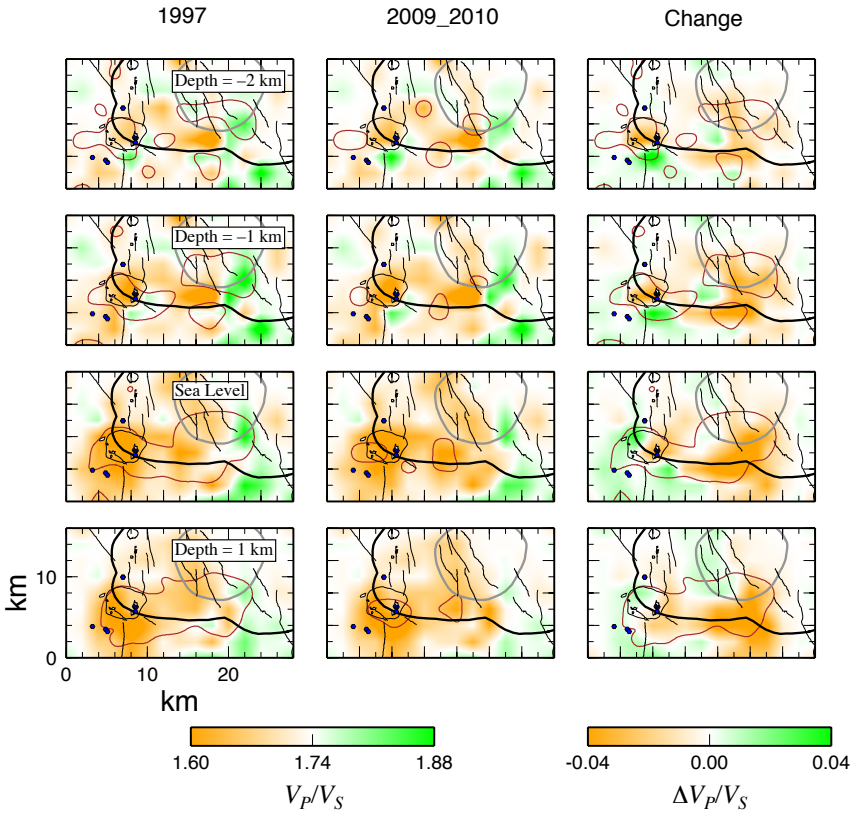

Figure 4.24: Same as Figure 4.19 but for the inversion using *tomo4d*. Note different colour scales used.

4.8.2 Earthquake locations

Locations of the events used for the inversions obtained with *tomo4d* are shown in Figure 4.25 and Figure 4.26. Compared to the results from *simul2000A*, the locations of the earthquakes before and after inversion changed little when inverted using *tomo4d*. This is expected as the damping used in *tomo4d* more strongly limits the magnitudes of changes made to the hypocentre parameters at each iteration during the inversion.

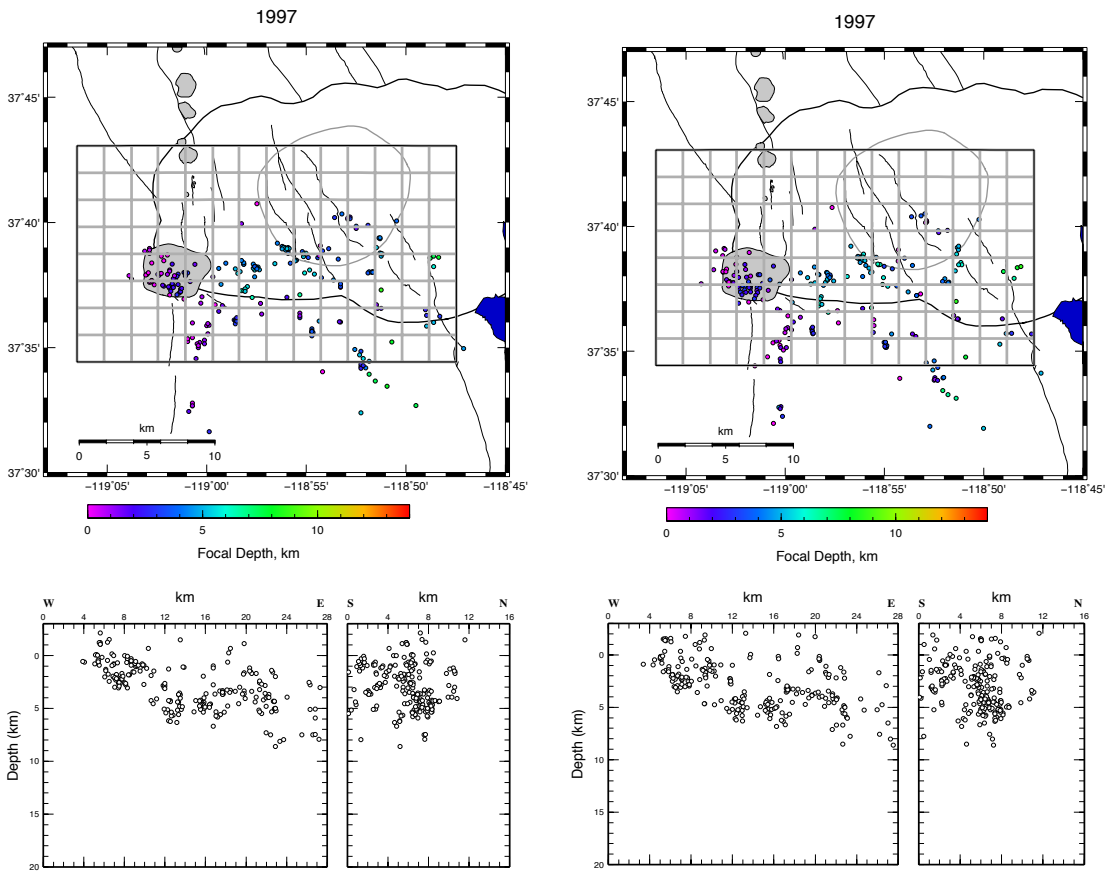

Figure 4.25: Same as Figure 4.20 but for inversion using *tomo4d*.

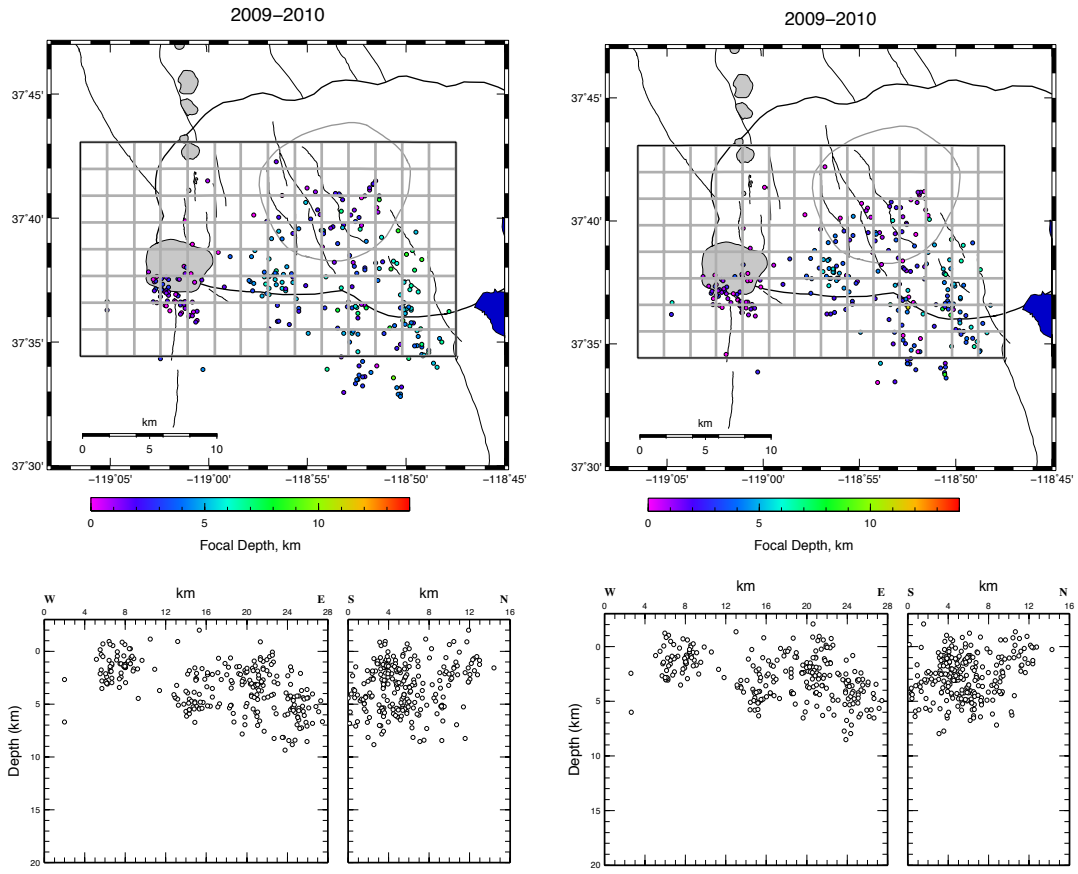

Figure 4.26: Same as Figure 4.21 but for inversion using *tomo4d*.

4.9 Summary

Arrival times for 267 selected earthquakes from Long Valley caldera were carefully measured using program *epick*. Among these events, 3727 *P*-wave and 1170 *S*-wave arrival times were measured. An inversion was conducted for the combined dataset (1989, 1997, and 2009-2010 data) using *simul2000A*, first with high damping values (COMB-20: 20 s^2/km for V_p and 20 s for V_p/V_s) to obtain an average model, then using lower damping values (COMB-5: 5 s^2/km for V_p and 5 s for V_p/V_s). The resulting three-dimensional model was used as a starting model for separate inversion for both of the years 1997 and 2009-2010. High damping values (20 s^2/km for V_p and 20 s for V_p/V_s) were used for the inversions for separate years. The final total RMS was 0.09 s for all inversions. The inversion performed for the same data from 1997 and 2009-2010 using *tomo4d* gave final total RMS of 0.11 s for 1997 and 0.09 s for 2009-2010.

Both the V_p and the V_s fields in the models obtained using *simul2000A* show good correlation with the caldera boundary and the edge of the resurgent dome. An even better correlation down to 1 km b.s.l. was shown in the model obtained using *tomo4d*. Low wave speeds are dominant inside the caldera, and high wave speeds characterize the Sierra Nevada outside the caldera except near Mammoth Mountain. Low wave speeds dominate in the west part of the resurgent dome at a depth of 1 km a.s.l. and below.

For both *simul2000A* and *tomo4d* results, the V_p/V_s field is dominated by negative anomalies beneath the south moat and Mammoth Mountain down to 1 km b.s.l. The anomaly spreads laterally and becomes stronger with depth in the results from *tomo4d*.

Differencing the structures obtained using *simul2000A* for 1997 and 2009-2010 yielded an apparent increase in wave speeds in the south moat, with the strongest increase being >10% in V_p and V_s. This resulted in an apparent decrease in V_p/V_s in the south moat down to 1 km b.s.l., with the strongest decrease being ~3%. A volume where wave speed apparently decreased in the west part of Mammoth Mountain showed about 10% decrease in V_p and a weaker decrease in V_s. Thus, resulted in an apparent decrease in V_p/V_s (~2%). This is surrounded by areas of increased V_p/V_s (~2%) to the southeast and west.

For the inversion using *tomo4d*, weaker structural changes were detected between 1997 and 2009-2010 compared to the results from *simul2000A*. An increase in wave speed was detected in the south moat down to 1 km b.s.l. of ~6% increase in V_p and a stronger increase in V_s. Weaker wave-speed changes in volumes to the east and west of Mammoth Mountain were detected. The change in V_p/V_s was generally a decrease in the south moat with the strongest change in V_p/V_s ~2%.

CHAPTER 5

TOMOGRAPHIC INVERSION : THE COSO GEOTHERMAL AREA

5.1 Background

Foulger [2007] performed tomographic inversions for crustal structure beneath the Coso geothermal area. Local earthquakes recorded by the US Navy network for the time period 1996-2006 were used. Average one-dimensional crustal models were first obtained using the program *velest* [*Kissling et al.*, 1994]. Using these one-dimensional models for V_p and V_s, graded inversions were then conducted for a combined data set from the years 1996-2006 using both 2- and 1-km nodal-spacing grids to obtain three-dimensional models. For each inversion optimal damping values for both V_p and V_p/V_s were tested and selected. *Foulger* [2007] chose damping values on the basis of "damping trade-off curves" [*Evans and Achauer*, 1993]. Sets of one-iteration inversions with damping values set successively at 999, 100, 50, 20, 10, 5, 2, 1 and 0.1 s^2 km^{-1}, were conducted. Curves of data variance vs. model variance were then constructed. The optimal damping value was the one that optimized data variance reduction whilst keeping model variance low. The preferred average three-dimensional model resulted from inversion using the 2-km nodal spacing grid and damping values of 100 s^2 km^{-1} and 50 s for V_p and V_p/V_s respectively.

Using this as a starting model, independent inversions for separate years were conducted. The results hinted at temporal changes in structure in the geothermal field [*Foulger*, 2007]. Temporal growth of a negative-V_p/V_s anomaly in the geothermal field was suggested in the independent graded inversions for separate years with the 2-km nodal spacing grid (Figure 2.10). However, the changes were subtle and uncertain. Studying these possible changes in more detail is the subject of this chapter of the thesis.

5.2 The dataset

Earthquakes from the Coso geothermal area recorded by the US Navy seismometer network for the years 2007, 2008, 2010 and 2012 were processed (Figure 5.1). Data from 1996 and 2006 [from *Foulger*, 2007] were used in order to investigate longer-period variations in structure. Table 5.1 shows the total numbers of earthquakes for the years 1992-2012 from the US Navy catalogue. During this period, the year 2010 was the most active, with 12,130 earthquakes. The earthquakes are clustered in the centre of the field (Figure 5.1) with varying seismicity in the western part of the region ranging from relatively few earthquakes there in 2012 to a higher level of activity in years 2007 and 2008 and particularly intense activity in year 2010. A cluster in a new area appears to the north-northwest of the field in 2012.

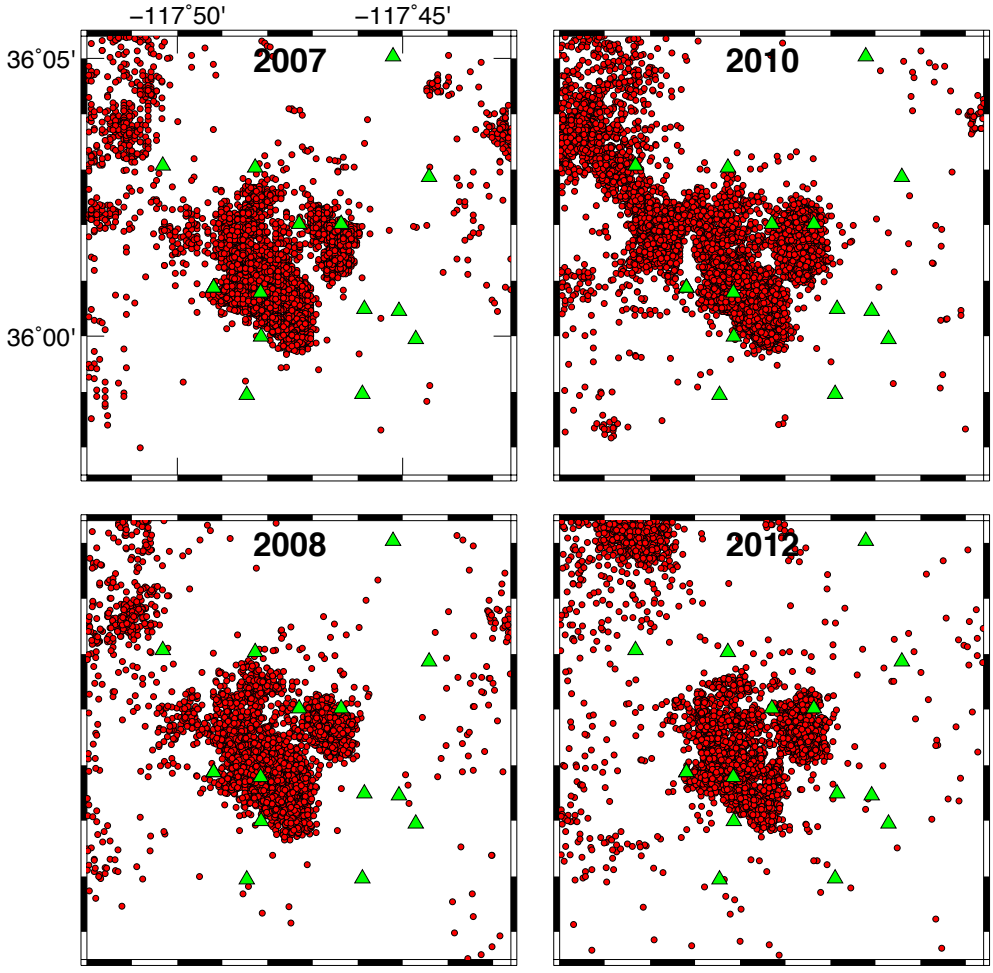

Figure 5.1: Maps of the Coso geothermal area showing earthquakes from 2007, 2008, 2010 and 2012 located by the Geothermal Program Office of the US Navy using their seismometer network. Green triangles are seismometer stations.

Table 5.1: Numbers of earthquakes located for the years 1992-2012 by the Geothermal Program Office of the US Navy, and reported in their earthquake catalogue.

Year	Number of earthquakes
1992	4,896
1993	5,461
1994	3,570
1995	4,500
1996	5,606
1997	4,003
1998	6,651
1999	8,439
2000	9,947
2001	5,140
2002	6,504
2003	5,025
2004	9,183
2005	7,671
2006	8,548
2007	10,558
2008	8,843
2009	5,325
2010	12,130
2011	6,696
2012	7,563

Subsets of the highest-quality events were extracted from the Navy database for processing for the year 2007. The highest-quality events were selected on the basis of the number of arrival times, root-mean-square (RMS) arrival-time residual, and azimuthal gap. Lower qualities were assigned to earthquakes with few arrival times, and/or a large RMS and/or a large azimuthal gap. A quality value was calculated for each earthquake using the following:

$$qual = wt\_n * (n - 4)/4 + wt\_rms * (0.03/rms) + wt\_gap * (150/gap)$$

where n is the number of *P*- and *S*-wave arrival time observations, *rms* is the root-mean-square of the residuals, *gap* is the azimuthal gap, and $wt\_n = wt\_rms = wt\_gap = 1$. The script used for the calculation is given in Appendix 12. Good-quality earthquakes were considered to be those with a quality > 5, and are plotted in Figure 5.2. Some of the 2008 data and the data from 2010 and 2012 were in a different format that lacked the required location parameters. Because of this, for those data quality control was based only on earthquake magnitude for the months April to December 2008 and January to December for 2010 and 2012.

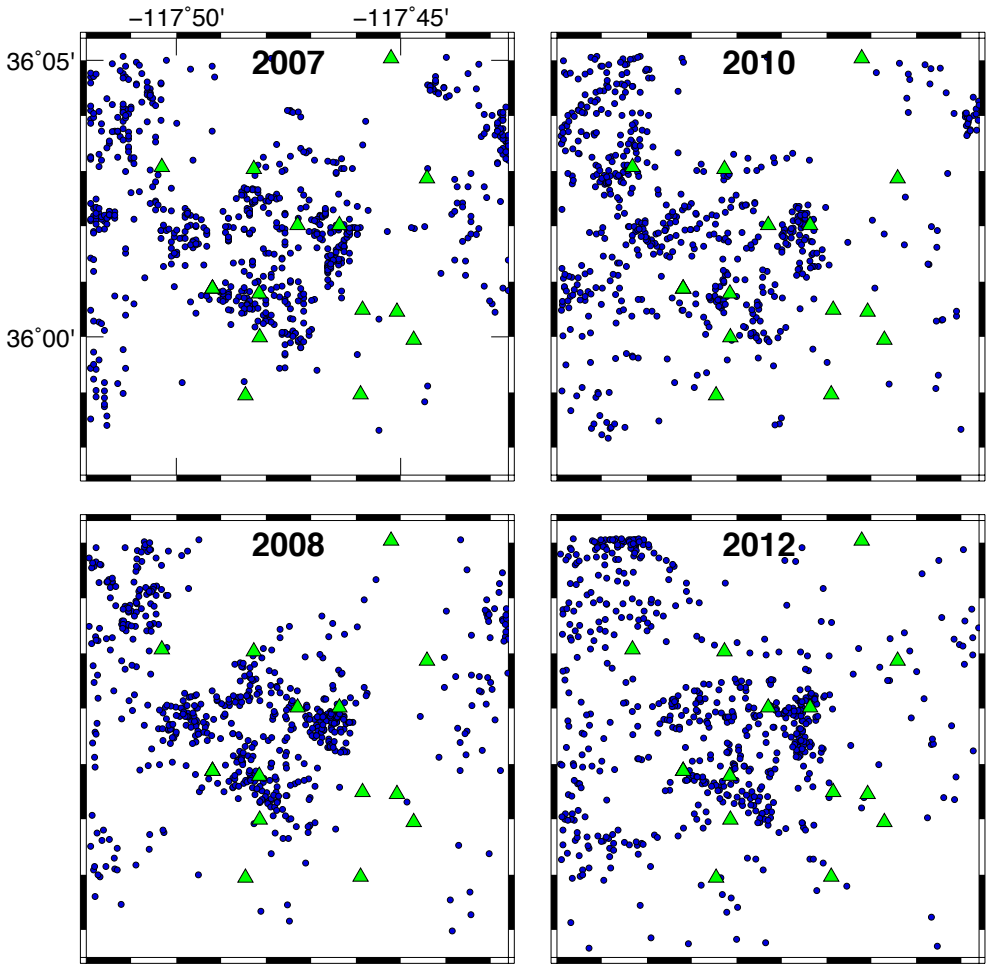

Figure 5.2: Same as Figure 5.1 but for the "good-quality" earthquakes selected for processing for 2007, 2008, 2010 and 2012.

5.2.1 Selecting data from 2007

Histograms of the numbers of earthquakes with various numbers of *P*- and *S*-wave arrival-time measurements, RMS arrival-time residuals and maximum azimuthal gaps for data from 2007 are shown in Figure 5.3. For 2007, many earthquakes had 5-7 *S*-wave arrival-time measurements, which is good for tomographic inversion. The RMS residuals of most earthquakes were 0.02-0.05 s, which reflects the high quality of the locations. Most of the earthquakes for 2007 have an azimuthal gap < 180°. Events with a gap > 180° are too poor to be included in tomographic inversions as their epicentres lie outside the seismic network and are thus expected to be greatly in error, even if the RMS is small.

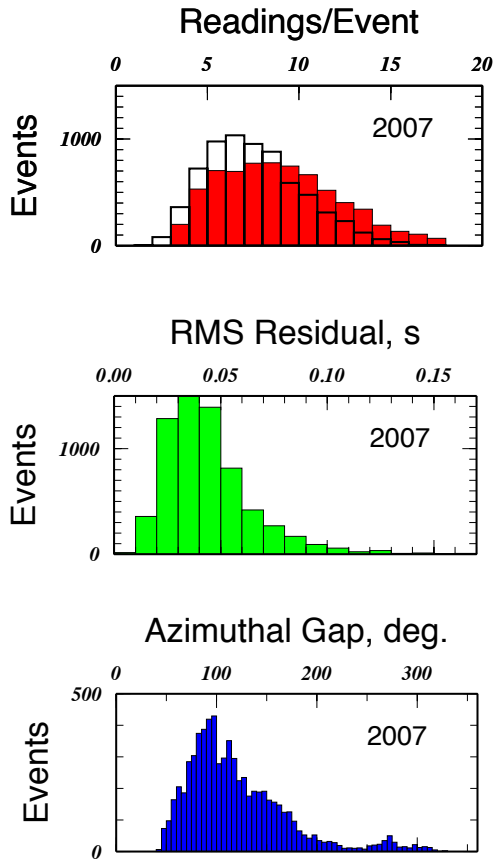

Figure 5.3: Histograms of numbers of earthquakes from 2007 showing (top) numbers of *P*-wave (red bars) and *S*-wave (heavy lines) arrival-time measurements, (middle) root-mean-square arrival-time residuals, and (bottom) maximum azimuthal gap, from the US Navy catalogue.

The datasets selected for inversion include the few hundred best earthquakes for each year, and ones well-distributed throughout the study volume. In order to choose these, the study volume was subdivided into 200 cubes (Figure 5.4). Earthquakes were then chose based on the following:

1. If the cube contained fewer than 10 earthquakes, they were all selected.
2. If the cube contained more than 10 earthquakes, they were ranked by the following criteria:
    - number of arrival-time measurements,
    - smallness of RMS and
    - smallness of azimuthal gap.

The highest-ranking 10 events were then selected using the script shown in Appendix 12. The final dataset contained 680 earthquakes (Figure 5.5).

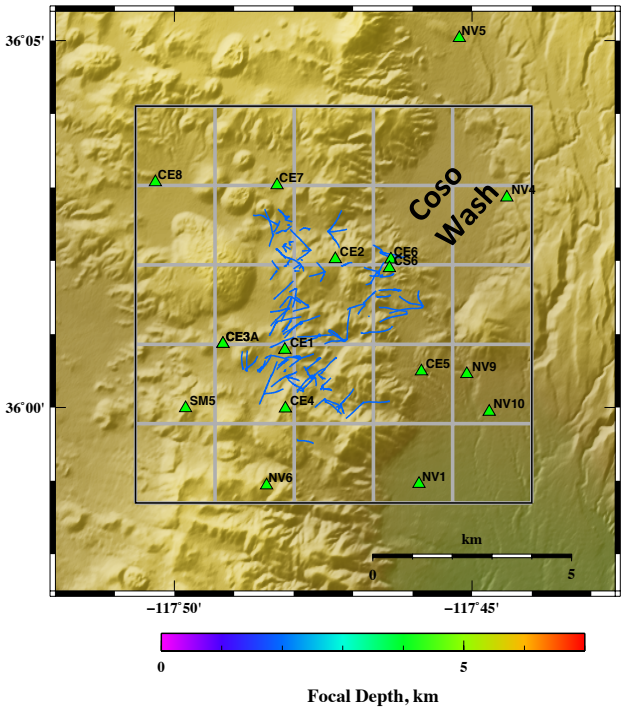

Figure 5.4: Topographic map of the Coso geothermal area showing the main geothermal field in the middle with the production wells (blue) and Coso Wash to the northeast of the geothermal field. The grid is the tomography inversion grid; green triangles are the US Navy seismometer network.

5.2.2 Selecting data from 2008, 2010 and 2012

For 2008, 2010 and 2012 the highest-magnitude 10 events in each cube were selected and if the cube contained fewer than 10 earthquakes, they were all selected. The final datasets contained 570, 512, and 504 earthquakes for 2008, 2010, and 2012 respectively (Figure 5.5). Magnitudes are 0.0 - 4.55 M.

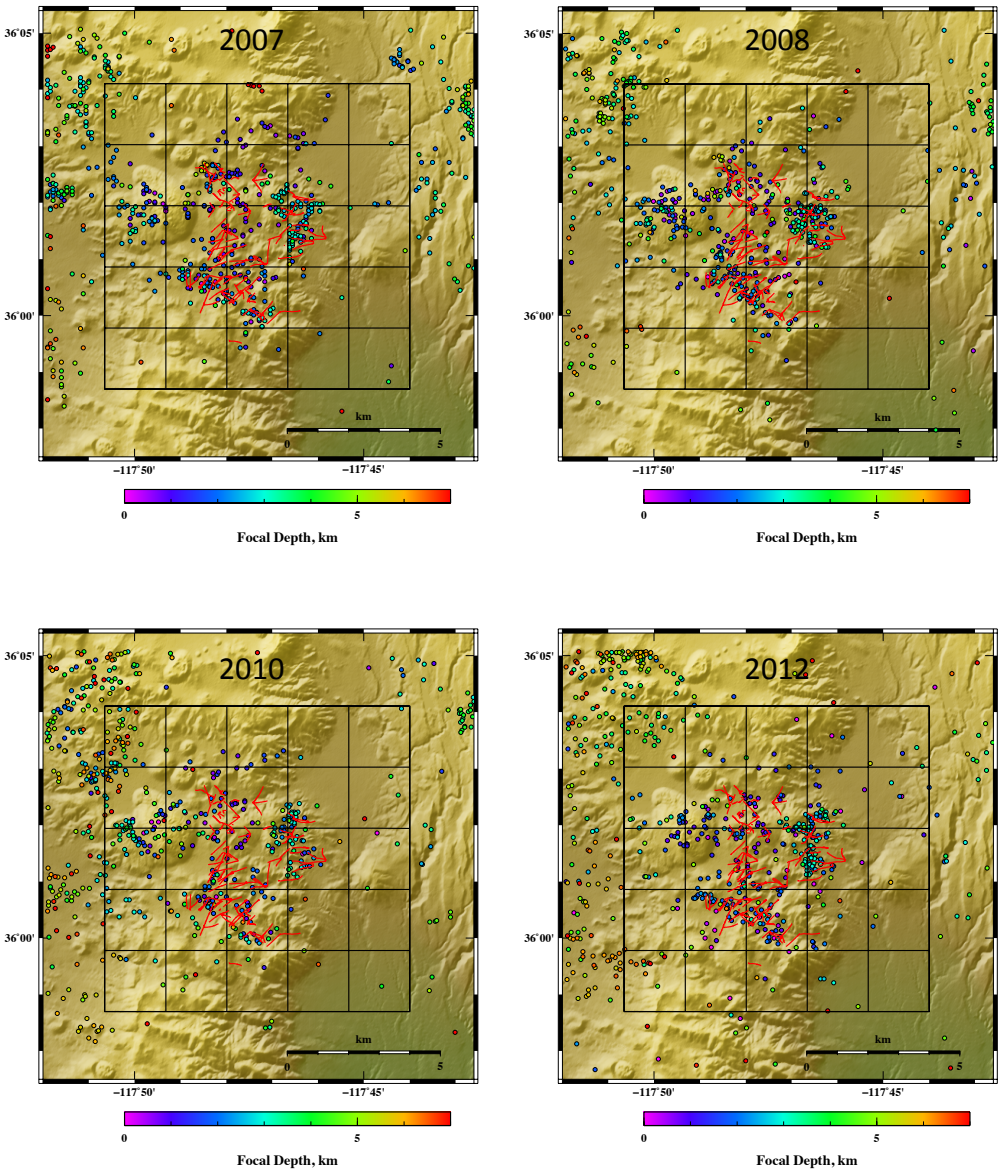

Figure 5.5: Maps showing epicentres of the earthquakes from the US Navy catalogue for 2007, 2008, 2010 and 2012 that were selected for tomographic inversion. Well paths in red.

5.3 Arrival-time measurements

There is one arrival-time measurement file for each earthquake. Appendix 13 shows an example of an arrival-time measurement file for an earthquake that occurred in 2007. The files are in XPED format, and were reformatted for tomographic inversion with *simul2000A*. A script (Appendix 14) was used to reformat the data.

The GPO of the US Navy measured the *P*- and *S*-wave arrival times for the events from 2007 automatically. For the years 2008, 2010, and 2012, arrival times were measured by hand using the program *epick* as part of this thesis. The accuracy with which arrival times could be measured is estimated to be ~0.01 s for *P*-waves and ~0.03 s for *S*-waves. The numbers of earthquakes and measured arrival times are shown in Figure 5.6. Many earthquakes for all years had 6-11 *S*-wave arrival-time measurements.

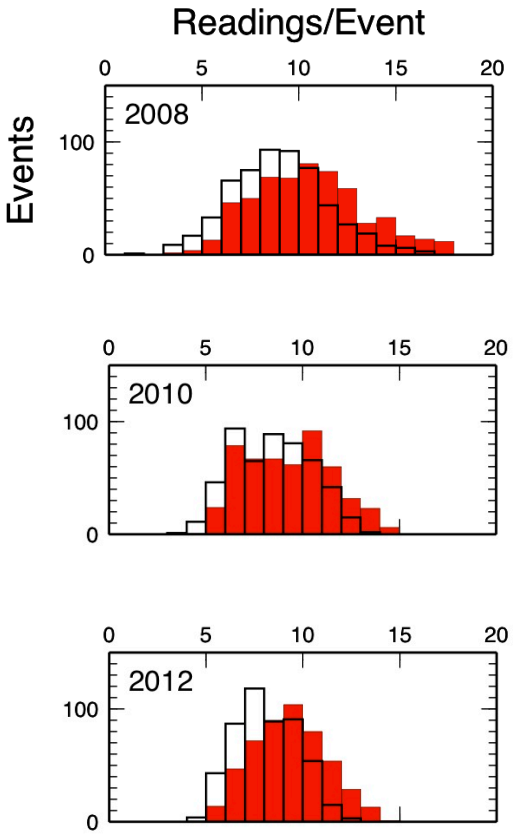

Figure 5.6: Same as Figure 5.3 (top) but for years 2008, 2010 and 2012.

5.4 Inversion using *simul2000A*

5.4.1 The inversion procedure

A combined data set (COMB) for the years 2007, 2008, 2010 and 2012 was inverted using the same starting model as used by *Foulger* [2007]. The model obtained was then used as a starting model for separate inversions for the years 1996, 2006, 2007,

2008, 2010 and 2012. During the inversion process, many trials were performed and outliers were identified and eliminated. The input files used to run the inversions are given in Appendix 15 and Appendix 16. Details of the final data used for the inversions are given in Table 5.2. The final RMS residual values ranged between 0.04 s for 2012 and 0.05-0.06 s for all other data sets. The *P*-data variance reduction varied from 19% for 1996 and 2008 to 30% for 2012 while *S*-*P*-data-variance reduction was lower, 7% for all data sets except for 2006 and 2010 where this was 10% and 11% respectively and even lower (5%) for COMB. The overall data variance reduction is fairly small because the starting model is derived from previous graded inversions and is close to the final model.

Table 5.2: *simul2000A* tomographic inversion details for the inversions of the 1996, 2006, 2007, 2008, 2010 and 2012 Coso data.

Parameters	COMB	1996	2006	2007	2008	2010	2012
No. of events	2266	486	743	680	570	512	504
No. of *P*-wave arrivals	22572	4408	7498	7915	5718	4502	4437
No. of *S*-wave arrivals	17896	3001	5351	5221	4802	4040	3383
V_p damping, s^2/km	100	20	20	20	20	20	20
V_p/V_s damping, s	50	10	10	10	10	10	10
Final RMS residuals, s	0.05	0.05	0.05	0.06	0.06	0.05	0.04
Variance reduction, %							
P	23	19	27	25	19	25	30
S-P	5	7	10	7	7	7	11

5.4.2 Damping parameters

Damping parameters were tested extensively by *Foulger* [2007] using combined and independent data sets inverted on 2-km and 1-km nodal spacing grids. For the combined data, high damping values of 100 s^2 km^{-1} for V_p and 50 s for V_p/V_s were used. For the independent inversions of each year, optimal damping values were selected to be 20 or 10 s^2 km^{-1} for V_p and half these values for V_p/V_s. I performed a simplified damping test to check whether the same damping values are suitable for the four epochs studied as part of this thesis. Sets of one-iteration inversions were conducted with V_p damping values set successively at 1000, 100, 50, 20, 10, 5, 2, 1 and 0.1 accompanied by V_p/V_s damping values of 500, 50, 25, 10, 5, 2.5, 1, 0.5 and 0.05. From the trade-off damping curves (Figure 5.7) for the combined data set, a value of 100 s^2 km^{-1} was selected for V_p damping and a value of 50 s for V_p/V_s. For the

independent inversions for each year, optimal damping values of 20 s^2 km^{-1} for V_p and 10 s for V_p/V_s were selected.

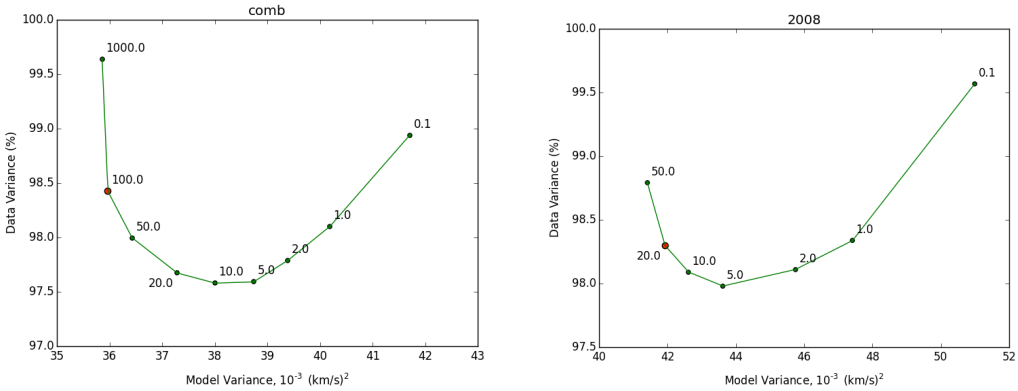

Figure 5.7: Examples of damping trade-off curves for V_p and V_p/V_s. (left) for the combined data; (right) for the year 2008. The values on the curve are V_p damping values where the V_p/V_s damping value was set to be half the V_p damping value. The highlighted value is the chosen optimal conservative damping value.

5.5 Inversion using *tomo4d*

5.5.1 The inversion procedure

A set of inversions was performed using *tomo4d* and the same data from the years 1996, 2006, 2007, 2008, 2010 and 2012 as were used for *simul2000A*. A different starting model was used. This was a one-dimensional model derived from the three-dimensional one used for *simul2000A*. The reason for this was that the three-dimensional model output by *simul2000A* works poorly with the ray-tracer used by *tomo4d* and resulted in too many rays not converging.

Inversions for the pairs of years 2007-2008, 2007-2010, 2007-2012, 2008-2010, 2008-2012, and 2010-2012 were performed. In order to investigate longer-period variations, another two inversions were performed, for 1996-2006 and 1996-2012. The one-dimensional *P*- and *S*-wave starting model is given in Appendix 17. Table 5.3 shows details of the inversions for 1996-2006 and 2007-2012. Details of the other inversions are given in Appendix 18.

χ^2 reduction for *P* varies from 15% for 2006 data to 42% for 1996 data. χ^2 reduction for *S* varies from 11% for 2012 to 32% for 1996 data. The final RMS was 0.04 s for 1996, 2010 and 2012 data and 0.05 s for 2006, 2007 and 2008 data.

Table 5.3: Details of *tomo4d* inversions for 1996-2006 and 2007-2012.

Parameters	1996	2006
No. of events	482	743
No. of *P*-wave arrivals	4075	7498
No. of *S*-wave arrivals	2946	5344
$\varepsilon_{Velocity}$, σ_{V_P} and σ_{Vs}	0.05, 0.1, 0.05	0.05, 0.1, 0.05
Final RMS residuals, s	0.04	0.05
χ^2 reduction, %		
P	42	15
S	32	14

Parameters	2007	2012
No. of events	616	497
No. of *P*-wave arrivals	6544	4165
No. of *S*-wave arrivals	4549	3783
$\varepsilon_{Velocity}$, σ_{V_P} and σ_{Vs}	0.05, 0.1, 0.05	0.05, 0.1, 0.05
Final RMS residuals, s	0.05	0.04
χ^2 reduction, %		
P	24	16
S	23	11

5.5.2 Damping parameters

To choose values for the parameters ε_{Origin}, $\varepsilon_{Velocity}$, and ε_{Epoch} that control the "damping" process, the same procedure was used as explained in Section 4.5.2. Figure 5.8 through Figure 5.10 show the results of the tests, conducted using data from the Coso geothermal area for 1996 and 2006. As damping parameters decrease from their largest values (left sides of figures), perturbations to the event origins/models increase and the fit to the data improves. For event-origin and wave-speed perturbations, however, the perturbations at some point become so large that the linearized approximation is no longer adequate and the improvement ceases. Optimal damping occurs for the smallest values that do not cause problems with nonlinearity. Thus, for example we chose $\varepsilon_{Velocity} = 0.05$ and $\varepsilon_{Origin} = 10$ as optimal values. For inter-epoch damping, nonlinearity never became a serious problem, so the fit to the

data improved with decreasing damping over the entire range of values tested. The chosen damping values were then tested for five iterations (Appendix 11) to ensure the optimal values were selected.

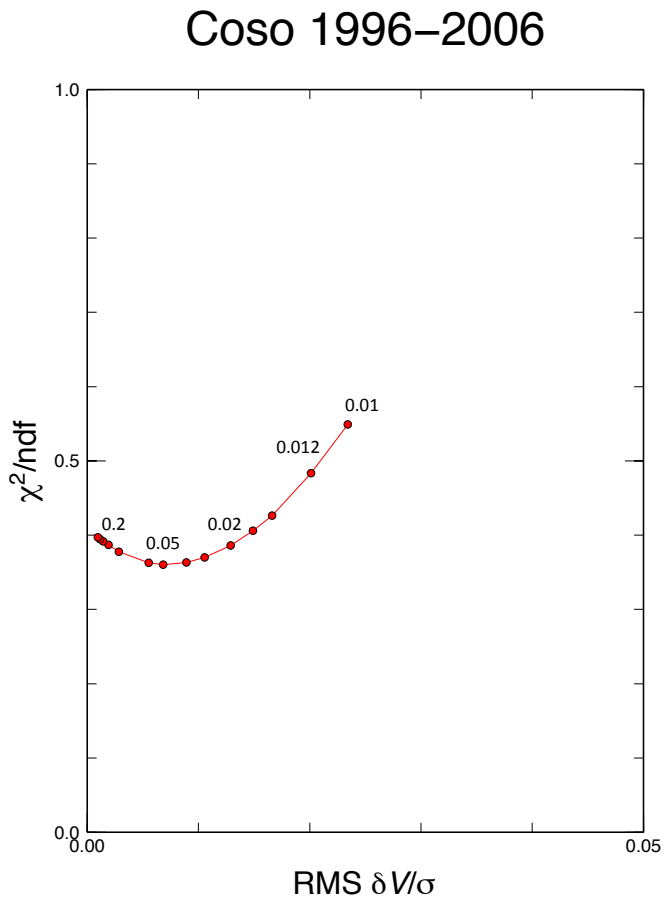

Figure 5.8: The effect of wave-speed damping $\varepsilon_{Velocity}$ on models of the Coso geothermal area derived from data for epochs 1996 and 2006. The abscissa gives the sum of the root-mean-square (RMS) scaled changes in V_P and V_S at all grid nodes for the two epochs during one iteration of the inversion process. The ordinate gives a measure of the lack of fit to the arrival-time data. The dots correspond to values of the damping parameter ε_V of 0.01 (rightmost), 0.012, 0.015, 0.017, 0.020, 0.025, 0.030, 0.040, 0.050, 0.100, 0.150, 0.200, 0.250, and 0.300 (leftmost), with $\sigma_{V_P} = 0.1$ km/s, and $\sigma_{V_S} = 0.05$ km/s. As the damping parameter $\varepsilon_{Velocity}$ decreases, the fit at first improves, and then becomes worse as nonlinear effects become more important. In this example, all other types of damping are disabled, except for event-origin damping with $\varepsilon_{Origin} = 1.0$, σ_h=$\sigma_z = 0.2\ km$, and $\sigma_t = 0.1\ s$.

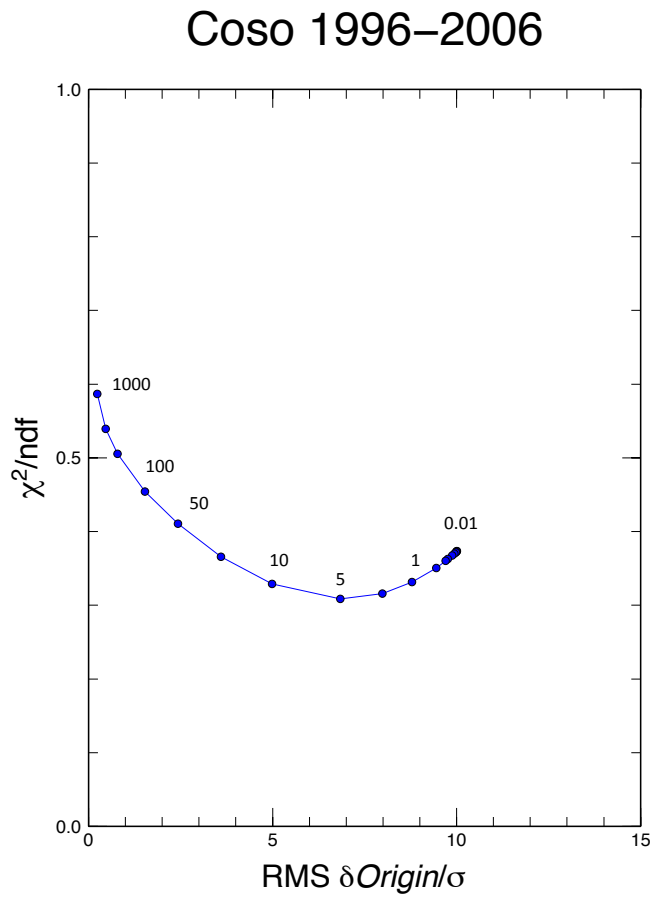

Figure 5.9: The effect of event-origin damping ε_{Origin} on models of the Coso geothermal area derived from data for epochs 1996 and 2006. The abscissa gives the sum of the root-mean-square (RMS) scaled changes in the origin components (four per event) for all events in both epochs during one iteration of the inversion process. The ordinate gives a measure of the lack of fit to the arrival-time data. The dots correspond to values of the damping parameter ε_{Origin} of 0.01 (rightmost), 0.02, 0.05, 0.1, 0.2, 0.4, 0.8, 1, 2, 5, 10, 20, 50, 100, 200, 400 and 1000 (leftmost), with $\sigma_h = \sigma_z = 0.2$ km, and $\sigma_t = 0.1$ s. As the damping parameter ε_{Origin} decreases, the fit at first improves, and then becomes worse as nonlinear effects become more important. In this example, all other types of damping were disabled, except for wave-speed damping with $\varepsilon_V = 0.05$, $\sigma_{V_P} = 0.1$ km/s, and $\sigma_{V_S} = 0.05$ km/s.

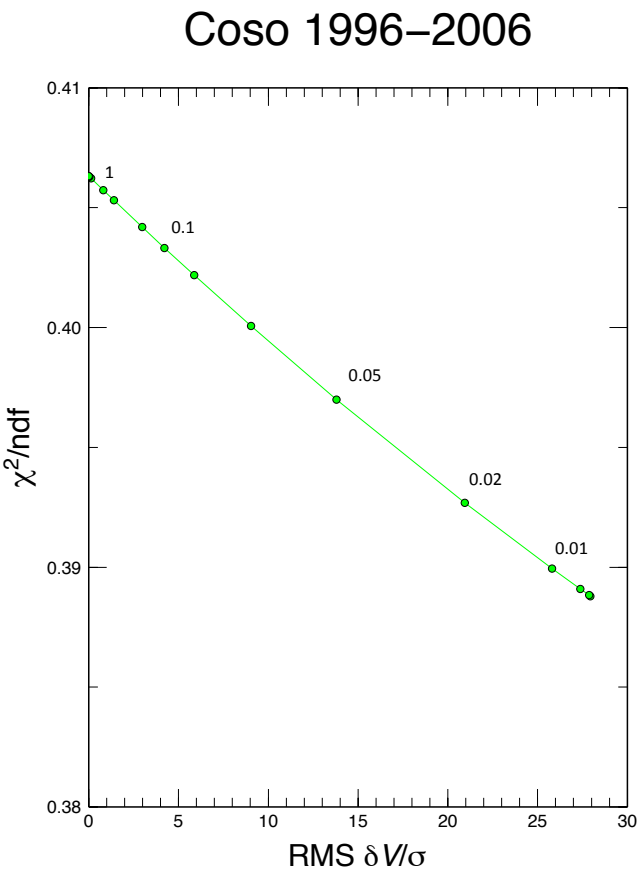

Figure 5.10: The effect of inter-epoch damping ε_{Epoch} on models of the Coso geothermal area derived from data for epochs 1996 and 2006. The abscissa gives the sum of the root-mean-square (RMS) scaled inter-epoch differences δV_P and δV_S at all grid nodes after one iteration of the inversion process. The ordinate gives a measure of the lack of fit of the model predictions to the arrival-time data. The dots correspond to values of the damping parameter ε_{Epoch} of 0.001 (rightmost), 0.002, 0.005, 0.010, 0.020, 0.035, 0.050, 0.067, 0.082, 0.1, 0.15, 0.2, 0.5, 1, 2, and 5 (leftmost), with $\sigma_{\delta V_P} = 0.01$ km/s, and $\sigma_{\delta V_S} = 0.05$ km/s. As the damping parameter ε_{Epoch} decreases, the fit becomes better. In this example, all other types of damping are disabled, except for event-origin damping with $\varepsilon_{Origin} = 10$, σ_h=$\sigma_z = 0.2\ km$, and $\sigma_t = 0.1\ s$ and wave-speed damping with $\varepsilon_{Velocity} = 0.05$, $\sigma_{V_P} = 0.1$ km/s, $\sigma_{V_S} = 0.05$ km/s.

5.6 Hit counts and quality of the results

The quality of the inversion results is assessed similarly for both the *simul2000A* and *tomo4d* results. The number of ray paths passing through or near the nodes of the inversion grid was plotted as ray-density maps (Figure 5.11 and Appendix 19) in order to illustrate the quality of the inversion results. The best-sampled area for the years 2007 and 2012 (Figure 5.11) is the main geothermal field down to 1 km b.s.l. This is expected because of the high level of induced seismicity within the geothermal area around the production wells. At 2 km b.s.l. there is a limited sampling, as seismicity reduces with depth. Ray-path density for the V_s model is almost as good as for the V_p model, because of the large number of *S* measurements. In this thesis, the best-sampled area will be interpreted.

The reduction in data residuals for the inversions of 2007 and 2012 using *simul2000A* are given as histograms in Figure 5.12. Histograms for other years are provided in Appendix 20. The final RMS travel-time residual for the 2007 data was ~0.04 s for *P*-waves and ~0.09 s for *S*-waves. For 2012 data, this was ~0.02 s for *P*-waves and ~0.05 s for *S*-waves. The higher final RMS for *S* residuals shows that the V_p/V_s model is not resolved as well as the V_p model.

The improvement in the data residuals for the same inversions using *tomo4d* was stronger (Appendix 21). Even though the initial residuals are larger than those found using *simul2000A* the final RMS residual achieved is similar to or smaller than that achieved using *simul2000A*. For 2007 and 2012 data (Figure 5.13), the final RMS travel-time residual was ~0.04 s for *P*-waves and ~0.07 s for *S*-waves for the 2007 data and ~0.03 s for *P*-waves and ~0.04 s for *S*-waves for the 2012 data.

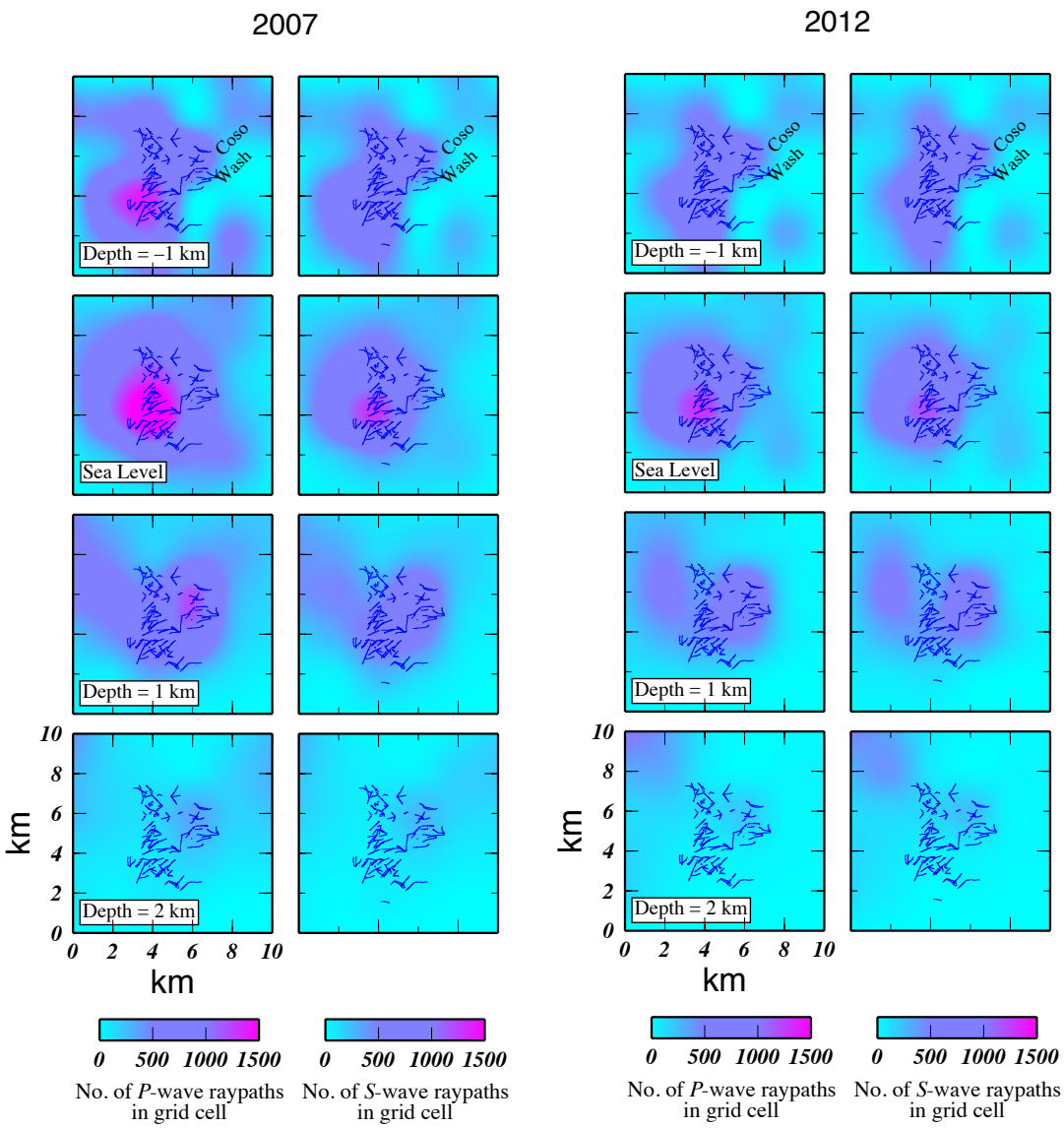

Figure 5.11: Hit-count maps showing the best-sampled areas in the study volume at different depths for the 2007 inversion (left pair of columns, left *P*, right *S*) and for the 2012 inversion (right).

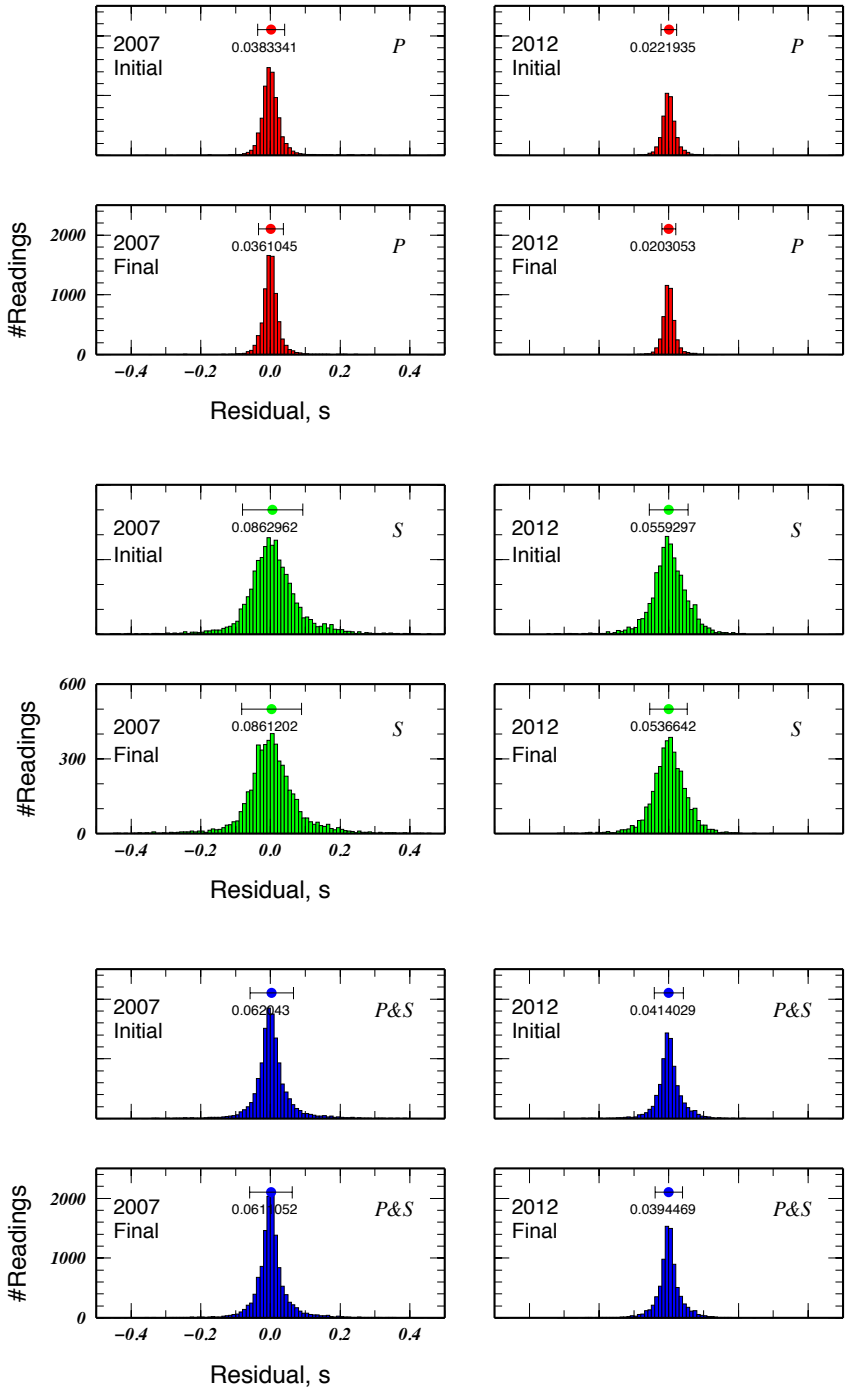

Figure 5.12: Histograms of the initial and final arrival-time residuals (red) for *P*-wave observations, (green) for *S*-wave observations and (blue) for both *P*- and *S*-wave observations, for the inversions of 2007 and 2012 data using program *simul2000A*. Coloured circle at the top of each histogram indicates the mean residual and the error bar shows the spread around the mean value. The number below the circle gives the RMS residual.

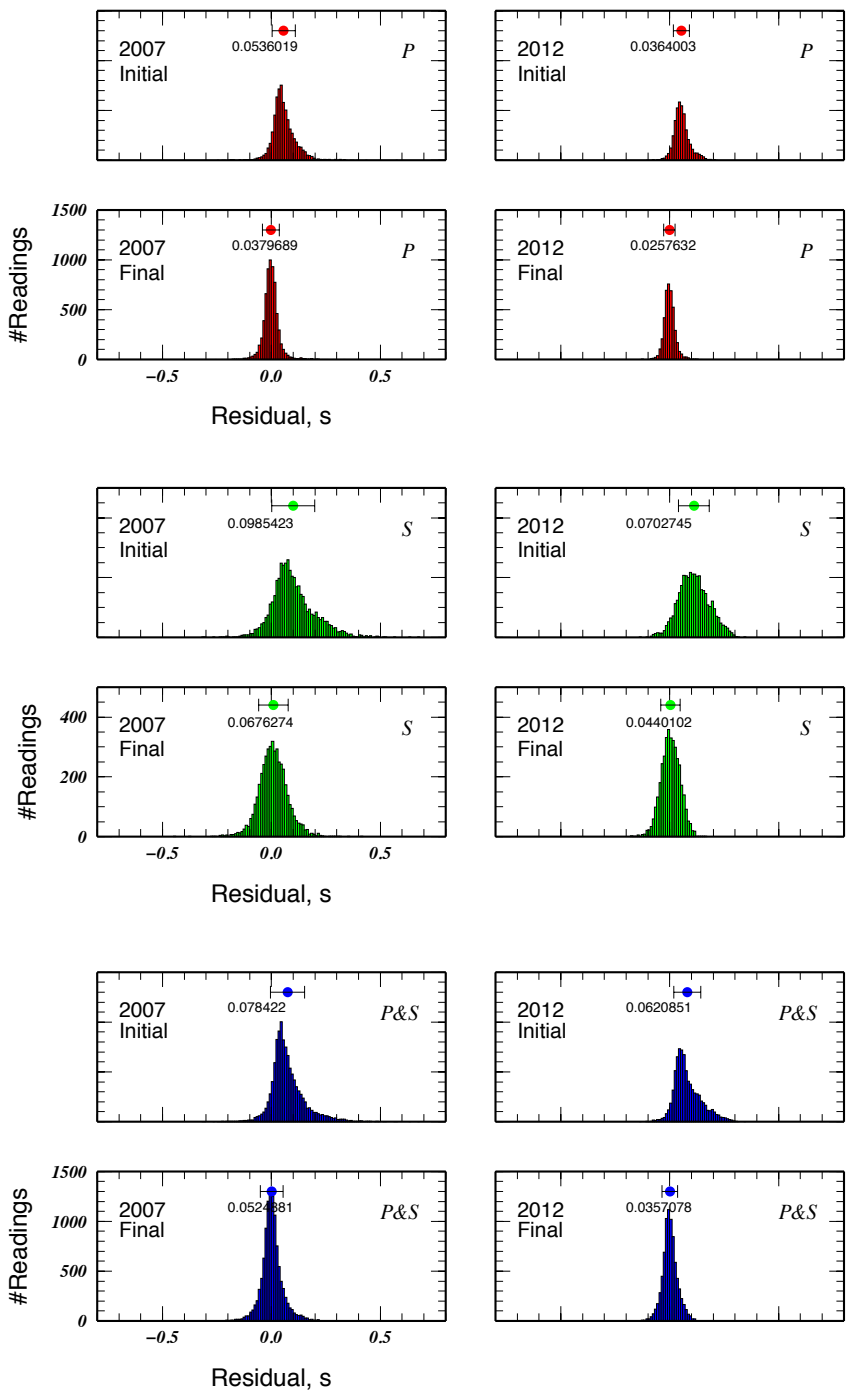

Figure 5.13: Same as Figure 5.12, for the inversion using *tomo4d*.

5.7 Results

5.7.1 Temporal variations in V_p , V_s , and V_p/V_s – *simul2000A* results

The overall structure obtained from the inversion COMB is shown in Figure 5.14. The eastern part of the study area is characterized by a major elongated low-V_p and low-V_s structure at depths of -1 and 0 km b.s.l. The south part of this anomaly extends to a depth of 1 km b.s.l. At 1 km a.s.l., the main geothermal field is occupied by high-V_p along with even higher V_s in the southwestern part and low-V_p but average- to high-V_s in the northern and eastern parts. At sea level, high-V_s dominates beneath the main geothermal field with low-V_p in the centre. Low-V_p and low-V_s anomalies extend beneath the main geothermal field at a depth of 2 km b.s.l.

A strong low-V_p/V_s anomaly at 1 km a.s.l. in the northwestern part of the main geothermal field correlates with low-V_p anomaly and high-V_s anomaly. At sea level, low-V_p/V_s is detected in the southwestern part of the geothermal area. This volume correlates with high-V_p and even higher-V_s. The low-V_p/V_s anomaly expands and weakens with depth.

The results for differencing pairs of years are shown in Figure 5.15, Figure 5.16 and Appendix 22. Between 1996 and 2006 (Figure 5.15), the low-V_p anomaly in the northwestern part of the geothermal field strengthened, as did the high anomalies in V_p and V_s in the southwestern part at 1 km a.s.l. This is not so clear between 2007-2012 (Figure 5.16).

These changes correlate with changes in V_p/V_s. In the northeastern part of the geothermal field, at sea level, a V_p/V_s decrease is caused by increase in both V_p and V_s with the increase in V_s is being stronger than in V_p. At -1 km b.s.l, the low-V_p/V_s anomalies in the northwestern part of the geothermal field decreased with time and correlated with the decrease in V_s and the stronger decrease in V_p. Again, these are not clear between 2007-2012. However, V_p/V_s increase in the southwestern part of the geothermal field appears at depth of 1 km a.s.l. and correlates with increase in V_p.

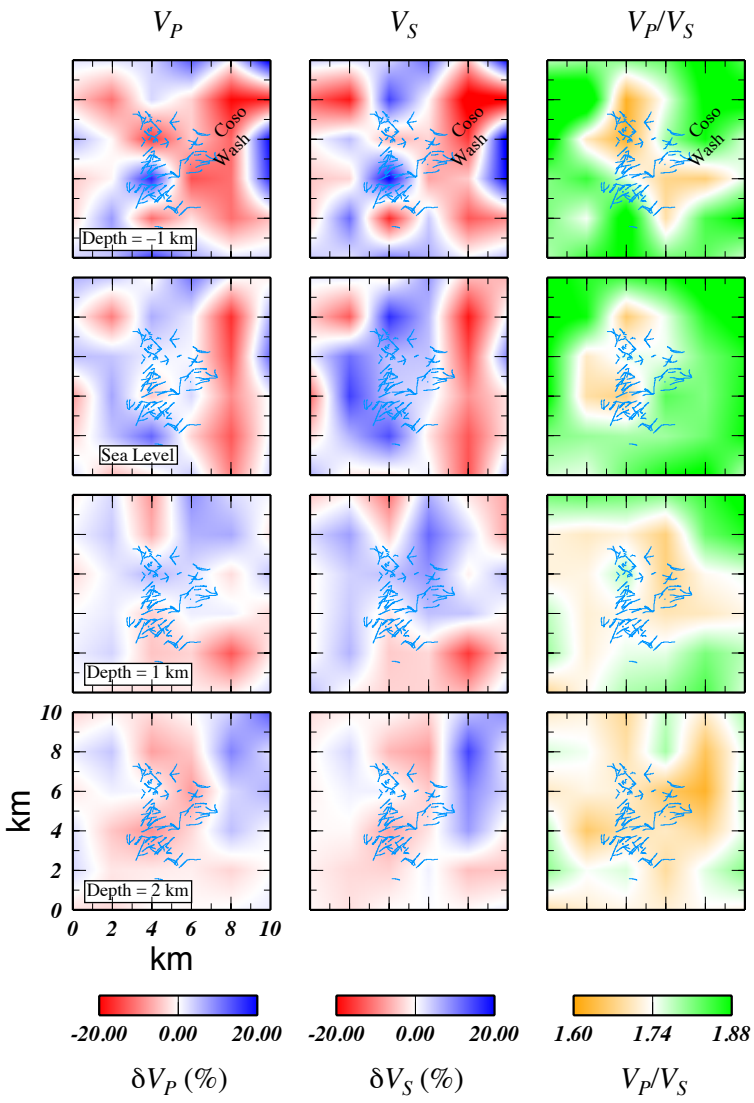

Figure 5.14: The average model resulting from inversion using *simul2000A* with the combined data (COMB). (left) V_p, (middle) V_s, and (right) V_p/V_s. Anomalies in V_p and V_s are shown as the percentage variation from the mean values at each depth and V_p/V_s is displayed by the absolute values at depths (-1, 0, 1 and 2 km b.s.l.). Light blue lines are surface traces of well bores.

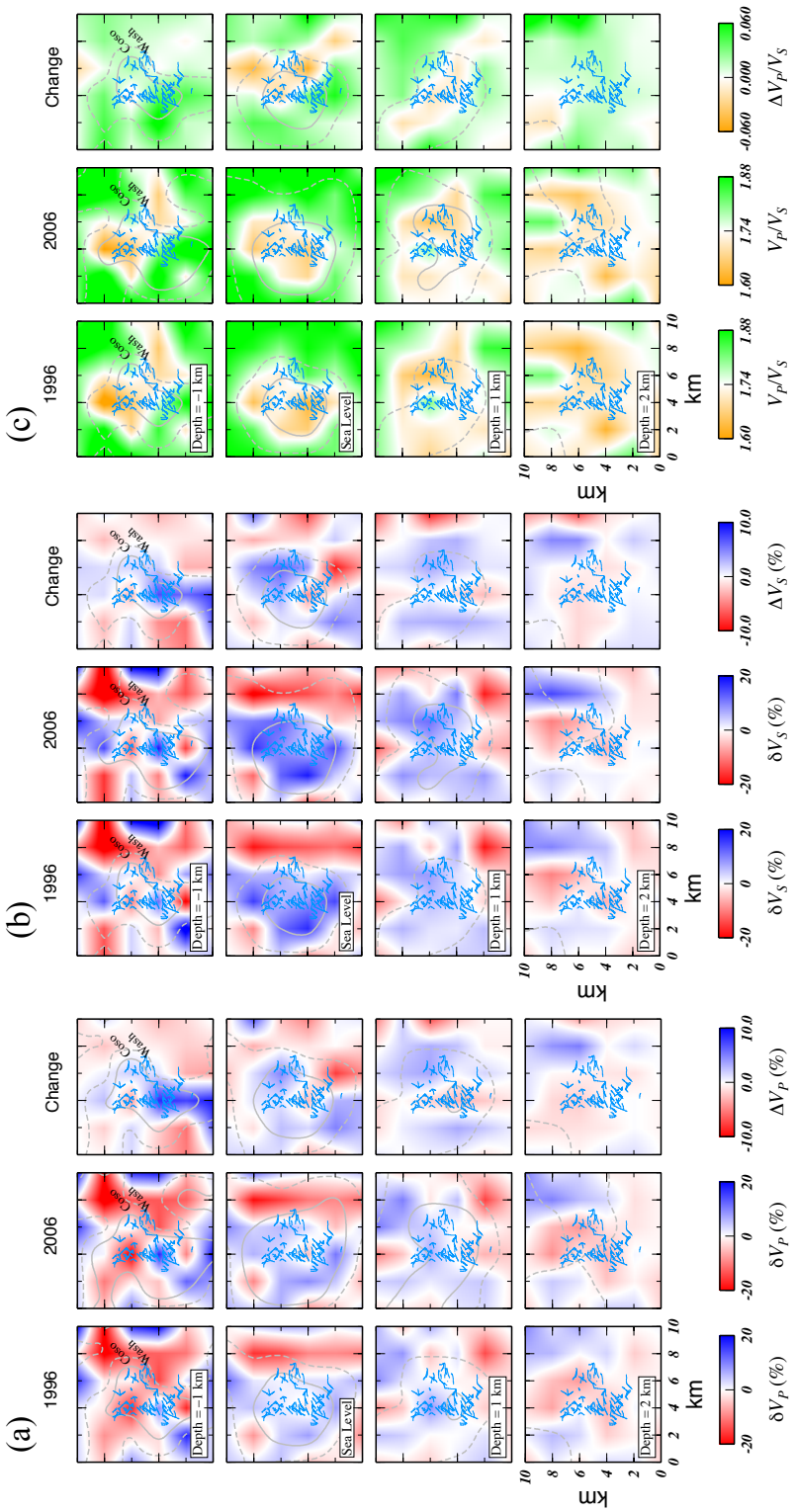

Figure 5.15: (a) The structure obtained from inversions using *simul2000A* for the years 1996 (left panel) and 2006 (middle panel) along with the change between the two epochs (right panel) for V_p. (b) same as (a) for V_s and, (c) same as (a) for V_p/V_s. Solid and dashed grey lines are the 500 and 150 hit-count contours respectively.

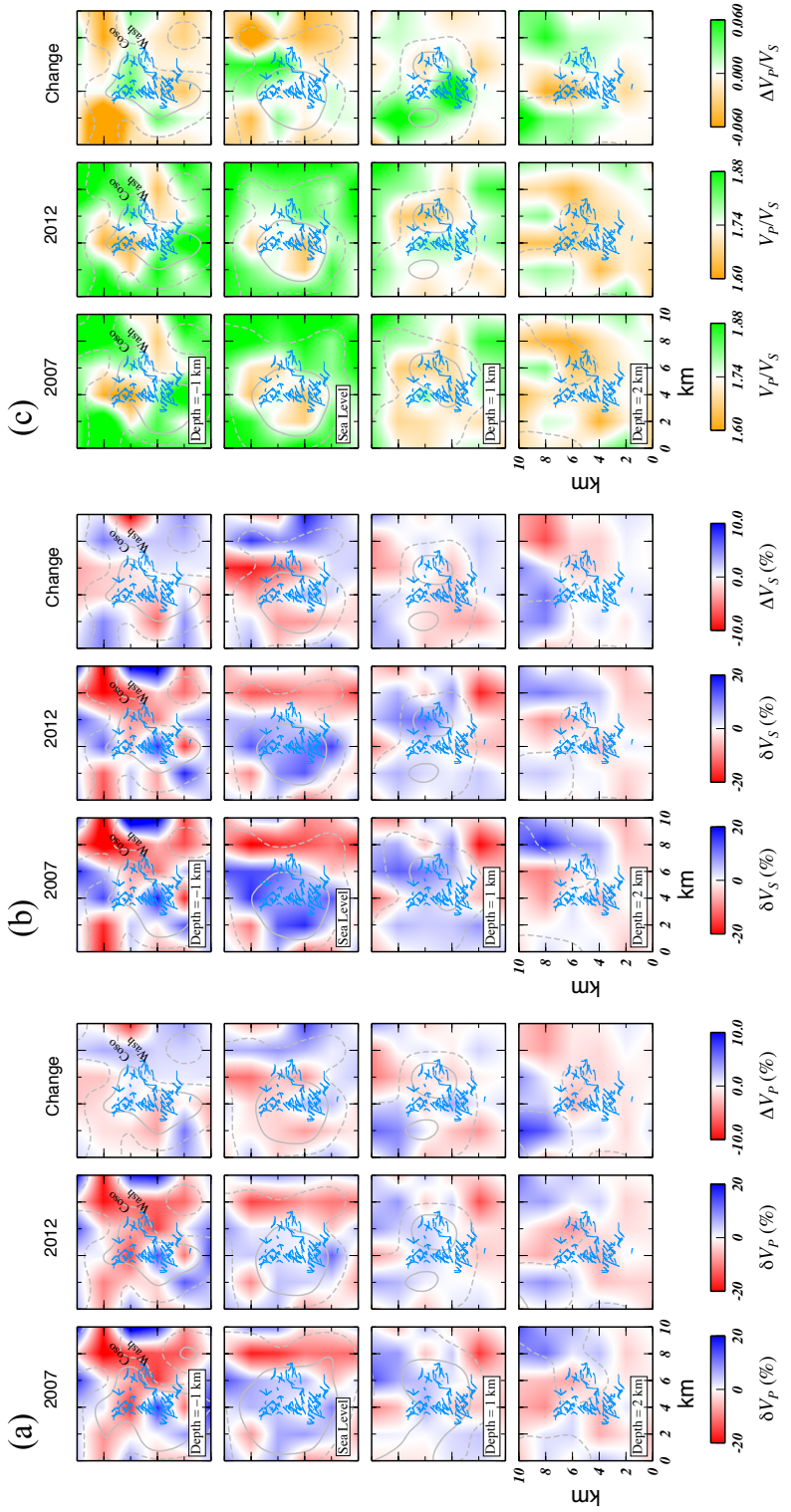

Figure 5.16: Same as Figure 5.15 but for the years 2007 and 2012.

5.7.2 Temporal variations in V_p , V_s , and V_p/V_s – *tomo4d* results

The overall structure obtained from the inversion of the combined data using *tomo4d* (Figure 5.17) is similar in pattern to a first order to that obtained using *simul2000A* (Figure 5.14). A major elongated low-V_p and low-V_s structure characterizes the Coso Wash in the top two layers. High-V_p and high-V_s volumes appear beneath the main geothermal field. However, the amplitudes of the anomalies obtained from these inversions are weaker with most anomalies falling in the range ±6% from the mean compared to ±20% obtained using *simul2000A*. Some anomalies shown in the results of *simul2000A* are not detected using *tomo4d* such as the low-V_p anomaly in the northwestern part of the main geothermal field at a depth of 1 km a.s.l.

The V_p/V_s structure shows low anomalies in the northwestern part of the geothermal field at a depth of 1 km a.s.l. This extends to the whole western part of the geothermal field at a depth of 1 km b.s.l.

Figure 5.18 and Figure 5.19 show the results of inversions for 1996-2006 and 2007-2012 (other inversion results are shown in Appendix 23). Between 1996 and 2006, changes in V_p and V_s are mainly an increase of ~2% in the geothermal field in the upper two kilometers. At a depth of 1 km b.s.l., the changes in V_p and V_s are a decrease within the geothermal field and an increase in V_p within the northeastern part. These changes are weaker (~1%) than those in the upper two kilometres. Changes in V_p/V_s between 1996-2006 are an increase of ~2% all over the geothermal field except for slight decrease ~0.5% in the northeastern part at 1 km a.s.l. and in the southern part at depth of 1 km b.s.l.

Between 2007 and 2012 however, the changes in V_p and V_s in the upper two kilometres of the geothermal filed are a general decrease of ~1% and an increase in V_p only in the eastern part. At 1 km b.s.l., V_p increased by ~1% in the western part and decreased by ~1% in the eastern part while V_s decreased all over the field except for an increase in the northwestern part. Changes in V_p/V_s are generally an increase of ~1% down to 1 km b.s.l. except for a decrease in the southern part at 1 km a.s.l. and in the northern part at sea level.

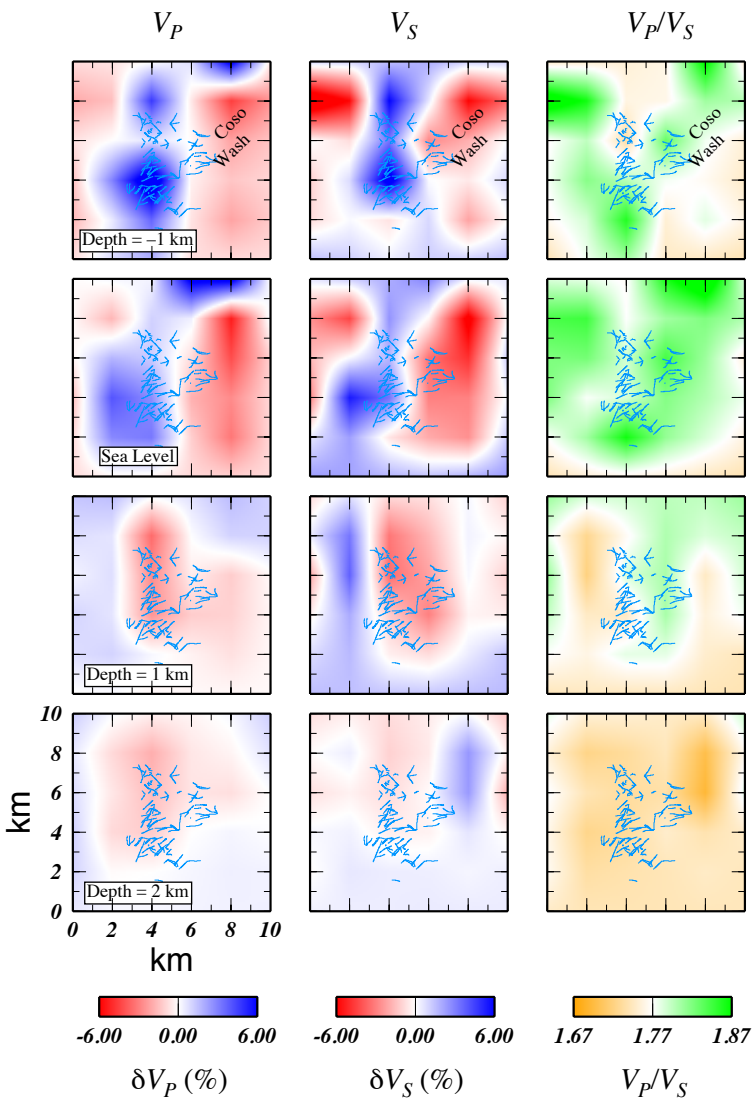

Figure 5.17: Same as Figure 5.14 but for the inversion using *tomo4d*. Note different colour scales used.

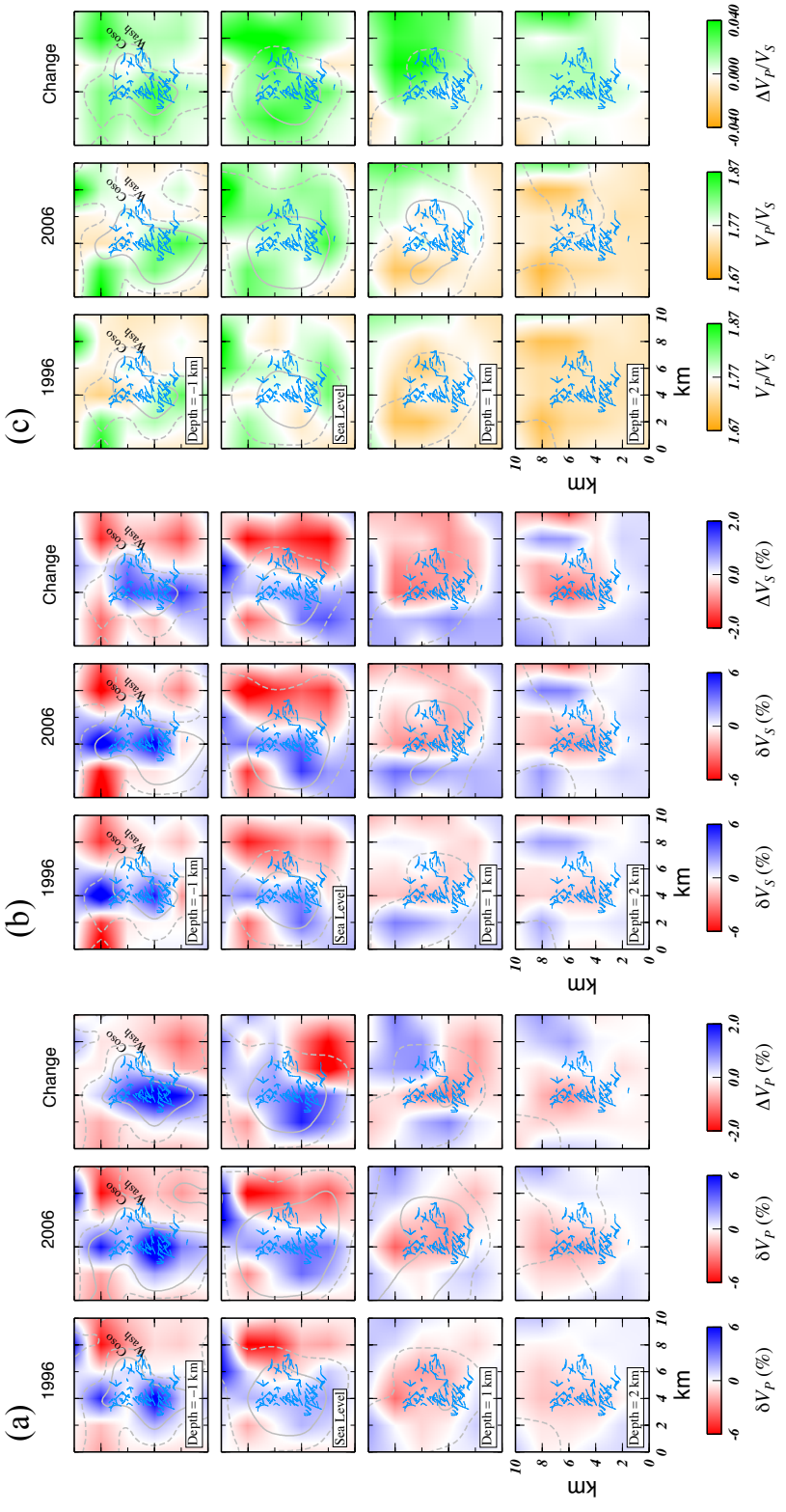

Figure 5.18: Same as Figure 5.15, for the inversion using *tomo4d*. Note different colour scales used.

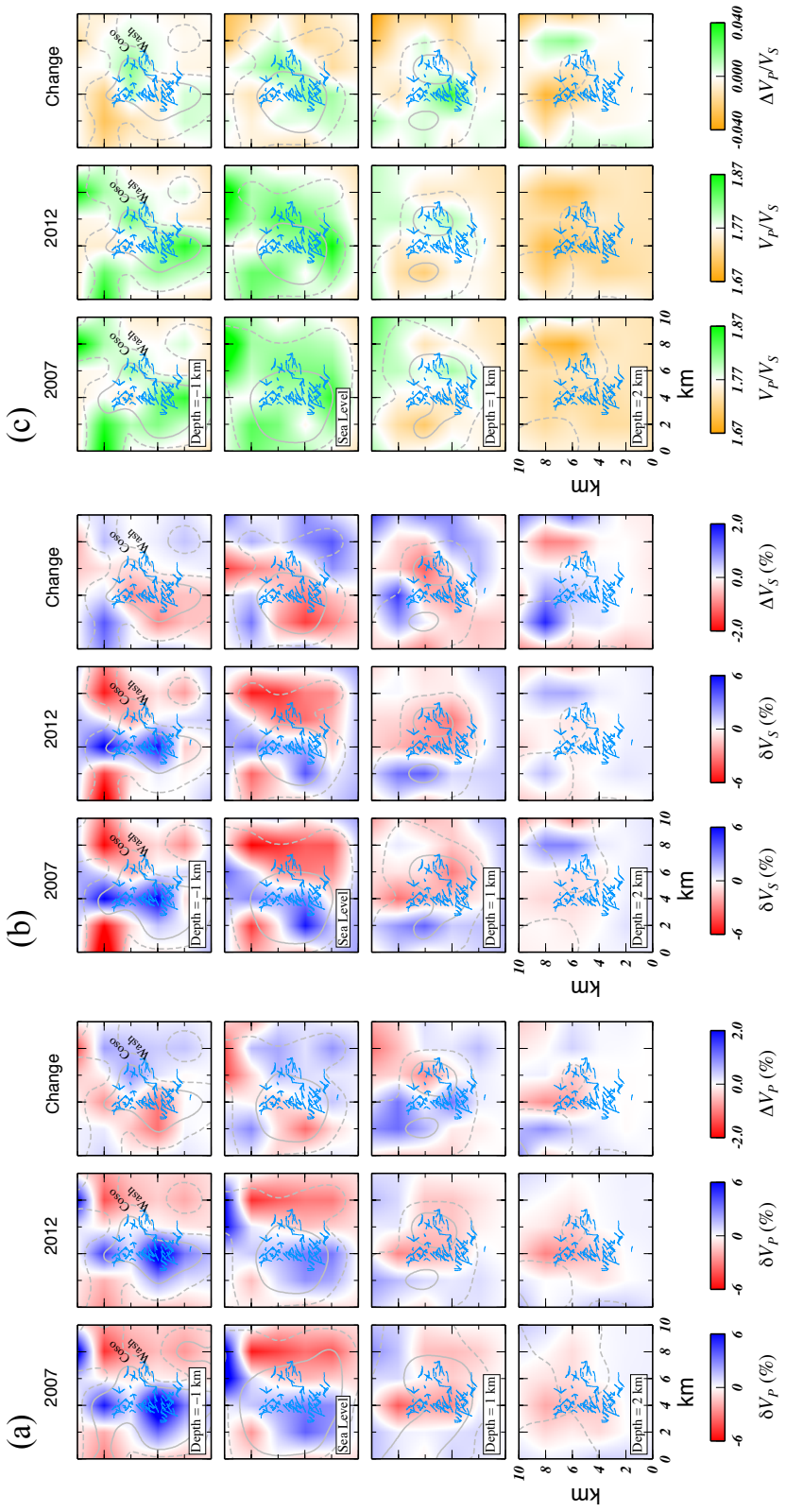

Figure 5.19: Same as Figure 5.16 but for the inversion using *tomo4d*. Note different colour scales used.

5.8 Summary

The *simul2000A* and *tomo4d* tomography programs were used for inversions of data from 1996, 2006, 2007, 2008, 2010, and 2012 for the Coso geothermal area. The earthquakes were recorded by the US Navy seismometer network. Sets of high-quality earthquakes were selected on the basis of the number of arrival times, RMS residuals, azimuthal gap, and magnitude. They comprise 486, 743, 680, 570, 512, and 504 earthquakes for the years 1996, 2006, 2007, 2008, 2010, and 2012 respectively. Arrival times were measured by hand for the 1996 and 2006 data and automatically for the 2007 data, by the GPO of the US Navy. The data for the other years were measured by hand using the program *epick*, as part of this thesis. In total 10520, 8542, and 8270 arrival times were measured for the years 2008, 2010, and 2012 respectively. Independent inversions for the selected years were performed using *simul2000A* following the same method used by *Foulger* [2007] for the years 1996-2006. The final RMS residual values ranged between 0.04 and 0.06 s. The same data sets were inverted using *tomo4d* where a stronger improvement in the data residuals was achieved.

The ray-density maps show the best-sampled area is the main geothermal field down to 1 km b.s.l., consistent with induced seismicity around the production wells. There is limited sampling at 2 km b.s.l., as seismicity reduces with depth.

The structure obtained using *simul2000A* is similar for both V_p and V_s with stronger variations in V_s than in V_p. Low-V_p and low-V_s structures are detected at depths of 1 km a.s.l. and 0 km b.s.l. in the eastern part of the study area and in the northwestern part of the main geothermal field. The structure obtained from inversions using *tomo4d* shows weaker but generally similar structure to that obtained using *simul2000A* except for the disappearance of the low-V_p body in the northern part of the geothermal field at depth of 1 km a.s.l.

Low-V_p/V_s anomalies beneath the geothermal field were detected using *simul2000A* at 1 km a.s.l. and beneath the western part at sea level. This result was not confirmed using *tomo4d* except for a small volume of low-V_p/V_s anomaly in the northern part at a depth of 1 km a.s.l.

Between 1996 and 2006, the low-V_p/V_s anomalies detected from the inversions using *simul2000A* became stronger. This was caused by either increase in both V_p and V_s with the increase in V_s is being stronger than in V_p such as in the northeastern part of the geothermal field at sea level, or by decrease in V_s and stronger decrease in V_p such as in the northwestern part of the geothermal field at 1 km a.s.l. However, this was not confirmed by the inversions using *tomo4d* where the changes in V_p/V_s were to increase all over the geothermal field except for slight decrease in the northeastern part at 1 km a.s.l. and in the southern part at depth of 1 km b.s.l.

Between 2007 and 2012, the inversions using *simul2000A* showed a V_p/V_s increase in the northwestern part of the geothermal field at a depth of 1 km a.s.l. correlated with increase in V_p. The inversions using *tomo4d* however, generally showed an increase in V_p/V_s down to 1 km b.s.l. in the geothermal field except for a decrease in the southern part at 1 km a.s.l. and in the northern part at sea level.

CHAPTER 6

INTERPRETATION AND CONCLUSIONS

6.1 Background

Inverting data from both Long Valley caldera and the Coso geothermal area using *simul2000A*, the traditional seismic tomographic method, resulted in large structural changes between the inverted epochs. Inverting the same data sets using *tomo4d* gave much smaller changes between epochs. Some changes imaged by *simul2000A* were shown to be not required by the data when inverted using *tomo4d*.

A brief recap of the relevant background to tomography studies at Long Valley caldera and the Coso geothermal field is as follows. Seismic tomography using *simul2000A* was performed using data from local earthquakes collected in 1989 by *Julian et al.* [1998] for the Mammoth Mountain area in the southwest of Long Valley caldera. A negative V_p/V_s anomaly (up to 9%) was imaged beneath Mammoth Mountain, extending from the surface to at least 1 km b.s.l. beneath surface CO_2 vents that killed trees. *Julian et al.* [1998] suggested that the low-V_p/V_s volume beneath Mammoth Mountain was a leaky CO_2 reservoir. A repeat study by *Foulger et al.* [2003] using the same tomography program and data collected in 1997 yielded a structural-change image for the period 1989-1997 characterised by an increase in V_p/V_s beneath the southwest, south and east of Mammoth Mountain. The largest increase (~3%) occurred in the east, with increases in V_p (9%) and V_s (5%). No significant changes in V_p and V_s were imaged at depths greater than 2.5 km. *Foulger et al.* [2003] suggested that CO_2 flowed into the top 2.5 km beneath the center of Mammoth Mountain between 1989 and 1997 and became depleted beneath the flanks to the northwest, southwest and east. *Gerlach et al.* [1998] and *Lewicki et al.* [2014] also postulate that the source of the CO_2 degassing on the flanks of the mountain is an underlying CO_2 reservoir rather than a shallow magma intrusion.

Previous tomography studies e.g., at The Geysers, showed that low-V_p/V_s anomalies correspond to the production areas in the geothermal field, and become stronger with time [e.g. *Foulger*, 2007; *Foulger et al.*, 1997; *Gunasekera et al.*, 2003; *Julian et al.*, 2008; *Ross*, 1996]. There, *Foulger et al.* [1997] detected a decrease of up to ~ 4% in the V_p/V_s ratio between 1991 and 1994. This was caused by decrease in V_p and was interpreted as a result of increasing pore-fluid compressibility due to decreasing pressure in the reservoir. Continuing reduction in the V_p/V_s ratio in The Geysers reservoir over time was confirmed by *Gunasekera et al.* [2003], who showed a clear, progressive continuing decrease in V_p/V_s when inverting data from the years 1991, 1993, 1994, 1996 and 1998. This continued decrease was up to 0.6% between 1991 and 1993 and up to 4.6% between 1991 and 1998.

Seismic tomography performed by *Foulger et al.* [2007] for the Coso geothermal area, using data from each of the years 1996-2006, imaged reductions in V_p/V_s in the upper ~ 2 km in the geothermal field between some epochs in the period 1996-2004. The reductions in V_p/V_s result from the progressive relative increase of V_s with respect to V_p. *Foulger et al.* [2007] interpreted this as a consequence of decrease in fluid pressure and drying of minerals such as illite as a result of geothermal operations. However, the changes were subtle and uncertain. *Foulger* [2007] experimented with a wide range of inversion criteria and found that in some cases the obtained structure did not reveal a systematic development of V_p/V_s with time. For this reason the new tomography program *tomo4d* was developed.

6.2 *simul2000A* vs. *tomo4d*

Seismic tomography has been used in a number of studies to investigate temporal changes in Earth structure by inverting for different epochs separately and comparing the resulting models. *simul2000A* is a program widely used for this purpose. However, this is not a robust approach. Changes in the models obtained are expected even if wave speeds in the Earth did not vary with time. This can be simply because of variation in the seismic ray distribution caused by natural variations in the locations of earthquakes or seismometer-network geometry between separate epochs data [*Julian and Foulger*, 2010]. Observational errors in measured arrival times can add to these effects. This was the motivation for developing the new tomography program

tomo4d, which gives changes only where required by the data. It can thus be used to test whether the changes determined using *simul2000A* are required.

The damping in *tomo4d* works in a more rational way than in *simul2000A*, taking into consideration both the quality and the density of the data. Some strong anomalies determined by inversions using *simul2000A* are not confirmed by *tomo4d*, suggesting that they were caused by poor data quality or varying ray distributions between two epochs. Also, as will be shown in this chapter, realistic expected changes in wave speeds in volcanic and geothermal areas are weaker than those often calculated by *simul2000A*. The lower-amplitude anomalies calculated using *tomo4d* are physically more realistic. This finding has implications for interpretation of time-dependent seismic tomography results obtained by differencing results using the *simul* family of programs in other studies. For these reasons, and in this chapter, results for Long Valley caldera and the Coso geothermal area obtained using *tomo4d* are considered to be more reliable than those of *simul2000A*. Therefore I interpret the results obtained using *tomo4d*.

6.3 Parameters that influence seismic wave speeds

Interpretation of both seismic-wave speeds and their changes is ambiguous, because they depend on factors including rock type, porosity and fluid saturation, pressure, temperature and fracturing, which all affect the elastic properties of the host rock [*Mavko*, 1980; *Sanders et al.*, 1995; *Walck*, 1988]. *P*-waves typically travel in the crust at speeds between ~1.5 km/s (*e.g.*, in mud) and ~5.5 km/s (*e.g.*, in basalt). The speed of *P*-waves depends on the elastic properties and density of a material and is defined by:

$$V_p = \sqrt{\frac{\kappa + \frac{4}{3}\mu}{\rho}} \tag{6.1}$$

where κ is the bulk modulus, μ is the shear modulus, and ρ is the density. These factors in turn depend on rock properties such as porosity, fluid saturation and texture.

S-waves travel more slowly than *P*-waves, typically from ~0.5 km/s in unconsolidated sediments to ~3 km/s in basalt. *S*-waves do not propagate through fluids. *S*-waves do

not change the volume of the material through which they propagate, but shear it. *S* wave-speed is given by:

$$V_s = \sqrt{\frac{\mu}{\rho}} \tag{6.2}$$

6.3.1 Rock type

Seismic-wave speeds depend on the rock type and thus they may be used to narrow down the composition of materials beneath the surface. However, different rock types may have the same seismic-wave speed, and other factors, *e.g.,* saturation, also influence wave-speed. Thus unique interpretations cannot be made in the absence of supporting data *e.g.*, from borehole cores. Similarly, rocks of similar types may have different wave speeds due to variations in chemistry or properties.

6.3.2 Saturation

The effect of saturation is illustrated using the simple example of a rock with zero-porosity (i.e., matrix) with V_p of 5 km/s. This rock might be an analogue for massive basalt close to the surface. Figure 6.1 shows the effects on V_p of saturation, where the pores are filled with air, water or a mixture of the two. A reduction in *P*-wave speed of 2.2% is expected if the whole 10% of the water-filled pore space is replaced by air, and 0.22% reduction if only 10% of the contained water is replaced by air (9% water and 1% air). *Toksoz et al.* [1976] reported that, at high pressures (depths > 1.5 km), the presence of small amount (5%) of gas in brine as an immiscible mixture reduces *P*-wave speeds significantly. The *P*-wave speeds in rock with a mixture of gas and liquid filling the pore space may even be lower than that of rock with 100% gas in the pore space.

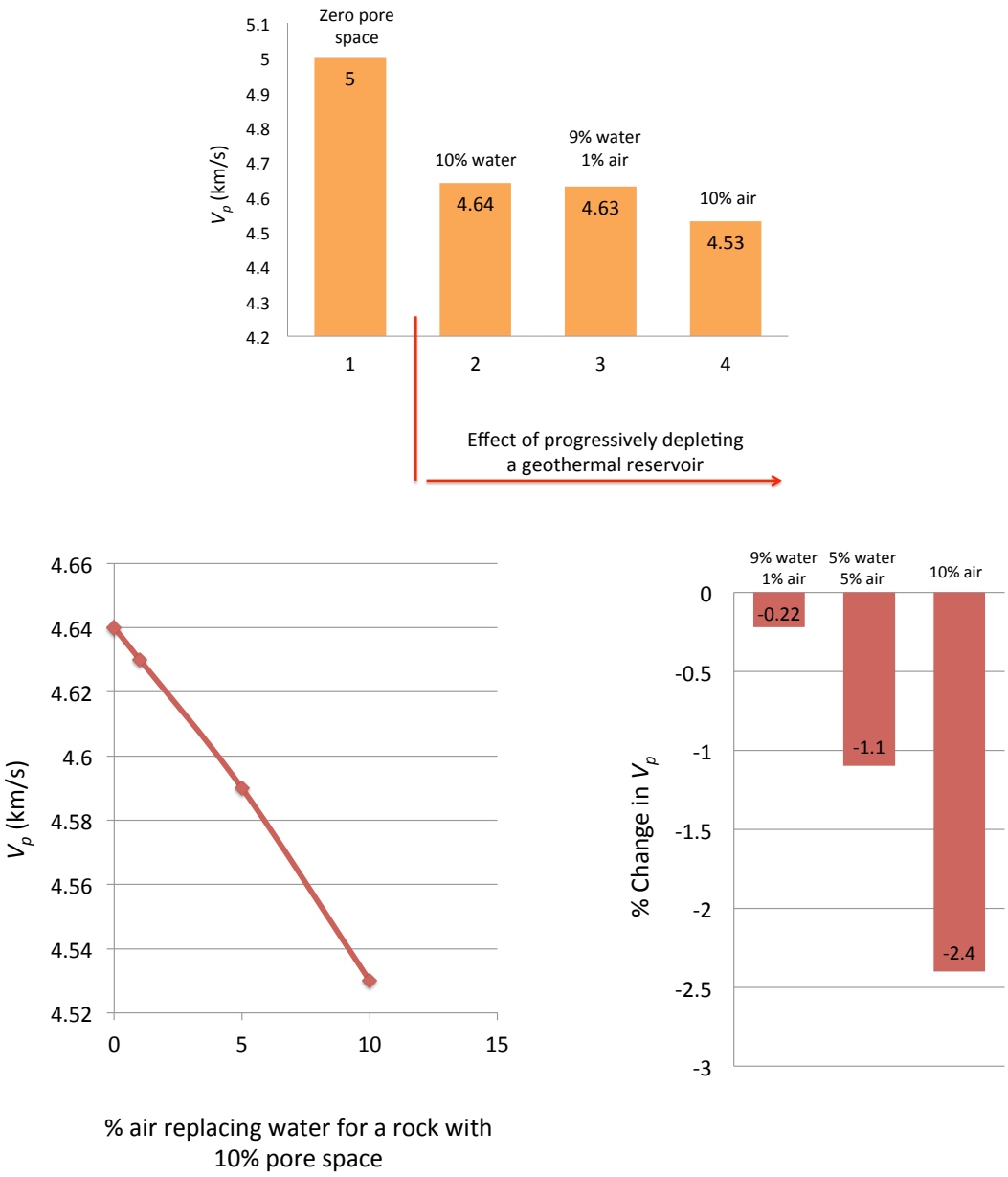

Figure 6.1: Histograms showing V_p at different saturations for a rock with an original V_p of 5 km/s (top) where (1) the rock has zero porosity (2) the rock contains 10% pore space filled with water, (3) when containing 9% water and 1% air and (4) when containing 10% pore space filled with air. (bottom-left) V_p vs. percentage of air replacing water in the 10% pore space in the rock. (bottom-right) the expected change in V_p when the contained water in a rock with 10% porosity is (right) completely replaced by air, (middle) 50% of the water is replaced by air (i.e., the rock contains 5% water and 5% air) and (left) only 10% of the water is replaced by air (i.e., the rock contains 9% water and 1% air).

P- and *S*-wave speeds for various rocks under different conditions of saturation and pressure have been studied in the laboratory. Figure 6.2 shows the effect on wave speeds of saturation for different rock types and depths (pressures). Generally, wave speeds increase with depth. *P*-wave speeds tend to be more sensitive to pore fluid content than *S*-wave speeds. Substituting air for water in the rock pores decreases *P*-wave speed by decreasing the bulk modulus of the rock (caused by the water being less compressible than air) and increases *S*-wave speed by decreasing density of the pore fluid [*Wang et al.*, 1990].

The effect of saturation on *P*-wave speed tends to be larger for low-wave-speed rocks (*e.g.*, Bedford Limestone) and smaller for high-wave-speed rocks (*e.g.*, Westerly Granite). This effect decreases with increasing pressure however. At 10 MPa (100 bars) effective pressure (equivalent to ~370 m depth), the *P*-wave speed in dry granite is 4% less than in saturated granite but it is only 2% different between dry and saturated granite at 20 MPa (200 bars) effective pressure (equivalent to ~740 m depth). At higher pressures (depths) the effect of saturation is smaller, probably because a) closure of cracks and thin pores reduces the porosity, and/or b) the decreased compressibility of gas with depth and overburden pressure causes wave speed to be less sensitive to change in gas content with depth.

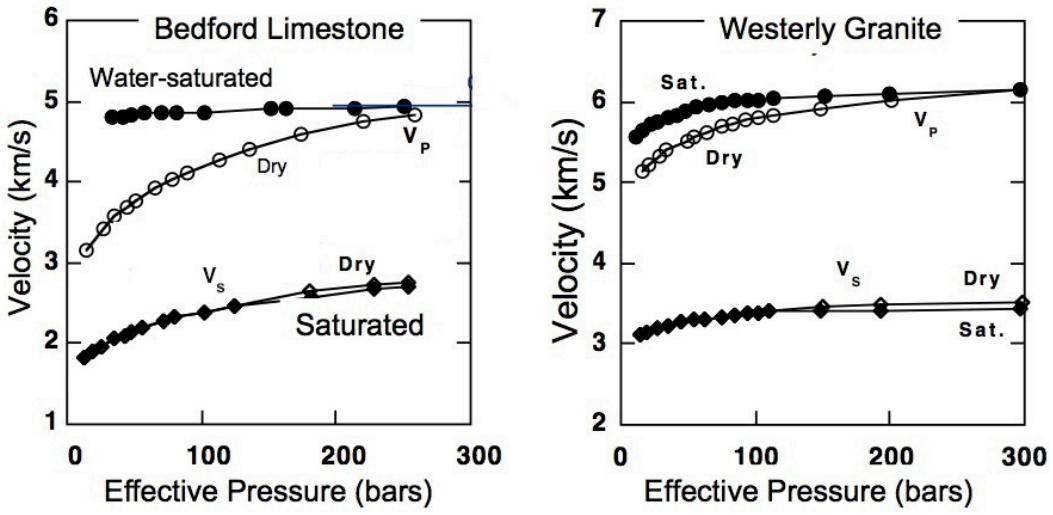

Figure 6.2: Graphs showing the effect on *P*- and S-wave speeds of saturation at different pressures and for different rocks (left) for limestone and (right) for granite [from *Mavko*, 2000].

6.3.3 Porosity

Porosity and the nature of the pore fluid strongly affect seismic-wave speeds. Figure 6.3 shows wave speeds in sandstone for different porosities, pore fluids and pressures. At low pressure from dry to oil-saturated to water-saturated sandstone, the wave speed increases by up to ~5% in Beaver sandstone with 6% porosity at pressure of 5 MPa (*i.e.,* a depth of ~185 m). For Fontainebleau sandstone with 15% porosity, the dry rock has slightly higher V_p than the oil-saturated rock at pressure grater than 3 MPa (*i.e.,* depths more than ~111 m). At higher pressures, up to 40-50 MPa (equivalent to ~ 1480-1850 m burial depth), V_p in the Beaver sandstone increases and the type of pore fluid becomes unimportant. In the case of the 15% porosity Fontainebleau sandstone, the fluid type continues to be influential with V_p for the dry rock being up to ~2% higher than for the oil-saturated rock.

For the same variations in lithology, porosity, pore fluid and pressure, the V_p/V_s ratios vary strongly. As shown in the lower panels of Figure 6.3, V_p/V_s decreases by 6% when moving from water-saturated to dry 6%-porosity Beaver sandstone at a pressure of ~ 5 MPa (~ 185 m below the surface). There is a much smaller change, ~ 1%, at greater pressures of ~ 40 MPa (~ 1480 m below the surface) where porosity is lower. For the Fontainebleau sandstone with 15% porosity, the change in V_p/V_s is ~ 4% at a pressure of 3 MPa (*i.e.,* a depth of ~ 111 m) and ~ 2% at a pressure of 50 MPa (*i.e.,* a depth of ~ 1850 m).

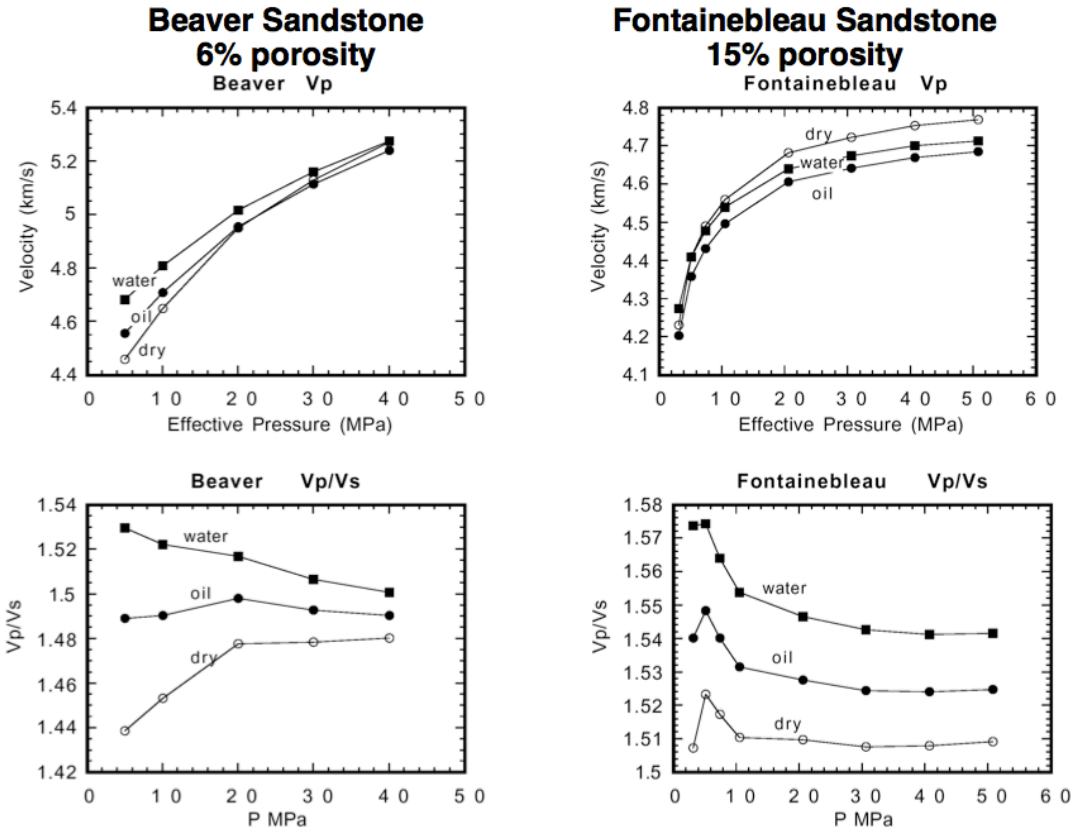

Figure 6.3: Seismic velocities in sandstone for different porosities, pressures and pore fluids. (top-left) Beaver sandstone with 6% porosity and (top-right) Fontainebleau sandstone with 15% porosity. Bottom graphs show V_p/V_s ratios [from *Mavko*, 2000].

6.3.4 Pressure

Pressure increases with depth as ρgh where ρ is density, g is the acceleration due to gravity and h is depth. In regions of uniform composition, despite the fact that the increase of temperature with depth works to lower the wave speed, the pressure effect is larger and wave speed generally increases with depth. In the shallow crust, wave speed increases rapidly with depth, mostly because of the closing of cracks and other asperities, which elastically stiffens the rock matrix. As the effective pressure increases and the cracks close, the bulk modulus increases and wave speed increases. Over-pressure can preserve porosity and even open cracks and grain boundaries if it increases with time. This works to soften the rock and lower wave speeds. Over-pressured zones can be detected by their anomalously low wave speeds [*Mavko*, 2000].

6.3.5 Fractures

The opening of new cracks and the widening of existing ones are expected to decrease both *P*- and *S*-wave speeds and increase the V_p/V_s ratio [*Moos and Zoback*, 1983]. Fracturing is also a source of wave-speed anisotropy (section 6.3.7). In regions where tectonic stresses are high, wave-speed anisotropy is an important parameter to be considered when interpreting field seismic data. Most of the energy of an earthquake powers fracture growth or is converted into heat by friction. As a result of these factors, increased anisotropy is expected in regions of high seismicity, tectonic activity, and in production fields associated with fault systems.

6.3.6 Temperature

As temperature increases, both *P*- and *S*-wave speeds decrease. This is mainly the result of thermal weakening of the rock and possibly because different thermal expansions of the mineral constituents cause widening of grain boundaries and opening of new cracks [*Kern and Tubia*, 1993]. However, in the Earth's crust, the primary influence of temperature is on pore fluid properties as the elastic mineral matrix properties are usually weakly dependent on temperature. For dry (gas-saturated) or wet (brine-saturated) rock, temperature has almost no effect on wave speeds in general and a very weak effect at elevated pore pressures. Wave speeds are most sensitive to temperature when the rocks contain liquid hydrocarbons (i.e., oil) because of the increase in compressibility and decrease in viscosity of oil with temperature. Other processes can also occur with increased temperature such as fluid phase changes. For example, gas might come out of solution as temperature increases. This can have a strong effect on wave speeds, particularly for high-porosity rocks at low pressure [*Mavko*, 2000].

6.3.7 Anisotropy

Rocks that have layering or fabric on a scale finer than the seismic wavelength are elastically and seismically anisotropic. Fabrics may include elongated and aligned grains, pores, cracks and fine-scale layering where wave speeds are usually higher when propagating along the layering and lower when propagating in the perpendicular direction. Cracks resulting from earthquakes and stress loading can therefore

introduce anisotropy into the rock. An experimental study by *Nur and Simmons* [1969] showed that applying uniaxial stress on an isotropic rock causes wave-speed anisotropy and waves propagate faster along the stress axis. The left panel of Figure 6.4 shows the dependence of *P*-wave speed on propagation direction at different stress levels. A similar pattern is observed for all stress levels, with V_p is higher when propagating along the stress axis and lower when propagating in the perpendicular direction. The overall change in V_p is larger at higher stress (*e.g.,* compare the drop in *P*-wave speed at 300 bar and 50 bar). It decreases with increasing angle from the stress axis for a given stress level. This is shown in the right panel where *P*-wave speed is shown as a function of propagation direction at different stress values. At 30 MPa (300 bar), for example, *P*-wave speed in the stress direction 0° increased by ~20% compared with 0 MPa, whereas in the perpendicular direction (90°) the increase is only ~5%.

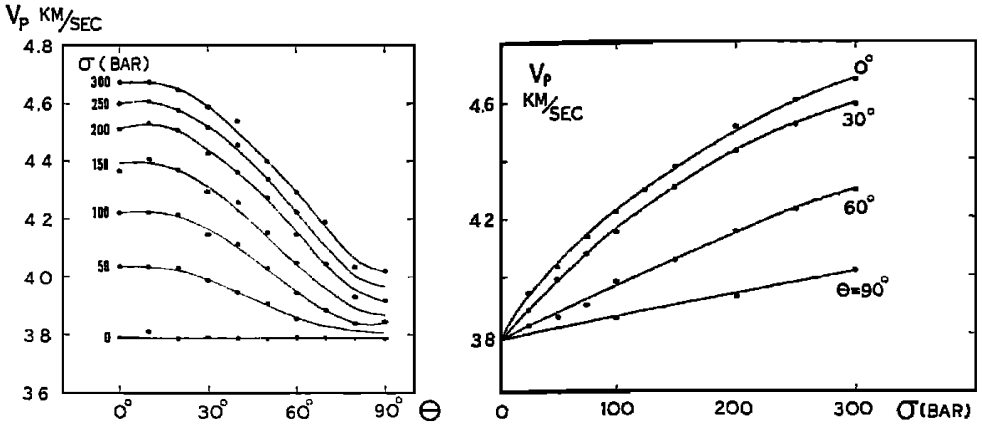

Figure 6.4: Stress-induced *P*-wave-speed anisotropy. *P*-wave speed vs. (left) angle from the stress axis for different stress values, and (right) stress for different directions of propagation from the stress axis [from *Nur and Simmons*, 1969].

6.3.8 CO_2 injection

A seismic survey by *Daley et al.* [2007] imaged a small scale CO_2 injection (1,600 tonne) at depth of 1,500 m in a brine aquifer of the Frio Formation near Houston, Texas. A time-lapse borehole seismic survey, and crosswell and vertical seismic profiles (VSP) were acquired to monitor the CO_2 distribution using two boreholes 30

m apart at a depth of 1,500 m. The tomographic image obtained showed V_p decrease (up to 500 m/s) and little change in V_s, as expected for fluid substitution (Figure 6.5). For fluid substitution with no change in matrix properties, a change in V_p is expected due to the change in bulk modulus with a minimal change in V_s expected due to the lack of change in shear modulus, which is a property of the rock matrix and not affected by pore fluid. *Daley et al.* [2007] used a rock physics model to estimate CO_2 saturation from the V_p change to be 10-20% (Figure 6.5).

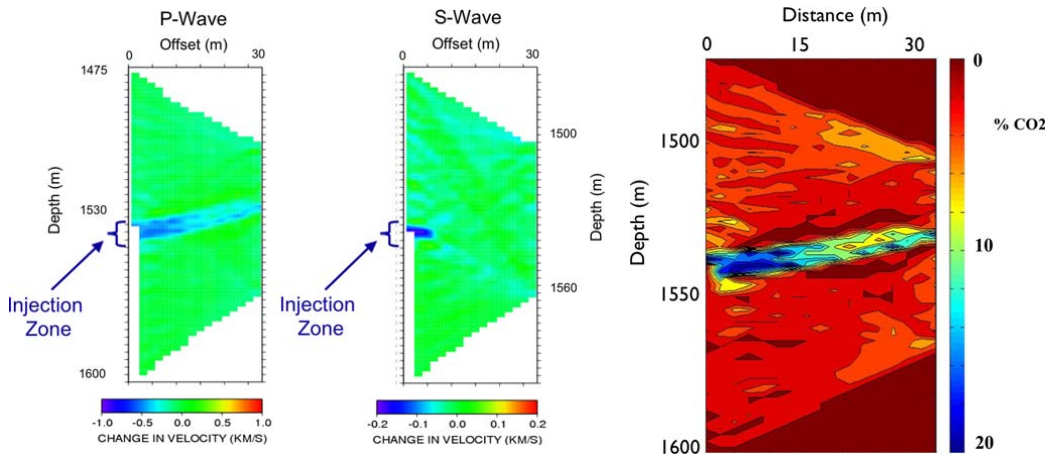

Figure 6.5: (left) tomographic images of V_p and V_s change from the crosswell survey and (right) CO_2 saturation estimated from the V_p change using a rock physics model [from *Daley et al.*, 2007].

Previous theoretical studies and laboratory experiments [*e.g.*, *Daley et al.*, 2007; *Gutierrez et al.*, 2012; *Khatiwada et al.*, 2012; *Mavko and Mukerji*, 1995; *Mavko et al.*, 1995; *Wang and Nur*, 1989] show that CO_2 flooding (i.e., replacement of liquid pore fluid with gas) causes a decrease in V_p as a result of increased bulk compressibility. There is less change in V_s, leading to a decrease in V_p/V_s. *Wang et al.* [1998] demonstrated that *S*-wave speed is insensitive to CO_2 saturation but sensitive to pore pressure increases such that pore pressure increase accompanying CO_2 flooding reduces V_s by approximately the same percentage as V_p is reduced by the increase in compressibility. Thus, in some cases V_p/V_s may be unchanged. A decrease in V_p/V_s would therefore be expected to result from CO_2 flooding where there is little pressure increase, and an increase in V_p/V_s could result from CO_2 depletion with a pressure decrease.

6.3.9 Summary

A summary of the effects discussed in sections 6.3.1-6.3.8 is given in Table 6.1. This table shows that:

- Low-V_p/V_s can occur with pore pressure decrease, drying of minerals, increase in anisotropy and/or CO_2 flooding.
- High-V_p/V_s can occur if water replaces steam, pressure increases and/or fracturing occurs or temperature increases.

Table 6.1: The effects on V_p, V_s and V_p/V_s of processes described in sections 6.3.1-6.3.8. Large arrows indicate the dominant effect, and small arrows indicate subsidiary or negligible effects.

	V_p	V_s	V_p/V_s
Water saturation	↑	—	↑
Pressure increase and fracturing	↓	↓	↑
Pore pressure decrease	↑	↑	↓
Drying of minerals	↑	↑	↓
Temperature	↓	↓	↑
Anisotropy	↓	↓	↓
Gas replacing water (CO_2 flooding)	↓	↓	↓

6.4 Long Valley caldera results

6.4.1 Structure

The wave-speed model obtained for Long Valley (Figure 4.22) shows agreement with the known geological structure of the area. Low-wave-speed volumes are detected inside the caldera and there is good correlation with the caldera boundary down to 1 km b.s.l. i.e., in the upper 4 km of crust. Low wave speeds in the caldera south moat correlate with low-density post-caldera rhyolitic flows, glacial till, landslide debris and lake sediments. This area has been intensively seismogenic for several decades (Section 1.3.1, Appendix 1) and is thus highly fractured. Some regions of the moat at shallow depth to the west and south of the resurgent dome have higher wave speeds. The resurgent dome is characterized by both high and low wave speeds, probably because of the resurgence of welded Bishop Tuff [*McConnell et al.*, 1995] which is expected to have higher wave speeds than the postcaldera rhyolitic flows and unconsolidated rocks [*Bailey*, 1989; *Hill et al.*, 1985]. Well drilling showed that the Bishop tuff exists at depths of 0.6 - 1.8 km beneath the resurgent dome [*McConnell et al.*, 1995]. High wave-speeds outside the caldera characterize Sierran crystalline rocks, which are mainly Mesozoic granitic rocks of the Sierra Nevada batholith. This result agrees with those of *Foulger et al*. [2003].

6.4.2 Structural change between 1997 and 2009/2010

Figure 6.6 shows the changes in the V_p, V_s and V_p/V_s models between 1997 and 2009-2010 obtained using *tomo4d*. The area inside the 75 hit-count contour, where the results are more reliable, is interpreted. An increase in V_p and V_s in the south moat is detected down to 1km b.s.l. with the largest change being ~6%.

The main changes in V_p/V_s are as follows. A decrease of ~2% in V_p/V_s in the south moat at sea level and 1km a.s.l. results from an increase in V_p but a stronger increase in V_s. Resolution is insufficient at 2km a.s.l. and 1k a.s.l. to verify whether this anomaly continues to the surface. Possible effects that can cause increase in V_p and a stronger increase in V_s are (Table 6.2):

- Pore pressure decrease
- Drying of minerals
- Reduction in temperature

Reduction in temperature is unlikely and probably too small an effect to explain the observations. Pore pressure decrease and/or drying of minerals could occur if water is removed and this is more likely to explain the changes in this region.

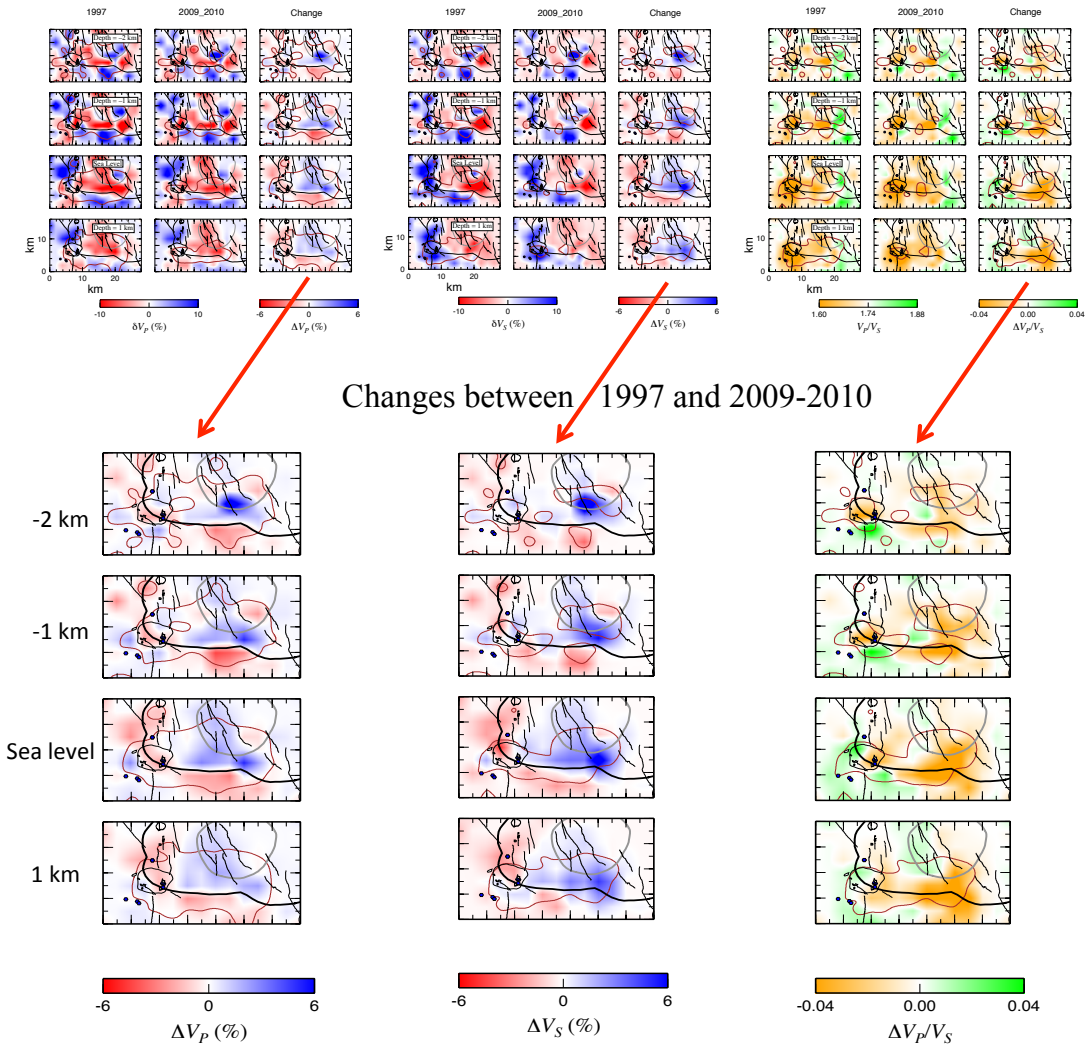

Figure 6.6: Top panels: same as Figure 4.23 and Figure 4.24. Bottom panels: enlargements of the change panels only showing the change in V_p (left), V_s (middle) and V_p/V_s (right) between 1997 and 2009-2010 for Long Valley caldera. Brown line is the 75 hit-count contour.

Table 6.2: Same as Table 6.1 with blue circles indicating effects discussed in the corresponding text.

	V_p	V_s	V_p/V_s
Water saturation	↑	–	↑
Pressure increase and fracturing	↓	↓	↑
Pore pressure decrease	(↑)	(↑)	(↓)
Drying of minerals	(↑)	(↑)	(↓)
Temperature	↓	↓	↑
Anisotropy	↓	↓	↓
Gas replacing water (CO_2 flooding)	↓	↓	↓

A decrease of ~2% in V_p/V_s beneath Mammoth Mountain at sea level and above results from a decrease in V_p and a small decrease in V_s. Possible effects that can explain this are (Table 6.3):

- Heat flow
- Pore pressure increase
- CO_2 flooding

Heat flow and pore pressure increase can cause V_p to decrease and V_s to decrease even more. CO_2 flooding causes V_p to decrease and has little effect on V_s. Therefore, CO_2 flooding with a small pressure increase can explain the decrease in V_p which in turn can cause the decrease in V_p/V_s in this region.

Table 6.3: Same as Table 6.1 with blue circles indicating effects discussed in the corresponding text.

	V_p	V_s	V_p/V_s
Water saturation	↑	–	↑
Pressure increase and fracturing	↓	↓	↑
Pore pressure decrease	↑	↑	↓
Drying of minerals	↑	↑	↓
Temperature	↓	↓	↑
Anisotropy	↓	↓	↓
Gas replacing water (CO_2 flooding)	↓	↓	↓

An increase of ~2% in V_p/V_s results from decrease in V_p and stronger decrease in V_s in northwestern part of Mammoth Mountain at sea level. This is consistent with locations of CO_2 degassing areas mapped by *Werner et al.* [2014]. Thus, CO_2 depletion with a small pressure decrease can explain the decrease in V_p and V_s, which in turn can result in V_p/V_s increasing in this area.

6.5 The Coso geothermal area results

6.5.1 Structure

The overall structure obtained from the inversions is shown in Figure 5.17. Anomalies correlate with the geological and geothermal features in the area. The eastern part of the region is characterized by a major elongated low-V_p and low-V_s structure that correlates with the Coso Wash. It extends from the surface to sea level. High wave speeds dominate within the geothermal field in the top two kilometres except for its eastern part. Below sea level however, low wave speeds dominate within the geothermal field.

The V_p/V_s model shows high anomalies beneath the geothermal field in the top two kilometres, consistent with the results of *Kaven et al.* [2011]. Previous studies [*Julian et al.*, 2006; *Simiyu*, 1999; *Stevens et al.*, 2000; *Zucca et al.*, 1994] reported low V_p/V_s

anomalies associated with geothermal reservoirs. This can be seen in parts of the geothermal field here such as a small volume in the northern part at 1 km a.s.l. and the southwestern part at 1 km b.s.l. Variations are weaker below sea level and less reliable at 2 km b.s.l. because many earthquakes are above this level and so there are fewer rays.

6.5.2 Structural change between 1996 and 2006

Between 1996 and 2006, changes in V_p and V_s comprise mainly an increase of ~2% in the geothermal field at the upper two kilometres (Figure 6.7). The anomaly changes sign and becomes weaker below sea level with a decrease of ~1% within the geothermal field except for an increase in V_p in the eastern part at a depth of 1km b.s.l. Changes in V_p/V_s between 1996 and 2006 are a ~2% increase within the geothermal field as the result of an increase in V_s and a stronger increase in V_p at sea level and 1km a.s.l.

Possible factors that could cause increases in V_p and V_s are:

a) Increase in water saturation
b) Decrease in pore pressure
c) Drying of minerals
d) Temperature decrease

It is known that the top 1-2 km of the Coso geothermal field is heavily depleted in water. Thus a) can be ruled out. On the other hand the Coso geothermal reservoir is known to be depleting and thus b) - d) are expected. In all cases b) - d), a larger increase in V_s than V_p is expected, and thus a decrease in V_p/V_s. This is not observed and instead a large increase in V_p is seen, along with an increase in V_p/V_s.

The explanation for this unexpected observation must lie in different relative effects on V_p and V_s than expected. More detailed study of this is warranted in future, in particular in collaboration with the operators at the Coso geothermal field.

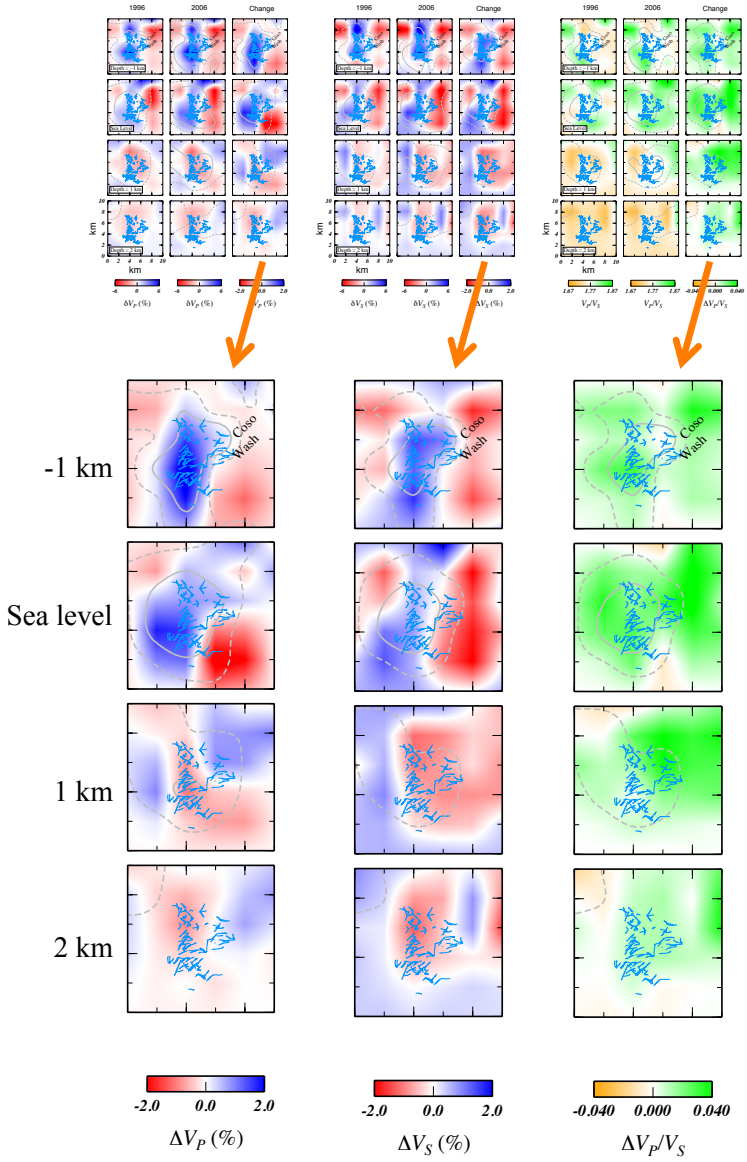

Figure 6.7: Top panels are same as Figure 5.18. Bottom panels are enlargements of the change panels only showing the change in V_p (left), V_s (middle) and V_p/V_s (right) between 1996 and 2006 for the Coso geothermal area. Solid and dashed grey lines are the 500 and 150 hit-count contours respectively.

Two volumes where V_p/V_s decreased are as follows. At 1km a.s.l. in the northeastern part of the geothermal field there is a small increase in V_p and a stronger increase in V_s. This could be caused by pore pressure decrease and drying of minerals (Table 6.2).

A second decrease in V_p/V_s occurs in the southwestern part of the geothermal field at 1km b.s.l. This results from decrease in both V_p and V_s with the decrease in V_p being stronger than in V_s. This is expected as a result of depletion in geothermal reservoirs and steam replacing water (Table 6.3).

6.5.3 Structural change between 2007 and 2012

The change detected between 2007 and 2012 is significantly different from the earlier epoch. Between 2007 and 2012, the changes in V_p and V_s are reversed and a general decrease of ~1% down to 1km b.s.l. is detected. In some peripheral volumes, V_p increases (Figure 6.8). These are the northeastern part of the geothermal field at 1km a.s.l., the east and southeastern part at sea level, and the southwestern part at 1km b.s.l. These three anomalies correlate with an increase in V_p/V_s.

Increased water saturation, drying of minerals and pore pressure decrease cause V_p to increase but only water saturation causes V_p/V_s to increase (Table 6.4). Increased water injection activity in recent years may explain the increased V_p/V_s in these areas.

The reversal in sign of the main anomaly is surprising and it implies a change in operational activity. While the main structural change between 1996-2006 is consistent with water depletion and drying of minerals, after 2007 these trends appear to have reversed and changes detected are consistent with replenishment of the reservoir. We are not aware of any changes in operational parameters, but information from Coso is restricted. We hope to work more closely with the operators in future to explore possible correlations between operations and the seismic results. Additional inversions for different epochs, selected on the basis of operational changes, may provide additional information.

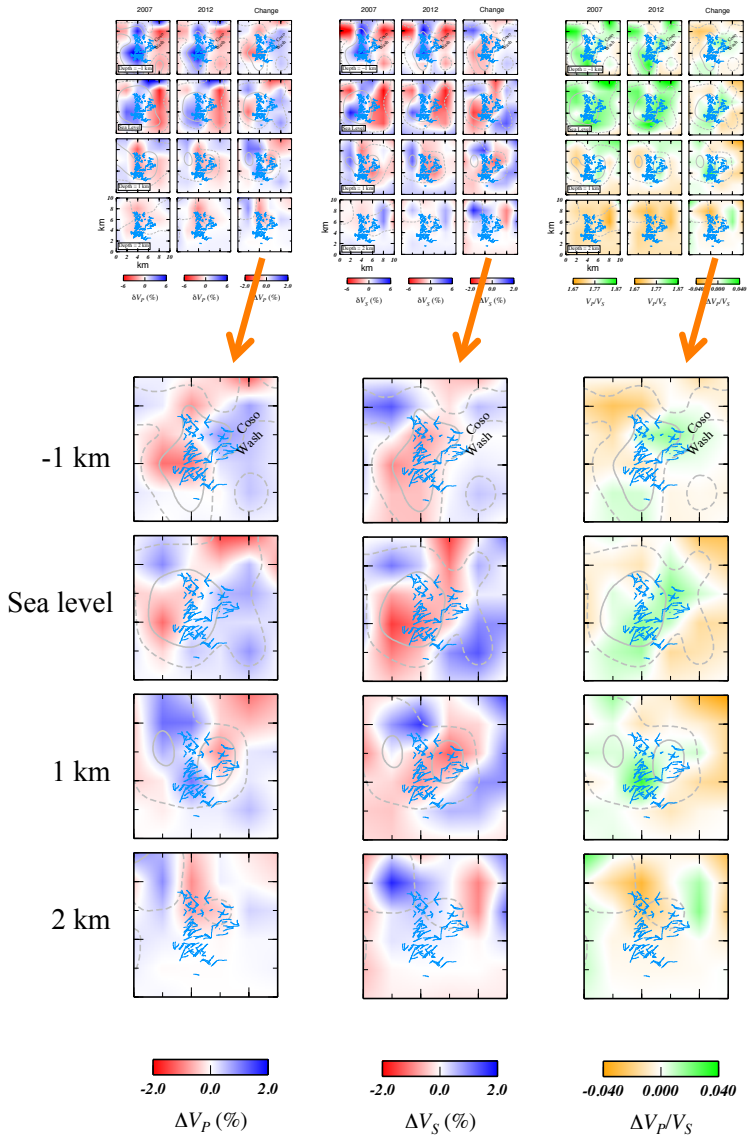

Figure 6.8: Same as Figure 6.7 but for the years 2007 and 2012.

Table 6.4: Same as Table 6.1 with blue circles indicating effects discussed in the corresponding text.

	V_p	V_s	V_p/V_s
Water saturation	↑	–	↑
Pressure increase and fracturing	↓	↓	↑
Pore pressure decrease	↑	↑	↓
Drying of minerals	↑	↑	↓
Temperature	↓	↓	↑
Anisotropy	↓	↓	↓
Gas replacing water (CO_2 flooding)	↓	↓	↓

6.6 Conclusions

Inversion of data from Long Valley caldera and the Coso geothermal area using *tomo4d* showed weaker anomalies than those obtained using *simul2000A*. Some anomaly changes imaged using *simul2000A* thus are not required by the data. Geologically reasonable changes in V_p, V_s and V_p/V_s are relatively small. For example, CO_2 flooding can cause a decrease of 0.2-2% in V_p and 1-2% in V_p/V_s at a depth of ~1000 m and smaller changes at greater depths. Thus the results of *tomo4d* are more geologically realistic than those of *simul2000A*.

For Long Valley caldera, changes detected in V_p and V_s of ~6% increase in the south moat correlate with a decrease of ~2% in V_p/V_s at sea level and 1 km a.s.l. A decrease of ~2% in V_p/V_s beneath Mammoth Mountain results from a decrease in V_p at sea level and 1 km a.s.l. which may have resulted from CO_2 flooding with a small pressure increase. In the northwestern part of Mammoth Mountain, an increase of ~2% in V_p/V_s results from decrease in V_p and stronger decrease in V_s at sea level. This may be explained by CO_2 depletion as it is consistent with locations of CO_2 degassing areas.

The changes in seismic structure detected at the Coso geothermal area between 1996-2006 are a general increase of ~2% in V_p/V_s within the geothermal field. This

correlates with an increase in V_s and a stronger increase in V_p at sea level and 1 km a.s.l. This may result from a combination of decrease in pore pressure, closing of fractures, drying of minerals and temperature decrease. The effect on V_p/V_s is surprising and warrants future study. Two volumes where V_p/V_s decreased are suggested to be caused by pore pressure decrease and drying of minerals as a result of depletion and steam replacing water. These two volumes are located in the northeastern part of the geothermal filed at 1 km a.s.l. and in the southwestern part at 1 km b.s.l. Between 2007-2012 however, in these two areas, the change in V_p/V_s became an increase and correlated with an increase in V_p. This may be explained by increasing water saturation as a result of increased water injection in recent years.

CHAPTER 7

WIDER ISSUES

7.1 Pros and cons of seismic tomography

Seismic tomography has been used to obtain seismic wave-speed models using arrival-time data. The seismic sources may include teleseismic earthquakes, local earthquakes, blasts and explosions at the surface and in boreholes. The images obtained by seismic tomography cover a broad range of features including subduction zones and fault zones. Local-earthquake tomography, in particular, has been applied extensively in volcanic and geothermal areas, where the level of seismicity is often high. It has been used to determine the extent of structural change and to reveal the depleted zone in geothermal reservoirs. It can be used to monitor how reservoirs are depleted with time and thus maximize the efficiency of commercial operations.

Higher resolution may be achieved by increasing the number and quality of earthquakes used for the inversions, and by choosing smaller block sizes for the inversion grid. *Toomey and Foulger* [1989] examined the effect of "coarse" and "fine" model parameterization on the resolution of the solution and found that the "fine" solution, although having poorer formal resolution, yielded a significant improvement in data fit and thus was a better solution.

Traditional methods yield results where the strength of the model spatial variations is strongly dependent on factors such as the number of observations and the damping. Thus, when comparing the results of two epochs inverted separately, false indications of changes in structure may result. *tomo4d* is able to separate true structural change from apparent ones that result from different experimental setups. The spatial variations in anomaly strength in the models obtained using *tomo4d* are weaker than those obtained when inverting the epochs separately using *simul2000A*. Some of the changes between two epochs shown using the traditional method are required by data but others disappear when inverting using *tomo4d*.

Local-earthquake tomography cannot provide information about the deeper portions of geothermal reservoirs or the regions below them. This is because waves from local earthquakes travel upward to surface and shallow-borehole seismometers. *tomo4d* can overcome this problem by using data from regional earthquakes as well as from local earthquakes. Waves from regional earthquakes arrive passing deep beneath geothermal areas and can thus illuminate the structure beneath the reservoir (Figure 7.1). It may even provide information about the heat source. Regional earthquakes can also be useful in particular for some geothermal areas that are only weakly seismogenic. This capability of *tomo4d* has not been applied yet to Long Valley or Coso but offers an interesting and potentially valuable avenue of future research.

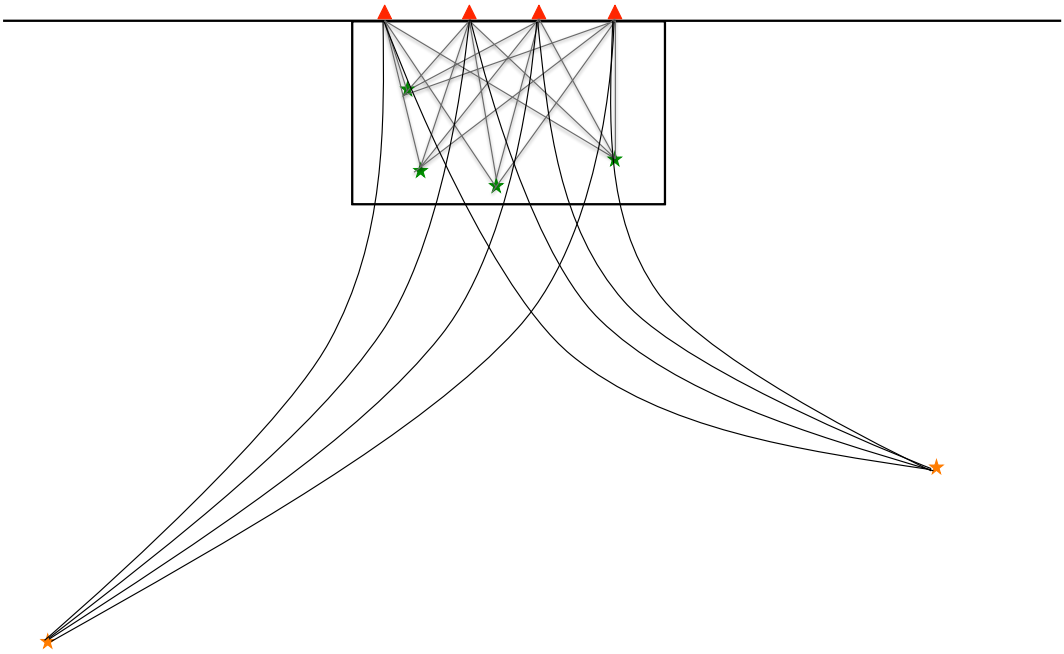

Figure 7.1: Schematic cross section illustrating ray-paths of local and regional earthquakes (green and orange stars, respectively) and how regional earthquakes can illuminate the structure beneath the study volume (black rectangle). Red triangles are seismometers.

7.2 Seismic tomography and geothermal exploration

7.2.1 Geothermal activity

Geothermal activity is caused by the transfer of heat from depth to Earth's surface. The surface manifestations of geothermal activity include warm ground, steaming ground, hot pools and springs, fumaroles, geysers and geothermal seepages. Hot springs are the most common type of geothermal activity. They are located where water from a geothermal system reaches the surface. The most commercially important geothermal areas in the world occur at plate margins (Figure 7.2). These comprise weak, fractured zones of the crust with intense seismicity, volcanic activity and high heat flow.

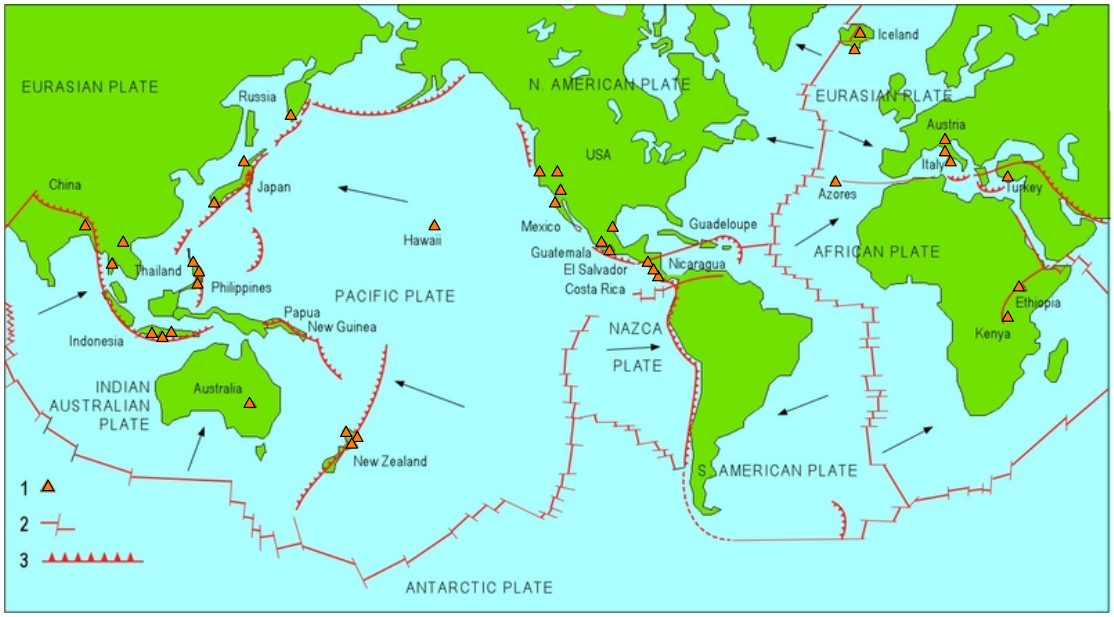

Figure 7.2: Map of the world showing plate boundaries and geothermal fields producing electricity [modified from *http://www.geothermal-energy.org/what_is_ geothermal_ energy.html*].

The heat source for a geothermal system can be either a young magmatic intrusion or simply the Earth's geothermal gradient. The geothermal fluid may be water or steam. Chemicals and gases such as CO_2 and H_2S are often carried with this water.

7.2.2 Exploration methods

In areas where geothermal exploration takes place for the first time, surveys are carried out in order to ascertain whether a useful geothermal field exists. Exploration methods may include:

- Geological and hydrological studies, to identify the area worth investigating in more detail.
- Geochemical surveys, to determine whether the geothermal system is water- or vapor-dominated and to infer the chemical characteristics of the deep fluid, its temperature, and the source of recharge water.
- Geophysical surveys including thermal, electrical, electromagnetic, seismic, gravity and magnetic surveys.
- Drilling of exploratory wells, which represents the final phase of a geothermal exploration program.

7.2.3 The role of seismic tomography

In the exploration phase, seismic tomography can give valuable information on the shape, size, depth and other important characteristics of geological structures that form the geothermal reservoir and surroundings. Information on the extent of geothermal fluids beneath the region can be obtained using electrical and electromagnetic prospecting, which are sensitive to the presence of fluids and variations in temperature. A good approach is to interpret tomography results jointly with other survey results. Conducting a full investigation of this sort for Long Valley and Coso is beyond the scope of this thesis, but it could provide an important avenue of future research.

Experience has shown that negative V_p/V_s anomalies can be caused by fractures filled with steam. Thus studying the V_p/V_s ratio is a promising technique for identifying geothermal resources and monitoring their exploitation. Application of this to the Coso geothermal area has shown, however, that more work needs to be done to fully understand why this parameter varies as it does in different geothermal areas. Accurate microearthquake locations, a byproduct of the seismic tomography method,

can delineate faults that comprise important zones of permeability and targets for new production wells.

7.3 Possible application to Syria

7.3.1 Geothermal activity in Syria

Syria has a long record of active seismicity and volcanism at the northern part of the Dead Sea fault zone (Figure 7.3 and Figure 7.4). The major fault system is characterized by relatively high seismic activity [*Dakkak et al.*, 2005]. During the last millennium, many large earthquakes affected Syrian territory, the most recent being the Ms 7.3 Aqaba earthquake in 1995. This earthquake may have trigged an earthquake swarm in southwestern Syria [*Mohamad et al.*, 2000]. Seismicity occurs in Syria in response to active deformation. The rate of movement is estimated to be < 1 to 2.7-3.3 mm/year [*Bilal*, 2009]. The last volcanic eruption occurred in the southern part of the country, Jabal Al Arab (Figure 7.3), about 10,000 years ago.

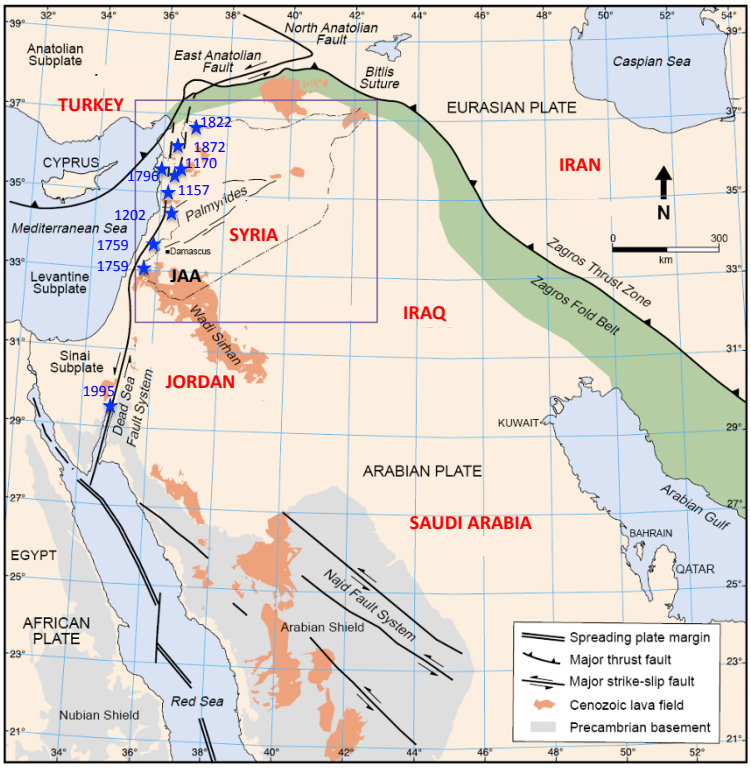

Figure 7.3: Major tectonic boundaries of Syria and the surrounding region [modified from *Abdul-Wahed et al.*, 2011] with large historical earthquakes indicated as blue stars [from *Ambraseys and Barazangi*, 1989]. JAA: Jabal Al Arab. The rectangle shows the location of Figure 7.4.

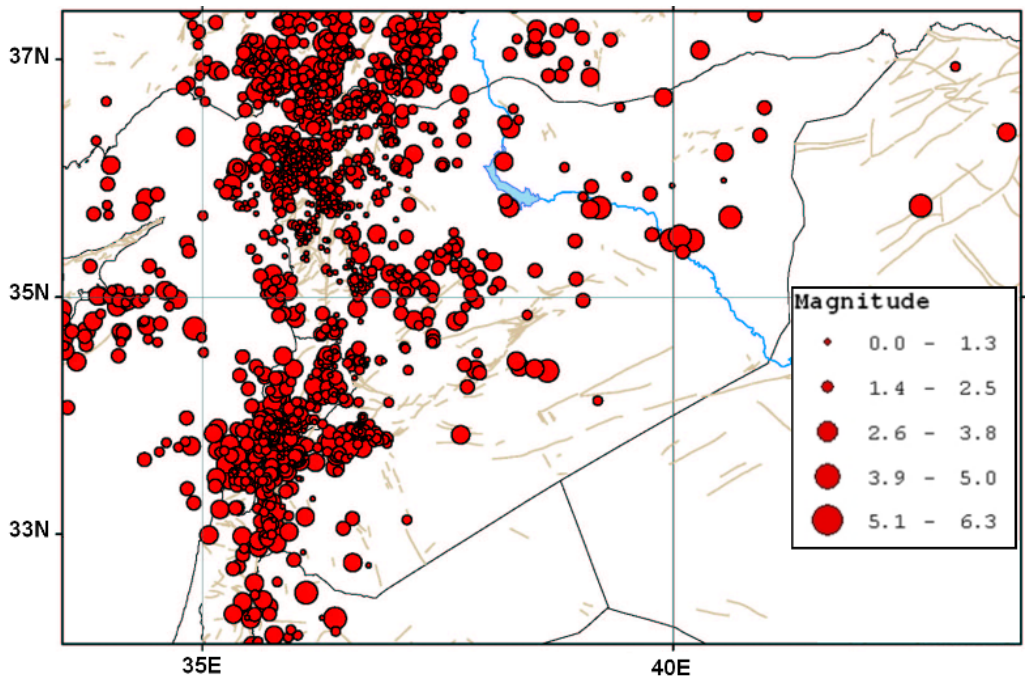

Figure 7.4: Seismicity map of Syria and vicinity for the period 1995-2004 [from *Abdul-Wahed et al.*, 2011], documented by the Syrian National Seismological Network (SNSN) (Figure 7.5).

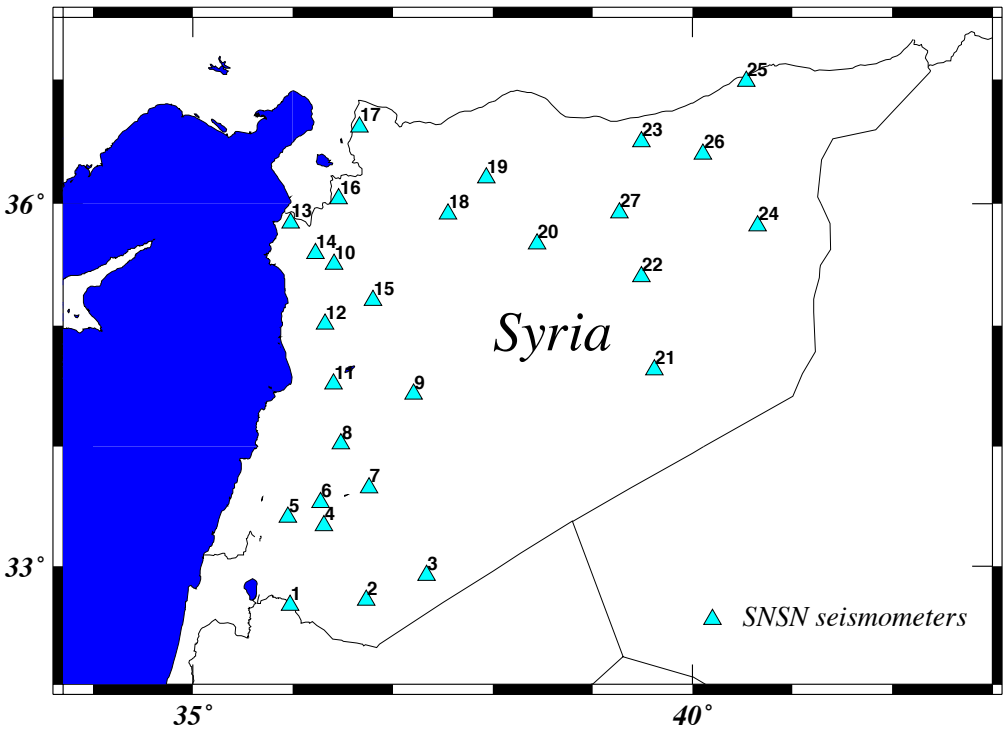

Figure 7.5: Map of Syria showing SNSN seismic stations (light blue triangles). Locations from *Dakkak et al.* [2005].

Surface geothermal manifestations in Syria comprise hot springs with temperatures of 30-60 °C and seeping steam in some locations. Hot springs that are used as spa and for tourism purposes (Figure 7.6) include:

- Sheck Esa – in the northwest of Syria between Latakia and Aleppo city, rich in H_2S and with a temperature of 38 °C;
- Abo Rabah – close to Homs city, with temperatures of ~60 °C accompanied by steam;
- Afka springs – close to Palmyra city, with temperatures of ~60 °C, rich in H_2S and steam;
- Ras Al Ain hot spring near Hasaka city rich in H_2S with temperatures reaching ~39 °C;
- Daraa hot springs 45 km south of Damascus city, rich in H_2S.

These locations have been identified as offering scope for power generation [*International Business Puplications*, 2015], with water discharge ranges of 42-980 m^3/hour accompanied by steam in the central region near Palmyra. However, the geothermal potential itself needs investigation to verify these initial findings and to assess geothermal resources.

Figure 7.6: Map of Syria showing locations of hot springs (red squares).

7.3.2 Geothermal exploration in surrounding regions

Geothermal exploration in countries neighbouring Syria include:

- Turkey to the north of Syria, is the seventh richest country in the world in geothermal energy potential [*Kaygusuz and Kaygusuz*, 2004]. Geothermal energy exploration started there in 1962 using geological, geophysical, geomorphological and geochemical methods. In addition to the known hot-water sources, some new areas with considerable geothermal energy potential were discovered.
- Iran built the first geothermal plant in the Middle East in 2015 at the foot of Sabalan mountain, famous for its mineral hot springs [*Porkhial and Yousefi*,

2015]. A pilot station was projected to come on stream in the following two years.

- Geothermal exploration started in Lebanon in 2012 and the Lebanese energy and water ministry intend to meet 0.2% of Lebanon's total power needs from geothermal sources by 2025 [from *http://www.al-monitor.com/ pulse/business/ 2014/03/lebanon-geothermal-energy-potential.html*].
- Several investigations of geothermal energy in Jordan have taken place in the last four decades. Rich geothermal potential low enthalpy resources have been discovered [*Swarieh*, 2000]. The first region is in the immediate vicinity of the east Dead Sea escarpment, where many springs discharge thermal water. The second is near the border with Syria and Iraq. The geothermal energy resources of Jordan are both medium- and low-energy with variation of temperature in the range 110–114 °C and 30–65 °C. Electric power generation could be achieved through the utilization of geothermal binary power plants at hot springs with temperatures more that 80 °C and geothermal Sterling engines at hot springs with temperature more than 20 °C [*Abu-Hamatteh et al.*, 2011].

7.3.3 Syria's energy

The majority of the electric power generation in Syria is based on heavy fuel oil and gas with these two fuels accounting for more than 90% of total electric power generation. The remainder comes from hydropower and limited biomass. In 2002, the Syrian government launched a master plan for the development of renewable energy and for renewables to cover 4.3% of total energy demand by 2011. That target was not met, however. In 2010, the government developed an updated plan run until 2030. Syria has since encountered a number of challenges as a result of the military conflict that started in 2011. In the energy sector, damage to energy infrastructure including oil and gas pipelines and electricity transmission networks have hindered exploration, development and production.

7.4 Recommendations and future work

The following is a list of some avenues of future work indicated by the work described in this thesis:

1. The work presented in this thesis should be extended using the new tomography program *tomo4d* with regional earthquake data.
2. An optimal approach is to interpret tomography results jointly with other geological and geophysical surveys.
3. Apply the rock physics model used by *Daley et al.* [2007] and *Hoversten et al.* [2003] to estimate CO_2 saturation from the seismic velocity.
4. Compare the current *tomo4d* results with the numerous tomography studies described in the first two chapters.
5. Interpret in more detail the current results.
6. Work with the producer at Coso and the GPO of the US Navy to improve the interpretation of the V_p/V_s results.
7. Invert more pairs of epochs for the Coso geothermal area with *tomo4d*.
8. Study the 1989-1997 Mammoth Mountain data to check the *simul2000A* results of *Foulger et al.* [2003] with *tomo4d*.
9. Investigate why *simul2000A* gives structural models with very strong (~20%) anomalies.
10. Study resolution and spread function for the *tomo4d* results.
11. Study possible improvements to *tomo4d* such as saving the ray paths created in earlier iterations so they can be used as starting paths in the following iteration. This may reduce ray convergence failures.

REFERENCES

Abdul-Wahed, M. K., J. Asfahan, and I. Al-Tahhan (2011), A combined methodology of multiplet and composite focal mechanism techniques for identifying seismologically active zones in Syria, *Acta Geophysica*, *59*, 26.

Abu-Hamatteh, Z. S. H., K. Al-Zughoul, and S. Al-Jufout (2011), Potential geothermal energy utilization in Jordan: Possible electrical power generation, *International Journal of Thermal and Environment Engineering*, *3*, 9-14.

Adams, M. C., J. N. Moore, S. Bjornstad, and D. I. Norman (2000), Geologic history of the Coso geothermal system, *Geothermal Resources Council Transactions*, *24*, 205-209.

Aki, K., and W. H. K. Lee (1976), Determination of three-dimensional velocity anomalies under a seismic array using first P arrival times from local earthquakes, *Journal of Geophysical Research*, *81*, 4381-4399.

Aki, K., A. Christoffersson, and E. Husebye (1976), Determination of the three-dimensional seismic structure of the lithosphere, *Journal of Geophysical Research*, *82*, 277-296.

Ambraseys, N. N., and M. Barazangi (1989), The 1759 earthquake in the Bekaa Valley: Implications for earthquake hazard assessment in the eastern Mediterranean region, *Journal of Geophysical Research*, *94*, 7.

Bacon, C. R. (1982), Time-predictable bimodal volcanism in the Coso range, California., *Geology*, *10*, 65-69.

Bacon, C. R., and J. Metz (1984), Magmatic inclusions in rhyolites, contaminated basalts, and compositional zonation beneath the Coso volcanic field, California, *Contributions to Mineralogy and Petrology*, *85*, 346– 365.

Bailey, R. (1989), Geologic map of Long Valley caldera, Mono-Inyo Craters volcanic chain, and vicinity, Eastern California, IMAP-1933, U.S. Geological Survey.

Bailey, R., G. D. Dalrymple, and M. A. Lanphere (1976), Volcanism, structure, and geochronology of Long Valley Caldera, Mono County, California, *Journal of Geophysical Research*, *81*, 725-744.

Barker, B. J., M. S. Gulati, M. A. Bryan, and K. L. Riedel (1992), Geysers reservoir performance, in *Monograph on The Geysers Geothermal Field*, edited by C. Stone, pp. 167-177, Geothermal Resources Council, Davis, California.

Barmin, M. P., M. H. Ritzwoller, and A. L. Levshin (2001), A fast and reliable method of surface wave tomography, *Pure and Applied Geophysics*, *158*, 1351-1375.

Battaglia, M., C. Robert, and P. Segall (1999), Magma intrusion beneath Long Valley caldera confirmed by temporal changes in gravity, *Science*, *285*, 2119-2122.

Bhattacharyya, J., and J. M. Lees (2002), Seismicity and seismic stress in the Coso Range, Coso geothermal field, and Indian Wells Valley region, southeast-central California, *Geological Society of America*, *195*, 243-257.

Bilal, A. (2009), Seismicity and volcanism in the rifted zone of western Syria, *Comptes Rendus Geoscience 341*, 299-305.

Combs, J. (1980), Heat-flow in the Coso geothermal area, Inyo County, California, *Journal of Geophysical Research*, *85*, 2411-2424.

Crosson, R. A. (1976), Crustal structure modeling of earthquake data. 1. Simultaneous least square estimation of hypocenter and velocity parameters, *Journal of Geophysical Research*, *81*, 3036-3046.

Dakkak, R., M. Daoud, M. Mreish, and G. Hade (2005), The Syrian national seismological network (SNSN): Monitoring a major continental transform fault, *Seismological Research Letters*, *76*, 10.

Daley, T. M., L. R. Myer, J. E. Peterson, E. L. Majer, and G. M. Hoversten (2007), Time-lapse crosswell seismic and VSP monitoring for injected CO_2 in a brine aquifer, *Environmental Geology*, *54*, 1657-1665.

Davatzes, N., and S. Hickman (2005), Comparison of acoustic and electrical image logs from the Coso geothermal field, California, paper presented at Thirtieth Workshop on Geothermal Reservoir Engineering, Stanford University, Stanford, California, 31 January - 2 February.

Davatzes, N., and S. Hickman (2006), Stress and faulting in the Coso geothermal field: Update and recent results from the East Flank and Coso Wash, paper presented at Thirty-first Workshop on Geothermal Reservoir Engineering, Stanford University, Stanford, California, January 30-February 1.

Davatzes, N., and S. Hickman (2010), The feedback between stress, faulting, and fluid flow: Lessons from the Coso geothermal field, California, USA, paper presented at World Geothermal Congress 2010, Bali, Indonesia, 25-29 April.

Dawson, P. B., J. R. Evans, and H. M. Iyer (1990), Teleseismic tomography of the compressional-wave velocity structure beneath the Long Valley region, California, *Journal of Geophysical Research*, *95*, 11021-11050.

Dreger, D. S., H. Tkalcic, and M. Johnston (2000), Dilational processes accompanying earthquakes in the Long Valley caldera, *Science*, *288*, 122-125.

Duffield, W. (1975), Late Cenozoic ring faulting and volcanism in the Coso Range of California, *Geology*, *3*, 335-338.

Duffield, W., C. Bacon, and G. Dalrymple (1980), Late Cenozoic volcanism, geochronology, and structure of the Coso Range, Inyo County, California, *Journal of Geophysical Research*, *85*, 2381-2404.

Eberhart-Phillips, D. (1993), Local earthquake tomography: Earthquake source regions, in *Seismic Tomography: Theory and Practice*, edited by H. M. Iyer and K. Hirahara, pp. 613-643, Chapman and Hall.

Ekström, G., and A. M. Dziewonski (1983), Evidence for source complexities of 1980 Mammoth Lakes earthquakes (abstract), *EOS Trans. AGU*, *64*.

Evans, J. R., and U. Achauer (1993), Teleseismic velocity tomography using the ACH method: theory and application to continental-scale studies, in *Seismic Tomography: Theory and Applications*, edited by H. M. Iyer and K. Hirahara, pp. 319-360, Chapman and Hall, London.

Evans, J. R., D. Eberhart-Phillips, and C. H. Thurber (1994), User's manual for *simulps12* for imaging V_P and V_P/V_S, a derivative of the Thurber tomographic inversion *simul3* for local earthquakes and explosions, U.S. Geological Survey Open-File Report, 94-431, 142 pp.

Farrar, C. D., M. L. Sorey, W. C. Evans, J. F. Howle, B. D. Kerr, B. M. Kennedy, C.-Y. King, and J. R. Southon (1995), Forest-killing diffuse CO_2 emission at Mammoth Mountain as a sign of magmatic unrest, *Nature*, *376*, 675-678.

Feng, Q., and J. M. Lees (1998), Microseismicity, stress, and fracture in the Coso geothermal field, California, *Tectonophysics*, *289*, 221-238.

Fialko, Y., and M. Simons (2000), Deformation and seismicity in the Coso geothermal area, Inyo County, California: Observations and modeling using satellite radar interferometry, *Journal of Geophysical Research*, *105*, 21781-21793.

Fink, J. H. (1985), The geometry of silicic dikes beneath the Inyo domes, California, *Journal of Geophysical Research*, *90*, 11127-11133.

Foulger, G. R. (2007), Report to the US Geological Survey on time-dependent seismic tomography of the Coso geothermal area, Inyo County, CA covering the years 1996-2006, Technical Report to the US Geological Survey, pp iv + 119, 6th March, 2007.

Foulger, G. R., and D. R. Toomey (1989), Structure and evolution of the Hengill-Grensdalur volcanic complex, Iceland: Geology, geophysics, and seismic tomography, *Journal of Geophysical Research*, *94*, 17511-17522.

Foulger, G. R., B. R. Julian, and F. C. Monastero (2007), Time-dependent seismic tomography of the Coso geothermal area, 1996-2006, paper presented at AGU Fall Meeting, American Geophysical Union, San Francisco.

Foulger, G. R., C. C. Grant, A. Ross, and B. R. Julian (1997), Industrially induced changes in Earth structure at The Geysers geothermal area, California, *Geophysical Research Letters*, *24*, 135-137.

Foulger, G. R., P. E. Malin, E. Shalev, B. R. Julian, and D. P. Hill (1998a), Seismic monitoring and activity increase in California caldera, *EOS*, *79*, 357-363.

Foulger, G. R., B. R. Julian, A. M. Pitt, D. P. Hill, P. Malin, and E. Shalev (2003), Three-dimensional crustal structure of Long Valley caldera, California, and evidence for the migration of CO_2 under Mammoth Mountain, *Journal of Geophysical Research*, *108*, 2147-2163.

Foulger, G. R., B. R. Julian, D. P. Hill, A. M. Pitt, P. Malin, and E. Shalev (2004), Non-double-couple microearthquakes at Long Valley caldera, California, provide evidence for hydraulic fracturing, *Journal of Volcanology and Geothermal Research*, *132*, 45-71.

Foulger, G. R., B. R. Julian, D. P. Hill, G. Sharer, L. E. Foulger, R. Perlroth, N. Dotson, A. M. Pitt, and E. Brodsky (1998b), A microearthquake survey of the Mammoth Mountain area, Long Valley caldera, California, summer 1997, U.S. Geological Survey Open-File Report, 98-236, 63 pp.

Fournier, R. O., J. M. Thompson, and C. F. Austin (1980), Interpretaion of chemical-analysis of water collected from 2 geothermal wells at Coso, California, *Journal of Geophysical Research*, *85*, 2405-2410.

Gerlach, T. M., M. P. Doukas, K. A. McGee, and R. Kessler (1998), Three-year decline of magmatic CO_2 emissions from soils of a Mammoth Mountain tree kill: Horseshoe Lake, CA, 1995-1997, *Geophysical Research Letters*, *25*, 1947-1950.

Given, J. W., T. C. Wallace, and H. Kanamori (1982), Teleseismic analysis of the 1980 Mammoth Lakes earthquake sequence, *Bulletin of the Seismological Society of America*, *72*, 1093-1109.

Gunasekera, R. C., G. R. Foulger, and B. R. Julian (2003), Reservoir depletion at The Geysers geothermal area, California, shown by four-dimensional seismic tomography, *Journal of Geophysical Research*, *108*, 11.

Gutierrez, M., D. Katsuki, and A. Almrabat (2012), Effects of CO_2 injuction on the seismic velocity of sandstone saturated with saline water, *International Journal of Geosciences*, *3*, 908-917.

Hauksson, E., and J. Unruh (2007), Regional tectonics of the Coso geothermal area along the intracontinental plate boundary in central eastern California: Three-dimensional V_p and V_p/V_s models, spatial-temporal seismicity patterns, and seismogenic deformation, *Journal of Geophysical Research*, *112*, 24.

Hauksson, E., K. Hutton, H. Kanamori, L. Jones, J. Mori, S. Hough, and G. Roquemore (1995), Preliminary report on the 1995 Ridgecrest earthquake sequence in eastern California, Institute of Technology, 54-60 pp, California.

Hill, D. P. (1996), Earthquakes and carbon dioxide beneath Mammoth Mountain, California, *Seismological Research Letters*, *67*, 8-15.

Hill, D. P. (2006), Unrest in Long Valley caldera, California, 1978-2004, *Geological Society Special Publications*, *269*, 1-24.

Hill, D. P., R. A. Bailey, and A. S. Ryall (1985), Active tectonic and magmatic processes beneath Long Valley caldera, eastern California: An overview, *Journal of Geophysical Research*, *90*, 11111-11120.

Hill, D. P., J. H. Kissling, J. H. Luetgert, and U. Kradolver (1985), Constraints on the upper crustal structure of the Long Valley – Mono craters volcanic complex, eastern California, from seismic refraction measurements, *Journal of Geophysical Research*, *90*, 11135-11150.

Hill, D. P., M. J. Johnston, J. O. Langbein, and R. Bilham (1995), Response of Long Valley caldera to the Mw = 7.3 Landers, California, earthquake, *Journal of Geophysical Research*, *100*, 12985-13005.

Hill, D. P., W. L. Ellsworth, M. S. Johnston, J. O. Langbein, D. H. Oppenheimer, A. M. Pitt, P. A. Reasenberg, M. L. Sorey, and S. R. McNutt (1990), The 1989 earthquake swarm beneath Mammoth Mountain, California: An initial look at the 4 May through 30 September activity, *Bulletin of the Seismological Society of America*, *80*, 325-339.

Hoversten, G. M., R. Gritto, J. Washbourne, and T. M. Daley (2003), Pressure and fluid saturation prediction in a multicomponent reservoir, using combined seismic and electromagnetic imaging, *Geophysics*, *68*, 1580-1591.

Hulen, J. B. (1978), Geology and alteration of the Coso geothermal area, Inyo County, California, U. S. Department of Energy, Division of Geothermal Energy, 31 pp.

International Business Puplications, Washington, DC (2015), *Syria Energy Policy, Laws and Regulations Handbook*, 262 pp., International Business Puplications, USA.

Iyer, H. M., and K. Hirahara (Eds.) (1993), *Seismic tomography: theory and practice*, 848 pp., Chapman & Hall, London.

Julian, B. R. (1983), Evidence for dyke intrusion earthquake mechanisms near Long Valley caldera, California, *Nature*, *303*, 323-325.

Julian, B. R. (1986), Analysing seismic-source mechanisms by linear-programming methods, *Geophysical Journal of the Royal Astronomical Society*, *84*, 431-443.

Julian, B. R., and D. Gubbins (1977), Three-dimensional seismic ray tracing, *Journal of Geophysics*, *43*, 95-113.

Julian, B. R., and S. A. Sipkin (1985), Earthquake processes in the Long Valley caldera area, California, *Journal of Geophysical Research*, *90*, 11155-11169.

Julian, B. R., and G. R. Foulger (1996), Earthquake mechanisms from linear-programming inversion of seismic-wave amplitude ratios, *Bulletin of the Seismological Society of America*, *86*(4), 972-980.

Julian, B. R., and G. R. Foulger (2010), Time-dependent seismic tomography, *Geophysical Journal International*, *182*, 1327–1338.

Julian, B. R., A. M. Pitt, and G. R. Foulger (1998), Seismic image of a CO_2 reservoir beneath a seismically active volcano, *Geophysical Journal International*, *133*, 7-10.

Julian, B. R., G. R. Foulger, and K. Richards-Dinger (2004), The Coso geothermal area: A laboratory for advanced MEQ studies for geothermal monitoring, paper presented at Geothermal Resources Council Annual Meeting, Geothermal Resources Council, Palm Springs, August 2004.

Julian, B. R., G. R. Foulger, and F. Monastero (2007), Microearthquake moment tensors from the Coso geothermal area, paper presented at Thirty-Second Workshop

on Geothermal Reservoir Engineering, Stanford University, Stanford, California, 22-24 January.

Julian, B. R., G. R. Foulger, and F. Monastero (2008), Time-dependent seismic tomography and its application to the Coso geothermal area, 1996-2006, paper presented at Thirty-Third Workshop on Geothermal Reservoir Engineering, Stanford University, Stanford, California, 28-30 January.

Julian, B. R., G. R. Foulger, and F. Monastero (2009), Seismic monitoring of EGS stimulation tests at the Coso geothermal field, California, using microearthquake locations and moment tensors, paper presented at Thirty-Fourth Workshop on Geothermal Reservoir Engineering, Stanford University, Stanford, California, 9-11 February.

Julian, B. R., A. Ross, G. R. Foulger, and J. R. Evans (1996), Three-dimensional seismic image of a geothermal reservoir: The Geysers, California, *Geophysical Research Letters*, *23*, 685-688.

Julian, B. R., J. R. Evans, M. J. Pritchard, and G. R. Foulger (2000), A geometrical error in some versions of the ACH method of teleseismic tomography, *Bulletin of the Seismological Society of America*, *90*, 1554-1558.

Julian, B. R., G. R. Foulger, K. Richards-Dinger, and F. Monastero (2006), Time-dependent seismic tomography of the Coso geothermal area, 1996-2004, paper presented at Thirty-First Workshop on Geothermal Reservoir Engineering, Stanford University, Stanford, California, 30 January - 1 February.

Julian, B. R., G. R. Foulger, F. C. Monastero, and S. Bjornstad (2010), Imaging hydraulic fractures in a geothermal reservoir, *Geophysical Research Letters*, *37*, 5.

Kaven, J. O., S. H. Hickman, and N. C. Davatzes (2011), Micro-seismicity, fault structure, and hydraulic compartmentalization within the Coso geothermal field, California, paper presented at Thirty-Sixth Workshop on Geothermal Reservoir Engineering, Stanford University, Stanford, California, 31 January - 2 February.

Kaven, J. O., S. H. Hickman, and N. C. Davatzes (2013), Micro-seismicity within the Coso geothrmal field, California, from 1996-2012, paper presented at Thirty-Eighth Workshop on Geothermal Reservoir Engineering, Stanford University, Stanford, California.

Kaygusuz, K., and A. Kaygusuz (2004), Geothermal energy in Turkey: the sustainable future, *Renewable and Sustainable Energy Reviews*, *8*, 545-563.

Kern, H., and J. M. Tubia (1993), Pressure and temperature dependence of *P*- and *S*-wave velocities, seismic anisotropy and density of sheared rocks from the Sierra Alpujata massif (Ronda peridotites, Southern Spain) *Earth and Planetary Science Letters*, *119*, 191-205.

Khatiwada, M., L. Adam, M. Morrison, and K. Wijk (2012), A feasibility study of time-lapse seismic monitoring of CO_2 sequestration in a layered basalt reservoir, *Journal of Applied Geophysics*, *82*, 145-152.

Kissling, E., W. L. Ellsworth, D. Eberhart-Phillips, and U. Kradolfer (1994), Initial reference models in local earthquake tomography, *Journal of Geophysical Research*, *99*, 19635-19646.

Langbein, J., D. Hill, T. Parker, and S. Wilkinson (1993), An episode of reinflation of the Long Valley caldera, eastern California: 1989–1991, *Journal of Geophysical Research*, *98*, 15851-15870.

Langbein, J., D. Dzurisin, G. Marshall, R. Stein, and J. Rundle (1995), Shallow and peripheral volcanic sources of inflation revealed by modeling two-color geodimeter and leveling data from Long Valley caldera, California, *Journal of Geophysical Research*, *100*, 12487-12495.

Lees, J. M., and R. S. Crosson (1989), Tomographic inversion for three-dimensional velocity structure at Mount St. Helens using earthquake data, *Journal of Geophysical Research*, *94*, 5716-5728.

Lewicki, J. L., G. E. Hilley, D. R. Shelly, J. C. King, J. P. McGeehin, and M. Mangan (2014), Crustal migration of CO_2-rich magmatic fluids recorded by tree-ring radiocarbon and seismicity at Mammoth Mountain, CA, USA, *Earth and Planetary Science Letters*, *390*, 52-58.

Lin, G. (2015), Seismic velocity structure and earthquake relocation for the magmatic system beneath Long Valley caldera, eatern California, *Journal of Volcanology and Geothermal Research*, *296*, 19-30.

Lin, G., F. Amelung, P. M. Shearer, and P. G. Okubo (2015), Location and size of the shallow magma reservoir beneath Kilauea caldera, constraints from near-source V_p/V_s ratios, *Geophysical Research Letters*, *42*, 8349-8357.

Mavko, G. (1980), Velocity and attenuation in partially molten rocks, *Journal of Geophysical Research*, *85*, 5173-5189.

Mavko, G. (2000), Introduction to rock physics course notes, https://pangea.stanford.edu/courses/gp262/Notes/8.SeismicVelocity.pdf.

Mavko, G., and T. Mukerji (1995), Seismic pore space compressibility and Gassman's relation, *Geophysics*, *60*, 1743-1749.

Mavko, G., C. Chan, and T. Mukerji (1995), Fluid substitution: Estimating changes in V_p without knowing V_s, *Geophysics*, *60*, 1750-1755.

McConnell, J. S., C. K. Shearer, J. C. Eichelberger, M. J. Keskinson, P. W. Layer, and J. J. Papike (1995), Rhyolite intrusions in the intracaldera Bishop Tuff, Long Valley caldera, California, *Journal of Volcanology and Geothermal Research*, *67*, 41-60.

Menke, W. (1989), *Geophysical data analysis: Discrete inverse theory*, Academic Press, San Diego, California.

Miller, A. D., B. R. Julian, and G. R. Foulger (1998), Three-dimensional seismic structure and moment tensors of non-double-couple earthquakes at the Hengill-Grensdalur volcanic complex, Iceland, *Geophysical Journal International*, *133*, 309-325.

Miller, C. D. (1985), Holocene eruptions at the Inyo Craters volcanic chain, California: Implications for possible eruptions in Long Valley caldera, *Geology*, *13*, 14-17.

Miller, M. M., D. J. Johnson, T. H. Dixon, and R. K. Dokka (2001), Refined kinematics of the eastern California shear zone from GPS observations, 1993-1998, *Journal of Geophysical Research*, *106*, 2245-2264.

Mohamad, R., A. N. Darkal, D. Seber, E. Sandvol, F. Gomez, and M. Barazangi (2000), Remote earthquake trigging along the Dead Sea fault in Syria following the 1995 Gulf of Aqapa earthquake (M_s=7.3), *Seismological Research Letters*, *71*, 47-52.

Monastero, F. C., A. M. Katzenstein, J. S. Miller, J. R. Unruh, M. C. Adams, and K. Richards-Dinger (2005), The Coso geothermal field: A nascent metamorphic core complex, *Bulletin of the Geological Society of America*, *117*, 1534-1553.

Moos, D., and M. D. Zoback (1983), In situ studies of velocity in fractured crystalline rocks, *Journal of Geophysical Research*, *88*, 2345-2358.

Mordick, B. E., and A. F. Glazner (2006), Clinopyroxene thermobarometry of basalts from the Coso and Big Pine volcanic fields, California, *Contributions to Mineralogy and Petrology*, *152*, 111-124.

Nakanishi, I. (1985), Three-dimensional structure beneath the Hokkaido-Tohoku region as derived from a tomographic inversion of *P*-arrival times, *Journal of the Physics of the Earth*, *33*, 241-256.

Nixon, L. (1992), S wave attenuation structure of Long Valley caldera, California, using three-component S/P amplitude ratio data, M.S. thesis, 106 pp, Arizona State University.

Nur, A., and G. Simmons (1969), Stress-induced velocity anisotropy in rock: an experimental study, *Journal of Geophysical Research*, *74*, 6667-6674.

Paige, C. C., and M. A. Saunders (1982), LSQR: An algorithm for sparse linear equations and sparse least squares, *Transaction on Mathematical Software*, 8, 43-71.

Pitt, A. M., and D. P. Hill (1994), Long-period earthquakes in the Long Valley caldera region, eastern California, *Geophysical Research Letters*, *21*, 1679-1682.

Ponko, S., and C. Sanders (1994), Inversion for P and S wave differential attenuation structure, Long Valley caldera, California, *Journal of Geophysical Research*, *99*, 2619-2635.

Porkhial, S., and P. Yousefi (2015), Geothermal energy in Iran, paper presented at World Geothermal Congress 2015, Melbourne, Australia, 19-25 April 2015.

Press, W. H., S. A. Teukolsky, W. T. Vetterling, and B. P. Flannery (2007), *Numerical Recipes - The Art of Scientific Computing*, 3rd ed., 1235 pp., Cambridge University Press, Cambridge.

Rahn, T. A., J. E. Fessenden, and M. Wahlen (1996), Flux chamber measurements of anomalous CO_2 emission from the flanks of Mammoth Mountain, California, *Geophysical Research Letters*, *23*, 1861-1864.

Reasenberg, P. A., W. L. Ellsworth, and A. W. Walter (1980), Teleseismic evidence for a low-velocity body under the Coso geothermal area, *Journal of Geophysical Research*, *85*, 2471-2483.

Roquemore, G. (1980), Structure, tectonics, and stress field of the Coso Range, Inyo County, California, *Journal of Geophysical Research*, *85*, 2434-2440.

Rose, P., J. McCulloch, M. Adams, and M. Mella (2005), An EGS stimulation experiment under low wellhead pressures, paper presented at Thirtieth Workshop on Geothermal Reservoir Engineering, Stanford University, Stanford, California, 31-January - 2 February.

Ross, A. (1996), The Geysers geothermal area, California: Tomographic images of the depleted steam reservoir and non-double-couple earthquakes, Ph.D. thesis, 240 pp, Durham, U.K.

Ross, A., G. R. Foulger, and B. R. Julian (1999), Source processes of industrially-induced earthquakes at The Geysers geothermal area, California, *Geophysics*, *64*, 1877-1889.

Rundle, J. B., and D. P. Hill (1988), The geophysics of a restless caldera – Long Valley, California, *Annual Review of Earth and Planetary Sciences*, *16*, 251-271.

Sackett, P. C., V. S. McConnell, A. L. Roach, S. S. Priest, and J. H. Sass (1999), Long Valley coring project, Inyo County, California, 1998 - preliminary stratigraphy and images of recovered core, U.S. Geological Survey Open-File Report 99-158.

Sanders, C. (1993), Reanalysis of S to P amplitude ratios for gross attenuation structure, Long Valley caldera, California, *Journal of Geophysical Research*, *98*, 22069-22080.

Sanders, C., and L. Nixon (1995), S wave attenuation structure in Long Valley caldera, California, from three-component S to P amplitude ratio data, *Journal of Geophysical Research*, *100*, 12395-12404.

Sanders, C., S. C. Ponko, L. D. Nixon, and E. A. Schwartz (1995), Seismological evidence for magmatic and hydrothermal structure in Long Valley caldera from local earthquake attenuation and velocity tomography, *Journal of Geophysical Research*, *100*, 8311-8326.

Savage, J. C., and M. M. Clark (1982), Magmatic resurgence in Long Valley caldera, California: Possible cause of the 1980 Mammoth Lakes earthquakes, *Science*, *217*, 531-533.

Savage, J. C., and R. S. Cockerham (1984), Earthquake swarm in Long Valley caldera, California, January 1983: Evidence for dike inflation, *Journal of Geophysical Research*, *89*, 8315-8324.

Schoenball, M., J. O. Kaven, J. M. G. Glen, and N. C. Davatzes (2015), Natural or induced: Identifying natural and induced swarms from pre-production and co-production microseismic catalogs at the Coso geothermal field, paper presented at Thirty-Ninth Workshop on Geothermal Reservoir Engineering, Stanford University, Stanford, California, 26-28 January.

Schwartz, E. A. (1993), Three-dimensional variations in the compersional to shear wave velocity ratio for Long Valley caldera, California, M.S. thesis, 118 pp, Arizona State University.

Seccia, D., C. Chiarabba, P. De Gori, and D. P. Hill (2011), Evidence for the contemporary magmatic system beneath Long Valley caldera from local earthquake tomography and receiver function analysis, *Journal of Geophysical Research*, *116*, 22.

Sheridan, J., and S. Hickman (2004), In situ stress, fracture and fluid flow analysis in well 38C-9: An enhanced geothermal system in the Coso geothermal field, paper presented at Twenty-ninth Workshop on Geothermal Reservoir Engineering, Stanford University, Stanford, California, 26-28 January.

Sheridan, J., K. Kovac, P. Rose, C. Barton, J. McCulloch, B. Berard, J. Moore, S. Petty, and P. Spielman (2003), In situ stress, fracture and fluid flow analysis - east flank of the Coso geothermal field, paper presented at Twenty-eighth Workshop on Geothermal Reservoir Engineering, Stanford University, Stanford, California, 27-29 January.

Simakin, A. G., and A. Ghassemi (2007), The mechanics of a magma chamber-fault system in trans-tension with application to Coso, *Journal of Structural Geology*, *29*, 1971-1983.

Simiyu, S. M. (1999), Seismic velocity analysis in the Olkaria geothermal field, paper presented at Twenty-Fourth Workshop on Geothermal Reservoir Engineering, Stanford University, Stanford, California, 25 - 27 January.

Sorey, M. L. (1985), Evolution and present state of the hydrothermal system in Long Valley caldera, *Journal of Geophysical Research*, *90*, 11219-11228.

Sorey, M. L., B. M. Kennedy, W. C. Evans, C. D. Farrar, and G. A. Suemnicht (1993), Helium isotope and gas discharge variations associated with crustal unrest in Long Valley caldera, California, 1989-1992, *Journal of Geophysical Research*, *98*, 15871-15889.

Sorey, M. L., W. C. Evans, B. M. Kennedy, C. D. Farrar, L. J. Hainsworth, and B. Hausback (1998), Carbon dioxide and helium emissions from a reservoir of magmatic gas beneath Mammoth Mountain, California, *Journal of Geophysical Research*, *103*, 15303-15323.

Spencer, C., and D. Gubbins (1980), Travel-time inversion for simultaneous earthquake location and velocity structure determination in laterally varying media, *Geophysical Journal International*, *63*, 95-116.

Stark, M. A., W. Tom Box Jr, J. J. Beall, K. P. Goyal, and A. S. Pingol (2005), The Santa Rosa -- Geysers recharge project, Geysers geothermal field, California, USA, paper presented at World Geothermal Congress 2005, Antalya, Turkey, 24-29 April.

Stevens, C. H., P. Stone, and R. J. Blakely (2013), Structural evolution of the East Sierra Valley System (Owens Valley and vicinity), California: A geologic and geophysical synthesis, *Geosciences*, *3*, 176-215.

Stevens, J. L., J. W. Pritchett, G. S.K., K. Ariki, S. Nakanishi, and S. Yamazawa (2000), Seismic methods for observing geothermal field evolution, paper presented at World Geothermal Congress 2000, Tohoku, Japan, 28 May - 10 June.

Swarieh, A. (2000), Geothermal energy resources in Jordan, country update report, paper presented at World Geothermal Congress 2000, Kyushu, Tohoku, Japan, 28 May - 10 June.

Thurber, C. H. (1981), Earth structure and earthquake locations in the Coyote Lake area, central California, Ph.D. thesis, 332 pp, Massachusetts Institute of Technology, Cambridge, Mass.

Thurber, C. H. (1983), Earthquake locations and three-dimensional crustal structure in the Coyote Lake area, central California, *Journal of Geophysical Research*, *88*, 8226-8236.

Thurber, C. H. (1993), Local earthquake tomography: velocities and V_p/V_s - Theory, in *Seismic Tomography: Theory and Practice*, edited by H. M. Iyer and K. Hirahara, pp. 563-583, Chapman and Hall, London.

Thurber, C. H., and W. L. Ellsworth (1980), Rapid solution of ray tracing problem in heterogeneous media, *Bulletin of the Seismological Society of America*, *70*, 1137-1148.

Tizzani, P., P. Berardino, F. Casu, P. Euillades, M. Manzo, G. P. Ricciardi, G. Zeni, and R. Lanari (2007), Surface deformation of Long Valley caldera and Mono Basin, California, investigated with SBAS-InSAR approach, *Remote Sensing of Environment*, *108*, 277-289.

Toksoz, M. N., C. H. Cheng, and A. Timur (1976), Velocities of seismic waves in porous rocks, *Geophysics*, *41*, 621-645.

Toomey, D. R., and G. R. Foulger (1989), Tomographic inversion of local earthquake data from the Hengill-Grensdalur central volcano complex, Iceland, *Journal of Geophysical Research*, *94*, 17497-17510.

Um, J., and C. H. Thurber (1987), A fast algorithm for two-point seismic ray tracing, *Bulletin of the Seismological Society of America*, *77*, 792-786.

Unruh, J., and A. Streig (2004), Mapping and characterization of neotectonic structures in a releasing stepover, northern Coso Range, eastern California: Final technical report, U.S. Navy Geothermal Program Office, China Lake Naval Air Warfare Center, 46 pp.

Unruh, J., A. Streig, and S. Sundermann (2003), Mapping and characterization of neotectonic structures in a releasing stepover, northern Coso Range, eastern California, paper presented at The eighth Annual Technical Symposium, U.S. Navy Geothermal Program Office, University of CA-Davis, Monastero, F (Ed), 29-30 May.

Vlahovic, G., M. Elkibbi, and J. A. Rial (2002), Shear-wave splitting and reservoir crack characterization: the Coso geothermal field, *Journal of Volcanology and Geothermal Research*, *120*, 123-140.

Walck, M. C. (1988), Three-dimensional V_p/V_s variations for the Coso Region, California, *Journal of Geophysical Research*, *93*, 2047-2052.

Walck, M. C., and R. W. Clayton (1987), *P*-wave velocity variations in the Coso Region, California, derived from local earthquake travel times, *Journal of Geophysical Research*, *92*, 393-405.

Waldhauser, F., and W. L. Ellsworth (2000), A double-difference earthquake location algorithm: Method and application to the northern Hayward Fault, California, *Bulletin of the Geological Society of America*, *90*, 1353-1368.

Walter, A. W., and C. S. Weaver (1980), Seismicity of the Coso range, California, *Journal of Geophysical Research*, *85*, 2441-2458.

Wamalwa, A. M., K. L. Mickus, L. F. Serpa, and D. I. Doser (2013), A joint geophysical analysis of the Coso geothermal field, south-eastern California, *Physics of the Earth and Planetary Interiors*, *214*, 25-34.

Wang, Z., and A. M. Nur (1989), Effects of CO_2 flooding on wave velocities in rocks with hydrocarbons, *Society of Petroleum Engineers Reservoir Engineering*, *3*, 429-436.

Wang, Z., M. L. Batzle, and A. M. Nur (1990), Effect of different pore fluids on seismic velocities in rocks, *Canadian Jounrnal of Exploration Geophysics*, *26*, 104-112.

Wang, Z., M. E. Cates, and R. T. Langen (1998), Seismic monitoring of CO_2 flooding of a carbonate reservoir: a rock physics study, *Geophysics*, *63*, 1604-1617.

Weiland, C. M., L. K. Steck, P. B. Dawson, and V. A. Korneev (1995), Nonlinear teleseismic tomography at Long Vallley caldera, using three-dimensional minimum travel time ray tracing, *Journal of Geophysical Research*, *100*, 20379-20390.

Werner, C., D. Bergfeld, C. D. Farrar, M. P. Doukas, P. J. Kelly, and C. Kern (2014), Decadal-scale variability of diffuse CO_2 emissions and seismicity revealed from long-term monitoring (1995-2013) at Mammoth Mountain, California, USA, *Journal of Volcanology and Geothermal Research*, *289*, 51-63.

Wesson, R. L. (1971), Travel-time inversion for laterally inhomogeneous crustal velocity models, *Bulletin of the Seismological Society of America*, *61*, 729-746.

Whitmarsh, R. S. (1998), Geologic map of the Coso Range, IMAP-1130, Geological Society of America on-line map, *Department of Geology, University of Kansas, USA*.

Wicks, C., W. Thatcher, F. Monastero, and M. Hasting (2001), Steady-state deformation of the Coso Range, east-central California, inferred from satellite radar interferometry, *Journal of Geophysical Research*, *106*, 13769-13780.

Wilson, C. K., C. H. Jones, and H. J. Gilbert (2003), Single-chamber silicic magma system inferred from shear wave discontinuities of the crust and uppermost mantle, Coso geothermal area, California, *Journal of Geophysical Research*, *108*, 148-227.

Wu, H. T., and J. M. Lees (1999), Three-dimensional P and S wave velocity structures of the Coso geothermal area, California, from microseismic travel time data, *Journal of Geophysical Research*, *104*, 13217-13233.

Yang, Y., M. H. Ritzwoller, and C. H. Jones (2011), Crustal structure determined from ambient noise tomography near the magmatic centers of the Coso region, southeastern California, *Geochemistry Geophysics Geosystems*, *12*, 20.

Zucca, J. J., L. J. Hutchings, and P. W. Kasameyer (1994), Seismic velocity and attenuation structure of the Geysers geothermal field, California, *Geothermics*, *23*, 111-126.

APPENDICES

Appendix 1: Seismicity maps of Long Valley caldera and vicinity for the years 1983 through 2014. Mammoth Mountain and the Inyo Domes are shown in light grey. Resurgent dome is bounded by thin grey line. Thick line is topographic margin of caldera; thin grey lines are faults; coloured dots are epicenters of the earthquakes. The grid is the tomography inversion grid used by *Foulger et al.* [2003] and in this thesis. Red squares are the seismometer stations. Blue region at right is Crowley Lake.

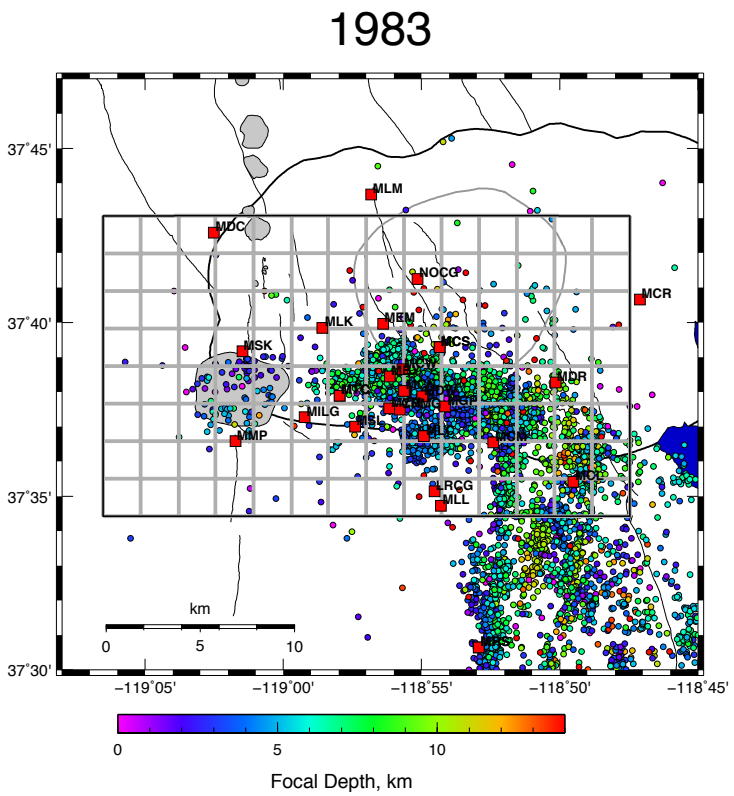

1984

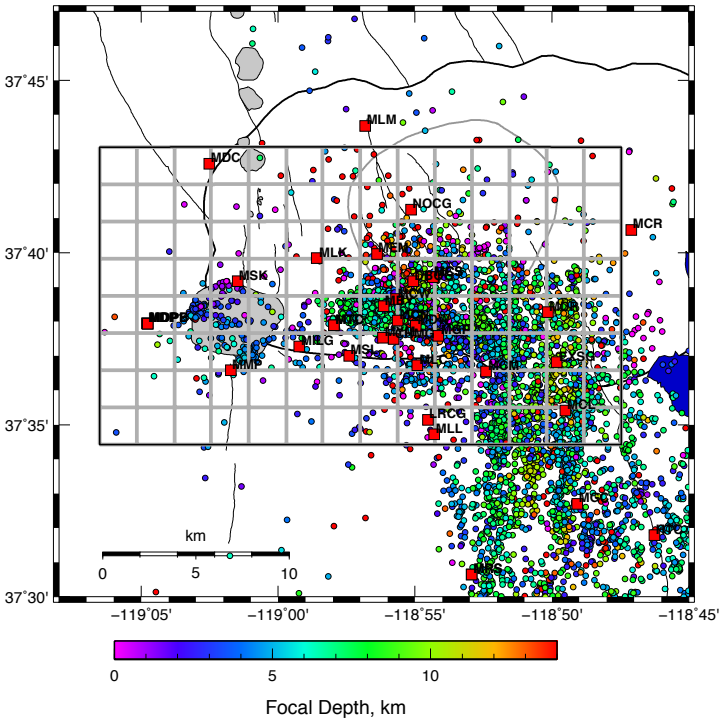
37°45'
37°40'
37°35'
37°30'
−119°05'
−119°00'
−118°55'
−118°50'
−118°45'
MLM
MDC
NCCG
MCR
MLK
MEM
MSK
MDPB
MILG
MSL
MMP
RCG
MLL
km
0
5
10
0
5
10
Focal Depth, km

1985

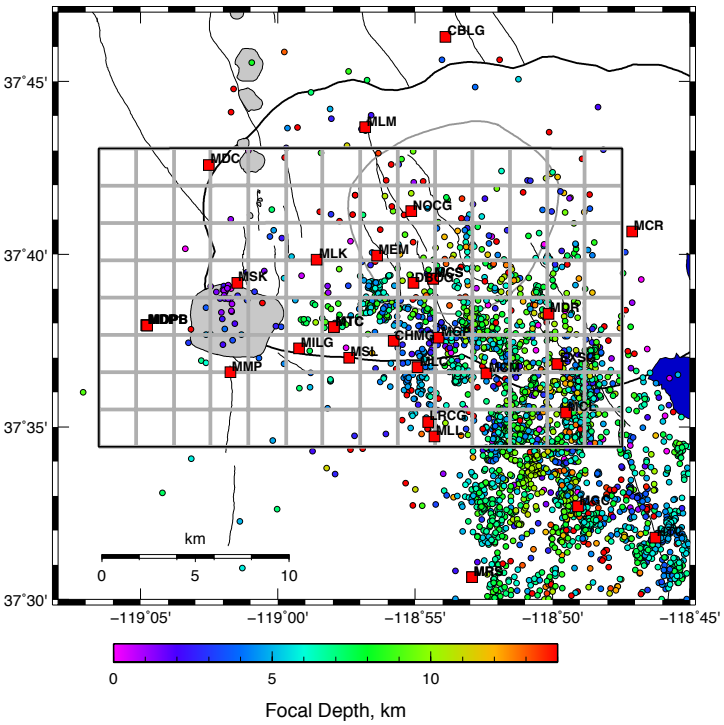
CBLG
37°45'
37°40'
37°35'
37°30'
−119°05'
−119°00'
−118°55'
−118°50'
−118°45'
MLM
MDC
NCCG
MCR
MLK
MEM
MSK
MDPB
MTC
CHMG
MILG
MSL
MMP
RCG
MLL
km
0
5
10
0
5
10
Focal Depth, km

1986

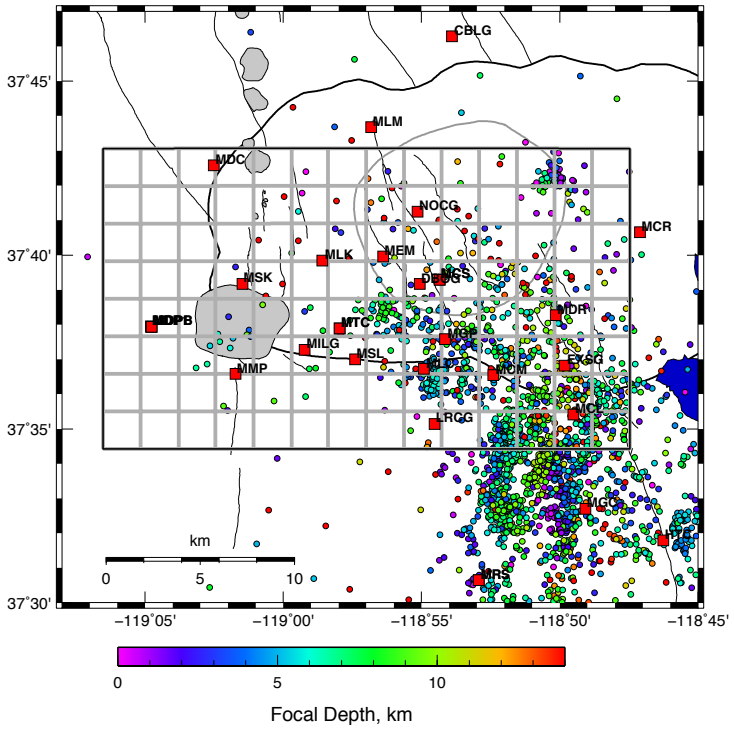
CBLG
MLM
MDC
NOCG
MCR
MLK
MEM
MSK
MDR
MDPB
MTC
MILG
MSL
MMP
FXSG
LRCG
MCL
MRS
km
0
5
10
37°45'
37°40'
37°35'
37°30'
−119°05'
−119°00'
−118°55'
−118°50'
−118°45'
0
5
10
Focal Depth, km

1987

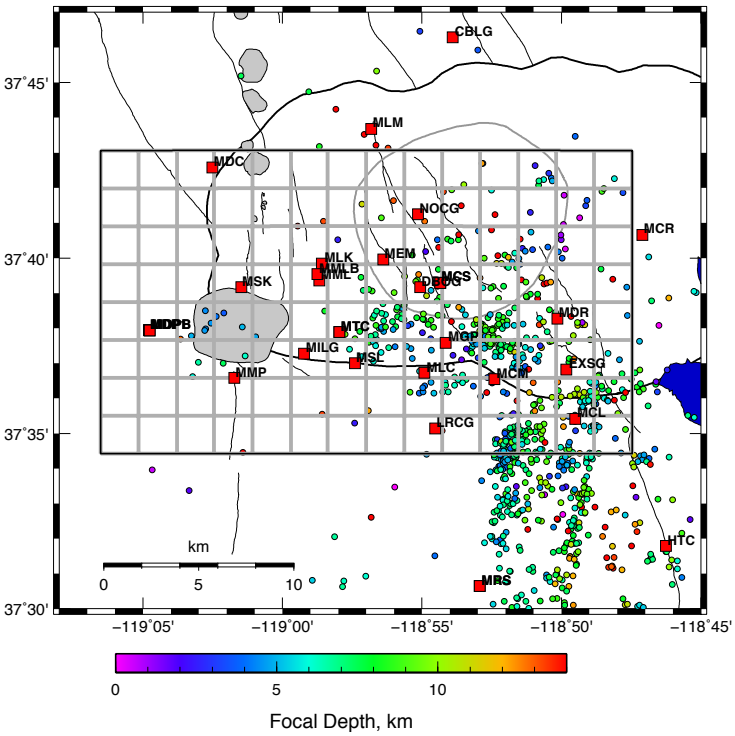
CBLG
MLM
MDC
NOCG
MCR
MLK
MEM
MSK
MDR
MDPB
MTC
MILG
MSL
MMP
FXSG
MLC
LRCG
MCL
HTC
MRS
km
0
5
10
37°45'
37°40'
37°35'
37°30'
−119°05'
−119°00'
−118°55'
−118°50'
−118°45'
0
5
10
Focal Depth, km

1988

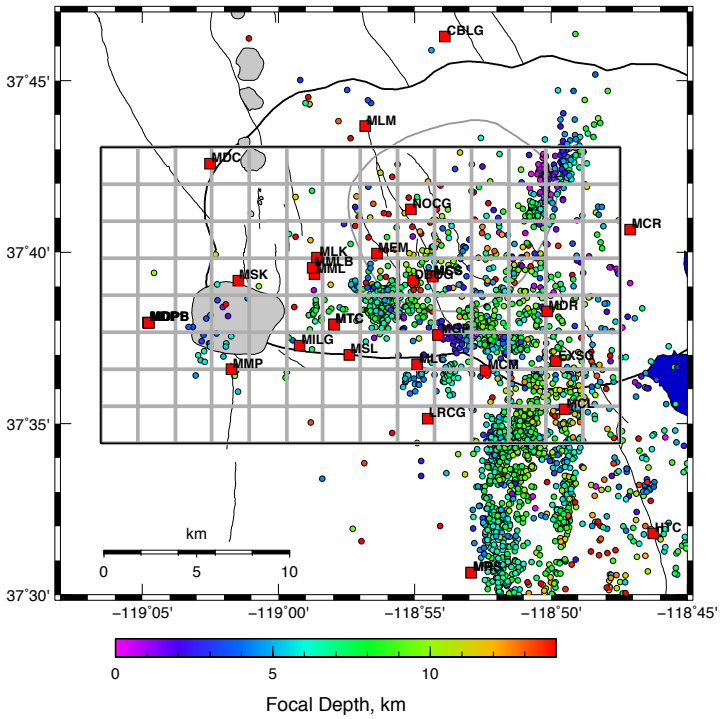
CBLG
MLM
MDC
ROCG
MCR
MLK
MML
MEM
MSK
MDPB
MTC
MDR
MILG
MSL
MMP
MCM
EXSC
LRCG
LFC
km
0
5
10
37°45'
37°40'
37°35'
37°30'
−119°05'
−119°00'
−118°55'
−118°50'
−118°45'
0
5
10
Focal Depth, km

1989

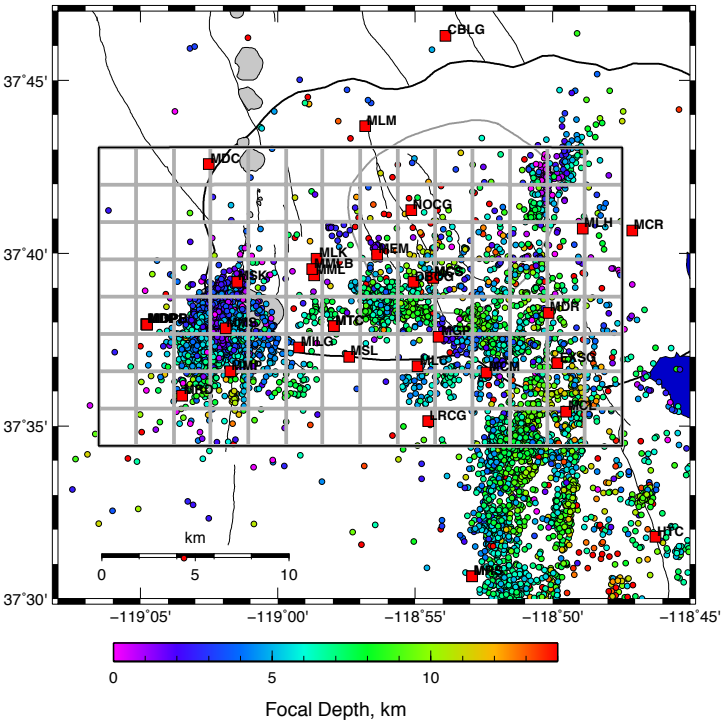
CBLG
MLM
MDC
ROCG
MLH
MCR
MLK
MML
MEM
MSK
MDPB
MTC
MDR
MILG
MSL
MMP
MCM
EXSC
LRCG
LFC
km
0
5
10
37°45'
37°40'
37°35'
37°30'
−119°05'
−119°00'
−118°55'
−118°50'
−118°45'
0
5
10
Focal Depth, km

1990

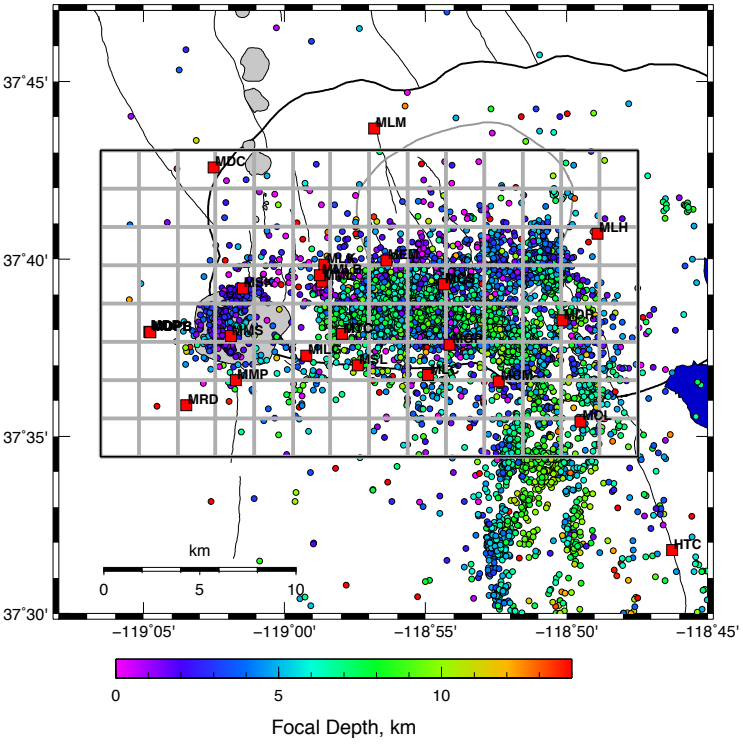
37°45'
37°40'
37°35'
37°30'
−119°05'
−119°00'
−118°55'
−118°50'
−118°45'
MLM
MDC
MLH
MSK
MMS
MLG
MSL
MMP
MRD
MDL
HTC
km
0
5
10
0
5
10
Focal Depth, km

1991

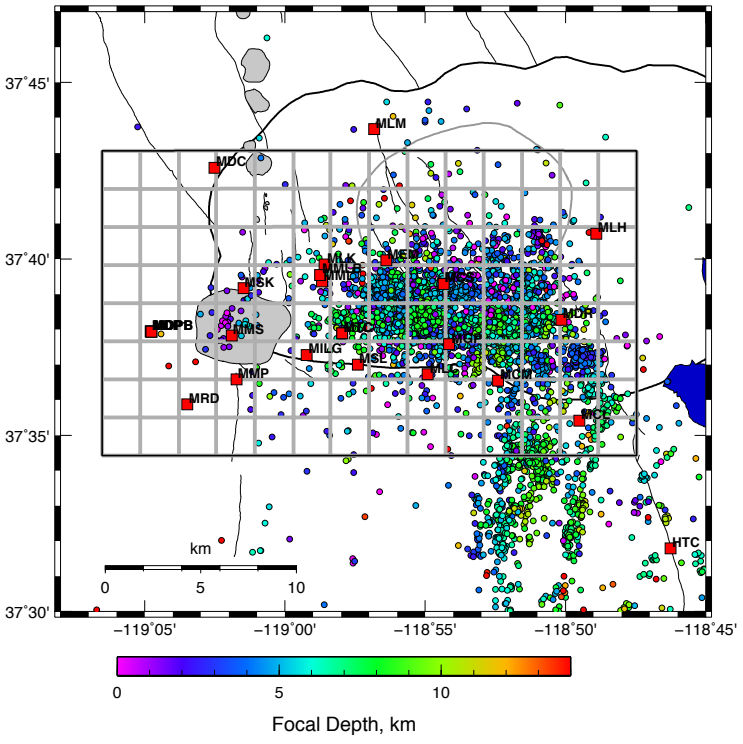
37°45'
37°40'
37°35'
37°30'
−119°05'
−119°00'
−118°55'
−118°50'
−118°45'
MLM
MDC
MLH
MSK
MMS
MLG
MSL
MMP
MRD
HTC
km
0
5
10
0
5
10
Focal Depth, km

1992

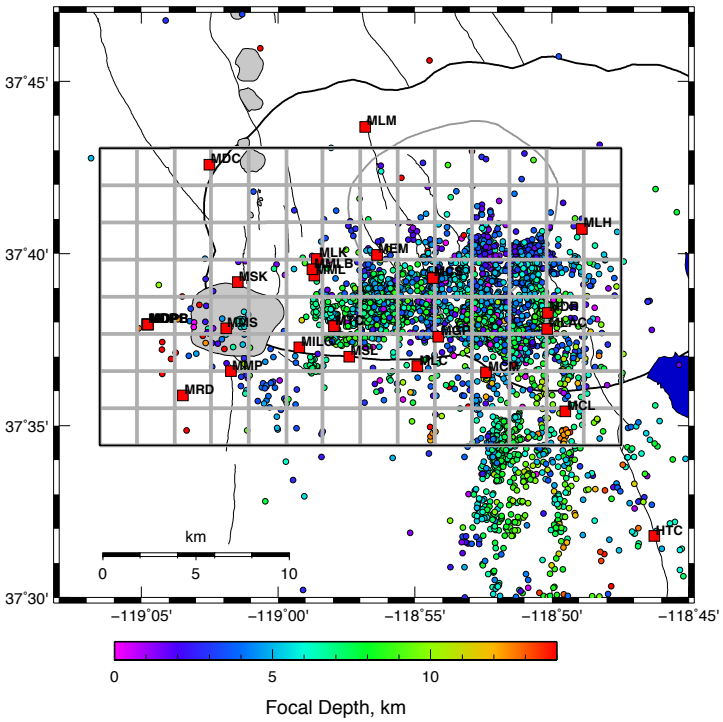
37°45'
37°40'
37°35'
37°30'
−119°05'
−119°00'
−118°55'
−118°50'
−118°45'
MLM
MDC
MLH
MSK
MDPB
MMS
MILG
MMP
MRD
MCL
HTC
km
0
5
10
0
5
10
Focal Depth, km

1993

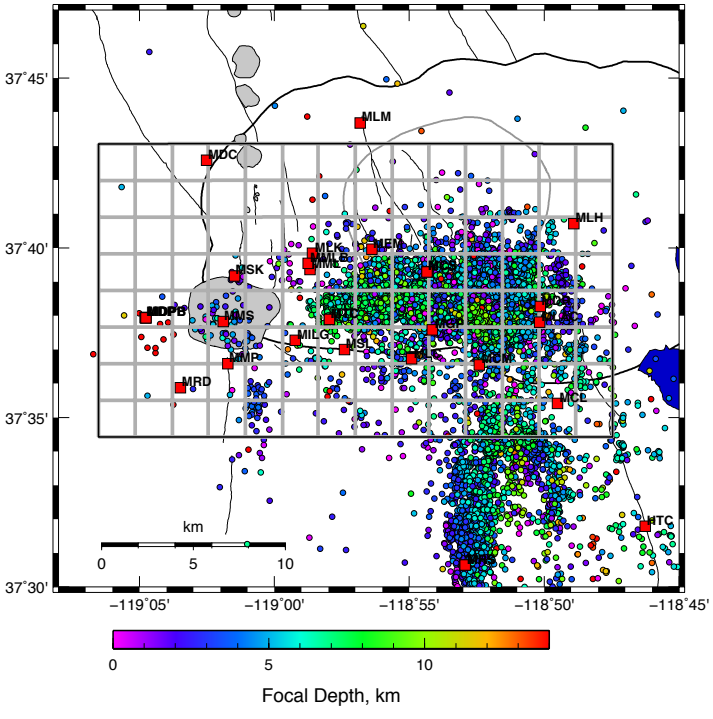
37°45'
37°40'
37°35'
37°30'
−119°05'
−119°00'
−118°55'
−118°50'
−118°45'
MLM
MDC
MLH
MSK
MDPB
MMS
MILG
MMP
MRD
MCL
HTC
km
0
5
10
0
5
10
Focal Depth, km

1994

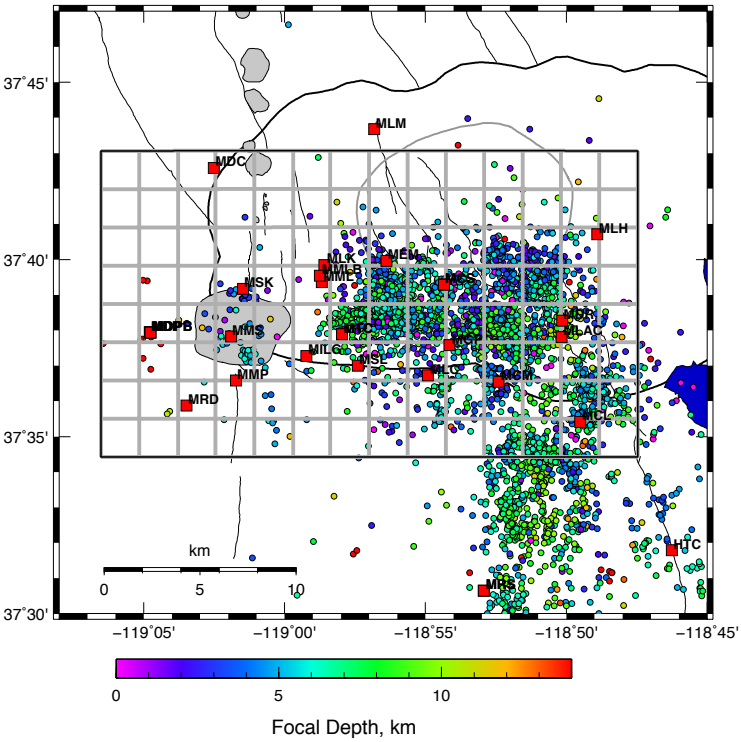
37°45'
37°40'
37°35'
37°30'
−119°05'
−119°00'
−118°55'
−118°50'
−118°45'
MLM
MDC
MLH
MLK
MEM
MSK
MDPB
MMS
MILG
MSL
MMP
MRD
MDR
MLAC
MCL
HTC
MRS
km
0
5
10
0
5
10
Focal Depth, km

1995

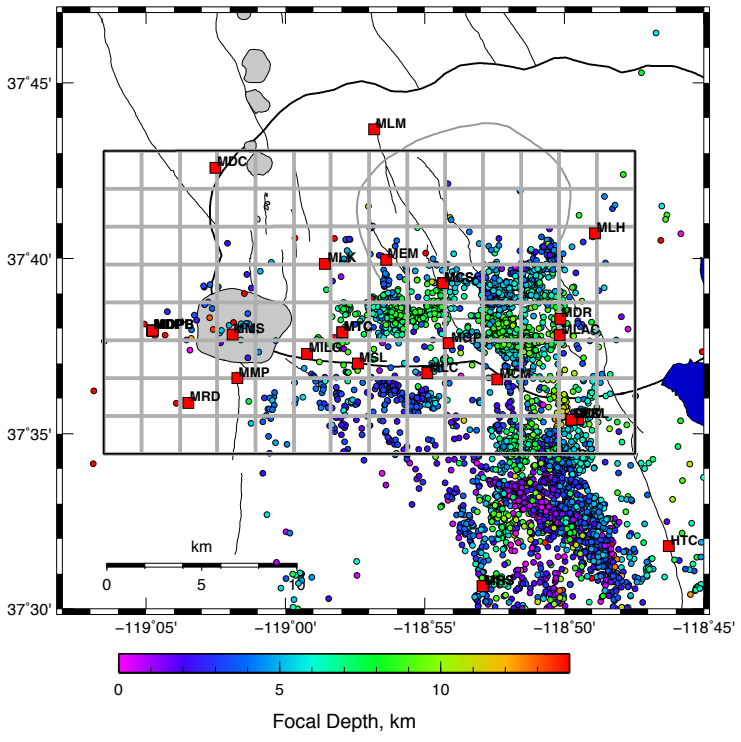
37°45'
37°40'
37°35'
37°30'
−119°05'
−119°00'
−118°55'
−118°50'
−118°45'
MLM
MDC
MLH
MLK
MEM
MSK
MDPB
MMS
MILG
MSL
MMP
MRD
MDR
MLAC
HTC
MRS
km
0
5
10
0
5
10
Focal Depth, km

1996

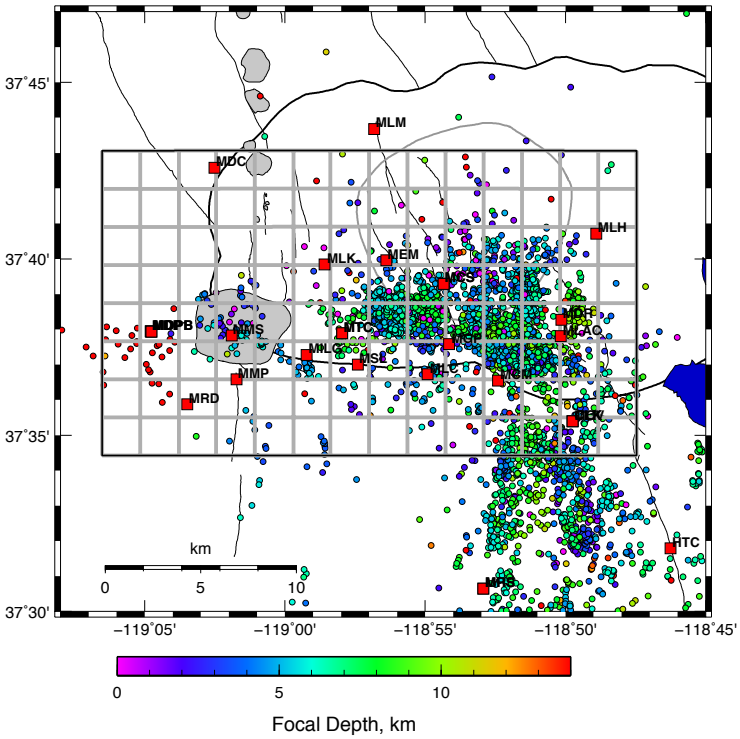
37°45'
37°40'
37°35'
37°30'
MLM
MDC
MLH
MLK
MEM
MMS
MTC
MLC
MMP
MRD
HTC
km
0
5
10
−119°05'
−119°00'
−118°55'
−118°50'
−118°45'
0
5
10
Focal Depth, km

1997

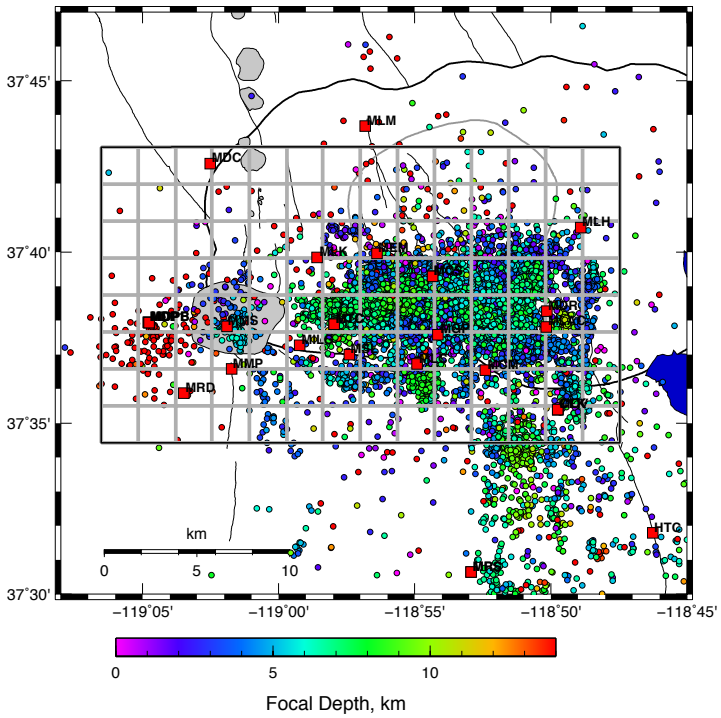
37°45'
37°40'
37°35'
37°30'
MLM
MDC
MLH
MLK
MMP
MRD
HTC
km
0
5
10
−119°05'
−119°00'
−118°55'
−118°50'
−118°45'
0
5
10
Focal Depth, km

1998

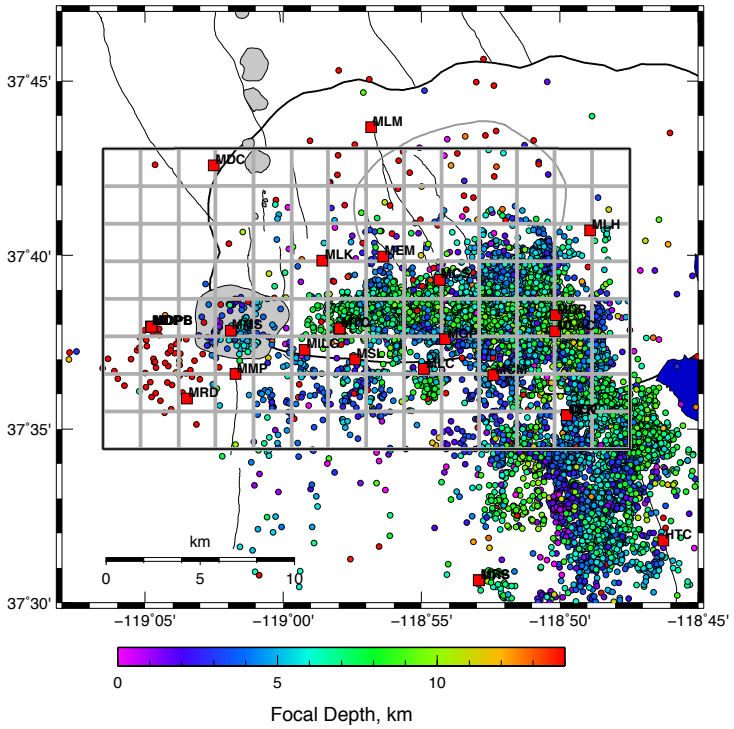
37°45'
37°40'
37°35'
37°30'
−119°05'
−119°00'
−118°55'
−118°50'
−118°45'
MLM
MDC
MLH
MLK
MEM
MCS
MMP
MRD
MSL
MLC
HTC
km
0
5
10
0
5
10
Focal Depth, km

1999

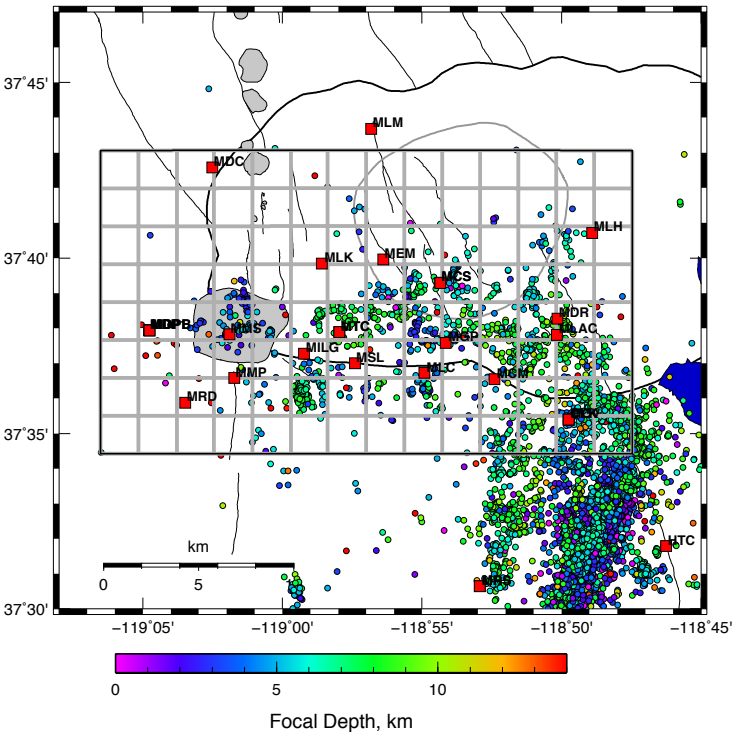
37°45'
37°40'
37°35'
37°30'
−119°05'
−119°00'
−118°55'
−118°50'
−118°45'
MLM
MDC
MLH
MLK
MEM
MCS
MMP
MRD
MSL
MLC
HTC
km
0
5
0
5
10
Focal Depth, km

2000

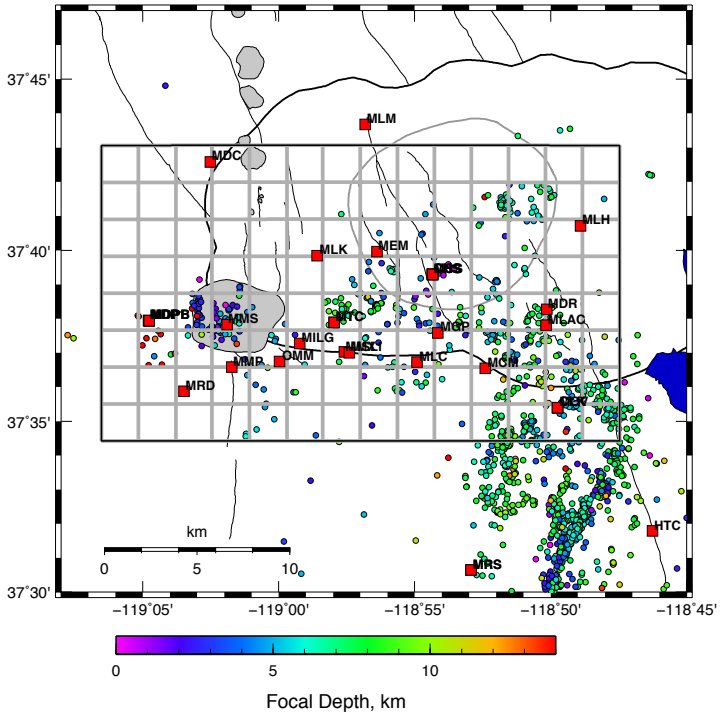
37°45'
37°40'
37°35'
37°30'
−119°05'
−119°00'
−118°55'
−118°50'
−118°45'
MLM
MDC
MLH
MLK
MEM
MDR
MLAC
MDPB
MMS
MTC
MILG
MMP
OMM
MLC
MCM
MRD
HTC
MRS
km
0
5
10
0
5
10
Focal Depth, km

2001

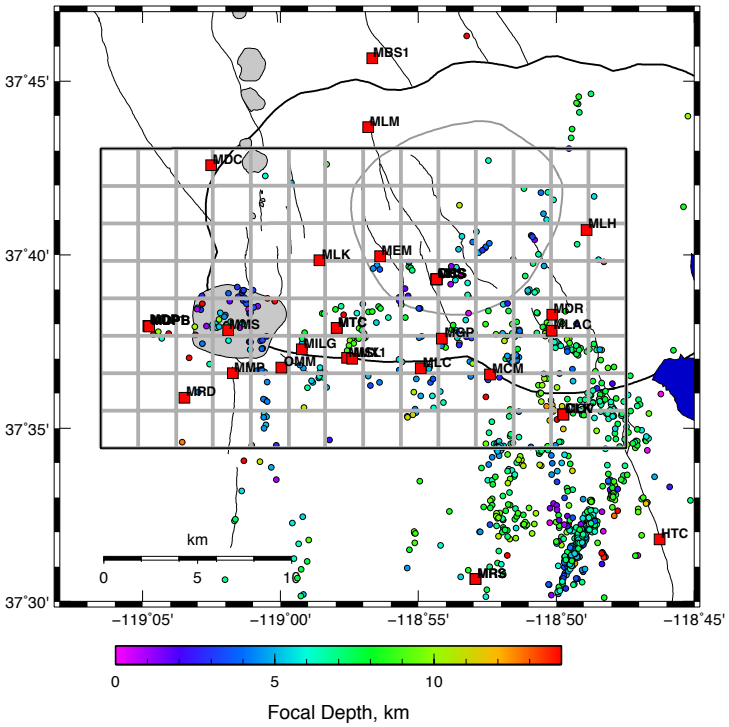
MBS1
37°45'
37°40'
37°35'
37°30'
−119°05'
−119°00'
−118°55'
−118°50'
−118°45'
MLM
MDC
MLH
MLK
MEM
MDR
MLAC
MDPB
MMS
MTC
MILG
MMP
OMM
MLC
MCM
MRD
HTC
MRS
km
0
5
10
0
5
10
Focal Depth, km

2002

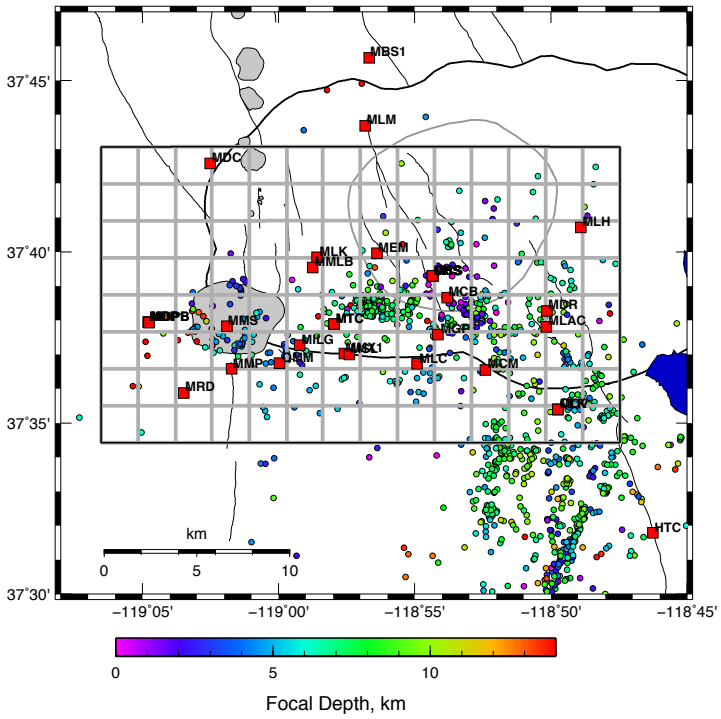
MBS1
MLM
MDC
MLH
MLK
MMLB
MEM
MCB
MDR
MLAC
MDPB
MMS
MTC
MLG
MMSX1
MMP
OMM
MLC
MCM
MRD
HTC
37°45'
37°40'
37°35'
37°30'
km
0
5
10
−119°05'
−119°00'
−118°55'
−118°50'
−118°45'
0
5
10
Focal Depth, km

2003

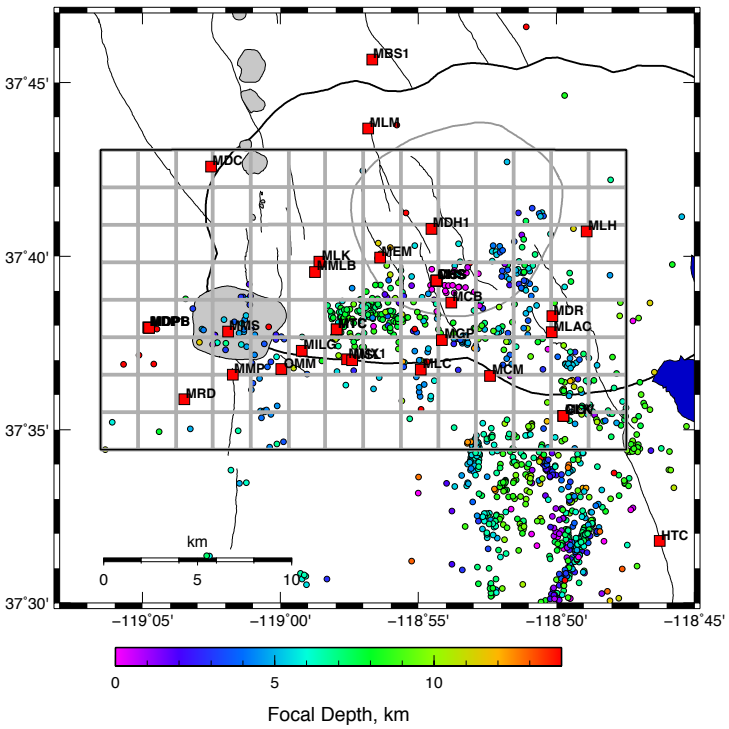
MBS1
MLM
MDC
MDH1
MLH
MLK
MMLB
MEM
MCB
MDR
MLAC
MDPB
MMS
MTC
MLG
MMSX1
MMP
OMM
MLC
MCM
MRD
HTC
37°45'
37°40'
37°35'
37°30'
km
0
5
10
−119°05'
−119°00'
−118°55'
−118°50'
−118°45'
0
5
10
Focal Depth, km

2004

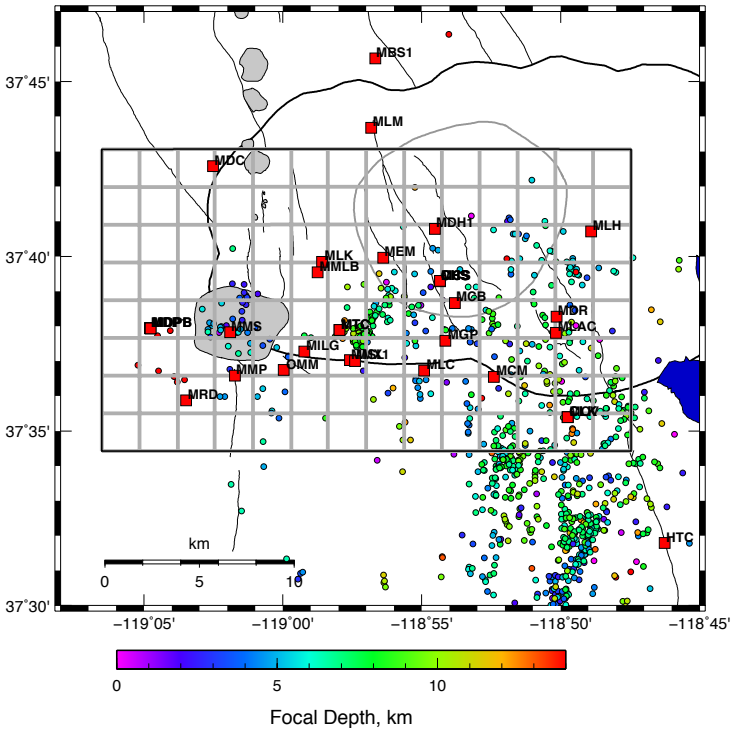
MBS1
MLM
MDC
MDH1
MLH
MLK
MMLB
MEM
MGB
MDR
MMS
MILG
MMP
DMM
MLC
MCM
MRD
HTC
km
0
5
10
37°45'
37°40'
37°35'
37°30'
−119°05'
−119°00'
−118°55'
−118°50'
−118°45'
0
5
10
Focal Depth, km

2005

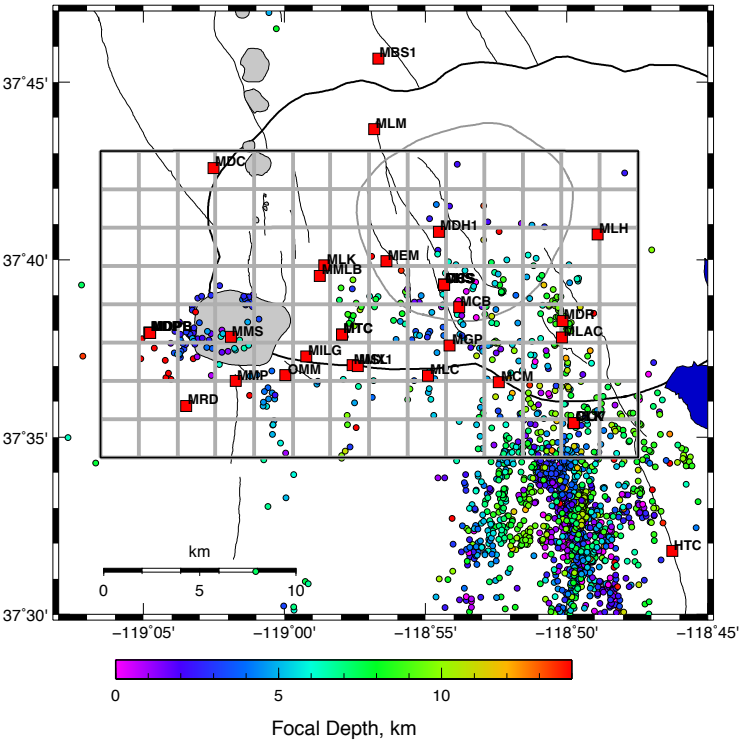
MBS1
MLM
MDC
MDH1
MLH
MLK
MMLB
MEM
MCB
MDR
MLAC
MMS
MILG
MMP
DMM
MLC
MCM
MRD
HTC
km
0
5
10
37°45'
37°40'
37°35'
37°30'
−119°05'
−119°00'
−118°55'
−118°50'
−118°45'
0
5
10
Focal Depth, km

2006

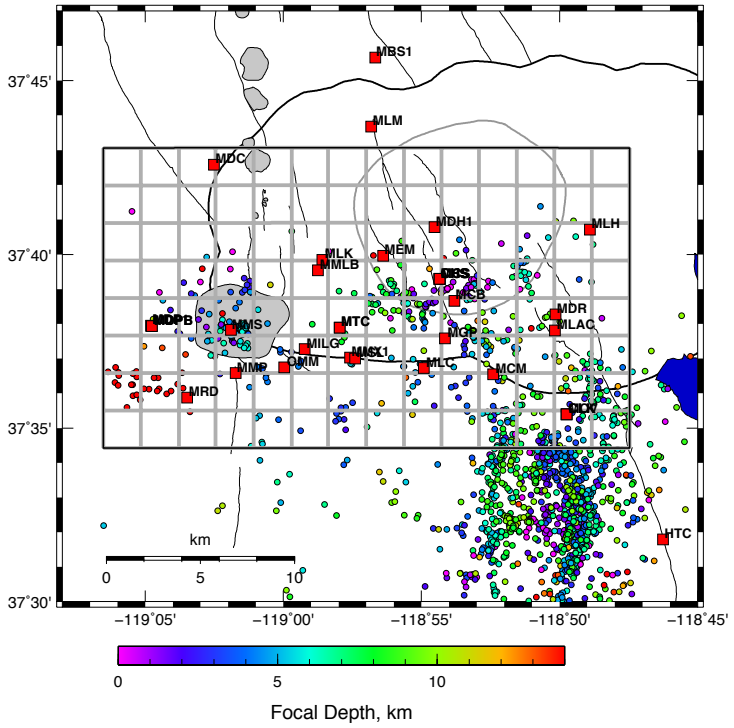
MBS1
MLM
MDC
MDH1
MLH
MLK
MMLB
MEM
MCB
MDR
MLAC
MDPB
MMS
MTC
MGP
MILG
MMX1
MMP
OMM
MLC
MCM
MRD
HTC
km
0
5
10
37°45'
37°40'
37°35'
37°30'
−119°05'
−119°00'
−118°55'
−118°50'
−118°45'
0
5
10
Focal Depth, km

2007

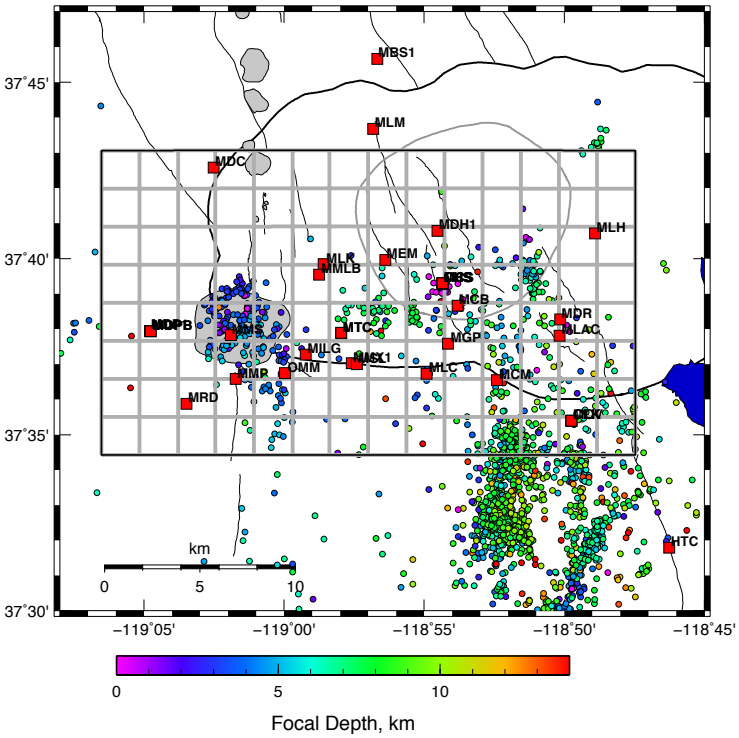
MBS1
MLM
MDC
MDH1
MLH
MLK
MMLB
MEM
MCB
MDR
MLAC
MDPB
MMS
MTC
MGP
MILG
MMX1
MMP
OMM
MLC
MCM
MRD
HTC
km
0
5
10
37°45'
37°40'
37°35'
37°30'
−119°05'
−119°00'
−118°55'
−118°50'
−118°45'
0
5
10
Focal Depth, km

2008

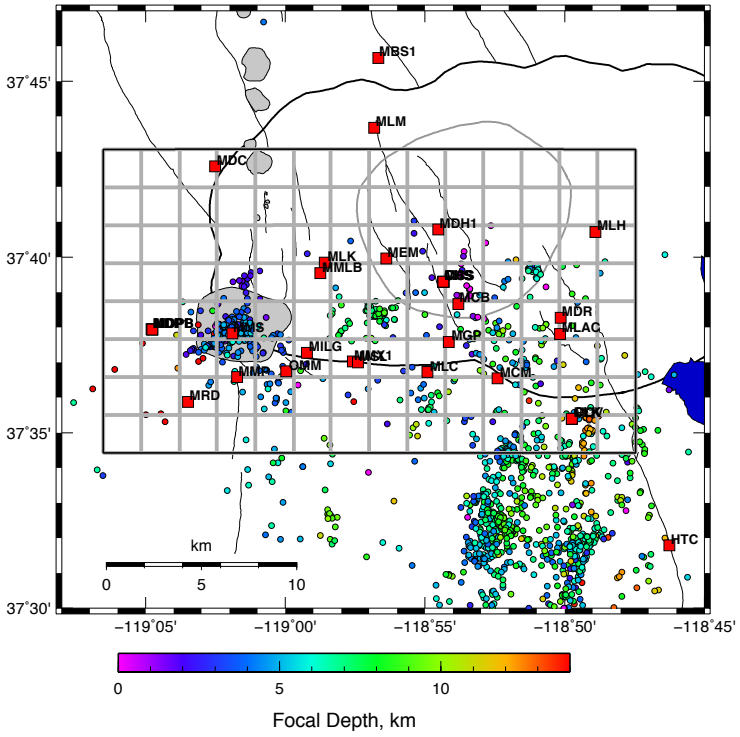
MBS1
MLM
MDC
MDH1
MLH
MLK
MMLB
MEM
MCB
MDR
MLAC
MGP
MILG
MLC
MCM
MRD
HTC
km
0
5
10
37°45'
37°40'
37°35'
37°30'
−119°05'
−119°00'
−118°55'
−118°50'
−118°45'
0
5
10
Focal Depth, km

2009

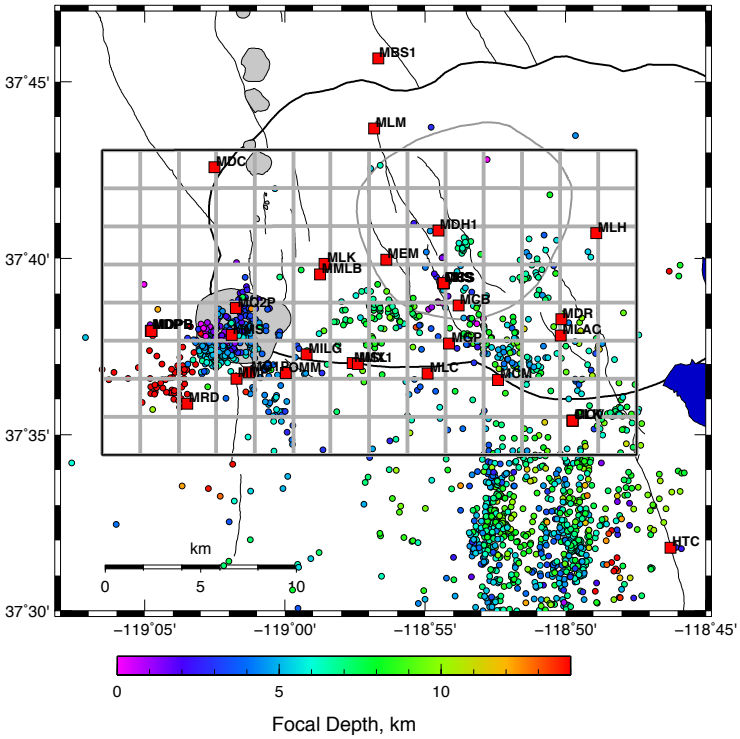
MBS1
MLM
MDC
MDH1
MLH
MLK
MMLB
MEM
MCB
MDR
MLAC
MGP
MILG
MLC
MRD
HTC
km
0
5
10
37°45'
37°40'
37°35'
37°30'
−119°05'
−119°00'
−118°55'
−118°50'
−118°45'
0
5
10
Focal Depth, km

2010

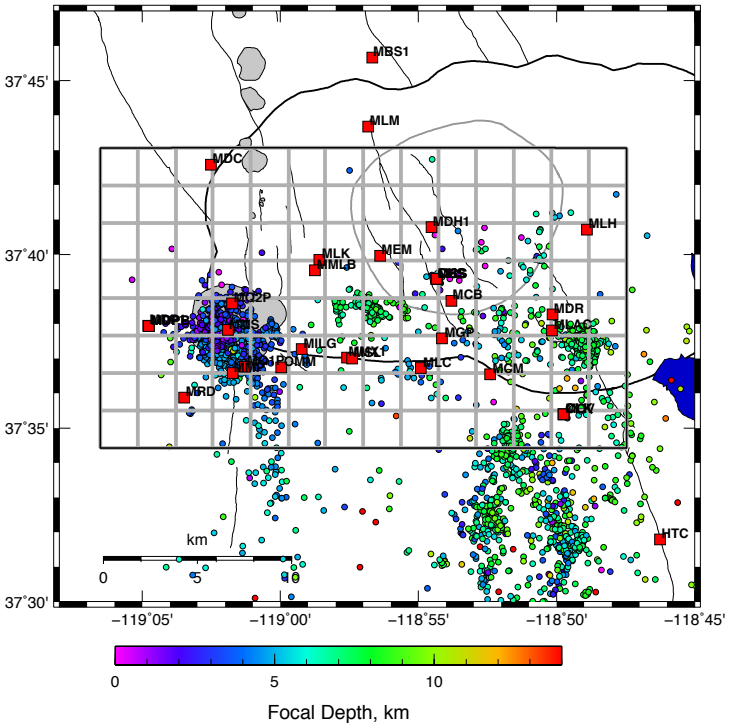
MBS1
MLM
MDC
MDH1
MLH
MLK
MEM
MCB
MDR
MLAC
MILG
MLC
MCM
MRD
HTC
km
0
5
10
37°45'
37°40'
37°35'
37°30'
−119°05'
−119°00'
−118°55'
−118°50'
−118°45'
0
5
10
Focal Depth, km

2011

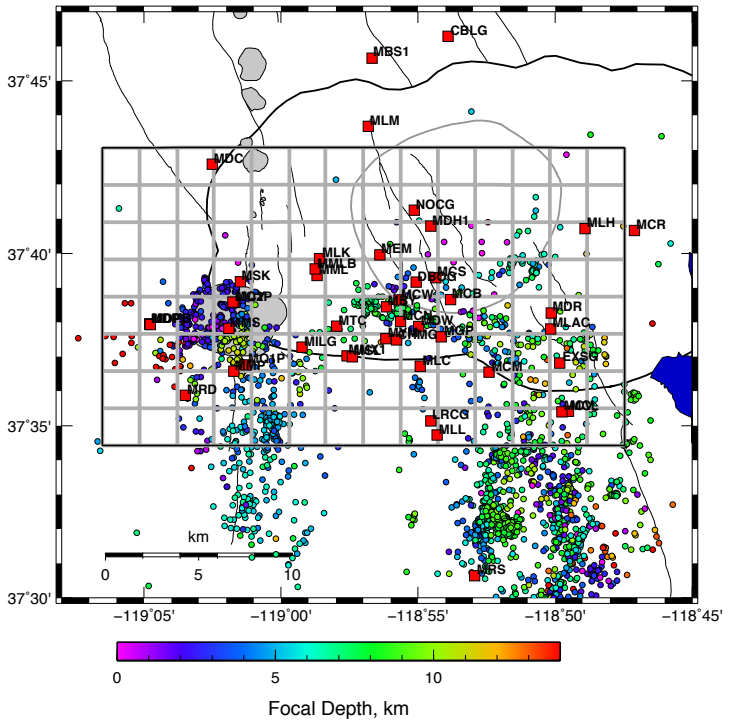
CBLG
MBS1
MLM
MDC
NOCG
MDH1
MLH
MCR
MLK
MEM
MSK
MCB
MDR
MLAC
MTC
MILG
MLC
MCM
MRD
LRCG
MLL
km
0
5
10
37°45'
37°40'
37°35'
37°30'
−119°05'
−119°00'
−118°55'
−118°50'
−118°45'
0
5
10
Focal Depth, km

2012

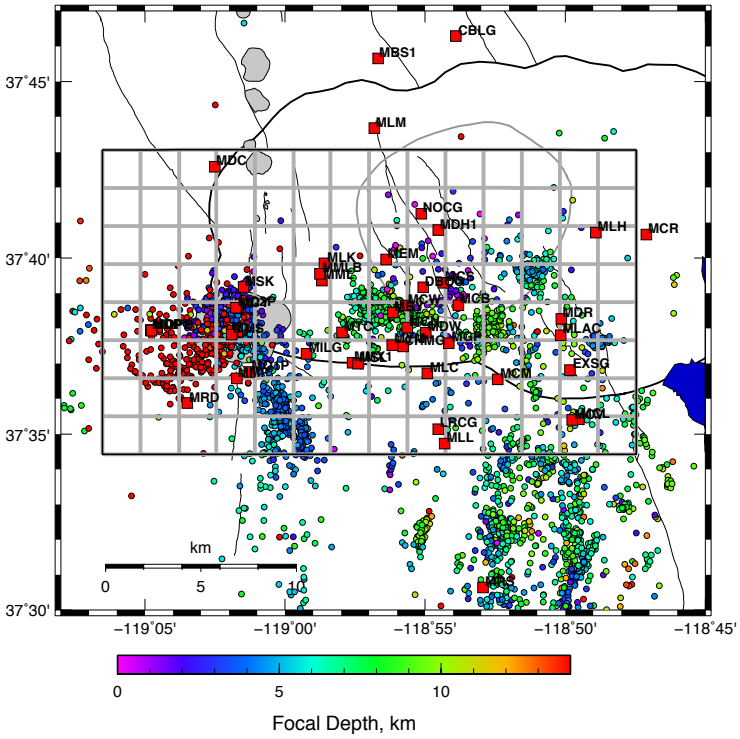
CBLG
MBS1
MLM
MDC
NOCG
MDH1
MLH
MCR
MEM
MLKB
MML
MSK
MDR
MLAC
WILG
MSL1
MLC
MCM
EXSG
MRD
RCG
MLL
km
0
5
10
37°45'
37°40'
37°35'
37°30'
−119°05'
−119°00'
−118°55'
−118°50'
−118°45'
0
5
10
Focal Depth, km

2013

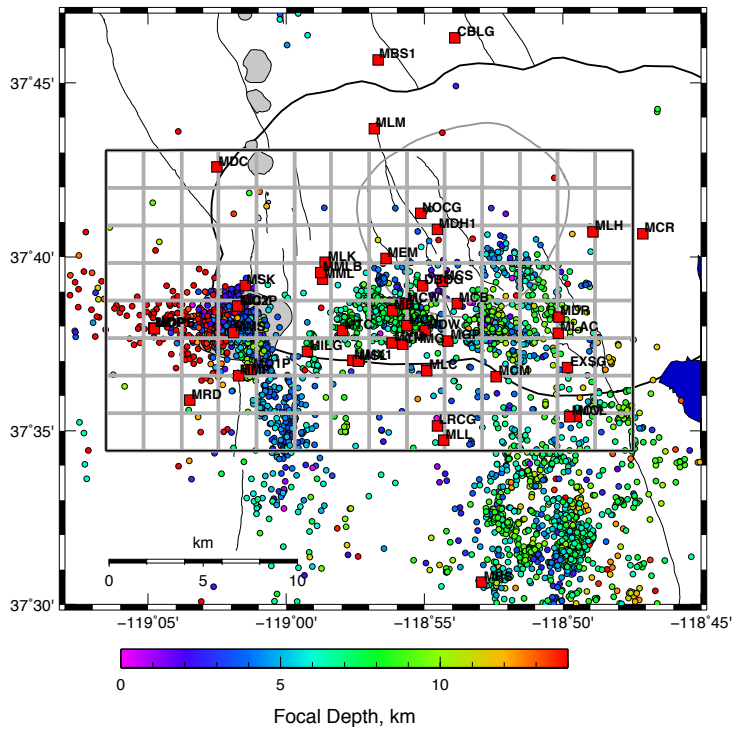
CBLG
MBS1
MLM
MDC
NOCG
MDH1
MLH
MCR
MEM
MLKB
MML
MSK
MDR
MLAC
WILG
MSL1
MLC
MCM
EXSG
MRD
LRCG
MLL
km
0
5
10
37°45'
37°40'
37°35'
37°30'
−119°05'
−119°00'
−118°55'
−118°50'
−118°45'
0
5
10
Focal Depth, km

2014

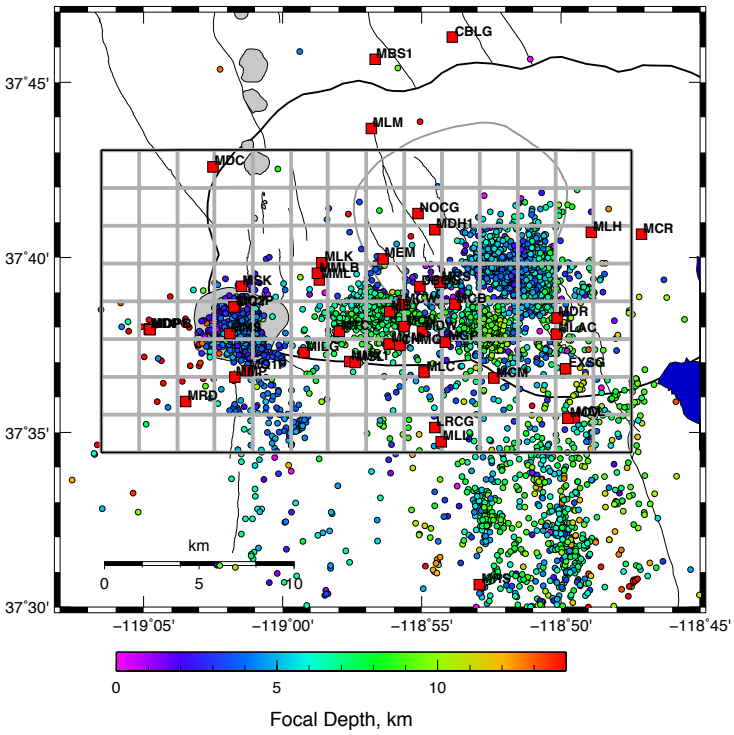
CBLG
MBS1
MLM
MDC
NOCG
MDH1
MLH
MCR
MLK
MEM
MSK
MRD
MLC
MCM
EVSG
LRCG
MLI2
MMS
37°45'
37°40'
37°35'
37°30'
−119°05'
−119°00'
−118°55'
−118°50'
−118°45'
km
0
5
10
0
5
10
Focal Depth, km

Appendix 2: (1) Example of a list file from Long Valley caldera data - an event that occurred 15th January 2010. Each line specifies a file containing a single seismogram in AH format; first column is the file name; second column is the number of seismographs within AH file; third column is group number (not used in this thesis); fourth column is the station name; fifth column is the channel name. (2) The script *eloc* which is used for locating earthquakes, calling the *qloc* program.

(1)

```
/db/seismic/Mammoth/Data/Events/2010/015/71340831/KCC.BHE.AH  1    _    KCC    BHE
/db/seismic/Mammoth/Data/Events/2010/015/71340831/KCC.BHN.AH  1    _    KCC    BHN
/db/seismic/Mammoth/Data/Events/2010/015/71340831/KCC.BHZ.AH  1    _    KCC    BHZ
/db/seismic/Mammoth/Data/Events/2010/015/71340831/KCC.HHE.AH  1    _    KCC    HHE
/db/seismic/Mammoth/Data/Events/2010/015/71340831/KCC.HHN.AH  1    _    KCC    HHN
/db/seismic/Mammoth/Data/Events/2010/015/71340831/KCC.HHZ.AH  1    _    KCC    HHZ
/db/seismic/Mammoth/Data/Events/2010/015/71340831/MBS1.EP1.AH  1    _    MBS1   EP1
/db/seismic/Mammoth/Data/Events/2010/015/71340831/MBS1.EP2.AH  1    _    MBS1   EP2
/db/seismic/Mammoth/Data/Events/2010/015/71340831/MBS1.HV1.AH 1    _    MBS1   HV1
/db/seismic/Mammoth/Data/Events/2010/015/71340831/MCB.HHE.AH  1    _    MCB    HHE
/db/seismic/Mammoth/Data/Events/2010/015/71340831/MCB.HHN.AH  1    _    MCB    HHN
/db/seismic/Mammoth/Data/Events/2010/015/71340831/MCB.HHZ.AH  1    _    MCB    HHZ
/db/seismic/Mammoth/Data/Events/2010/015/71340831/MCD.EHZ.AH  1    _    MCD    EHZ
/db/seismic/Mammoth/Data/Events/2010/015/71340831/MCM.EHZ.AH  1    _    MCM    EHZ
```

(2)

```
#!/bin/sh -
# Earthquake location script, invoked by epick

for file
do
        #read the ep.file writing it to the standard output
cat $file |

#convert seismic data to the binary format
ep2q -s $ELOC_STABLE -clock $ELOC_CLOCKDIR -calib $ELOC_CALDIR |

        #estimate location and origin time of the event
qloc -guess -maxiter 30 -mindep -2.5 -setdep 0 -mod $ELOC_MODEL\
-printall qloc.print |

#produce the output in the format for input to the simulps12
qprint -simnew

done
```

Appendix 3: Description of parameters for (1) *simul2000A* and (2) *tomo4d*

(1)

neqs	282	Number of earthquakes
nshot	0	Number of shots
nblast	0	Number of blasts
wtsht	1.0	Weight given to shots (relative to earthquakes)
kout	4	Output control parameter
kout2	1	Output control parameter
kout3	0	Output control parameter
nitloc	10	Maximum number of iterations of events location routine
wtsp	1.00	Weight given to *S*-P times (relative to P times)
eigtol	0.020	SVD cut-off in hypocentral adjustments
rmscut	0.010	RMS cut-off to terminate location iterations
zmmin	-3.00	Minimum earthquake depth
dxmax	0.50	Maximum horizontal hypocentre relocation per iteration
rderr	0.01	Estimate reading uncertainty
ercof	0.00	Used for hypocentre error calculations
hitct	5	DWS cut-off to remove node from inversion
dvpmax	0.10	Maximum V_p adjustment
dDvpvsmax	0.03	Maximum V_p/V_s adjustment
idmp	1	Damping control parameter
vpdmp	20.00	V_p damping parameter
vpvsdmp	20.00	V_p/V_s damping parameter
stadmp	99.0	Station delay damping parameter
stepl	0.500	Ray-path step length used in partial derivative calculations
ires	1	Resolution output control parameter
i3d	2	Three-dimensional ray tracing control parameter
nitmax	5	Maximum number of iterations of the hypocentre relocation model adjustment loop
snrmct	0.0025	Solution norm cut-off to terminate inversion
ihomo	0	Number of iterations to used ray-tracing in vertical planes
rmstop	0.010	RMS residual (for all events) to terminate inversion
ifixl	0	Number of iteration to fix hypocentre for
delt1	35.00	Ray-length cut-off used to weight residuals
delt2	50.00	Ray-length cut-off used to weight residuals
res1	0.40	Residual cut-off used for weighing
res2	0.80	Residual cut-off used for weighing
res3	1.00	Residual cut-off used for weighing
ndip	9	Number of planes searched during approximate ray-tracing (ART)
iskip	2	Number of planes near horizontal to skip during (ART)
scale1	0.50	Ray segment length
scale2	0.50	Controls number of paths tried during ray-tracing
xfax	1.20	Pseudo-bending control parameter
tlim	0.0010	Travel-time difference cut-off to terminate pseudo-bending iterations
nitpb1	15	Maximum number of iterations during pseudo-bending
nitpb2	15	Maximum number of iterations during pseudo-bending
iusep	1	Flag to use P travel times (0=N; 1=Y)
iuses	1	Flag to use *S*-P times (0=N; 1=Y)
invdel	0	Flag to invert for station delays (0=N; 1=Y)

(2)

-blasts	Reads arrival-time data for blasts (events with known locations but unknown times) for the two epoch from *file1*, and *file2* in the format of the *simul2000A* [*Evans et al.*, 1994]
-depoch	Adjust the strength of the constraint on differences in wave speeds at different epochs (default: 1.0)
-dorigin	Adjust the strength of the constraint on perturbations to the event origin parameters (default: 1.0)
-dratio	Adjust the strength of the constraint on the magnitudes of perturbations in the wave-speed ratio V_p/V_s at each iteration (default: 1.0)
-dspeed	Adjust the strength of the constraint on perturbations to the V_p and V_s (default: 1.0)
-maxiter	Maximum number of iterations (default: 10)
-pmodel	Read the initial model of the compressional-wave speed from the specified file
-psmodel	Read the initial model of the wave-speed ration V_p/V_s from the specified file
-qdistant	Read arrival-time data for distant earthquakes (outside the tomography grid) for the two epochs form from *file1*, and *file2* in the format of the *simul2000A*
-qlocal	Read arrival-time data for local earthquakes for the two epochs form from *file1*, and *file2* in the format of the *simul2000A*
-rayeps	In the "bending" ray-tracing computations, strive for an accuracy in the paths of a specified distance (default: 0.001)
-rayitmax	Maximum number of iterations for each ray (default: 10)
-rayseg	Divide each ray into segments of approximate specified length (default: 0.2)
-sedvel	Set the values of the *a priori* standard errors to use in damping inter-epoch differences in the perturbations to the V_p and V_s (default: 0.01 0.005)
-seorigin	Set the values of the *a priori* standard errors to use in damping perturbation to the event origins (horizontal and vertical hypocentre position and the origin time) (default: 0.2 0.2 0.1)
-sevel	Set the values of the *a priori* standard errors to use in damping perturbation to the V_p and V_s (default: 0.1 0.05)
-sevgrad	Set the values of the *a priori* standard errors to use in damping perturbation to the relative wave-speed gradients (default: 0.0 0.0)
-sewfront	Set the values of the *a priori* standard errors to use in damping perturbation to the wave-front direction and the wave-front time (default: 2.0 1.0)
-shots	Read arrival-time data for shots for the two epochs form from *file1*, and *file2* in the format of the *simul2000A*
-smodel	Read the initial model of the shear-wave speed from the specified file
-station	Read seismometer station coordinates from the specified file
-vpvs	Set the *a priori* value of the ratio V_p/V_s (default: 1.732)
-vgrad	Set the value of the relative vertical wave-speed gradient (default: 0.0, so that initial guesses are straight lines)
-wdamp	Adjust the strength of the constraint on perturbations to the directions of incoming wavefronts from distant events (default: 1.0)

Appendix 4: Origins of earthquakes from Long Valley caldera processed from 2009 and 2010 from USGS catalogue.

yymmdd	hhmm	sec	latitude	longitude	Depth (km)
090117	1921	15.05	37N34.20	118W53.20	1.92
090124	347	33.42	37N37.89	118W57.06	5.5
090130	2102	48.29	37N37.72	119W00.33	0.69
090202	1741	44.96	37N34.69	118W49.08	3.7
090209	113	46.91	37N39.91	118W52.69	3.84
090209	356	52.16	37N40.51	118W52.82	3.35
090210	1523	10.46	37N40.40	118W52.56	2.39
090213	1206	12.38	37N36.39	118W53.81	3.21
090215	238	3.73	37N35.08	118W48.77	5.7
090309	2016	26.4	37N35.88	118W49.68	1.15
090309	2030	3.36	37N36.01	118W49.82	0.67
090322	1059	49.11	37N38.79	118W53.54	5.68
090402	1056	37.69	37N37.73	119W01.56	3.52
090404	1742	8.85	37N40.27	118W52.27	1.89
090406	1408	7.45	37N39.74	118W53.68	2.16
090413	559	37.68	37N36.69	118W51.09	7.32
090605	1308	0.03	37N36.41	118W52.26	2.3
090612	1719	22.3	37N40.43	118W53.62	0.37
090618	31	23.53	37N35.25	118W50.18	3.93
090619	1144	31.85	37N37.51	118W52.61	5
090622	807	13.53	37N36.57	118W59.44	2.69
090105	1340	57.12	37N40.80	118W54.51	-0.01
090105	1353	58.44	37N41.23	118W54.57	1.23
090105	1434	20.77	37N41.19	118W54.96	0.73
090105	1506	54.38	37N39.57	118W54.19	3.72
090105	1611	14.87	37N41.35	118W52.91	-2.21
090105	1656	17.32	37N41.13	118W54.80	0.92
090105	1734	39.83	37N40.65	118W54.07	0.34
090105	1902	56.18	37N41.69	118W54.76	-0.5
090106	31	3.23	37N40.78	118W54.52	0
090109	1824	51.83	37N36.78	118W52.75	2.81
090109	1826	4.15	37N36.84	118W52.61	3.11
090422	950	25.27	37N36.54	118W52.00	2.4
090506	2133	58.23	37N36.63	118W55.13	6.43
090509	1621	57.39	37N34.03	118W54.43	5.82
090515	1851	51.42	37N50.23	118W41.90	63.39
090515	1920	45.81	37N37.70	118W54.69	-0.58
090520	239	30.68	37N39.40	118W59.06	1.5
090520	1336	28.48	37N32.74	118W52.36	2.01
090522	325	18.68	37N36.57	119W02.10	2.9
090525	1526	37.66	37N33.06	119W03.11	7.55

090526	553	1.71	37N37.82	118W52.00	5.17
090529	118	26.45	37N39.50	118W56.64	7.04
090529	344	30.49	37N38.76	119W02.19	0.17
091006	2135	47.04	37N37.20	119W02.42	2.7
090221	235	38.47	37N36.86	118W49.40	5.47
090412	1104	21.92	37N35.34	118W49.13	6.67
090505	1932	0.97	37N37.02	118W51.77	1.2
090605	1338	43.53	37N36.72	118W51.55	4
090615	207	37.91	37N37.71	119W16.64	-2.5
090704	1548	55.4	37N38.91	118W54.33	6.86
090705	2001	2.16	37N35.59	119W03.40	-2.5
090706	721	15.2	37N37.32	119W01.82	3.16
090707	2307	8.23	37N33.53	118W53.18	3.37
090712	1654	49.37	37N37.24	118W52.90	2.35
090712	2220	22.79	37N37.14	119W02.59	2.83
090714	11	25.9	37N36.11	118W50.07	8.3
090716	2314	4.05	37N34.21	118W51.29	3.35
090717	1608	48.86	37N47.73	118W47.40	17.49
090720	558	17.91	37N36.76	118W55.60	4.41
090724	244	36.2	37N35.13	118W49.61	1.61
090727	641	23.51	37N43.86	118W50.02	8.56
090729	438	36.13	37N39.30	119W01.00	-0.06
090729	1243	20.15	37N36.70	118W52.81	0.19
090731	304	40.23	37N38.11	118W57.18	5.62
090731	541	7.93	37N39.79	118W54.70	3.37
090731	548	4.82	37N40.41	118W54.33	4.57
090731	608	20.59	37N38.28	118W47.91	10.85
090801	1536	24.75	37N38.36	118W57.10	5.88
090802	2129	39.44	37N38.39	118W56.93	6.45
090810	1105	19.58	37N41.82	118W57.07	-0.79
090815	114	40.24	37N36.99	118W57.14	6.29
090815	414	14	37N39.42	118W57.11	5.75
090817	2358	12.53	37N38.49	118W51.42	3.09
090818	532	45.83	37N40.86	118W48.85	6.41
090818	545	58.77	37N40.72	118W48.91	0
090819	1312	58.85	37N36.21	118W51.00	4.08
090823	128	17.83	37N38.87	118W57.78	8.74
090825	1455	30.8	37N37.36	119W02.62	3.25
090906	59	34.52	37N36.93	119W02.82	2.13
090906	452	0.6	37N40.73	118W54.17	1.44
090906	1410	52.08	37N39.25	118W56.64	9.14
090906	1525	29.44	37N39.42	118W57.09	7.7
090829	1150	39.88	37N37.22	119W02.59	2.86
090829	1434	43.61	37N38.41	118W54.45	4.85
090903	857	27.15	37N33.41	118W50.03	2.25
090915	1555	16.88	37N36.50	119W02.21	-1.09

090915	144	47.62	37N39.29	118W54.35	0
090917	327	9.83	37N41.56	118W55.77	-1.1
090921	1651	4.67	37N38.59	118W52.06	4.36
090921	1826	52.29	37N33.93	118W51.49	5.89
090922	2110	9.49	37N37.15	119W02.00	3.54
090924	2138	43.94	37N33.77	118W52.06	5.89
090929	1536	1.54	37N36.67	119W04.73	18.89
090929	1657	24.54	37N35.74	119W06.33	25.44
090929	1713	57.43	37N36.78	119W04.46	19.09
090929	1718	39.82	37N36.58	119W01.72	0
090929	1930	41.33	37N36.81	119W04.96	17.7
090929	2028	41.52	37N36.78	119W04.08	17.48
090929	2051	33.06	37N23.88	119W19.56	17.21
090929	2143	19.91	37N32.22	118W57.46	3.62
090929	2322	42.02	37N36.99	119W04.16	18.36
090930	39	5.33	37N37.59	119W03.13	15.2
090930	216	33.44	37N15.84	119W30.38	-2.5
090930	351	22.63	37N35.91	119W06.47	22.26
090930	423	38.29	37N36.73	119W05.07	17.37
091001	1527	51.84	37N44.77	118W58.70	-2.5
091006	2135	46.99	37N37.22	119W02.46	3.01
091017	627	46.18	37N34.72	118W49.73	3.51
091017	631	58.22	37N35.74	118W49.71	3.82
091019	1038	52.62	37N34.48	118W48.89	4.29
091009	2239	9.81	37N37.80	119W03.06	0.02
091021	710	43.79	37N38.26	118W53.17	2.74
091024	212	7.51	37N37.93	119W01.93	1.67
091029	727	29.51	37N35.00	118W49.41	4.38
091031	623	17.82	37N33.50	118W50.22	5.46
091102	50	22.78	37N34.45	118W49.40	3.92
091106	53	24.16	37N40.57	118W53.04	7.31
091109	357	48.53	37N37.24	119W01.99	3.06
091109	721	54.44	37N37.93	119W02.76	3.72
091109	1040	3.14	37N39.69	118W56.39	5.32
091115	2027	3.46	37N37.18	119W02.58	2.01
091120	2351	29.26	37N37.67	118W58.07	5.86
091204	21	10.56	37N35.77	118W56.45	2.96
091204	1021	5.22	37N34.70	118W50.89	6.21
091122	1151	24.36	37N37.14	119W02.81	2.81
091122	1528	59.77	37N36.38	119W05.07	3.54
091122	1740	8.16	37N39.35	118W57.12	7.03
091122	1958	34.96	37N38.73	118W57.04	8.82
091123	1904	32.07	37N36.29	118W51.36	2.62
091124	424	51.93	37N37.38	119W01.55	2.81
091125	235	58.55	37N33.33	118W49.82	6.24
091129	200	31.02	37N33.32	118W50.47	5.04

091210	1321	0.45	37N40.79	118W54.53	0
091129	1843	57.49	37N36.79	119W01.95	1.33
091212	849	25.82	37N59.18	119W17.88	-0.91
091212	937	44.05	37N33.79	118W50.67	10.03
091212	1013	38.73	37N36.39	119W01.57	-1.09
091213	1211	38.71	37N38.44	118W59.04	4.11
091216	1109	49.27	37N33.22	118W50.49	4.2
091224	400	50.06	37N38.34	119W03.23	-0.6
091224	400	50.27	37N36.71	119W02.14	0.85
091229	143	44.8	37N35.14	118W50.17	3.61
100103	1010	40.88	37N36.70	118W55.29	3.44
100110	1229	18.05	37N37.02	119W02.77	1.93
100111	937	57.62	37N36.44	118W51.73	8.34
100114	1400	21.46	37N37.82	119W01.90	0
100115	1426	35.76	37N37.04	119W02.19	2.54
100117	345	29.58	37N36.62	119W02.94	3.06
100119	1454	10.08	37N36.11	118W55.05	4.93
100121	2341	7.55	37N37.68	118W55.71	5.66
100121	2344	51.1	37N39.02	118W55.60	4.33
100121	2348	20.48	37N40.56	118W56.98	2.27
100121	2358	6.95	37N39.43	118W55.85	2.01
100122	18	7.01	37N37.75	118W55.83	5.12
100122	530	12.31	37N42.39	118W56.20	-2.5
100129	339	54.21	37N34.55	118W49.07	4.2
100202	1425	56.34	37N37.25	119W02.52	1.97
100205	932	5.02	37N39.74	119W02.16	-0.64
100207	826	39.76	37N37.05	119W04.20	4.33
100207	1753	51.76	37N36.44	118W52.55	0.27
100212	1442	27.81	37N40.06	118W54.47	0.94
100223	1949	33.33	37N37.06	119W03.22	4.61
100217	1353	15.34	37N34.42	118W50.06	6.22
100303	1903	33.24	37N33.10	118W53.10	2.16
100308	842	8.79	37N39.86	118W52.26	2.79
100310	122	15.91	37N34.45	118W48.92	5.47
100318	842	18.57	37N40.19	118W52.72	1.37
100321	1204	1.15	37N34.23	119W00.25	-2.5
100322	1147	54.67	37N41.98	118W51.79	2.05
100327	506	48.99	37N33.66	118W52.79	0.96
100329	1225	17.81	37N35.98	118W50.60	7.25
100331	1546	20.37	37N37.86	119W01.17	0.37
100331	1549	27.18	37N37.86	119W01.30	1.02
100410	146	31.98	37N36.75	119W01.91	1.21
100410	615	42.04	37N36.25	118W56.10	4.92
100410	635	24.56	37N35.43	118W54.88	7.45
100416	1129	50.78	37N35.16	118W48.08	6.67
100419	9	57.68	37N37.32	118W57.67	3.8

100420	718	51.48	37N41.08	118W51.04	5.2
100420	808	59.87	37N40.93	118W52.86	0.96
100420	809	48.14	37N41.24	118W51.22	2.54
100420	827	29.72	37N41.05	118W51.71	0.78
100420	832	17.85	37N40.48	118W50.05	5.35
100420	936	25.79	37N41.00	118W51.57	3.38
100420	1603	17.06	37N40.57	118W51.52	2.95
100422	1547	34.53	37N36.44	118W52.33	0.83
100425	1632	46.02	37N36.54	119W01.97	2.63
100508	618	27.3	37N36.26	119W02.38	0.76
100429	1653	20.38	37N37.37	118W57.68	4.04
100429	1821	32.64	37N37.87	118W58.26	5.83
100430	724	12.1	37N36.62	119W01.21	0.72
100510	1011	32.74	37N41.41	118W53.01	3.21
100512	611	12.08	37N36.79	118W53.48	6.64
100526	1923	58.98	37N37.06	119W02.08	1.14
100527	11	58.75	37N36.82	119W01.98	1.36
100528	1021	55.16	37N34.12	118W48.34	5.75
100602	830	38.17	37N38.60	118W52.84	3.08
100722	1140	17.54	37N19.42	119W19.12	0
101122	1410	31.19	37N35.87	118W52.51	10.63

Appendix 5: Sample of the grid file used for inversion using *simul2000A* of Long Valley caldera data from the year 2009-2010.

```
1.0 17 11 15
-50.0  0.0  2.0  4.0  6.0  8.0  10.0  12.0  14.0  16.0  18.0  20.0  22.0  24.0  26.0  28.0 78.0
-50.0  0.0  2.0  4.0  6.0  8.0  10.0  12.0  14.0  16.0 66.0
-50.0 -4.0 -2.0 -1.0  0.0  1.0  2.0  3.0  4.0  5.0  6.0  7.0  8.0  10.0 60.0
2  2  2
3  2  2
4  2  2
5  2  2
6  2  2
7  2  2
8  2  2
9  2  2
10  2  2
11  2  2
12  2  2
13  2  2
14  2  2
15  2  2
.
.
.
.
0  0  0

2.50 2.50 2.50 2.50 2.50 2.50 2.50 2.50 2.50 2.50 2.50 2.50 2.50 2.50 2.50 2.50 2.50
2.50 2.50 2.50 2.50 2.50 2.50 2.50 2.50 2.50 2.50 2.50 2.50 2.50 2.50 2.50 2.50 2.50
2.50 2.50 2.50 2.50 2.50 2.50 2.50 2.50 2.50 2.50 2.50 2.50 2.50 2.50 2.50 2.50 2.50
2.50 2.50 2.50 2.50 2.50 2.50 2.50 2.50 2.50 2.50 2.50 2.50 2.50 2.50 2.50 2.50 2.50
2.50 2.50 2.50 2.50 2.50 2.50 2.50 2.50 2.50 2.50 2.50 2.50 2.50 2.50 2.50 2.50 2.50
2.50 2.50 2.50 2.50 2.50 2.50 2.50 2.50 2.50 2.50 2.50 2.50 2.50 2.50 2.50 2.50 2.50
2.50 2.50 2.50 2.50 2.50 2.50 2.50 2.50 2.50 2.50 2.50 2.50 2.50 2.50 2.50 2.50 2.50
2.50 2.50 2.50 2.50 2.50 2.50 2.50 2.50 2.50 2.50 2.50 2.50 2.50 2.50 2.50 2.50 2.50
2.50 2.50 2.50 2.50 2.50 2.50 2.50 2.50 2.50 2.50 2.50 2.50 2.50 2.50 2.50 2.50 2.50
2.50 2.50 2.50 2.50 2.50 2.50 2.50 2.50 2.50 2.50 2.50 2.50 2.50 2.50 2.50 2.50 2.50
2.50 2.50 2.50 2.50 2.50 2.50 2.50 2.50 2.50 2.50 2.50 2.50 2.50 2.50 2.50 2.50 2.50
3.00 3.00 3.00 3.00 3.00 3.00 3.00 3.00 3.00 3.00 3.00 3.00 3.00 3.00 3.00 3.00 3.00
3.00 3.00 3.00 3.00 3.00 3.00 3.00 3.00 3.00 3.00 3.00 3.00 3.00 3.00 3.00 3.00 3.00
3.00 3.00 3.00 3.00 3.00 3.00 3.00 3.00 3.00 3.00 3.00 3.00 3.00 3.00 3.00 3.00 3.00
3.00 3.00 3.00 3.00 3.00 3.00 3.00 3.00 3.00 3.00 3.00 3.00 3.00 3.00 3.00 3.00 3.00
3.00 3.00 3.00 3.00 3.00 3.00 3.00 3.00 3.00 3.00 3.00 3.00 3.00 3.00 3.00 3.00 3.00
3.00 3.00 3.00 3.00 3.00 3.00 3.00 3.00 3.00 3.00 3.00 3.00 3.00 3.00 3.00 3.00 3.00
3.00 3.00 3.00 3.00 3.00 3.00 3.00 3.00 3.00 3.00 3.00 3.00 3.00 3.00 3.00 3.00 3.00
3.00 3.00 3.00 3.00 3.00 3.00 3.00 3.00 3.00 3.00 3.00 3.00 3.00 3.00 3.00 3.00 3.00
3.00 3.00 3.00 3.00 3.00 3.00 3.00 3.00 3.00 3.00 3.00 3.00 3.00 3.00 3.00 3.00 3.00
3.00 3.00 3.00 3.00 3.00 3.00 3.00 3.00 3.00 3.00 3.00 3.00 3.00 3.00 3.00 3.00 3.00
3.00 3.00 3.00 3.00 3.00 3.00 3.00 3.00 3.00 3.00 3.00 3.00 3.00 3.00 3.00 3.00 3.00
3.00 3.00 3.00 3.00 3.00 3.00 3.00 3.00 3.00 3.00 3.00 3.00 3.00 3.00 3.00 3.00 3.00
3.55 3.55 3.55 3.55 3.55 3.55 3.55 3.55 3.55 3.55 3.55 3.55 3.55 3.55 3.55 3.55 3.55
3.55 4.39 3.99 4.52 4.22 4.13 4.72 4.57 4.14 3.94 3.79 3.64 3.43 3.26 3.54 3.81 3.55
3.55 3.79 4.21 4.23 3.99 4.14 4.65 4.68 4.03 4.36 4.40 4.12 3.79 3.22 3.47 3.83 3.55
3.55 3.57 3.38 3.03 3.17 4.60 4.52 4.48 3.83 4.30 4.51 4.42 4.04 2.70 3.67 4.28 3.55
3.55 3.52 3.32 3.15 2.95 4.31 3.23 3.15 3.00 3.25 4.03 4.10 3.25 4.20 3.15 3.56 3.55
3.55 3.50 3.27 2.60 3.29 4.00 3.90 3.79 3.40 2.69 3.54 3.07 4.27 4.87 3.33 3.23 3.55
3.55 3.40 3.03 3.37 4.04 3.36 3.12 3.85 3.82 3.10 3.30 3.65 4.38 4.87 4.21 3.72 3.55
3.55 3.25 3.00 3.39 3.53 3.99 4.33 3.97 3.88 4.24 4.16 3.65 3.92 4.35 4.79 4.59 3.55
3.55 3.49 3.53 3.63 3.65 3.19 3.05 3.37 3.27 3.47 3.72 3.69 4.48 4.24 4.26 4.26 3.55
3.55 3.69 3.55 3.55 3.46 3.39 3.18 2.84 2.57 3.00 3.52 3.51 4.31 4.22 4.22 4.50 3.55
```

3.55 3.55 3.55 3.55 3.55 3.55 3.55 3.55 3.55 3.55 3.55 3.55 3.55 3.55 3.55 3.55 3.55 3.55
4.45 4.45 4.45 4.45 4.45 4.45 4.45 4.45 4.45 4.45 4.45 4.45 4.45 4.45 4.45 4.45 4.45 4.45
4.45 4.02 4.31 5.29 5.25 4.93 5.05 5.53 5.02 4.72 4.66 4.38 4.27 4.43 4.43 4.72 4.45 4.45
4.45 4.17 4.58 4.99 4.99 4.51 4.73 5.42 5.11 5.06 5.05 4.84 4.08 4.26 4.30 4.77 4.45 4.45
4.45 4.42 4.21 3.97 3.54 4.40 4.84 5.05 5.12 5.16 4.98 5.05 4.01 4.14 4.77 5.05 4.45 4.45
4.45 4.36 4.03 3.50 3.48 4.52 3.72 3.80 3.81 3.94 4.78 3.75 4.64 4.02 4.54 4.54 4.45 4.45
4.45 4.25 4.02 3.82 4.26 3.75 3.53 4.52 4.47 3.86 4.46 3.80 4.79 4.18 4.12 4.30 4.45 4.45
4.45 4.21 3.62 3.68 4.73 4.78 4.40 3.96 4.57 4.53 4.04 4.39 5.16 5.45 5.26 4.66 4.45 4.45
4.45 4.08 3.67 3.86 4.30 4.94 4.45 3.75 3.89 5.19 4.91 5.05 5.49 4.99 5.63 5.00 4.45 4.45
4.45 4.47 4.30 4.32 4.44 4.12 3.75 4.09 3.92 4.17 4.54 4.43 5.35 4.93 4.98 5.12 4.45 4.45
4.45 4.50 4.43 4.45 4.34 4.24 4.06 4.06 3.91 3.54 4.60 4.48 4.56 4.86 4.92 5.32 4.45 4.45
4.45 4.45 4.45 4.45 4.45 4.45 4.45 4.45 4.45 4.45 4.45 4.45 4.45 4.45 4.45 4.45 4.45 4.45
5.35 5.35 5.35 5.35 5.35 5.35 5.35 5.35 5.35 5.35 5.35 5.35 5.35 5.35 5.35 5.35 5.35 5.35
5.35 5.62 5.11 5.54 5.90 6.03 6.18 6.38 6.11 5.87 5.85 5.31 5.09 5.22 5.33 5.71 5.35 5.35
5.35 4.98 4.95 5.75 5.82 5.30 5.57 6.01 5.84 5.59 5.70 5.14 5.21 5.27 5.28 5.54 5.35 5.35
5.35 5.26 5.48 5.19 5.11 4.92 4.94 5.44 5.18 5.20 5.07 4.72 5.57 5.32 5.47 5.54 5.35 5.35
5.35 5.22 4.83 4.52 4.42 4.21 4.52 4.66 5.65 5.17 4.89 4.79 5.70 5.04 5.27 5.46 5.35 5.35
5.35 5.05 4.87 5.21 5.29 4.34 4.33 4.67 5.14 4.63 4.66 5.58 5.75 5.03 5.30 5.38 5.35 5.35
5.35 5.17 4.60 4.51 5.27 5.36 4.44 4.53 4.86 4.74 4.87 5.44 5.87 6.21 6.04 5.66 5.35 5.35
5.35 5.19 4.69 4.56 5.42 5.18 4.73 4.44 4.89 5.32 5.13 5.95 5.86 5.66 6.21 5.98 5.35 5.35
5.35 5.65 5.21 5.13 5.26 5.28 4.88 4.95 4.40 4.51 5.43 5.42 5.56 5.69 5.81 6.29 5.35 5.35
5.35 5.19 5.32 5.35 5.32 5.28 5.12 5.20 5.06 4.74 5.55 5.57 5.41 5.35 5.40 6.16 5.35 5.35
5.35 5.35 5.35 5.35 5.35 5.35 5.35 5.35 5.35 5.35 5.35 5.35 5.35 5.35 5.35 5.35 5.35 5.35
5.56 5.56 5.56 5.56 5.56 5.56 5.56 5.56 5.56 5.56 5.56 5.56 5.56 5.56 5.56 5.56 5.56 5.56
5.56 6.06 5.35 5.49 5.97 5.86 5.70 5.92 5.70 5.54 5.55 5.85 5.66 5.63 5.67 5.96 5.56 5.56
5.56 5.30 5.14 5.23 5.35 5.14 5.15 5.79 5.88 5.92 5.79 5.51 6.07 5.47 5.70 5.69 5.56 5.56
5.56 5.43 5.81 5.23 5.64 5.30 5.18 5.36 4.83 5.01 5.44 6.07 5.93 5.56 5.85 5.59 5.56 5.56
5.56 5.40 5.01 5.06 5.61 4.49 5.10 5.18 4.96 5.70 5.70 5.50 5.55 6.30 5.86 5.63 5.56 5.56
5.56 5.20 4.97 5.16 5.32 4.96 5.40 5.50 5.17 4.95 5.02 5.33 6.22 6.06 5.84 5.67 5.56 5.56
5.56 5.47 5.01 5.09 5.48 5.30 4.89 4.73 5.47 4.98 5.40 5.82 5.52 6.43 6.28 6.11 5.56 5.56
5.56 5.69 5.48 5.18 5.46 5.15 5.43 4.81 4.71 4.97 5.39 6.10 5.66 5.84 6.29 6.73 5.56 5.56
5.56 5.88 5.51 5.49 5.49 5.51 5.31 4.89 4.72 4.85 5.59 6.05 5.83 5.81 5.99 6.48 5.56 5.56
5.56 5.23 5.49 5.56 5.54 5.58 5.70 5.67 5.59 5.85 5.72 5.66 5.54 5.22 5.54 6.01 5.56 5.56
5.56 5.56 5.56 5.56 5.56 5.56 5.56 5.56 5.56 5.56 5.56 5.56 5.56 5.56 5.56 5.56 5.56 5.56
5.78 5.78 5.78 5.78 5.78 5.78 5.78 5.78 5.78 5.78 5.78 5.78 5.78 5.78 5.78 5.78 5.78 5.78
5.78 5.66 6.19 6.12 6.05 5.92 5.60 5.96 6.24 5.83 6.22 6.03 6.04 5.92 5.86 6.28 5.78 5.78
5.78 5.57 5.47 5.35 5.56 5.76 5.78 6.18 6.06 6.15 5.73 5.90 6.13 5.83 5.90 5.91 5.78 5.78
5.78 5.66 5.23 5.17 5.92 6.15 6.44 6.33 5.64 6.29 6.04 5.54 6.12 5.60 6.00 5.78 5.78 5.78
5.78 5.58 5.23 5.36 5.60 5.70 5.56 5.63 5.52 5.48 6.26 5.35 5.81 6.26 6.00 5.86 5.78 5.78
5.78 5.42 5.30 5.46 5.31 5.29 5.72 4.90 5.65 5.86 5.66 5.69 5.71 6.29 6.09 5.93 5.78 5.78
5.78 5.84 5.65 5.80 5.30 5.02 5.62 4.99 5.67 5.73 5.78 5.76 5.72 6.52 6.33 6.14 5.78 5.78
5.78 6.04 5.86 5.82 5.64 5.33 5.36 5.47 5.45 5.64 6.20 6.08 6.06 5.98 6.65 6.41 5.78 5.78
5.78 5.99 5.77 5.79 5.69 5.59 5.11 5.04 5.26 5.96 6.21 5.86 5.91 5.68 6.10 6.13 5.78 5.78
5.78 5.29 5.67 5.78 5.75 5.78 6.12 6.11 6.06 6.24 5.95 5.49 5.28 5.22 5.41 5.93 5.78 5.78
5.78 5.78 5.78 5.78 5.78 5.78 5.78 5.78 5.78 5.78 5.78 5.78 5.78 5.78 5.78 5.78 5.78 5.78
5.87 5.87 5.87 5.87 5.87 5.87 5.87 5.87 5.87 5.87 5.87 5.87 5.87 5.87 5.87 5.87 5.87 5.87
5.87 5.23 6.46 6.33 6.28 6.47 6.71 6.65 6.34 5.70 5.67 5.47 5.77 6.11 6.30 6.38 5.87 5.87
5.87 5.55 5.87 6.21 6.03 5.83 6.50 6.09 6.16 6.04 5.93 5.96 5.99 6.11 5.93 5.98 5.87 5.87
5.87 5.59 5.30 5.53 5.64 5.94 6.17 6.74 6.36 6.15 5.86 5.38 5.49 6.08 5.75 5.87 5.87 5.87
5.87 5.77 5.41 5.41 6.11 6.15 6.05 6.08 6.56 5.68 6.44 5.33 5.96 6.44 5.95 5.88 5.87 5.87
5.87 5.83 5.84 5.70 5.09 5.02 5.41 5.85 5.59 6.11 5.64 5.34 5.72 6.61 6.13 5.90 5.87 5.87
5.87 5.99 5.96 5.90 5.80 5.74 5.15 5.64 5.50 5.75 5.93 6.05 6.06 6.38 6.35 5.92 5.87 5.87
5.87 6.06 5.94 5.90 5.58 5.37 5.26 5.35 5.57 5.65 6.28 6.14 6.12 6.15 6.41 5.95 5.87 5.87
5.87 5.90 5.83 5.87 5.75 5.58 5.86 5.56 5.91 6.11 6.38 5.93 5.91 5.84 6.20 5.91 5.87 5.87
5.87 5.39 5.66 5.84 5.84 5.81 6.29 6.03 5.95 5.93 5.85 5.67 5.51 5.41 5.71 5.91 5.87 5.87
5.87 5.87 5.87 5.87 5.87 5.87 5.87 5.87 5.87 5.87 5.87 5.87 5.87 5.87 5.87 5.87 5.87 5.87
5.96 5.96 5.96 5.96 5.96 5.96 5.96 5.96 5.96 5.96 5.96 5.96 5.96 5.96 5.96 5.96 5.96 5.96
5.96 5.32 6.51 6.97 6.19 5.97 6.45 6.60 6.04 5.81 6.04 5.95 6.15 6.16 6.17 6.21 5.96 5.96
5.96 5.66 6.47 6.73 5.78 5.87 6.15 6.88 6.63 6.44 6.18 5.97 6.00 6.09 6.06 6.01 5.96 5.96
5.96 5.74 6.10 6.45 6.11 6.03 6.03 6.38 6.56 6.35 6.32 5.61 5.68 6.10 6.05 5.96 5.96 5.96

5.96 6.00 5.69 5.77 5.99 6.04 5.79 5.87 6.12 6.53 5.81 5.98 6.31 6.29 5.97 5.96 5.96
5.96 5.75 5.98 5.37 5.40 5.93 6.23 6.21 5.55 5.66 6.09 6.65 6.27 6.11 5.97 5.96 5.96
5.96 5.69 5.90 5.80 6.08 5.54 5.88 6.34 5.88 5.76 6.15 6.59 6.23 6.24 6.02 5.96 5.96
5.96 6.11 6.00 5.90 5.55 5.91 5.94 5.85 6.06 6.06 5.98 6.16 6.16 6.23 6.10 5.96 5.96
5.96 5.86 5.94 5.79 5.78 5.94 6.25 6.04 6.19 6.31 6.11 5.78 5.98 6.06 6.04 5.96 5.96
5.96 5.82 5.72 5.84 5.91 5.95 5.99 5.96 5.88 5.95 6.21 6.28 5.82 5.62 5.92 5.96 5.96
5.96 5.96 5.96 5.96 5.96 5.96 5.96 5.96 5.96 5.96 5.96 5.96 5.96 5.96 5.96 5.96 5.96
6.00 6.00 6.00 6.00 6.00 6.00 6.00 6.00 6.00 6.00 6.00 6.00 6.00 6.00 6.00 6.00 6.00
6.00 5.58 6.33 6.14 6.36 6.42 5.97 5.90 6.17 6.26 6.21 6.18 6.14 6.30 6.33 6.01 6.00
6.00 5.86 6.09 6.14 6.18 6.29 6.02 6.08 6.03 6.22 6.13 6.00 6.09 6.24 6.04 6.00 6.00
6.00 5.76 6.35 6.54 6.49 6.41 6.13 6.04 5.98 6.06 6.00 6.07 6.13 6.05 6.10 6.00 6.00
6.00 5.83 5.96 6.52 6.43 6.04 6.19 6.19 6.08 6.33 5.89 6.24 6.12 5.96 5.96 6.00 6.00
6.00 5.64 5.99 5.67 5.99 6.08 6.10 5.79 5.82 5.74 6.19 6.18 6.13 5.98 6.00 6.00 6.00
6.00 5.86 5.95 5.78 6.30 5.90 5.98 5.85 6.38 5.85 5.97 6.16 6.17 6.03 6.00 6.00 6.00
6.00 5.96 6.01 5.93 5.65 5.74 5.70 6.09 6.45 6.51 5.78 5.98 6.00 6.02 6.01 6.00 6.00
6.00 6.04 6.01 5.88 5.87 5.88 5.83 5.81 6.10 6.44 6.17 5.73 5.98 6.01 6.00 6.00 6.00
6.00 5.98 5.94 5.95 5.96 5.99 5.96 5.88 5.77 5.91 6.36 6.14 5.77 5.96 6.00 6.00 6.00
6.00 6.00 6.00 6.00 6.00 6.00 6.00 6.00 6.00 6.00 6.00 6.00 6.00 6.00 6.00 6.00 6.00
6.04 6.04 6.04 6.04 6.04 6.04 6.04 6.04 6.04 6.04 6.04 6.04 6.04 6.04 6.04 6.04 6.04
6.04 5.53 6.32 6.33 6.08 5.76 6.58 6.64 6.29 6.13 6.18 6.21 6.15 6.11 6.08 6.04 6.04
6.04 5.88 6.06 5.87 6.15 6.03 6.04 6.37 6.24 6.15 6.13 6.12 6.08 6.08 6.06 6.04 6.04
6.04 6.09 6.26 6.00 6.06 6.14 6.28 6.40 6.18 6.01 6.08 6.04 6.00 6.02 6.04 6.04 6.04
6.04 5.80 6.24 6.34 6.11 6.23 6.22 6.31 6.43 6.17 6.04 6.06 6.06 6.12 5.98 6.04 6.04
6.04 5.91 5.97 5.66 6.09 6.06 5.83 6.07 6.03 6.04 6.09 6.06 6.19 6.12 6.04 6.04 6.04
6.04 6.01 6.05 5.83 5.94 5.84 5.90 6.26 6.29 6.03 6.11 6.07 6.05 6.04 6.04 6.04 6.04
6.04 6.06 6.03 5.95 5.82 6.00 6.11 6.17 6.25 6.25 5.99 6.07 6.05 6.04 6.04 6.04 6.04
6.04 6.05 6.03 5.98 6.00 6.02 6.04 6.03 6.08 6.18 6.09 6.07 6.05 6.04 6.04 6.04 6.04
6.04 6.04 6.03 6.02 6.03 6.04 6.04 6.04 6.05 6.08 6.08 6.07 6.05 6.04 6.04 6.04 6.04
6.04 6.04 6.04 6.04 6.04 6.04 6.04 6.04 6.04 6.04 6.04 6.04 6.04 6.04 6.04 6.04 6.04
6.06 6.06 6.06 6.06 6.06 6.06 6.06 6.06 6.06 6.06 6.06 6.06 6.06 6.06 6.06 6.06 6.06
6.06 5.37 6.13 6.56 6.12 6.27 6.24 6.08 6.04 6.05 6.09 6.09 6.08 6.06 6.06 6.06 6.06
6.06 6.27 6.06 6.08 5.82 6.05 6.14 6.21 6.12 6.10 6.08 6.08 6.07 6.06 6.06 6.06 6.06
6.06 6.14 6.24 6.15 6.14 6.27 6.32 6.22 6.22 6.11 6.08 6.06 6.06 6.06 6.07 6.06 6.06
6.06 5.86 6.10 6.25 6.45 6.14 6.12 6.18 6.17 6.09 6.08 6.06 6.06 6.14 6.06 6.06 6.06
6.06 6.03 5.96 6.15 6.06 6.00 5.95 5.99 6.10 6.10 6.08 6.06 6.06 6.06 6.06 6.06 6.06
6.06 6.07 5.98 5.87 6.12 6.15 6.06 5.94 6.03 6.10 6.08 6.06 6.06 6.06 6.06 6.06 6.06
6.06 6.06 6.05 6.05 6.06 6.08 6.08 6.07 6.08 6.10 6.08 6.06 6.06 6.06 6.06 6.06 6.06
6.06 6.06 6.06 6.05 6.06 6.06 6.07 6.07 6.07 6.08 6.07 6.06 6.06 6.06 6.06 6.06 6.06
6.06 6.06 6.06 6.06 6.06 6.06 6.06 6.06 6.06 6.06 6.06 6.06 6.06 6.06 6.06 6.06 6.06
6.06 6.06 6.06 6.06 6.06 6.06 6.06 6.06 6.06 6.06 6.06 6.06 6.06 6.06 6.06 6.06 6.06
6.07 6.07 6.07 6.07 6.07 6.07 6.07 6.07 6.07 6.07 6.07 6.07 6.07 6.07 6.07 6.07 6.07
6.07 5.80 5.99 6.14 6.12 6.07 6.03 6.03 6.06 6.07 6.07 6.07 6.07 6.07 6.07 6.07 6.07
6.07 6.06 6.09 6.13 5.97 6.11 6.08 6.07 6.07 6.07 6.07 6.07 6.07 6.07 6.07 6.07 6.07
6.07 6.02 6.09 6.12 6.04 6.05 6.08 6.07 6.07 6.07 6.07 6.07 6.07 6.07 6.07 6.07 6.07
6.07 5.95 6.09 6.08 6.13 5.99 6.02 6.07 6.07 6.07 6.07 6.07 6.07 6.07 6.07 6.07 6.07
6.07 5.97 6.03 6.07 6.04 6.06 6.07 6.07 6.07 6.07 6.07 6.07 6.07 6.07 6.07 6.07 6.07
6.07 6.05 6.06 6.07 6.07 6.07 6.07 6.07 6.07 6.07 6.07 6.07 6.07 6.07 6.07 6.07 6.07
6.07 6.07 6.07 6.07 6.07 6.07 6.07 6.07 6.07 6.07 6.07 6.07 6.07 6.07 6.07 6.07 6.07
6.07 6.07 6.07 6.07 6.07 6.07 6.07 6.07 6.07 6.07 6.07 6.07 6.07 6.07 6.07 6.07 6.07
6.07 6.07 6.07 6.07 6.07 6.07 6.07 6.07 6.07 6.07 6.07 6.07 6.07 6.07 6.07 6.07 6.07
6.07 6.07 6.07 6.07 6.07 6.07 6.07 6.07 6.07 6.07 6.07 6.07 6.07 6.07 6.07 6.07 6.07
6.08 6.08 6.08 6.08 6.08 6.08 6.08 6.08 6.08 6.08 6.08 6.08 6.08 6.08 6.08 6.08 6.08
6.08 6.08 6.08 6.08 6.08 6.08 6.08 6.08 6.08 6.08 6.08 6.08 6.08 6.08 6.08 6.08 6.08
6.08 6.08 6.08 6.08 6.08 6.08 6.08 6.08 6.08 6.08 6.08 6.08 6.08 6.08 6.08 6.08 6.08
6.08 6.08 6.08 6.08 6.08 6.08 6.08 6.08 6.08 6.08 6.08 6.08 6.08 6.08 6.08 6.08 6.08
6.08 6.08 6.08 6.08 6.08 6.08 6.08 6.08 6.08 6.08 6.08 6.08 6.08 6.08 6.08 6.08 6.08
6.08 6.08 6.08 6.08 6.08 6.08 6.08 6.08 6.08 6.08 6.08 6.08 6.08 6.08 6.08 6.08 6.08
6.08 6.08 6.08 6.08 6.08 6.08 6.08 6.08 6.08 6.08 6.08 6.08 6.08 6.08 6.08 6.08 6.08
6.08 6.08 6.08 6.08 6.08 6.08 6.08 6.08 6.08 6.08 6.08 6.08 6.08 6.08 6.08 6.08 6.08
6.08 6.08 6.08 6.08 6.08 6.08 6.08 6.08 6.08 6.08 6.08 6.08 6.08 6.08 6.08 6.08 6.08

6.08 6.08 6.08 6.08 6.08 6.08 6.08 6.08 6.08 6.08 6.08 6.08 6.08 6.08 6.08 6.08 6.08
6.08 6.08 6.08 6.08 6.08 6.08 6.08 6.08 6.08 6.08 6.08 6.08 6.08 6.08 6.08 6.08 6.08
7.00 7.00 7.00 7.00 7.00 7.00 7.00 7.00 7.00 7.00 7.00 7.00 7.00 7.00 7.00 7.00 7.00
7.00 7.00 7.00 7.00 7.00 7.00 7.00 7.00 7.00 7.00 7.00 7.00 7.00 7.00 7.00 7.00 7.00
7.00 7.00 7.00 7.00 7.00 7.00 7.00 7.00 7.00 7.00 7.00 7.00 7.00 7.00 7.00 7.00 7.00
7.00 7.00 7.00 7.00 7.00 7.00 7.00 7.00 7.00 7.00 7.00 7.00 7.00 7.00 7.00 7.00 7.00
7.00 7.00 7.00 7.00 7.00 7.00 7.00 7.00 7.00 7.00 7.00 7.00 7.00 7.00 7.00 7.00 7.00
7.00 7.00 7.00 7.00 7.00 7.00 7.00 7.00 7.00 7.00 7.00 7.00 7.00 7.00 7.00 7.00 7.00
7.00 7.00 7.00 7.00 7.00 7.00 7.00 7.00 7.00 7.00 7.00 7.00 7.00 7.00 7.00 7.00 7.00
7.00 7.00 7.00 7.00 7.00 7.00 7.00 7.00 7.00 7.00 7.00 7.00 7.00 7.00 7.00 7.00 7.00
7.00 7.00 7.00 7.00 7.00 7.00 7.00 7.00 7.00 7.00 7.00 7.00 7.00 7.00 7.00 7.00 7.00
7.00 7.00 7.00 7.00 7.00 7.00 7.00 7.00 7.00 7.00 7.00 7.00 7.00 7.00 7.00 7.00 7.00
1.74 1.74 1.74 1.74 1.74 1.74 1.74 1.74 1.74 1.74 1.74 1.74 1.74 1.74 1.74 1.74 1.74
1.74 1.74 1.74 1.74 1.74 1.74 1.74 1.74 1.74 1.74 1.74 1.74 1.74 1.74 1.74 1.74 1.74
1.74 1.74 1.74 1.74 1.74 1.74 1.74 1.74 1.74 1.74 1.74 1.74 1.74 1.74 1.74 1.74 1.74
1.74 1.74 1.74 1.74 1.74 1.74 1.74 1.74 1.74 1.74 1.74 1.74 1.74 1.74 1.74 1.74 1.74
1.74 1.74 1.74 1.74 1.74 1.74 1.74 1.74 1.74 1.74 1.74 1.74 1.74 1.74 1.74 1.74 1.74
1.74 1.74 1.74 1.74 1.74 1.74 1.74 1.74 1.74 1.74 1.74 1.74 1.74 1.74 1.74 1.74 1.74
1.74 1.74 1.74 1.74 1.74 1.74 1.74 1.74 1.74 1.74 1.74 1.74 1.74 1.74 1.74 1.74 1.74
1.74 1.74 1.74 1.74 1.74 1.74 1.74 1.74 1.74 1.74 1.74 1.74 1.74 1.74 1.74 1.74 1.74
1.74 1.74 1.74 1.74 1.74 1.74 1.74 1.74 1.74 1.74 1.74 1.74 1.74 1.74 1.74 1.74 1.74
1.74 1.74 1.74 1.74 1.74 1.74 1.74 1.74 1.74 1.74 1.74 1.74 1.74 1.74 1.74 1.74 1.74
1.74 1.74 1.74 1.74 1.74 1.74 1.74 1.74 1.74 1.74 1.74 1.74 1.74 1.74 1.74 1.74 1.74
1.74 1.74 1.74 1.74 1.74 1.74 1.74 1.74 1.74 1.74 1.74 1.74 1.74 1.74 1.74 1.74 1.74
1.74 1.74 1.74 1.74 1.74 1.74 1.74 1.74 1.74 1.74 1.74 1.74 1.74 1.74 1.74 1.74 1.74
1.74 1.74 1.74 1.74 1.74 1.74 1.74 1.74 1.74 1.74 1.74 1.74 1.74 1.74 1.74 1.74 1.74
1.74 1.74 1.74 1.74 1.74 1.74 1.74 1.74 1.74 1.74 1.74 1.74 1.74 1.74 1.74 1.74 1.74
1.74 1.74 1.74 1.74 1.74 1.74 1.74 1.74 1.74 1.74 1.74 1.74 1.74 1.74 1.74 1.74 1.74
1.74 1.74 1.74 1.74 1.74 1.74 1.74 1.74 1.74 1.74 1.74 1.74 1.74 1.74 1.74 1.74 1.74
1.74 1.74 1.74 1.74 1.74 1.74 1.74 1.74 1.74 1.74 1.74 1.74 1.74 1.74 1.74 1.74 1.74
1.74 1.74 1.74 1.74 1.74 1.74 1.74 1.74 1.74 1.74 1.74 1.74 1.74 1.74 1.74 1.74 1.74
1.74 1.74 1.74 1.74 1.74 1.74 1.74 1.74 1.74 1.74 1.74 1.74 1.74 1.74 1.74 1.74 1.74
1.74 1.74 1.74 1.74 1.74 1.74 1.74 1.74 1.74 1.74 1.74 1.74 1.74 1.74 1.74 1.74 1.74
1.74 1.74 1.74 1.74 1.74 1.74 1.74 1.74 1.74 1.74 1.74 1.74 1.74 1.74 1.74 1.74 1.74
1.74 1.74 1.74 1.74 1.74 1.74 1.74 1.74 1.74 1.74 1.74 1.74 1.74 1.74 1.74 1.74 1.74
1.74 1.74 1.74 1.74 1.74 1.74 1.74 1.74 1.74 1.74 1.74 1.74 1.74 1.74 1.74 1.74 1.74
1.74 1.67 1.75 1.74 1.72 1.70 1.60 1.58 1.69 1.70 1.71 1.72 1.71 1.69 1.68 1.65 1.74
1.74 1.75 1.75 1.75 1.74 1.71 1.56 1.55 1.68 1.60 1.59 1.70 1.82 1.83 1.70 1.69 1.74
1.74 1.74 1.76 1.78 1.75 1.69 1.67 1.63 1.69 1.79 1.56 1.81 1.74 1.77 1.71 1.64 1.74
1.74 1.74 1.77 1.78 1.90 1.72 1.65 1.68 1.80 1.85 1.58 1.80 1.67 1.68 1.78 1.71 1.74
1.74 1.74 1.78 1.90 1.89 1.63 1.60 1.60 1.74 1.68 1.75 1.62 1.58 1.60 1.74 1.74 1.74
1.74 1.74 1.76 1.78 1.65 1.68 1.72 1.75 1.71 1.64 1.69 1.74 1.69 1.67 1.70 1.73 1.74
1.74 1.74 1.76 1.78 1.76 1.68 1.62 1.76 1.77 1.73 1.74 1.74 1.70 1.67 1.67 1.70 1.74
1.74 1.74 1.74 1.74 1.73 1.74 1.75 1.74 1.74 1.74 1.73 1.71 1.62 1.68 1.69 1.70 1.74
1.74 1.74 1.74 1.74 1.75 1.75 1.77 1.85 1.67 1.74 1.73 1.81 1.66 1.69 1.69 1.66 1.74
1.74 1.74 1.74 1.74 1.74 1.74 1.74 1.74 1.74 1.74 1.74 1.74 1.74 1.74 1.74 1.74 1.74
1.74 1.74 1.74 1.74 1.74 1.74 1.74 1.74 1.74 1.74 1.74 1.74 1.74 1.74 1.74 1.74 1.74
1.74 1.72 1.74 1.74 1.73 1.71 1.68 1.64 1.69 1.72 1.73 1.74 1.70 1.65 1.65 1.64 1.74
1.74 1.76 1.75 1.75 1.74 1.74 1.61 1.56 1.59 1.65 1.63 1.70 1.80 1.75 1.68 1.69 1.74
1.74 1.74 1.76 1.81 1.80 1.76 1.74 1.68 1.63 1.81 1.64 1.62 1.78 1.73 1.67 1.67 1.74
1.74 1.74 1.78 1.78 1.91 1.88 1.77 1.66 1.72 1.84 1.60 1.66 1.59 1.76 1.69 1.71 1.74
1.74 1.74 1.78 1.87 1.91 1.69 1.68 1.58 1.64 1.68 1.69 1.62 1.61 1.68 1.71 1.74 1.74
1.74 1.74 1.76 1.82 1.71 1.65 1.66 1.74 1.72 1.69 1.73 1.72 1.69 1.66 1.69 1.73 1.74
1.74 1.74 1.76 1.80 1.76 1.68 1.64 1.73 1.79 1.73 1.73 1.71 1.67 1.68 1.69 1.72 1.74
1.74 1.74 1.75 1.75 1.74 1.74 1.78 1.78 1.75 1.74 1.73 1.73 1.64 1.70 1.70 1.71 1.74
1.74 1.74 1.74 1.74 1.75 1.75 1.78 1.81 1.67 1.74 1.74 1.79 1.73 1.72 1.70 1.66 1.74
1.74 1.74 1.74 1.74 1.74 1.74 1.74 1.74 1.74 1.74 1.74 1.74 1.74 1.74 1.74 1.74 1.74
1.74 1.74 1.74 1.74 1.74 1.74 1.74 1.74 1.74 1.74 1.74 1.74 1.74 1.74 1.74 1.74 1.74
1.74 1.76 1.69 1.73 1.73 1.71 1.71 1.71 1.70 1.71 1.72 1.72 1.69 1.64 1.69 1.68 1.74
1.74 1.76 1.77 1.76 1.76 1.73 1.66 1.69 1.60 1.62 1.69 1.70 1.76 1.67 1.68 1.72 1.74

1.74 1.74 1.76 1.81 1.79 1.74 1.72 1.76 1.65 1.74 1.73 1.54 1.72 1.66 1.67 1.71 1.74
1.74 1.74 1.78 1.80 1.70 1.87 1.81 1.66 1.63 1.70 1.74 1.57 1.62 1.71 1.67 1.73 1.74
1.74 1.74 1.76 1.82 1.82 1.74 1.71 1.64 1.61 1.64 1.65 1.65 1.63 1.67 1.70 1.74 1.74
1.74 1.74 1.76 1.81 1.78 1.67 1.66 1.67 1.70 1.76 1.73 1.71 1.64 1.66 1.69 1.73 1.74
1.74 1.74 1.75 1.77 1.74 1.70 1.75 1.72 1.71 1.70 1.70 1.68 1.66 1.68 1.70 1.73 1.74
1.74 1.74 1.75 1.75 1.75 1.74 1.79 1.79 1.75 1.73 1.72 1.71 1.71 1.71 1.71 1.73 1.74
1.74 1.74 1.74 1.74 1.75 1.75 1.74 1.70 1.66 1.71 1.74 1.74 1.74 1.73 1.69 1.68 1.74
1.74 1.74 1.74 1.74 1.74 1.74 1.74 1.74 1.74 1.74 1.74 1.74 1.74 1.74 1.74 1.74 1.74
1.74 1.74 1.74 1.74 1.74 1.74 1.74 1.74 1.74 1.74 1.74 1.74 1.74 1.74 1.74 1.74 1.74
1.74 1.77 1.72 1.66 1.72 1.70 1.72 1.73 1.73 1.73 1.73 1.72 1.65 1.68 1.71 1.69 1.74
1.74 1.75 1.77 1.78 1.82 1.74 1.70 1.74 1.73 1.68 1.66 1.69 1.67 1.67 1.70 1.74 1.74
1.74 1.74 1.78 1.75 1.76 1.70 1.73 1.71 1.76 1.74 1.56 1.53 1.65 1.63 1.69 1.74 1.74
1.74 1.74 1.76 1.78 1.65 1.72 1.79 1.65 1.68 1.65 1.66 1.71 1.66 1.63 1.70 1.74 1.74
1.74 1.74 1.75 1.81 1.77 1.82 1.65 1.63 1.64 1.67 1.69 1.72 1.72 1.68 1.71 1.74 1.74
1.74 1.74 1.75 1.77 1.74 1.72 1.70 1.67 1.67 1.72 1.72 1.71 1.65 1.67 1.71 1.74 1.74
1.74 1.74 1.75 1.75 1.72 1.73 1.76 1.74 1.73 1.74 1.69 1.67 1.69 1.70 1.71 1.74 1.74
1.74 1.74 1.74 1.75 1.75 1.74 1.77 1.77 1.77 1.73 1.70 1.70 1.72 1.71 1.72 1.71 1.74
1.74 1.74 1.74 1.74 1.74 1.73 1.69 1.69 1.69 1.68 1.73 1.74 1.73 1.71 1.70 1.71 1.74
1.74 1.74 1.74 1.74 1.74 1.74 1.74 1.74 1.74 1.74 1.74 1.74 1.74 1.74 1.74 1.74 1.74
1.74 1.74 1.74 1.74 1.74 1.74 1.74 1.74 1.74 1.74 1.74 1.74 1.74 1.74 1.74 1.74 1.74
1.74 1.77 1.76 1.71 1.67 1.70 1.72 1.73 1.73 1.74 1.74 1.67 1.70 1.72 1.74 1.67 1.74
1.74 1.75 1.76 1.76 1.78 1.78 1.77 1.79 1.77 1.71 1.67 1.64 1.66 1.70 1.73 1.74 1.74
1.74 1.74 1.79 1.73 1.75 1.69 1.78 1.79 1.80 1.69 1.68 1.58 1.61 1.67 1.72 1.74 1.74
1.74 1.72 1.76 1.75 1.71 1.66 1.78 1.63 1.70 1.66 1.70 1.67 1.62 1.68 1.72 1.74 1.74
1.74 1.74 1.76 1.79 1.75 1.77 1.72 1.65 1.67 1.71 1.77 1.70 1.72 1.73 1.73 1.74 1.74
1.74 1.74 1.75 1.76 1.74 1.75 1.72 1.69 1.70 1.73 1.74 1.68 1.70 1.74 1.75 1.74 1.74
1.74 1.74 1.74 1.74 1.74 1.73 1.75 1.73 1.75 1.72 1.69 1.71 1.73 1.73 1.74 1.74 1.74
1.74 1.74 1.74 1.74 1.74 1.73 1.69 1.72 1.74 1.72 1.71 1.73 1.72 1.72 1.73 1.74 1.74
1.74 1.74 1.74 1.74 1.74 1.73 1.74 1.71 1.69 1.74 1.74 1.73 1.71 1.66 1.70 1.72 1.74
1.74 1.74 1.74 1.74 1.74 1.74 1.74 1.74 1.74 1.74 1.74 1.74 1.74 1.74 1.74 1.74 1.74
1.74 1.74 1.74 1.74 1.74 1.74 1.74 1.74 1.74 1.74 1.74 1.74 1.74 1.74 1.74 1.74 1.74
1.74 1.74 1.76 1.74 1.72 1.67 1.68 1.71 1.73 1.73 1.72 1.71 1.72 1.65 1.66 1.68 1.74
1.74 1.75 1.76 1.77 1.74 1.76 1.78 1.73 1.70 1.70 1.67 1.68 1.70 1.73 1.73 1.74 1.74
1.74 1.74 1.76 1.79 1.76 1.71 1.75 1.82 1.80 1.73 1.67 1.64 1.66 1.73 1.73 1.74 1.74
1.74 1.72 1.76 1.76 1.71 1.68 1.66 1.70 1.74 1.73 1.68 1.67 1.70 1.74 1.74 1.74 1.74
1.74 1.74 1.76 1.76 1.73 1.71 1.73 1.66 1.71 1.66 1.62 1.67 1.72 1.74 1.74 1.74 1.74
1.74 1.74 1.74 1.75 1.74 1.73 1.69 1.70 1.72 1.72 1.70 1.70 1.72 1.74 1.74 1.74 1.74
1.74 1.74 1.74 1.74 1.75 1.74 1.72 1.73 1.73 1.68 1.72 1.73 1.73 1.73 1.74 1.74 1.74
1.74 1.74 1.74 1.74 1.74 1.75 1.75 1.73 1.70 1.71 1.73 1.73 1.73 1.73 1.73 1.74 1.74
1.74 1.74 1.74 1.74 1.74 1.74 1.77 1.74 1.72 1.74 1.73 1.71 1.68 1.70 1.73 1.74 1.74
1.74 1.74 1.74 1.74 1.74 1.74 1.74 1.74 1.74 1.74 1.74 1.74 1.74 1.74 1.74 1.74 1.74
1.74 1.74 1.74 1.74 1.74 1.74 1.74 1.74 1.74 1.74 1.74 1.74 1.74 1.74 1.74 1.74 1.74
1.74 1.74 1.77 1.78 1.75 1.76 1.74 1.72 1.73 1.72 1.74 1.74 1.74 1.76 1.74 1.74 1.74
1.74 1.75 1.77 1.79 1.71 1.72 1.76 1.74 1.71 1.70 1.71 1.73 1.74 1.76 1.74 1.74 1.74
1.74 1.74 1.77 1.81 1.75 1.72 1.76 1.76 1.72 1.69 1.71 1.67 1.68 1.75 1.74 1.74 1.74
1.74 1.72 1.73 1.78 1.71 1.63 1.68 1.73 1.68 1.70 1.68 1.69 1.71 1.74 1.74 1.74 1.74
1.74 1.74 1.75 1.75 1.71 1.70 1.77 1.80 1.71 1.66 1.68 1.71 1.73 1.74 1.74 1.74 1.74
1.74 1.74 1.74 1.74 1.74 1.69 1.71 1.70 1.70 1.69 1.68 1.73 1.73 1.74 1.74 1.74 1.74
1.74 1.74 1.74 1.74 1.75 1.76 1.74 1.70 1.69 1.70 1.71 1.72 1.74 1.74 1.74 1.74 1.74
1.74 1.74 1.74 1.74 1.74 1.77 1.75 1.73 1.72 1.72 1.72 1.70 1.73 1.74 1.74 1.74 1.74
1.74 1.74 1.74 1.74 1.74 1.74 1.74 1.74 1.74 1.72 1.71 1.69 1.72 1.74 1.74 1.74 1.74
1.74 1.74 1.74 1.74 1.74 1.74 1.74 1.74 1.74 1.74 1.74 1.74 1.74 1.74 1.74 1.74 1.74
1.74 1.74 1.74 1.74 1.74 1.74 1.74 1.74 1.74 1.74 1.74 1.74 1.74 1.74 1.74 1.74 1.74
1.74 1.74 1.74 1.75 1.73 1.73 1.72 1.72 1.73 1.74 1.74 1.73 1.72 1.73 1.74 1.74 1.74
1.74 1.74 1.75 1.76 1.73 1.74 1.73 1.73 1.73 1.73 1.72 1.73 1.74 1.74 1.74 1.74 1.74
1.74 1.74 1.75 1.74 1.75 1.77 1.74 1.71 1.71 1.70 1.71 1.72 1.73 1.74 1.74 1.74 1.74
1.74 1.74 1.75 1.76 1.72 1.74 1.72 1.69 1.70 1.71 1.70 1.73 1.72 1.74 1.74 1.74 1.74
1.74 1.74 1.76 1.76 1.71 1.73 1.76 1.73 1.68 1.71 1.74 1.73 1.74 1.74 1.74 1.74 1.74
1.74 1.74 1.74 1.75 1.77 1.73 1.72 1.71 1.71 1.71 1.72 1.74 1.74 1.74 1.74 1.74 1.74
1.74 1.74 1.74 1.74 1.75 1.75 1.73 1.71 1.73 1.73 1.74 1.74 1.74 1.74 1.74 1.74 1.74

1.74 1.74 1.74 1.74 1.74 1.74 1.73 1.73 1.72 1.73 1.74 1.74 1.74 1.74 1.74 1.74 1.74
1.74 1.74 1.74 1.74 1.74 1.74 1.74 1.74 1.74 1.72 1.74 1.74 1.74 1.74 1.74 1.74 1.74
1.74 1.74 1.74 1.74 1.74 1.74 1.74 1.74 1.74 1.74 1.74 1.74 1.74 1.74 1.74 1.74 1.74
1.74 1.74 1.74 1.74 1.74 1.74 1.74 1.74 1.74 1.74 1.74 1.74 1.74 1.74 1.74 1.74 1.74
1.74 1.74 1.74 1.75 1.72 1.71 1.72 1.72 1.74 1.74 1.74 1.74 1.74 1.74 1.74 1.74 1.74
1.74 1.74 1.74 1.74 1.73 1.72 1.72 1.73 1.73 1.74 1.74 1.74 1.74 1.74 1.74 1.74 1.74
1.74 1.74 1.75 1.75 1.74 1.73 1.72 1.72 1.72 1.72 1.74 1.74 1.74 1.74 1.74 1.74 1.74
1.74 1.74 1.75 1.76 1.75 1.73 1.73 1.72 1.72 1.73 1.74 1.74 1.74 1.74 1.74 1.74 1.74
1.74 1.74 1.75 1.75 1.74 1.72 1.73 1.72 1.72 1.73 1.74 1.74 1.74 1.74 1.74 1.74 1.74
1.74 1.74 1.74 1.74 1.74 1.74 1.74 1.74 1.74 1.74

Appendix 6: Control files used for inversion of (a) combined (b) 1989 (c) 1997 and (d) 2009-2010 data for Long Valley caldera using *simul2000A*.

(a)

```
606  0  0 1.0  4 1 0        neqs, nshot, nblast, wtsht, kout, kout2, kout3
10  1.00  0.020  0.010  -3.00  0.50  0.01  0.00  nitloc, wtsp, eigtol, rmscut, zmin, dxmax, rderr, ercof
5  0.10  0.03  1 5.00  5.00  99.00  0.500  hitct, dvpmax, dvpvsmax, idmp, vpdmp, vpvsdmp, stadmp,
stepl
1  2  5  0.00250 0 0.010  0     ires, i3d, nitmax, snrmct, ihomo, rmstop, ifixl
35.00  50.00  0.40  0.80  1.00    delt1, delt2, res1, res2, res3
9  2  0.50  0.50               ndip, iskip, scale1, scale2
1.20  0.0010 15 15              xfax, tlim, nitpb1, nitpb2
1  1  0                    iusep, iuses, invdel
0  0  0                           iuseq, dqmax, qdamp
```

(b)

```
106  0  0 1.0  4 1 0        neqs, nshot, nblast, wtsht, kout, kout2, kout3
10  1.00  0.020  0.010  -3.00  0.50  0.01  0.00  nitloc, wtsp, eigtol, rmscut, zmin, dxmax, rderr, ercof
5  0.10  0.03  1 20.00  20.00  99.00  0.500  hitct, dvpmax, dvpvsmax, idmp, vpdmp, vpvsdmp, stadmp,
stepl
1  2  2  0.00250 0 0.010  0     ires, i3d, nitmax, snrmct, ihomo, rmstop, ifixl
35.00  50.00  0.40  0.80  1.00    delt1, delt2, res1, res2, res3
9  2  0.50  0.50               ndip, iskip, scale1, scale2
1.20  0.0010 15 15              xfax, tlim, nitpb1, nitpb2
1  1  0                    iusep, iuses, invdel
0  0  0                           iuseq, dqmax, qdamp
```

(c)

```
233  0  0 1.0  4 1 0        neqs, nshot, nblast, wtsht, kout, kout2, kout3
10  1.00  0.020  0.010  -3.00  0.50  0.01  0.00  nitloc, wtsp, eigtol, rmscut, zmin, dxmax, rderr, ercof
5  0.10  0.03  1 20.00  20.00  99.00  0.500  hitct, dvpmax, dvpvsmax, idmp, vpdmp, vpvsdmp, stadmp,
stepl
1  2  3  0.00250 0 0.010  0     ires, i3d, nitmax, snrmct, ihomo, rmstop, ifixl
35.00  50.00  0.40  0.80  1.00    delt1, delt2, res1, res2, res3
9  2  0.50  0.50               ndip, iskip, scale1, scale2
1.20  0.0010 15 15              xfax, tlim, nitpb1, nitpb2
1  1  0                    iusep, iuses, invdel
0  0  0                           iuseq, dqmax, qdamp
```

(d)

```
267  0  0 1.0  4 1 0        neqs, nshot, nblast, wtsht, kout, kout2, kout3
10  1.00  0.020  0.010  -3.00  0.50  0.01  0.00  nitloc, wtsp, eigtol, rmscut, zmin, dxmax, rderr, ercof
5  0.10  0.03  1 20.00  20.00  99.00  0.500  hitct, dvpmax, dvpvsmax, idmp, vpdmp, vpvsdmp, stadmp,
stepl
1  2  4  0.00250 0 0.010  0     ires, i3d, nitmax, snrmct, ihomo, rmstop, ifixl
35.00  50.00  0.40  0.80  1.00    delt1, delt2, res1, res2, res3
9  2  0.50  0.50               ndip, iskip, scale1, scale2
1.20  0.0010 15 15              xfax, tlim, nitpb1, nitpb2
1  1  0                    iusep, iuses, invdel
0  0  0                           iuseq, dqmax, qdamp
```

Appendix 7: Sample of the station file for Long Valley caldera data in the format used by *simul2000A*.

Station Name and Latitude (degrees)	Latitudes (minutes)	Longitudes (degrees)	Longitudes (degrees)	Elevation (meter)	Corrections (s)		
AAR39	16.55	121	1.62	911	0.00	0.00	0
AAS38	25.81	121	6.58	31	0.00	0.00	0
ABJ39	9.95	121	11.58	434	0.00	0.00	0
ABR39	8.29	121	29.29	-1	0.00	0.00	0
ADW38	26.34	120	50.96	228	0.00	0.00	0
AFD38	56.76	120	58.14	505	0.00	0.00	0
AFH39	2.39	120	47.70	1039	0.00	0.00	0
AFO38	56.69	120	58.10	524	0.00	0.00	0
AFR38	47.53	121	20.96	10	0.00	0.00	0
AGI38	50.68	120	58.88	305	0.00	0.00	0
AHR38	51.29	121	4.32	349	0.00	0.00	0
ALA38	34.03	120	57.41	263	0.00	0.00	0
ALN38	55.75	121	17.22	27	0.00	0.00	0
AOD38	36.88	120	43.81	504	0.00	0.00	0
AOH39	22.58	121	15.46	410	0.00	0.00	0
APG38	47.56	121	21.52	2	0.00	0.00	0
APR38	52.62	121	13.09	113	0.00	0.00	0
ARJ38	41.18	120	57.46	437	0.00	0.00	0
ARR38	45.90	121	10.35	100	0.00	0.00	0
ARW38	57.38	121	9.73	320	0.00	0.00	0
ASM38	49.43	120	41.10	1160	0.00	0.00	0
AVR39	1.46	121	16.31	95	0.00	0.00	0
BAP36	10.82	121	38.66	1193	0.00	0.00	0
BAV36	38.76	121	1.81	572	0.00	0.00	0
BBG36	34.68	121	2.35	1065	0.00	0.00	0
BBGB36	34.71	121	2.38	1089	0.00	0.00	0
BBN36	30.60	121	4.53	412	0.00	0.00	0
BCG36	42.58	121	20.57	250	0.00	0.00	0
BCW36	18.39	121	34.01	1505	0.00	0.00	0
BEH36	39.89	121	10.52	334	0.00	0.00	0
BEM36	39.67	121	5.81	464	0.00	0.00	0
BHR36	43.65	121	15.99	175	0.00	0.00	0
BHS36	21.35	121	32.39	646	0.00	0.00	0
BJC36	32.82	121	23.53	173	0.00	0.00	0
BJO36	36.66	121	18.85	1020	0.00	0.00	0
BJOB36	37.09	121	18.88	1052	0.00	0.00	0
BLR36	40.02	121	16.40	189	0.00	0.00	0
BMS36	39.79	120	47.57	780	0.00	0.00	0
BPC36	34.40	121	37.61	173	0.00	0.00	0
BPF36	13.82	121	46.32	349	0.00	0.00	0
BPI36	29.41	121	10.18	301	0.00	0.00	0
BPO36	13.70	121	46.06	330	0.00	0.00	0
BPP36	10.12	121	22.68	1591	0.00	0.00	0

Appendix 8: Sample of the *simul*-format arrival-time measurement file for Long Valley caldera data for the year 2009-2010.

100103 1010 40.88 37N36.70 118W55.29 3.44
MCB_Pu1 1.550 MCM_Pu1 1.356 MCS_Pu1 1.645MDH1_Pd1 1.601 MDR_Pu1 2.156 MGP_Pu1 1.286 MMLB_Pd1 2.074 MMP_Pu1 2.206 MMT_Pu1 6.306 MRD_Pu1 2.666 MSL_Pu1 1.326 MTU_Pd1 7.886

100110 1229 18.05 37N37.02 119W02.77 1.93
MCB_Pu1 2.901 MCV_Pu1 3.637MDPB_Pd1 1.088 MDR_Pu1 3.847 MEM_Pd1 1.327 MGP_Pu1 2.747 MLC_Pu1 2.387 MLK_Pu1 1.993MMLB_Pu1 1.865 MMP_Pd1 1.027MQ2P_Pu1 1.208 MRD_Pd1 1.127

100111 0937 57.62 37N36.44 118W51.73 8.34
MCB_Pd1 2.315 MCM_Pd1 2.011 MCS_Pu1 2.451 MCV_Pd1 2.121 MDC_Pu1 4.111MDPB_Pd1 4.031 MDR_Pu1 2.012 MGP_Pd1 2.221MLAC_Pd1 2.137MMLB_Pu1 3.129 MMP_Pu1 3.411 MMS_Pu1 3.682 MMT_Pu1 7.182MQ2P_Pu1 3.651 MRD_Pu1 3.851 MSL_Pu1 2.601

100115 1426 35.62 37N36.90 119W02.93 3.38
MCB_Pu1 3.036 MCM_Pu1 3.123 MDC_Pu1 2.303MDPB_Pd1 1.273 MGP_Pu1 2.873 MLC_Pu1 2.523 MLK_Pu1 2.208MMLB_Pu1 2.050 MMP_Pd1 1.213 MMT_Pu2 5.643 MRD_Pd1 1.373

100117 0345 29.74 37N36.48 119W02.52 2.12
MCB_Pu1 2.929 MCM_Pu1 2.995 MDC_Pu1 2.165MDPB_Pu1 1.115 MGP_Pu1 2.755 MLK_Pu1 2.100 MLM_Pu1 3.416MMLB_Pu1 1.933 MMP_Pd1 1.094 MMS_Pd1 1.285MQ2P_Pu1 1.295 MSL_Pd1 1.846

100119 1454 10.08 37N36.11 118W55.05 4.93
MCB_Pu1 1.818 MCS_Pu1 1.875 MDC_Pd1 3.265MDH1_Pu1 1.658 MDR_Pu1 2.114 MEM_Pu1 2.104 MGP_Pu1 1.604MLAC_Pu1 2.000 MLC_Pu1 1.464 MLM_Pu1 3.355 MMP_Pd1 2.375 MMS_Pd1 2.665 MRD_Pd1 2.795 MSL_Pd1 1.685 MTU_Pd1 7.264

100121 2341 07.55 37N37.68 118W55.71 5.66
MCB_Pd1 1.804 MCS_Pd1 1.770 MCV_Pd1 2.370 MDC_Pu1 2.800MDH1_Pd1 1.319MDH1_Sp2 0.826 MDR_Pu1 2.290 MEM_Pd1 1.810 MLC_Pd1 1.660 MLM_Pu1 2.750MMLB_Pd1 2.008 MMP_Pd1 2.360 MMS_Pd1 2.550MQ2P_Pd1 2.430 MRD_Pd1 2.810 MSL_Pd1 1.740

100121 2344 51.02 37N37.38 118W55.27 5.22
MCB_Pd1 1.811 MEM_Pu1 1.767 MLC_Pd1 1.667 MLM_Pu1 2.787MMLB_Pd1 2.006 MMP_Pd1 2.358 MMS_Pd1 2.557 MRD_Pd1 2.807 MSL_Pd1 1.738

100121 2348 20.48 37N40.56 118W56.98 2.27
MCB_Pd1 1.739 MDR_Pu1 2.345 MGP_Pd1 1.665 MLC_Pd1 1.595 MMP_Pu1 2.316 MRD_Pd1 2.746 MSL_Pd1 1.656

100121 2358 06.95 37N39.43 118W55.85 2.01
MCB_Pd1 1.382 MCS_Pd1 1.339 MDC_Pu1 2.399MDH1_Pd1 0.902MDH1_Sp2 0.830 MDR_Pd1 1.899 MGP_Pd1 1.329 MLC_Pd1 1.259 MLM_Pu1 2.349MMLB_Pd1 1.617 MMP_Pd1 1.949 MMS_Pd1 2.159 MMT_Pu1 6.149 MRD_Pd1 2.399 MSL_Pd1 1.329

100122 0018 07.01 37N37.75 118W55.83 5.12
MCB_Pd1 1.696 MCS_Pu1 1.653MDH1_Pd1 1.217MDH1_Sp2 0.838 MEM_Pd1 1.693 MGP_Pd1 1.624 MLC_Pd1 1.553 MLM_Pu1 2.673MMLB_Pu1 1.781 MMP_Pd1 2.244 MMS_Pd1 2.463 MRD_Pd1 2.703 MSL_Pd1 1.633

100129 0339 54.22 37N34.70 118W48.80 3.99
MCB_Pu1 2.461 MCD_Pu1 6.237 MCM_Pu1 1.767 MCS_Pu1 2.657 MCV_Pu1 1.337MDPB_Pu1 4.637 MGP_Pu1 2.307MLAC_Pu1 1.662 MLC_Pu1 2.347 MLH_Pd1 2.427 MLK_Pu1 3.724MMLB_Pu1 3.645 MMP_Pu1 3.877 MMS_Pu1 4.177MQ2P_Pu1 4.152 MRD_Pu1 4.337

Appendix 9: *simul2000A* program execute script used for inversion of 2009-2010 data for Long Valley caldera.

```
#!/bin/csh

################## INPUT FILES: ##################
ln -s control          CNTL          # Control file
ln -s stations  STNS          # Station data file
ln -s grid                    MOD           # Node grid and initial-wave speed model
ln -s picks           EQKS          # Traveltime data for earthquakes
#ln -s ../data/in.shot91                fort.7         # Traveltime data for shots
# ln -s |><|                            fort.8         # Traveltime data for blasts

#################  RUN SIMULPS: #################
echo "Start:  `date`."
simul2000A
echo "Stop:  `date`."

#################  CLEAN UP: ###################
echo "Unlinking files..."
\rm     CNTL
\rm     EQKS
\rm     STNS
\rm     MOD
\rm     f28
\rm     finalsmpout
\rm     fort.47
\rm     hypo.gmt
\rm     hypo71list
\rm     resfile
\rm     results.for_plot
\rm     summary
\rm     velfile
#/bin/rm                fort.1
#/bin/rm                fort.2
#/bin/rm                fort.3
#/bin/rm                fort.4
#/bin/rm                fort.7
#/bin/rm             fort.8

mv      output  print.out
#mv     fort.18 nodes.out
mv      residuals resid.out
mv      f24 ttfin.out
mv      pseudo rays.out
mv      itersum summary.out
```

Appendix 10: (a) The initial V_p model - the initial V_p/V_s ratio is 1.74 - and (b) sample of the station file used for inversion with *tomo4d* for Long Valley caldera for the years 1997 and 2009-2010

(a)

```
6371.2
37:34.42  -118:47.47  90.00
17 11 15
-50.0   0.0   2.0   4.0   6.0   8.0  10.0  12.0  14.0  16.0  18.0  20.0  22.0  24.0  26.0  28.0  78.0
-50.0   0.0   2.0   4.0   6.0   8.0  10.0  12.0  14.0  16.0  66.0
-50.0  -4.0  -2.0  -1.0   0.0   1.0   2.0   3.0   4.0   5.0   6.0   7.0   8.0  10.0  60.0

2.50 2.50 2.50 2.50 2.50 2.50 2.50 2.50 2.50 2.50 2.50 2.50 2.50 2.50 2.50 2.50 2.50
2.50 2.50 2.50 2.50 2.50 2.50 2.50 2.50 2.50 2.50 2.50 2.50 2.50 2.50 2.50 2.50 2.50
2.50 2.50 2.50 2.50 2.50 2.50 2.50 2.50 2.50 2.50 2.50 2.50 2.50 2.50 2.50 2.50 2.50
2.50 2.50 2.50 2.50 2.50 2.50 2.50 2.50 2.50 2.50 2.50 2.50 2.50 2.50 2.50 2.50 2.50
2.50 2.50 2.50 2.50 2.50 2.50 2.50 2.50 2.50 2.50 2.50 2.50 2.50 2.50 2.50 2.50 2.50
2.50 2.50 2.50 2.50 2.50 2.50 2.50 2.50 2.50 2.50 2.50 2.50 2.50 2.50 2.50 2.50 2.50
2.50 2.50 2.50 2.50 2.50 2.50 2.50 2.50 2.50 2.50 2.50 2.50 2.50 2.50 2.50 2.50 2.50
2.50 2.50 2.50 2.50 2.50 2.50 2.50 2.50 2.50 2.50 2.50 2.50 2.50 2.50 2.50 2.50 2.50
2.50 2.50 2.50 2.50 2.50 2.50 2.50 2.50 2.50 2.50 2.50 2.50 2.50 2.50 2.50 2.50 2.50
2.50 2.50 2.50 2.50 2.50 2.50 2.50 2.50 2.50 2.50 2.50 2.50 2.50 2.50 2.50 2.50 2.50
2.50 2.50 2.50 2.50 2.50 2.50 2.50 2.50 2.50 2.50 2.50 2.50 2.50 2.50 2.50 2.50 2.50

3.00 3.00 3.00 3.00 3.00 3.00 3.00 3.00 3.00 3.00 3.00 3.00 3.00 3.00 3.00 3.00 3.00
3.00 3.00 3.00 3.00 3.00 3.00 3.00 3.00 3.00 3.00 3.00 3.00 3.00 3.00 3.00 3.00 3.00
3.00 3.00 3.00 3.00 3.00 3.00 3.00 3.00 3.00 3.00 3.00 3.00 3.00 3.00 3.00 3.00 3.00
3.00 3.00 3.00 3.00 3.00 3.00 3.00 3.00 3.00 3.00 3.00 3.00 3.00 3.00 3.00 3.00 3.00
3.00 3.00 3.00 3.00 3.00 3.00 3.00 3.00 3.00 3.00 3.00 3.00 3.00 3.00 3.00 3.00 3.00
3.00 3.00 3.00 3.00 3.00 3.00 3.00 3.00 3.00 3.00 3.00 3.00 3.00 3.00 3.00 3.00 3.00
3.00 3.00 3.00 3.00 3.00 3.00 3.00 3.00 3.00 3.00 3.00 3.00 3.00 3.00 3.00 3.00 3.00
3.00 3.00 3.00 3.00 3.00 3.00 3.00 3.00 3.00 3.00 3.00 3.00 3.00 3.00 3.00 3.00 3.00
3.00 3.00 3.00 3.00 3.00 3.00 3.00 3.00 3.00 3.00 3.00 3.00 3.00 3.00 3.00 3.00 3.00
3.00 3.00 3.00 3.00 3.00 3.00 3.00 3.00 3.00 3.00 3.00 3.00 3.00 3.00 3.00 3.00 3.00
3.00 3.00 3.00 3.00 3.00 3.00 3.00 3.00 3.00 3.00 3.00 3.00 3.00 3.00 3.00 3.00 3.00

3.55 3.55 3.55 3.55 3.55 3.55 3.55 3.55 3.55 3.55 3.55 3.55 3.55 3.55 3.55 3.55 3.55
3.55 3.55 3.55 3.55 3.55 3.55 3.55 3.55 3.55 3.55 3.55 3.55 3.55 3.55 3.55 3.55 3.55
3.55 3.55 3.55 3.55 3.55 3.55 3.55 3.55 3.55 3.55 3.55 3.55 3.55 3.55 3.55 3.55 3.55
3.55 3.55 3.55 3.55 3.55 3.55 3.55 3.55 3.55 3.55 3.55 3.55 3.55 3.55 3.55 3.55 3.55
3.55 3.55 3.55 3.55 3.55 3.55 3.55 3.55 3.55 3.55 3.55 3.55 3.55 3.55 3.55 3.55 3.55
3.55 3.55 3.55 3.55 3.55 3.55 3.55 3.55 3.55 3.55 3.55 3.55 3.55 3.55 3.55 3.55 3.55
3.55 3.55 3.55 3.55 3.55 3.55 3.55 3.55 3.55 3.55 3.55 3.55 3.55 3.55 3.55 3.55 3.55
3.55 3.55 3.55 3.55 3.55 3.55 3.55 3.55 3.55 3.55 3.55 3.55 3.55 3.55 3.55 3.55 3.55
3.55 3.55 3.55 3.55 3.55 3.55 3.55 3.55 3.55 3.55 3.55 3.55 3.55 3.55 3.55 3.55 3.55
3.55 3.55 3.55 3.55 3.55 3.55 3.55 3.55 3.55 3.55 3.55 3.55 3.55 3.55 3.55 3.55 3.55
3.55 3.55 3.55 3.55 3.55 3.55 3.55 3.55 3.55 3.55 3.55 3.55 3.55 3.55 3.55 3.55 3.55

4.45 4.45 4.45 4.45 4.45 4.45 4.45 4.45 4.45 4.45 4.45 4.45 4.45 4.45 4.45 4.45 4.45
4.45 4.45 4.45 4.45 4.45 4.45 4.45 4.45 4.45 4.45 4.45 4.45 4.45 4.45 4.45 4.45 4.45
4.45 4.45 4.45 4.45 4.45 4.45 4.45 4.45 4.45 4.45 4.45 4.45 4.45 4.45 4.45 4.45 4.45
4.45 4.45 4.45 4.45 4.45 4.45 4.45 4.45 4.45 4.45 4.45 4.45 4.45 4.45 4.45 4.45 4.45
4.45 4.45 4.45 4.45 4.45 4.45 4.45 4.45 4.45 4.45 4.45 4.45 4.45 4.45 4.45 4.45 4.45
4.45 4.45 4.45 4.45 4.45 4.45 4.45 4.45 4.45 4.45 4.45 4.45 4.45 4.45 4.45 4.45 4.45
4.45 4.45 4.45 4.45 4.45 4.45 4.45 4.45 4.45 4.45 4.45 4.45 4.45 4.45 4.45 4.45 4.45
4.45 4.45 4.45 4.45 4.45 4.45 4.45 4.45 4.45 4.45 4.45 4.45 4.45 4.45 4.45 4.45 4.45
4.45 4.45 4.45 4.45 4.45 4.45 4.45 4.45 4.45 4.45 4.45 4.45 4.45 4.45 4.45 4.45 4.45
4.45 4.45 4.45 4.45 4.45 4.45 4.45 4.45 4.45 4.45 4.45 4.45 4.45 4.45 4.45 4.45 4.45
```

4.45 4.45 4.45 4.45 4.45 4.45 4.45 4.45 4.45 4.45 4.45 4.45 4.45 4.45 4.45 4.45 4.45
4.45 4.45 4.45 4.45 4.45 4.45 4.45 4.45 4.45 4.45 4.45 4.45 4.45 4.45 4.45 4.45 4.45

5.35 5.35 5.35 5.35 5.35 5.35 5.35 5.35 5.35 5.35 5.35 5.35 5.35 5.35 5.35 5.35 5.35
5.35 5.35 5.35 5.35 5.35 5.35 5.35 5.35 5.35 5.35 5.35 5.35 5.35 5.35 5.35 5.35 5.35
5.35 5.35 5.35 5.35 5.35 5.35 5.35 5.35 5.35 5.35 5.35 5.35 5.35 5.35 5.35 5.35 5.35
5.35 5.35 5.35 5.35 5.35 5.35 5.35 5.35 5.35 5.35 5.35 5.35 5.35 5.35 5.35 5.35 5.35
5.35 5.35 5.35 5.35 5.35 5.35 5.35 5.35 5.35 5.35 5.35 5.35 5.35 5.35 5.35 5.35 5.35
5.35 5.35 5.35 5.35 5.35 5.35 5.35 5.35 5.35 5.35 5.35 5.35 5.35 5.35 5.35 5.35 5.35
5.35 5.35 5.35 5.35 5.35 5.35 5.35 5.35 5.35 5.35 5.35 5.35 5.35 5.35 5.35 5.35 5.35
5.35 5.35 5.35 5.35 5.35 5.35 5.35 5.35 5.35 5.35 5.35 5.35 5.35 5.35 5.35 5.35 5.35
5.35 5.35 5.35 5.35 5.35 5.35 5.35 5.35 5.35 5.35 5.35 5.35 5.35 5.35 5.35 5.35 5.35
5.35 5.35 5.35 5.35 5.35 5.35 5.35 5.35 5.35 5.35 5.35 5.35 5.35 5.35 5.35 5.35 5.35

5.56 5.56 5.56 5.56 5.56 5.56 5.56 5.56 5.56 5.56 5.56 5.56 5.56 5.56 5.56 5.56 5.56
5.56 5.56 5.56 5.56 5.56 5.56 5.56 5.56 5.56 5.56 5.56 5.56 5.56 5.56 5.56 5.56 5.56
5.56 5.56 5.56 5.56 5.56 5.56 5.56 5.56 5.56 5.56 5.56 5.56 5.56 5.56 5.56 5.56 5.56
5.56 5.56 5.56 5.56 5.56 5.56 5.56 5.56 5.56 5.56 5.56 5.56 5.56 5.56 5.56 5.56 5.56
5.56 5.56 5.56 5.56 5.56 5.56 5.56 5.56 5.56 5.56 5.56 5.56 5.56 5.56 5.56 5.56 5.56
5.56 5.56 5.56 5.56 5.56 5.56 5.56 5.56 5.56 5.56 5.56 5.56 5.56 5.56 5.56 5.56 5.56
5.56 5.56 5.56 5.56 5.56 5.56 5.56 5.56 5.56 5.56 5.56 5.56 5.56 5.56 5.56 5.56 5.56
5.56 5.56 5.56 5.56 5.56 5.56 5.56 5.56 5.56 5.56 5.56 5.56 5.56 5.56 5.56 5.56 5.56
5.56 5.56 5.56 5.56 5.56 5.56 5.56 5.56 5.56 5.56 5.56 5.56 5.56 5.56 5.56 5.56 5.56
5.56 5.56 5.56 5.56 5.56 5.56 5.56 5.56 5.56 5.56 5.56 5.56 5.56 5.56 5.56 5.56 5.56

5.78 5.78 5.78 5.78 5.78 5.78 5.78 5.78 5.78 5.78 5.78 5.78 5.78 5.78 5.78 5.78 5.78
5.78 5.78 5.78 5.78 5.78 5.78 5.78 5.78 5.78 5.78 5.78 5.78 5.78 5.78 5.78 5.78 5.78
5.78 5.78 5.78 5.78 5.78 5.78 5.78 5.78 5.78 5.78 5.78 5.78 5.78 5.78 5.78 5.78 5.78
5.78 5.78 5.78 5.78 5.78 5.78 5.78 5.78 5.78 5.78 5.78 5.78 5.78 5.78 5.78 5.78 5.78
5.78 5.78 5.78 5.78 5.78 5.78 5.78 5.78 5.78 5.78 5.78 5.78 5.78 5.78 5.78 5.78 5.78
5.78 5.78 5.78 5.78 5.78 5.78 5.78 5.78 5.78 5.78 5.78 5.78 5.78 5.78 5.78 5.78 5.78
5.78 5.78 5.78 5.78 5.78 5.78 5.78 5.78 5.78 5.78 5.78 5.78 5.78 5.78 5.78 5.78 5.78
5.78 5.78 5.78 5.78 5.78 5.78 5.78 5.78 5.78 5.78 5.78 5.78 5.78 5.78 5.78 5.78 5.78
5.78 5.78 5.78 5.78 5.78 5.78 5.78 5.78 5.78 5.78 5.78 5.78 5.78 5.78 5.78 5.78 5.78
5.78 5.78 5.78 5.78 5.78 5.78 5.78 5.78 5.78 5.78 5.78 5.78 5.78 5.78 5.78 5.78 5.78

5.87 5.87 5.87 5.87 5.87 5.87 5.87 5.87 5.87 5.87 5.87 5.87 5.87 5.87 5.87 5.87 5.87
5.87 5.87 5.87 5.87 5.87 5.87 5.87 5.87 5.87 5.87 5.87 5.87 5.87 5.87 5.87 5.87 5.87
5.87 5.87 5.87 5.87 5.87 5.87 5.87 5.87 5.87 5.87 5.87 5.87 5.87 5.87 5.87 5.87 5.87
5.87 5.87 5.87 5.87 5.87 5.87 5.87 5.87 5.87 5.87 5.87 5.87 5.87 5.87 5.87 5.87 5.87
5.87 5.87 5.87 5.87 5.87 5.87 5.87 5.87 5.87 5.87 5.87 5.87 5.87 5.87 5.87 5.87 5.87
5.87 5.87 5.87 5.87 5.87 5.87 5.87 5.87 5.87 5.87 5.87 5.87 5.87 5.87 5.87 5.87 5.87
5.87 5.87 5.87 5.87 5.87 5.87 5.87 5.87 5.87 5.87 5.87 5.87 5.87 5.87 5.87 5.87 5.87
5.87 5.87 5.87 5.87 5.87 5.87 5.87 5.87 5.87 5.87 5.87 5.87 5.87 5.87 5.87 5.87 5.87
5.87 5.87 5.87 5.87 5.87 5.87 5.87 5.87 5.87 5.87 5.87 5.87 5.87 5.87 5.87 5.87 5.87
5.87 5.87 5.87 5.87 5.87 5.87 5.87 5.87 5.87 5.87 5.87 5.87 5.87 5.87 5.87 5.87 5.87

5.96 5.96 5.96 5.96 5.96 5.96 5.96 5.96 5.96 5.96 5.96 5.96 5.96 5.96 5.96 5.96 5.96
5.96 5.96 5.96 5.96 5.96 5.96 5.96 5.96 5.96 5.96 5.96 5.96 5.96 5.96 5.96 5.96 5.96
5.96 5.96 5.96 5.96 5.96 5.96 5.96 5.96 5.96 5.96 5.96 5.96 5.96 5.96 5.96 5.96 5.96
5.96 5.96 5.96 5.96 5.96 5.96 5.96 5.96 5.96 5.96 5.96 5.96 5.96 5.96 5.96 5.96 5.96
5.96 5.96 5.96 5.96 5.96 5.96 5.96 5.96 5.96 5.96 5.96 5.96 5.96 5.96 5.96 5.96 5.96
5.96 5.96 5.96 5.96 5.96 5.96 5.96 5.96 5.96 5.96 5.96 5.96 5.96 5.96 5.96 5.96 5.96
5.96 5.96 5.96 5.96 5.96 5.96 5.96 5.96 5.96 5.96 5.96 5.96 5.96 5.96 5.96 5.96 5.96
5.96 5.96 5.96 5.96 5.96 5.96 5.96 5.96 5.96 5.96 5.96 5.96 5.96 5.96 5.96 5.96 5.96
5.96 5.96 5.96 5.96 5.96 5.96 5.96 5.96 5.96 5.96 5.96 5.96 5.96 5.96 5.96 5.96 5.96
5.96 5.96 5.96 5.96 5.96 5.96 5.96 5.96 5.96 5.96 5.96 5.96 5.96 5.96 5.96 5.96 5.96

5.96 5.96 5.96 5.96 5.96 5.96 5.96 5.96 5.96 5.96 5.96 5.96 5.96 5.96 5.96 5.96 5.96
5.96 5.96 5.96 5.96 5.96 5.96 5.96 5.96 5.96 5.96 5.96 5.96 5.96 5.96 5.96 5.96 5.96

6.00 6.00 6.00 6.00 6.00 6.00 6.00 6.00 6.00 6.00 6.00 6.00 6.00 6.00 6.00 6.00 6.00
6.00 6.00 6.00 6.00 6.00 6.00 6.00 6.00 6.00 6.00 6.00 6.00 6.00 6.00 6.00 6.00 6.00
6.00 6.00 6.00 6.00 6.00 6.00 6.00 6.00 6.00 6.00 6.00 6.00 6.00 6.00 6.00 6.00 6.00
6.00 6.00 6.00 6.00 6.00 6.00 6.00 6.00 6.00 6.00 6.00 6.00 6.00 6.00 6.00 6.00 6.00
6.00 6.00 6.00 6.00 6.00 6.00 6.00 6.00 6.00 6.00 6.00 6.00 6.00 6.00 6.00 6.00 6.00
6.00 6.00 6.00 6.00 6.00 6.00 6.00 6.00 6.00 6.00 6.00 6.00 6.00 6.00 6.00 6.00 6.00
6.00 6.00 6.00 6.00 6.00 6.00 6.00 6.00 6.00 6.00 6.00 6.00 6.00 6.00 6.00 6.00 6.00
6.00 6.00 6.00 6.00 6.00 6.00 6.00 6.00 6.00 6.00 6.00 6.00 6.00 6.00 6.00 6.00 6.00
6.00 6.00 6.00 6.00 6.00 6.00 6.00 6.00 6.00 6.00 6.00 6.00 6.00 6.00 6.00 6.00 6.00
6.00 6.00 6.00 6.00 6.00 6.00 6.00 6.00 6.00 6.00 6.00 6.00 6.00 6.00 6.00 6.00 6.00

6.04 6.04 6.04 6.04 6.04 6.04 6.04 6.04 6.04 6.04 6.04 6.04 6.04 6.04 6.04 6.04 6.04
6.04 6.04 6.04 6.04 6.04 6.04 6.04 6.04 6.04 6.04 6.04 6.04 6.04 6.04 6.04 6.04 6.04
6.04 6.04 6.04 6.04 6.04 6.04 6.04 6.04 6.04 6.04 6.04 6.04 6.04 6.04 6.04 6.04 6.04
6.04 6.04 6.04 6.04 6.04 6.04 6.04 6.04 6.04 6.04 6.04 6.04 6.04 6.04 6.04 6.04 6.04
6.04 6.04 6.04 6.04 6.04 6.04 6.04 6.04 6.04 6.04 6.04 6.04 6.04 6.04 6.04 6.04 6.04
6.04 6.04 6.04 6.04 6.04 6.04 6.04 6.04 6.04 6.04 6.04 6.04 6.04 6.04 6.04 6.04 6.04
6.04 6.04 6.04 6.04 6.04 6.04 6.04 6.04 6.04 6.04 6.04 6.04 6.04 6.04 6.04 6.04 6.04
6.04 6.04 6.04 6.04 6.04 6.04 6.04 6.04 6.04 6.04 6.04 6.04 6.04 6.04 6.04 6.04 6.04
6.04 6.04 6.04 6.04 6.04 6.04 6.04 6.04 6.04 6.04 6.04 6.04 6.04 6.04 6.04 6.04 6.04
6.04 6.04 6.04 6.04 6.04 6.04 6.04 6.04 6.04 6.04 6.04 6.04 6.04 6.04 6.04 6.04 6.04

6.06 6.06 6.06 6.06 6.06 6.06 6.06 6.06 6.06 6.06 6.06 6.06 6.06 6.06 6.06 6.06 6.06
6.06 6.06 6.06 6.06 6.06 6.06 6.06 6.06 6.06 6.06 6.06 6.06 6.06 6.06 6.06 6.06 6.06
6.06 6.06 6.06 6.06 6.06 6.06 6.06 6.06 6.06 6.06 6.06 6.06 6.06 6.06 6.06 6.06 6.06
6.06 6.06 6.06 6.06 6.06 6.06 6.06 6.06 6.06 6.06 6.06 6.06 6.06 6.06 6.06 6.06 6.06
6.06 6.06 6.06 6.06 6.06 6.06 6.06 6.06 6.06 6.06 6.06 6.06 6.06 6.06 6.06 6.06 6.06
6.06 6.06 6.06 6.06 6.06 6.06 6.06 6.06 6.06 6.06 6.06 6.06 6.06 6.06 6.06 6.06 6.06
6.06 6.06 6.06 6.06 6.06 6.06 6.06 6.06 6.06 6.06 6.06 6.06 6.06 6.06 6.06 6.06 6.06
6.06 6.06 6.06 6.06 6.06 6.06 6.06 6.06 6.06 6.06 6.06 6.06 6.06 6.06 6.06 6.06 6.06
6.06 6.06 6.06 6.06 6.06 6.06 6.06 6.06 6.06 6.06 6.06 6.06 6.06 6.06 6.06 6.06 6.06
6.06 6.06 6.06 6.06 6.06 6.06 6.06 6.06 6.06 6.06 6.06 6.06 6.06 6.06 6.06 6.06 6.06

6.07 6.07 6.07 6.07 6.07 6.07 6.07 6.07 6.07 6.07 6.07 6.07 6.07 6.07 6.07 6.07 6.07
6.07 6.07 6.07 6.07 6.07 6.07 6.07 6.07 6.07 6.07 6.07 6.07 6.07 6.07 6.07 6.07 6.07
6.07 6.07 6.07 6.07 6.07 6.07 6.07 6.07 6.07 6.07 6.07 6.07 6.07 6.07 6.07 6.07 6.07
6.07 6.07 6.07 6.07 6.07 6.07 6.07 6.07 6.07 6.07 6.07 6.07 6.07 6.07 6.07 6.07 6.07
6.07 6.07 6.07 6.07 6.07 6.07 6.07 6.07 6.07 6.07 6.07 6.07 6.07 6.07 6.07 6.07 6.07
6.07 6.07 6.07 6.07 6.07 6.07 6.07 6.07 6.07 6.07 6.07 6.07 6.07 6.07 6.07 6.07 6.07
6.07 6.07 6.07 6.07 6.07 6.07 6.07 6.07 6.07 6.07 6.07 6.07 6.07 6.07 6.07 6.07 6.07
6.07 6.07 6.07 6.07 6.07 6.07 6.07 6.07 6.07 6.07 6.07 6.07 6.07 6.07 6.07 6.07 6.07
6.07 6.07 6.07 6.07 6.07 6.07 6.07 6.07 6.07 6.07 6.07 6.07 6.07 6.07 6.07 6.07 6.07
6.07 6.07 6.07 6.07 6.07 6.07 6.07 6.07 6.07 6.07 6.07 6.07 6.07 6.07 6.07 6.07 6.07

6.08 6.08 6.08 6.08 6.08 6.08 6.08 6.08 6.08 6.08 6.08 6.08 6.08 6.08 6.08 6.08 6.08
6.08 6.08 6.08 6.08 6.08 6.08 6.08 6.08 6.08 6.08 6.08 6.08 6.08 6.08 6.08 6.08 6.08
6.08 6.08 6.08 6.08 6.08 6.08 6.08 6.08 6.08 6.08 6.08 6.08 6.08 6.08 6.08 6.08 6.08
6.08 6.08 6.08 6.08 6.08 6.08 6.08 6.08 6.08 6.08 6.08 6.08 6.08 6.08 6.08 6.08 6.08
6.08 6.08 6.08 6.08 6.08 6.08 6.08 6.08 6.08 6.08 6.08 6.08 6.08 6.08 6.08 6.08 6.08
6.08 6.08 6.08 6.08 6.08 6.08 6.08 6.08 6.08 6.08 6.08 6.08 6.08 6.08 6.08 6.08 6.08
6.08 6.08 6.08 6.08 6.08 6.08 6.08 6.08 6.08 6.08 6.08 6.08 6.08 6.08 6.08 6.08 6.08
6.08 6.08 6.08 6.08 6.08 6.08 6.08 6.08 6.08 6.08 6.08 6.08 6.08 6.08 6.08 6.08 6.08
6.08 6.08 6.08 6.08 6.08 6.08 6.08 6.08 6.08 6.08 6.08 6.08 6.08 6.08 6.08 6.08 6.08
6.08 6.08 6.08 6.08 6.08 6.08 6.08 6.08 6.08 6.08 6.08 6.08 6.08 6.08 6.08 6.08 6.08

6.08 6.08 6.08 6.08 6.08 6.08 6.08 6.08 6.08 6.08 6.08 6.08 6.08 6.08 6.08 6.08 6.08
6.08 6.08 6.08 6.08 6.08 6.08 6.08 6.08 6.08 6.08 6.08 6.08 6.08 6.08 6.08 6.08 6.08

7.00 7.00 7.00 7.00 7.00 7.00 7.00 7.00 7.00 7.00 7.00 7.00 7.00 7.00 7.00 7.00 7.00
7.00 7.00 7.00 7.00 7.00 7.00 7.00 7.00 7.00 7.00 7.00 7.00 7.00 7.00 7.00 7.00 7.00
7.00 7.00 7.00 7.00 7.00 7.00 7.00 7.00 7.00 7.00 7.00 7.00 7.00 7.00 7.00 7.00 7.00
7.00 7.00 7.00 7.00 7.00 7.00 7.00 7.00 7.00 7.00 7.00 7.00 7.00 7.00 7.00 7.00 7.00
7.00 7.00 7.00 7.00 7.00 7.00 7.00 7.00 7.00 7.00 7.00 7.00 7.00 7.00 7.00 7.00 7.00
7.00 7.00 7.00 7.00 7.00 7.00 7.00 7.00 7.00 7.00 7.00 7.00 7.00 7.00 7.00 7.00 7.00
7.00 7.00 7.00 7.00 7.00 7.00 7.00 7.00 7.00 7.00 7.00 7.00 7.00 7.00 7.00 7.00 7.00
7.00 7.00 7.00 7.00 7.00 7.00 7.00 7.00 7.00 7.00 7.00 7.00 7.00 7.00 7.00 7.00 7.00
7.00 7.00 7.00 7.00 7.00 7.00 7.00 7.00 7.00 7.00 7.00 7.00 7.00 7.00 7.00 7.00 7.00
7.00 7.00 7.00 7.00 7.00 7.00 7.00 7.00 7.00 7.00 7.00 7.00 7.00 7.00 7.00 7.00 7.00
7.00 7.00 7.00 7.00 7.00 7.00 7.00 7.00 7.00 7.00 7.00 7.00 7.00 7.00 7.00 7.00 7.00

(b)

```
BCK 37:41.85 -118:22.32 1.634
BEN 37:42.93 -118:34.38 2.463
CAS 37:34.49 -118:33.12 2.107
CMB 38:02.10 -120:22.98 0.719
HTC 37:31.79 -118:46.26 3.012
KCC 37:19.42 -119:19.08 0.914
LUL 38:03.14 -119:10.80 2.243
M01 37:38.51 -118:55.60 2.237
M02 37:38.80 -118:55.83 2.279
M03 37:37.91 -118:55.54 2.251
M04 37:39.77 -118:54.55 2.306
M05 37:38.69 -118:54.18 2.205
M06 37:37.93 -118:54.46 2.192
M07 37:37.04 -118:54.22 2.23
M08 37:37.63 -118:52.12 2.141
M09 37:38.20 -118:51.62 2.134
M10 37:36.52 -118:52.39 2.208
M11 37:38.04 -118:50.59 2.138
M12 37:37.06 -118:51.20 2.222
M13 37:39.58 -118:58.24 2.464
M14 37:39.28 -118:56.74 2.344
M15 37:41.09 -118:56.87 2.372
M16 37:41.81 -118:55.72 2.393
M17 37:40.91 -118:54.29 2.356
M18 37:40.22 -118:55.63 2.327
M19 37:39.61 -118:53.26 2.15
M20 37:38.70 -118:52.78 2.152
M21 37:39.08 -118:51.59 2.214
M22 37:40.79 -118:52.34 2.2
M23 37:40.63 -118:50.95 2.171
M24 37:39.50 -118:50.09 2.126
M25 37:37.45 -118:56.90 2.355
M26 37:36.76 -118:55.53 2.386
M27 37:39.91 -118:51.74 2.27
M28 37:38.25 -118:57.35 2.362
M29 37:37.72 -118:52.88 2.168
M30 37:38.41 -118:50.90 2.144
M31 37:37.68 -118:50.20 2.137
M32 37:39.02 -118:52.01 2.153
```

Appendix 11: Graphs illustrating the effect of *tomo4d* damping on the changes in earthquake location and models of (a) Long Valley caldera derived from data for epochs 1997 and 2009-10 and (b) the Coso geothermal area derived from data for epochs 2007 and 2012, over five iterations (abscissa). The ordinate gives the changes in (top) goodness of fit for *P* and *S* phase, (middle) earthquake origin time and location, and (bottom) wave slowness for both *P* and *S* phase.

(a)

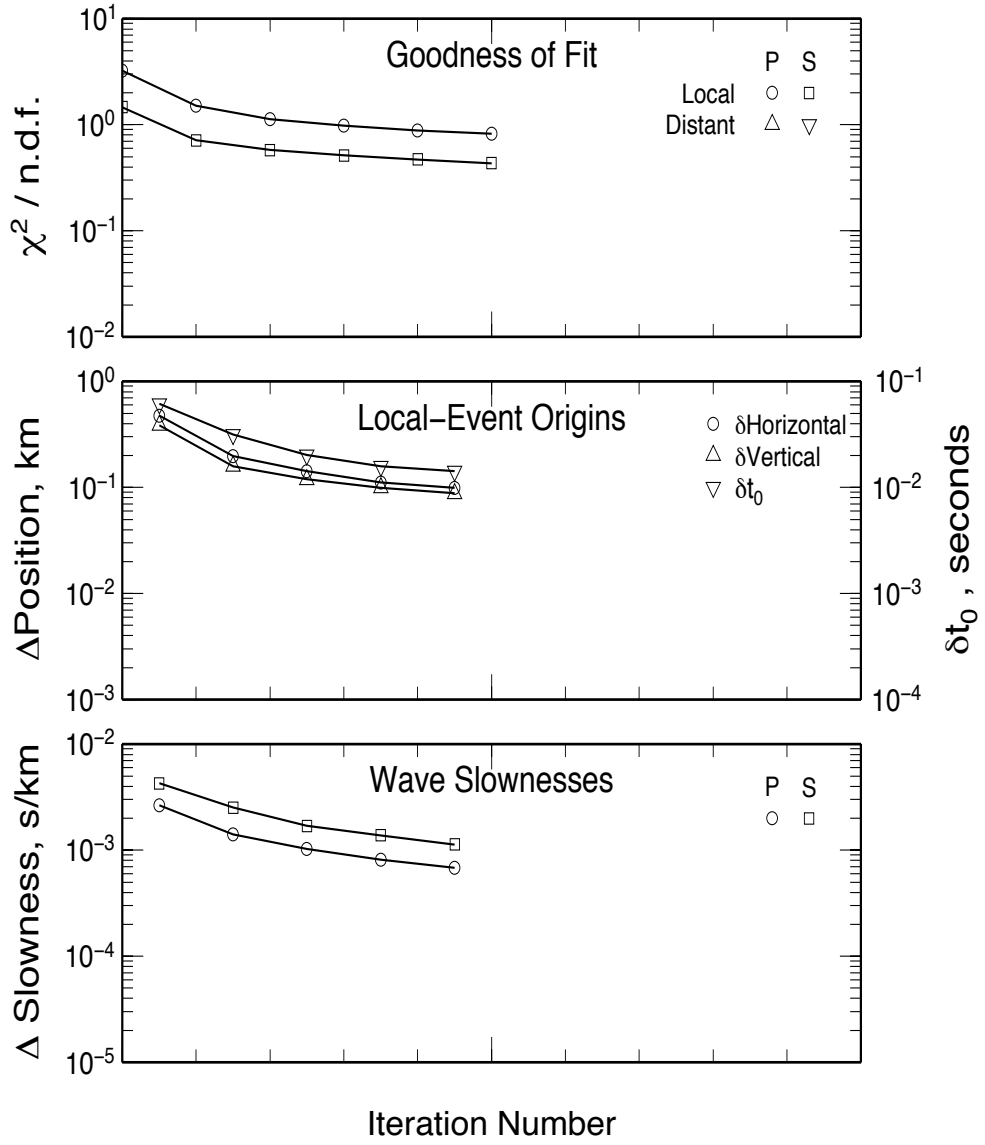

(b)

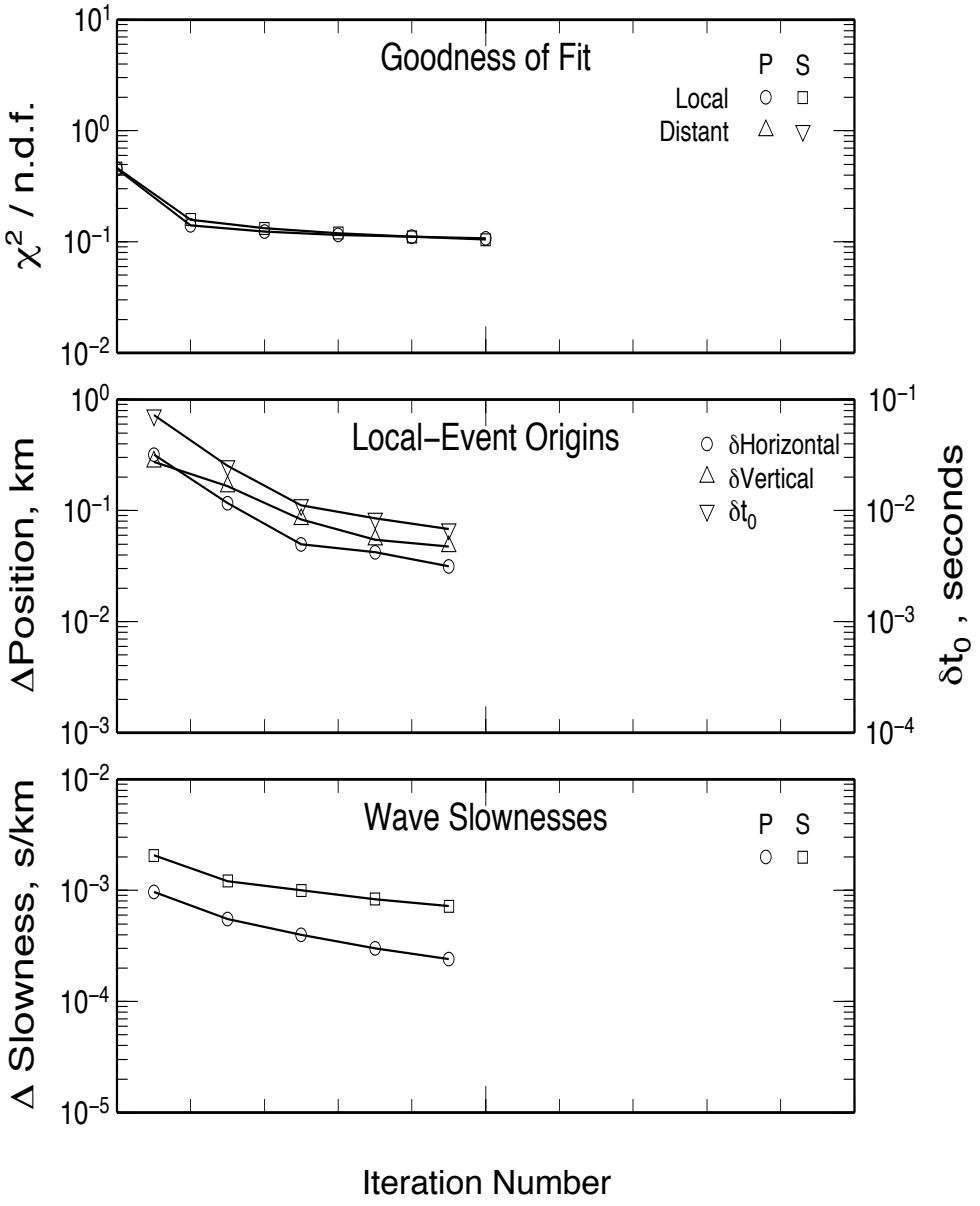
Goodness of Fit
P S
Local
Distant
χ^2 / n.d.f.
Local–Event Origins
δHorizontal
δVertical
δt_0
ΔPosition, km
δt_0 , seconds
Wave Slownesses
P S
Δ Slowness, s/km
Iteration Number

Appendix 12: Scripts (1) to calculate the qualities of earthquakes from the US Navy catalogues, based on numbers of arrival times, RMS arrival-time residuals and azimuthal gap, and (2) to select the highest-quality and best-distributed earthquakes for inversion for Coso.

(1)

```
#!/bin/sh
# Estimate data quality for Coso-format seismic events.

nawk '
BEGIN {
wt_n = 1; wt_gap = 1; wt_rms = 1;
}
{
# Estimate data quality
gap = substr($0,57,3);
n_P = substr($0,49,3);
n_S = substr($0,53,3);
n = n_P + n_S;
if(n<=4) rms = 1.0e6;
else {
rms = substr($0,64,4);
rms *= sqrt(n/(n-4));
}
if(rms+0 == 0 || gap+0 == 0)
next;
qual = wt_n*(n-4)/4 + wt_rms*(0.03/rms) + wt_gap*(150/gap);

# write summary record, followed by grid-square number and quality.
printf("%s %2f\n", $0, qual);
}
' $*

exit 0
```

(2)

```
#!/bin/sh
# high-ranking - Select the best 10 earthquakes in each grid cell
# najwa mhana : najwa.mhanna@durham.ac.uk

gawk '
function floor(x) { return (x>=0.0 ? int(x):int(x-1));}
BEGIN   {
RAD = 0.017453292519943;
R_EARTH = 6371.2;
DEG_PER_RAD = 57.295779513;
KM_PER_DEG = R_EARTH/DEG_PER_RAD;
#x0 = 35.958334*KM_PER_DEG;
x0 = 35.9766667*KM_PER_DEG;
#y0 = -117.866667*KM_PER_DEG*cos(36*RAD);
y0 = -117.8433334*KM_PER_DEG*cos(36*RAD);
dx = 2;
dy = 2;
}
```

```
{
# Convert angles in form degreesN[minutes[seconds]]
# to decimal degrees and its value in km
depth = $6;
latd = substr($4,1,2);
latm = substr($4,4)/100;
lond = substr($5,1,3);
lonm = substr($5,5)/100;
x = (latd+latm/60)*KM_PER_DEG;
y = -(lond+lonm/60)*KM_PER_DEG*cos(36*RAD);
Dx = (x - x0)/dx;
Dy = (y - y0)/dy;
i = floor(Dx);
j = floor(Dy);
d = floor(depth);

#if ($14>5)
print $0, i, j, d;
}
' $*    |
gawk '
BEGIN {
xmin = -1;
xmax = 5;
ymin = -1;
ymax = 5;
zmin = 0;
zmax = 8;
neq = 10;
}
{
# Count the events in each grid cell,
# and remember all the input lines.
nn = ++n[$15,$16,$17];
x[$15,$16,$17,nn] = $0;
}
END {
cmd = "sort -nr -k 14";
for (d=zmin; d<=zmax; d++)
for (i=xmin; i<=xmax; i++)
for (j=ymin; j<=ymax; j++) {
nn = n[i,j,d]
if (nn > 0) {
for (k=1; k<=nn; k++)
print x[i,j,d,k] |& cmd
close (cmd, "to")

for (l=0; l<neq; l++) {
if ((cmd |& getline) <= 0)
break;
print;
}
close (cmd)
}
}
}
'

exit 0
```

Appendix 13: The XPED-format arrival-time measurement file for the earthquake of 5/5/2007 00:52:23.56 from the US Navy catalogue for the Coso geothermal area.

```
A 200705050052 23.56 36N0758 117W5430  5.77  0.6 10/009 182  9 0.06  0.2AD RG
E LQ 0.058-0.004 0.060 0.060    6.89  15      0.20 0.15 0.80 0.06 0.58 0.00
F 107  9  0.05  17  4  0.19 264 80  0.71   0.00   0.00
.W2S.EHZ (P P U 25.828 0 0.012 0.006)
.CE8.EHZ (P P _ 26.080 0 0.036 0.104)
.W1S.EHZ (P P D 26.056 0 0.040 0.002)
.CE7.EHZ (P P D 26.356 0 0.028 0.077)
.CE3A.EHZ (P P U 26.744 0 0.040 0.038)
.CE2.EHZ (P P _ 26.788 0 0.060 0.054)
.SM5.EHZ (P P U 26.944 0 0.064 0.050)
.CE4.EHZ (P P D 27.060 0 0.096 -0.066)
.NV4.EHZ (P P U 27.256 0 0.032 0.041)
.NV3.EHZ (P P U 27.600 0 0.048 -0.062)
.W2S.EHN (P S _ 27.508 0 0.052 -0.128)
.CE8.EHN (P S _ 27.864 0 0.048 0.066)
.W1S.EHN (P S _ 27.712 0 0.060 -0.043)
.CE7.EHN (P S _ 28.232 0 0.064 0.050)
.CE3A.EHN (P S _ 28.824 0 0.044 -0.096)
.CE2.EHN (P S _ 28.852 0 0.060 -0.098)
.SM5.EHN (P S _ 29.264 0 0.036 0.024)
.CE4.EHN (P S _ 29.448 0 0.044 -0.169)
.NV3.EHN (P S _ 30.564 0 0.056 -0.153)
N 20070505005225p
H 2007 5 5 0 52  23.5621986 36.1263275 -117.9049530 5.7704153 0.0000000
O CE1.EHE CE1.EHN CE1.EHZ CE2.EHE CE3A.EHE CE4.EHE CE7.EHE CE8.EHE
O CS6.EHE CS6.EHN CS6.EHZ NV10.EHN NV10.EHZ NV2.EHE NV2.EHN NV2.EHZ
O NV3.EHE NV4.EHE NV4.EHN NV6.EHE NV6.EHN NV6.EHZ SM5.EHE W1S.EHE
O W2S.EHE
M F 090 44 G 319 57 U 270 46 V 139 33 P 194 62 T 297 06  fpfit 0.77 |      ÿ 00
```

Appendix 14: Script to reformat an XPED-format arrival-time measurement file for inversion by *simul2000A*.

```
#!/bin/bash -

# script2 - Reads an XPED file, generates the XPED p-files names and reformats them

# producing the output in the format for input to simul12.


while read line; do

#Get the event and the month ID

event_key=`echo $line | sed 's/..\(.....\).*/\1/'`

month=`echo $event_key | sed 's/....\(..\).*/\1/'`

sec=`echo $line | sed 's/.............\(.....\).*/\1/'`

second="$(printf '%2.0f\n' $sec | sed 's/ /0/')"


#Generate the input-file name

new_file_name=/db/seismic/Coso/CATALOGUES/Navy/XPED/2007/2007.$month/$event_key$second"p"

qpack -sort -station /db/seismic/coso/coso.sta -xped $new_file_name |

# convert seismic data to the binary format

qloc -guess -maxiter 30 -mindep -2.5 -setdep 0 -mod/db/seismic/coso\

/Models/coso.navy.mdl -printall qloc.print |

# estimate location and origin time of the event

qprint -simnew

# produce the output in the format for input to the simul12

done

exit 0
```

Appendix 15: (1) The active seismic stations during the year 2007 in the Coso geothermal area, belonging to the US Navy seismometer network and located using differential GPS. (2) Sample of an arrival-time measurement file used for inversion of data from 2007 using *simul2000A*.

(1)

Station Code	Latitude	longitude	height asl (m)
CE1	36:00.79	117:48.15	1194
CE2	36:02.02	117:47.30	1244
CE3	36:00.87	117:49.19	1259
CE3A	36:00.87	117:49.19	1259
CE4	35:59.99	117:48.14	1316
CE5	36:00.49	117:45.85	1035
CE6	36:02.02	117:46.36	1130
CE7	36:03.18	117:48.28	1239
CE8	36:03.07	117:50.32	1199
CS6	36:01.90	117:46.39	1202
NV1	35:58.96	117:45.89	775
NV2	36:01.53	117:37.28	1550
NV3	36:08.48	117:41.26	1946
NV4	36:02.86	117:44.42	1103
NV5	36:05.03	117:45.22	1070
NV6	35:58.94	117:48.46	1438
W1S	36:03.85	117:59.74	1223
W2S	36:06.98	118:00.19	1336
NV9	36:00.46	117:45.84	1069
NV10	35:59.94	117:44.71	960
SM5	35:59.99	117:49.81	138

(2)

070209 0442 52.24 36N01.71 117W48.91 -0.24
CE1_PD0 0.493 CE1_Sp0 0.380 CE2_PD0 0.601 CE2_Sp0 0.436CE3A_PU0 0.417CE3A_Sp0 0.364 CE4_PD0 0.777 CE4_Sp0 0.560 CE7_PU0 0.617 CE7_Sp0 0.420 CE8_PD0 0.745 CE8_Sp0 0.764 NV1_PD0 1.425NV10_PD0 1.501 NV4_P_0 1.573 NV4_Sp0 1.108 NV5_P_0 1.609 NV6_PD0 1.141 NV6_Sp0 0.916 SM5_PU0 0.801 SM5_Sp0 0.540

070110 1547 17.04 36N01.48 117W48.04 -0.71
CE1_PD0 0.316 CE1_Sp0 0.236 CE2_PU0 0.300 CE2_Sp0 0.372CE3A_P_0 0.476CE3A_Sp0 0.432 CE4_PD0 0.652 CE4_Sp0 0.452 CE7_PD0 0.704 CE7_Sp0 0.540 CE8_PD0 1.012 CE8_Sp0 0.776 NV10_PD0 1.284NV10_Sp0 0.960 NV4_P_0 1.424 NV4_Sp0 0.948 NV5_P_0 1.564 NV5_Sp0 1.292 NV6_PU0 1.064 NV6_Sp0 0.788 SM5_P_0 0.848 SM5_Sp0 0.648

070209 0142 11.37 36N01.79 117W48.84 -0.75
CE1_P_0 0.506 CE1_Sp0 0.308 CE2_PD0 0.562 CE2_Sp0 0.372CE3A_PU0 0.430 CE4_P_0 0.790 CE4_Sp0 0.572 CE7_P_0 0.546 CE7_Sp0 0.348 CE8_PD0 0.698 CE8_Sp0 0.700 NV1_PD0 1.430 NV1_Sp0 1.068NV10_PU0 1.606NV10_Sp0 1.112 NV6_P_0 1.138 NV6_Sp0 0.888 SM5_PD0 0.798 SM5_Sp0 0.708

070519 0617 40.30 36N01.57 117W48.06 -0.61
CE1_P_0 0.387 CE1_Sp0 0.216NV10_PD0 1.243 CE2_PD0 0.335 CE2_Sp0 0.316CE3A_PD0 0.503 CE3A_Sp0 0.428 CE4_PD0 0.663 CE4_Sp0 0.536 CE7_PD0 0.635 CE7_Sp0 0.432 CE8_P_0 0.899 CE8_Sp0 0.924 CS6_PD0 0.671 CS6_Sp0 0.644 NV1_PD0 1.203 NV1_Sp0 0.936 NV6_PU0 1.039 NV6_Sp0 0.928 SM5_P_0 0.903 SM5_Sp0 0.540

Appendix 16: The control files used for *simul2000A* inversions for the Coso geothermal area, years (a) 1996 (b) 2006 (c) 2007 (d) 2008 (e) 2010 and (f) 2012.

(a)

```
486  0  0 1.0  4 1 0        neqs, nshot, nblast, wtsht, kout, kout2, kout3
10  1.0  0.020  0.01  -1.9  0.50  0.01  0.00  nitloc, wtsp, eigtol, rmscut, zmin, dxmax, rderr, ercof
5  0.10  0.03  0  20.0  10.0  99.00  0.50  hitct, dvpmax, dvpvsmax, idmp, vpdmp, vpvsdmp, stadmp,
stepl
1  2  3  0.0025 0 0.01  0     ires, i3d, nitmax, snrmct, ihomo, rmstop, ifixl
20.0  30.0  0.10  0.30  0.40   delt1, delt2, res1, res2, res3
9  2  0.5  0.5              ndip, iskip, scale1, scale2
1.2  0.001 15 15             xfax, tlim, nitpb1, nitpb2
1  1  0                   iusep, iuses, invdel
0  0  0                   iuseq, dqmax, qdamp
```

(b)

```
743  0  0 1.0  4 1 0        neqs, nshot, nblast, wtsht, kout, kout2, kout3
10  1.0  0.020  0.01  -1.9  0.50  0.01  0.00  nitloc, wtsp, eigtol, rmscut, zmin, dxmax, rderr, ercof
5  0.10  0.03  0  20.0  10.0  99.00  0.50  hitct, dvpmax, dvpvsmax, idmp, vpdmp, vpvsdmp, stadmp,
stepl
1  2  4  0.0025 0 0.01  0     ires, i3d, nitmax, snrmct, ihomo, rmstop, ifixl
20.0  30.0  0.10  0.30  0.40   delt1, delt2, res1, res2, res3
9  2  0.5  0.5              ndip, iskip, scale1, scale2
1.2  0.001 15 15             xfax, tlim, nitpb1, nitpb2
1  1  0                   iusep, iuses, invdel
0  0  0                   iuseq, dqmax, qdamp
```

(c)

```
680  0  0 1.0  4 1 0        neqs, nshot, nblast, wtsht, kout, kout2, kout3
10  1.0  0.020  0.01  -1.9  0.50  0.01  0.00  nitloc, wtsp, eigtol, rmscut, zmin, dxmax, rderr, ercof
5  0.10  0.03  0 20.0  10.0  99.00  0.50  hitct, dvpmax, dvpvsmax, idmp, vpdmp, vpvsdmp, stadmp,
stepl
1  2  5  0.0025 0 0.01  0     ires, i3d, nitmax, snrmct, ihomo, rmstop, ifixl
20.0  30.0  0.10  0.30  0.40   delt1, delt2, res1, res2, res3
9  2  0.5  0.5              ndip, iskip, scale1, scale2
1.2  0.001 15 15             xfax, tlim, nitpb1, nitpb2
1  1  0                   iusep, iuses, invdel
0  0  0                   iuseq, dqmax, qdamp
```

(d)

```
570  0  0 1.0  4 1 0        neqs, nshot, nblast, wtsht, kout, kout2, kout3
10  1.0  0.020  0.01  -1.9  0.50  0.01  0.00  nitloc, wtsp, eigtol, rmscut, zmin, dxmax, rderr, ercof
5  0.10  0.03  0 20.0  10.0  99.00  0.50  hitct, dvpmax, dvpvsmax, idmp, vpdmp, vpvsdmp, stadmp, stepl
1  2  4  0.0025 0 0.01  0     ires, i3d, nitmax, snrmct, ihomo, rmstop, ifixl
20.0  30.0  0.10  0.30  0.40   delt1, delt2, res1, res2, res3
9  2  0.5  0.5              ndip, iskip, scale1, scale2
1.2  0.001 15 15             xfax, tlim, nitpb1, nitpb2
1  1  0                   iusep, iuses, invdel
0  0  0                   iuseq, dqmax, qdamp
```

(e)

```
512  0  0 1.0  4 1 0        neqs, nshot, nblast, wtsht, kout, kout2, kout3
10  1.0  0.020  0.01  -1.9  0.50  0.01  0.00  nitloc, wtsp, eigtol, rmscut, zmin, dxmax, rderr, ercof
5  0.10  0.03  0 20.0  10.0  99.00  0.50  hitct, dvpmax, dvpvsmax, idmp, vpdmp, vpvsdmp, stadmp, stepl
1   2   5  0.0025 0 0.01  0      ires, i3d, nitmax, snrmct, ihomo, rmstop, ifixl
20.0  30.0  0.10  0.30  0.40    delt1, delt2, res1, res2, res3
9  2  0.5  0.5                 ndip, iskip, scale1, scale2
1.2  0.001 15 15                xfax, tlim, nitpb1, nitpb2
1  1  0                      iusep, iuses, invdel
0  0  0                      iuseq, dqmax, qdamp
```

(f)

```
504  0  0 1.0  4 1 0        neqs, nshot, nblast, wtsht, kout, kout2, kout3
10  1.0  0.020  0.01  -1.9  0.50  0.01  0.00  nitloc, wtsp, eigtol, rmscut, zmin, dxmax, rderr, ercof
5  0.10  0.03  0 20.0  10.0  99.00  0.50  hitct, dvpmax, dvpvsmax, idmp, vpdmp, vpvsdmp, stadmp, stepl
1   2   5  0.0025 0 0.01  0      ires, i3d, nitmax, snrmct, ihomo, rmstop, ifixl
20.0  30.0  0.10  0.30  0.40    delt1, delt2, res1, res2, res3
9  2  0.5  0.5                 ndip, iskip, scale1, scale2
1.2  0.001 15 15                xfax, tlim, nitpb1, nitpb2
1  1  0                      iusep, iuses, invdel
0  0  0                      iuseq, dqmax, qdamp
```

Appendix 17: The initial V_p model used for inversion with *tomo4d* for different years from the Coso geothermal area. The initial V_p/V_s ratio used is 1.74.

```
6371.2
35:58.70 -117:44.00 90.00
8  8 16
-150.0   0.0   2.0   4.0   6.0   8.0  10.0 160.0
-150.0   0.0   2.0   4.0   6.0   8.0  10.0 160.0
-150.0  -4.0  -2.0  -1.0   0.0   1.0   2.0   3.0   4.0   5.0   6.0   7.0   8.0   9.0  10.0 160.0

4.25 4.25 4.25 4.25 4.25 4.25 4.25 4.25
4.25 4.25 4.25 4.25 4.25 4.25 4.25 4.25
4.25 4.25 4.25 4.25 4.25 4.25 4.25 4.25
4.25 4.25 4.25 4.25 4.25 4.25 4.25 4.25
4.25 4.25 4.25 4.25 4.25 4.25 4.25 4.25
4.25 4.25 4.25 4.25 4.25 4.25 4.25 4.25
4.25 4.25 4.25 4.25 4.25 4.25 4.25 4.25
4.25 4.25 4.25 4.25 4.25 4.25 4.25 4.25

4.25 4.25 4.25 4.25 4.25 4.25 4.25 4.25
4.25 4.25 4.25 4.25 4.25 4.25 4.25 4.25
4.25 4.25 4.25 4.25 4.25 4.25 4.25 4.25
4.25 4.25 4.25 4.25 4.25 4.25 4.25 4.25
4.25 4.25 4.25 4.25 4.25 4.25 4.25 4.25
4.25 4.25 4.25 4.25 4.25 4.25 4.25 4.25
4.25 4.25 4.25 4.25 4.25 4.25 4.25 4.25
4.25 4.25 4.25 4.25 4.25 4.25 4.25 4.25

4.25 4.25 4.25 4.25 4.25 4.25 4.25 4.25
4.25 4.25 4.25 4.25 4.25 4.25 4.25 4.25
4.25 4.25 4.25 4.25 4.25 4.25 4.25 4.25
4.25 4.25 4.25 4.25 4.25 4.25 4.25 4.25
4.25 4.25 4.25 4.25 4.25 4.25 4.25 4.25
4.25 4.25 4.25 4.25 4.25 4.25 4.25 4.25
4.25 4.25 4.25 4.25 4.25 4.25 4.25 4.25
4.25 4.25 4.25 4.25 4.25 4.25 4.25 4.25

4.70 4.70 4.70 4.70 4.70 4.70 4.70 4.70
4.70 4.70 4.70 4.70 4.70 4.70 4.70 4.70
4.70 4.70 4.70 4.70 4.70 4.70 4.70 4.70
4.70 4.70 4.70 4.70 4.70 4.70 4.70 4.70
4.70 4.70 4.70 4.70 4.70 4.70 4.70 4.70
4.70 4.70 4.70 4.70 4.70 4.70 4.70 4.70
4.70 4.70 4.70 4.70 4.70 4.70 4.70 4.70
4.70 4.70 4.70 4.70 4.70 4.70 4.70 4.70

5.16 5.16 5.16 5.16 5.16 5.16 5.16 5.16
5.16 5.16 5.16 5.16 5.16 5.16 5.16 5.16
5.16 5.16 5.16 5.16 5.16 5.16 5.16 5.16
5.16 5.16 5.16 5.16 5.16 5.16 5.16 5.16
5.16 5.16 5.16 5.16 5.16 5.16 5.16 5.16
5.16 5.16 5.16 5.16 5.16 5.16 5.16 5.16
5.16 5.16 5.16 5.16 5.16 5.16 5.16 5.16
5.16 5.16 5.16 5.16 5.16 5.16 5.16 5.16

5.54 5.54 5.54 5.54 5.54 5.54 5.54 5.54
5.54 5.54 5.54 5.54 5.54 5.54 5.54 5.54
5.54 5.54 5.54 5.54 5.54 5.54 5.54 5.54
5.54 5.54 5.54 5.54 5.54 5.54 5.54 5.54
```

5.54 5.54 5.54 5.54 5.54 5.54 5.54 5.54
5.54 5.54 5.54 5.54 5.54 5.54 5.54 5.54
5.54 5.54 5.54 5.54 5.54 5.54 5.54 5.54
5.54 5.54 5.54 5.54 5.54 5.54 5.54 5.54

5.74 5.74 5.74 5.74 5.74 5.74 5.74 5.74
5.74 5.74 5.74 5.74 5.74 5.74 5.74 5.74
5.74 5.74 5.74 5.74 5.74 5.74 5.74 5.74
5.74 5.74 5.74 5.74 5.74 5.74 5.74 5.74
5.74 5.74 5.74 5.74 5.74 5.74 5.74 5.74
5.74 5.74 5.74 5.74 5.74 5.74 5.74 5.74
5.74 5.74 5.74 5.74 5.74 5.74 5.74 5.74
5.74 5.74 5.74 5.74 5.74 5.74 5.74 5.74

5.79 5.79 5.79 5.79 5.79 5.79 5.79 5.79
5.79 5.79 5.79 5.79 5.79 5.79 5.79 5.79
5.79 5.79 5.79 5.79 5.79 5.79 5.79 5.79
5.79 5.79 5.79 5.79 5.79 5.79 5.79 5.79
5.79 5.79 5.79 5.79 5.79 5.79 5.79 5.79
5.79 5.79 5.79 5.79 5.79 5.79 5.79 5.79
5.79 5.79 5.79 5.79 5.79 5.79 5.79 5.79
5.79 5.79 5.79 5.79 5.79 5.79 5.79 5.79

5.82 5.82 5.82 5.82 5.82 5.82 5.82 5.82
5.82 5.82 5.82 5.82 5.82 5.82 5.82 5.82
5.82 5.82 5.82 5.82 5.82 5.82 5.82 5.82
5.82 5.82 5.82 5.82 5.82 5.82 5.82 5.82
5.82 5.82 5.82 5.82 5.82 5.82 5.82 5.82
5.82 5.82 5.82 5.82 5.82 5.82 5.82 5.82
5.82 5.82 5.82 5.82 5.82 5.82 5.82 5.82
5.82 5.82 5.82 5.82 5.82 5.82 5.82 5.82

5.82 5.82 5.82 5.82 5.82 5.82 5.82 5.82
5.82 5.82 5.82 5.82 5.82 5.82 5.82 5.82
5.82 5.82 5.82 5.82 5.82 5.82 5.82 5.82
5.82 5.82 5.82 5.82 5.82 5.82 5.82 5.82
5.82 5.82 5.82 5.82 5.82 5.82 5.82 5.82
5.82 5.82 5.82 5.82 5.82 5.82 5.82 5.82
5.82 5.82 5.82 5.82 5.82 5.82 5.82 5.82
5.82 5.82 5.82 5.82 5.82 5.82 5.82 5.82

5.82 5.82 5.82 5.82 5.82 5.82 5.82 5.82
5.82 5.82 5.82 5.82 5.82 5.82 5.82 5.82
5.82 5.82 5.82 5.82 5.82 5.82 5.82 5.82
5.82 5.82 5.82 5.82 5.82 5.82 5.82 5.82
5.82 5.82 5.82 5.82 5.82 5.82 5.82 5.82
5.82 5.82 5.82 5.82 5.82 5.82 5.82 5.82
5.82 5.82 5.82 5.82 5.82 5.82 5.82 5.82
5.82 5.82 5.82 5.82 5.82 5.82 5.82 5.82

5.82 5.82 5.82 5.82 5.82 5.82 5.82 5.82

5.82 5.82 5.82 5.82 5.82 5.82 5.82 5.82
5.82 5.82 5.82 5.82 5.82 5.82 5.82 5.82
5.82 5.82 5.82 5.82 5.82 5.82 5.82 5.82
5.82 5.82 5.82 5.82 5.82 5.82 5.82 5.82
5.82 5.82 5.82 5.82 5.82 5.82 5.82 5.82
5.82 5.82 5.82 5.82 5.82 5.82 5.82 5.82
5.82 5.82 5.82 5.82 5.82 5.82 5.82 5.82

5.82 5.82 5.82 5.82 5.82 5.82 5.82 5.82
5.82 5.82 5.82 5.82 5.82 5.82 5.82 5.82
5.82 5.82 5.82 5.82 5.82 5.82 5.82 5.82
5.82 5.82 5.82 5.82 5.82 5.82 5.82 5.82
5.82 5.82 5.82 5.82 5.82 5.82 5.82 5.82
5.82 5.82 5.82 5.82 5.82 5.82 5.82 5.82
5.82 5.82 5.82 5.82 5.82 5.82 5.82 5.82
5.82 5.82 5.82 5.82 5.82 5.82 5.82 5.82

5.82 5.82 5.82 5.82 5.82 5.82 5.82 5.82
5.82 5.82 5.82 5.82 5.82 5.82 5.82 5.82
5.82 5.82 5.82 5.82 5.82 5.82 5.82 5.82
5.82 5.82 5.82 5.82 5.82 5.82 5.82 5.82
5.82 5.82 5.82 5.82 5.82 5.82 5.82 5.82
5.82 5.82 5.82 5.82 5.82 5.82 5.82 5.82
5.82 5.82 5.82 5.82 5.82 5.82 5.82 5.82
5.82 5.82 5.82 5.82 5.82 5.82 5.82 5.82

6.00 6.00 6.00 6.00 6.00 6.00 6.00 6.00
6.00 6.00 6.00 6.00 6.00 6.00 6.00 6.00
6.00 6.00 6.00 6.00 6.00 6.00 6.00 6.00
6.00 6.00 6.00 6.00 6.00 6.00 6.00 6.00
6.00 6.00 6.00 6.00 6.00 6.00 6.00 6.00
6.00 6.00 6.00 6.00 6.00 6.00 6.00 6.00
6.00 6.00 6.00 6.00 6.00 6.00 6.00 6.00
6.00 6.00 6.00 6.00 6.00 6.00 6.00 6.00

Appendix 18: Details of the inversions for the 1996-2012, 2007-2008, 2007-2010, 2008-2010, 2008-2012 and 2010-2012 data from the Coso geothermal area using *tomo4d*.

Parameters	1996	2012
No. of events	482	497
No. of *P*-wave arrivals	5075	4165
No. of *S*-wave arrivals	2946	3783
$\varepsilon_{\text{Velocity}}$, σ_{V_P} and σ_{Vs}	0.05, 0.1, 0.05	0.05, 0.1, 0.05
Final RMS residuals, s	0.04	0.04
χ^2 reduction, %		
P	42	16
S	32	11

Parameters	2007	2008
No. of events	616	557
No. of *P*-wave arrivals	6544	5259
No. of *S*-wave arrivals	4549	4510
$\varepsilon_{\text{Velocity}}$, σ_{V_P} and σ_{Vs}	0.05, 0.1, 0.05	0.05, 0.1, 0.05
Final RMS residuals, s	0.05	0.05
χ^2reduction, %		
P	24	22
S	23	19

Parameters	2007	2010
No. of events	616	505
No. of *P*-wave arrivals	6544	4140
No. of *S*-wave arrivals	4549	3872
$\varepsilon_{\text{Velocity}}$, σ_{V_P} and σ_{Vs}	0.05, 0.1, 0.05	0.05, 0.1, 0.05
Final RMS residuals, s	0.05	0.04
χ^2reduction, %		
P	24	19
S	23	13

Parameters	2008	2010
No. of events	557	505
No. of *P*-wave arrivals	5259	4140
No. of *S*-wave arrivals	4510	3872
$\varepsilon_{\text{Velocity}}$, σ_{V_P} and σ_{Vs}	0.05, 0.1, 0.05	0.05, 0.1, 0.05
Final RMS residuals, s	0.05	0.04
χ^2reduction, %		
P	22	19
S	19	13

Parameters	2008	2012
No. of events	557	497
No. of *P*-wave arrivals	5259	4165
No. of *S*-wave arrivals	4510	3783
$\varepsilon_{\text{Velocity}}$, σ_{V_P} and σ_{Vs}	0.05, 0.1, 0.05	0.05, 0.1, 0.05
Final RMS residuals, s	0.05	0.04
χ^2reduction, %		
P	22	16
S	19	11

Parameters	2010	2012
No. of events	505	497
No. of *P*-wave arrivals	4140	4165
No. of *S*-wave arrivals	3872	3783
$\varepsilon_{\text{Velocity}}$, σ_{V_P} and σ_{Vs}	0.05, 0.1, 0.05	0.05, 0.1, 0.05
Final RMS residuals, s	0.04	0.04
χ^2reduction, %		
P	19	16
S	13	11

Appendix 19: Ray density maps for different years for the Coso geothermal area.

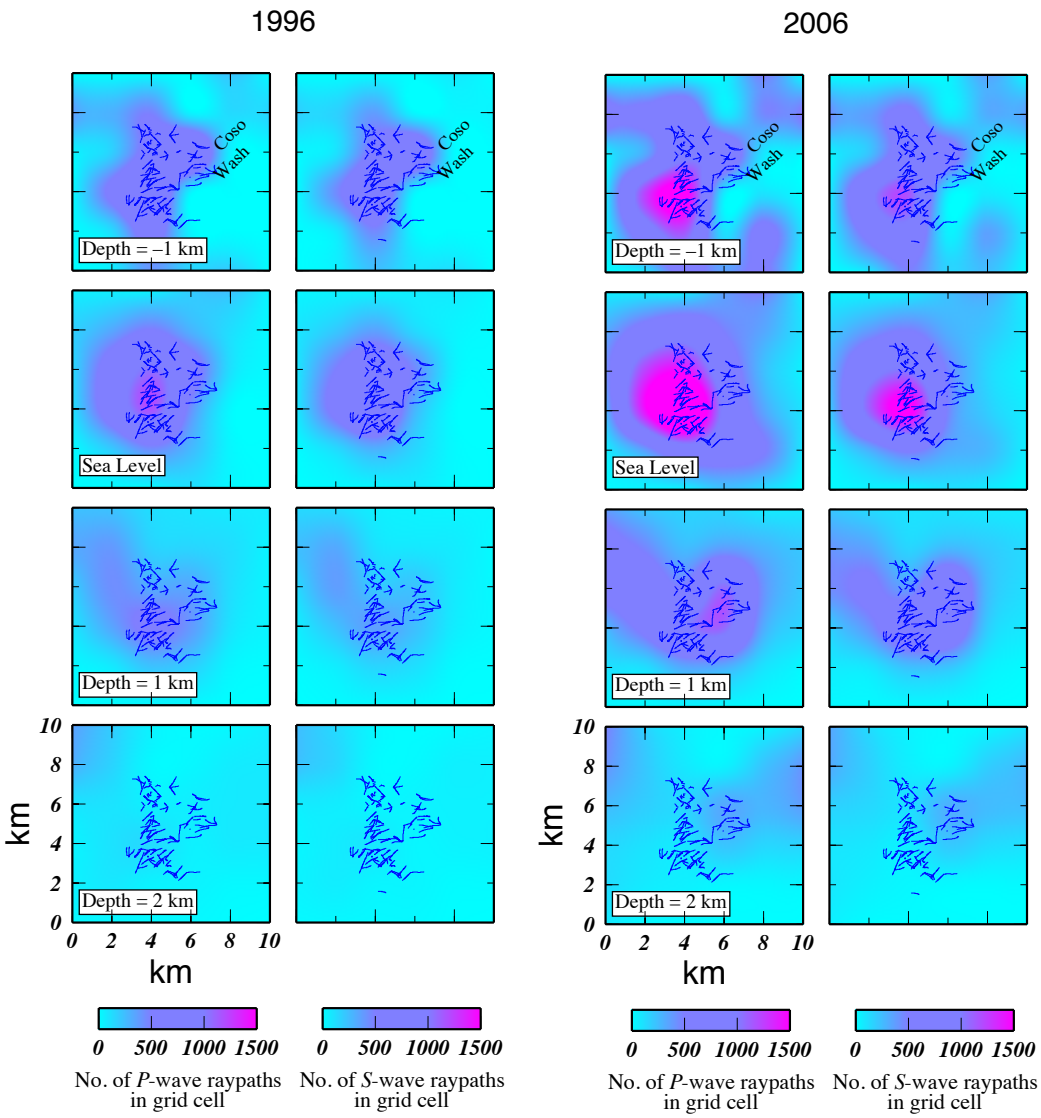

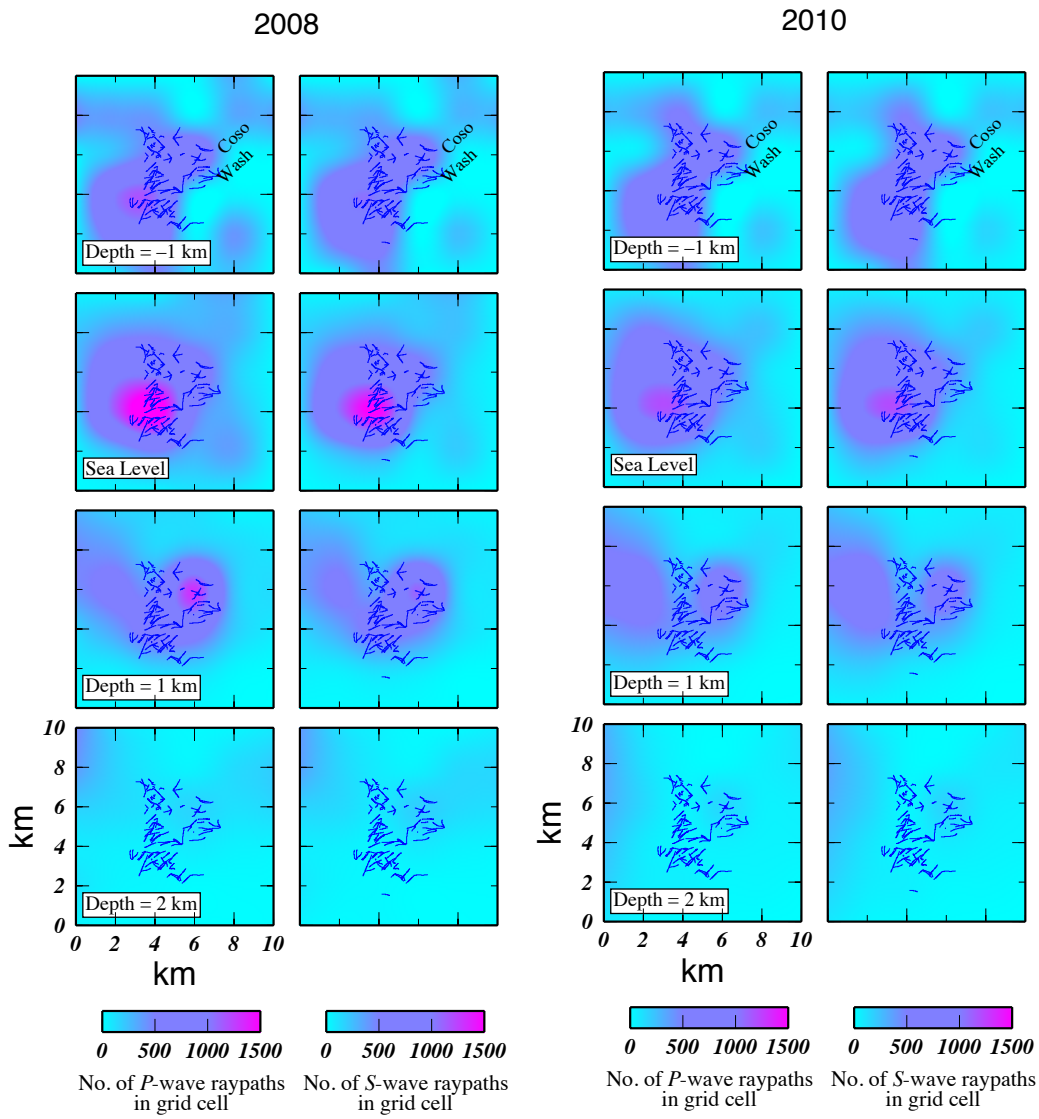
2008
2010
Coso
Wash
Depth = –1 km
Sea Level
Depth = 1 km
Depth = 2 km
km
0
2
4
6
8
10
0 500 1000 1500
No. of P-wave raypaths in grid cell
No. of S-wave raypaths in grid cell

1996

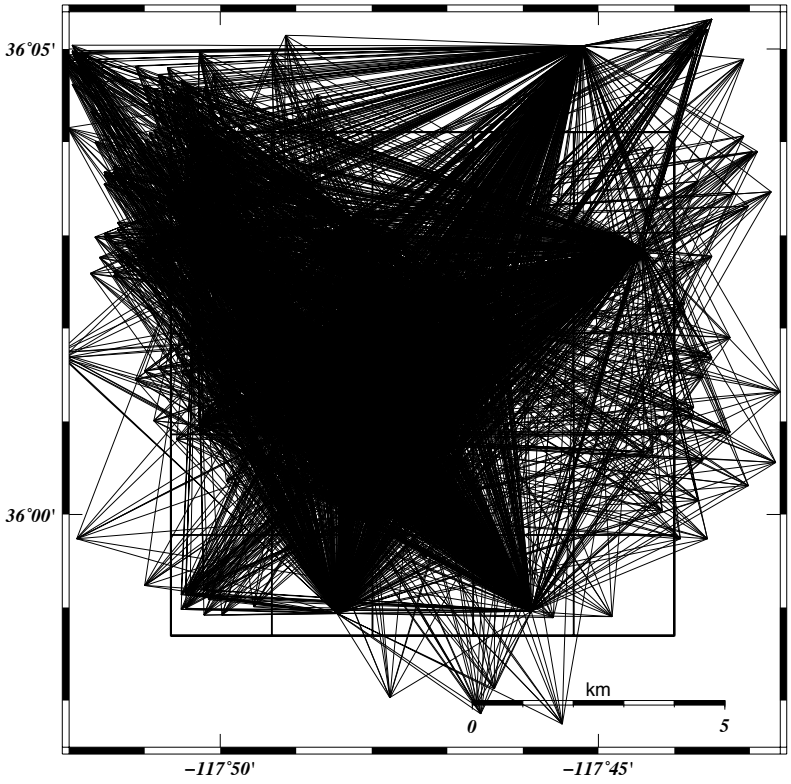

2006

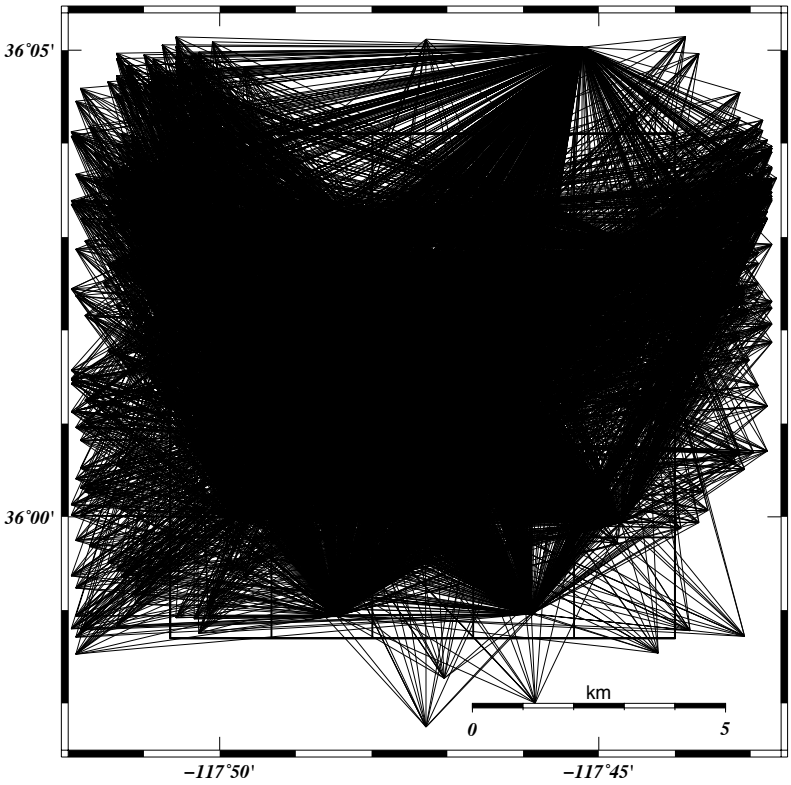

2007

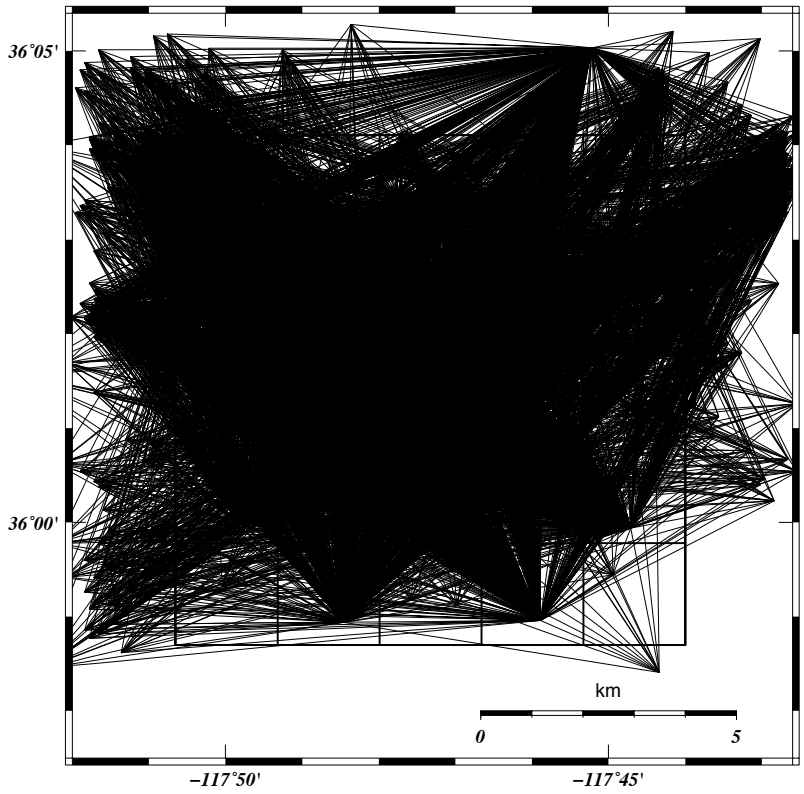

2008

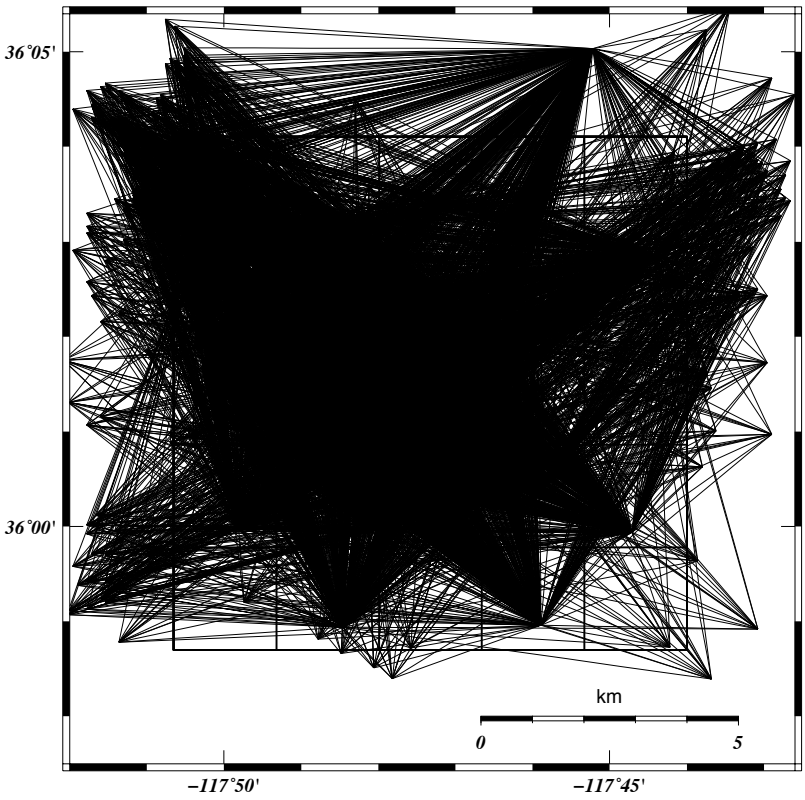

2010

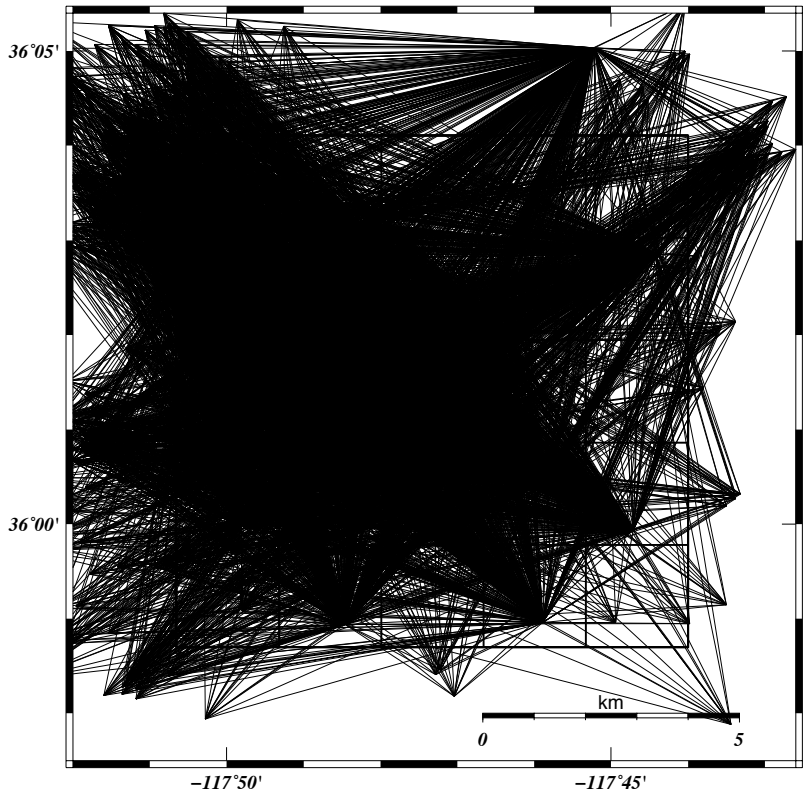

2012

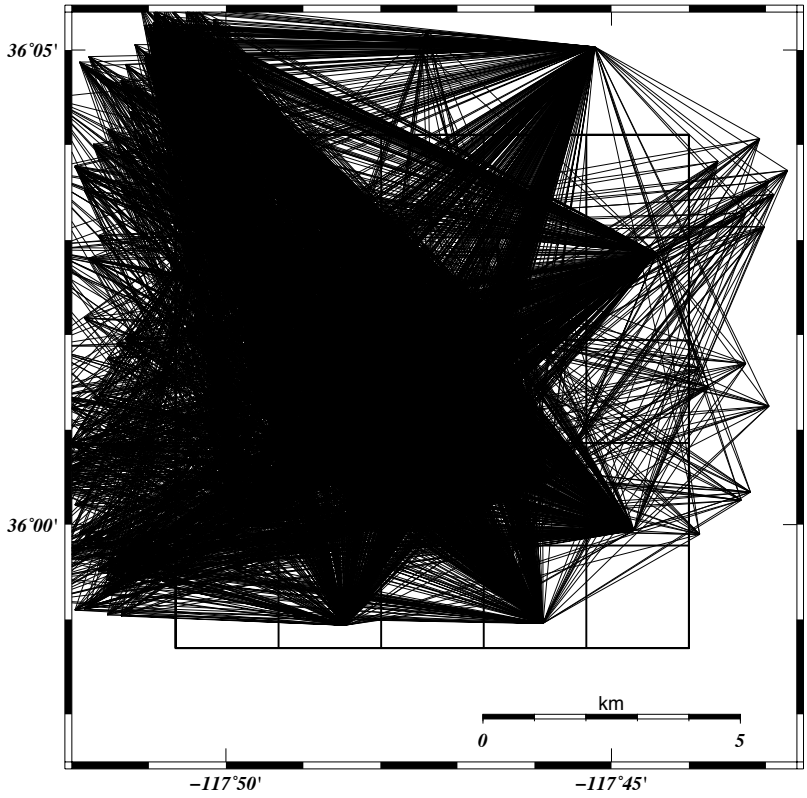

Appendix 20: Histograms of the initial and final arrival-time residuals for inversions for different years for the Coso geothermal area using *simul2000A*.

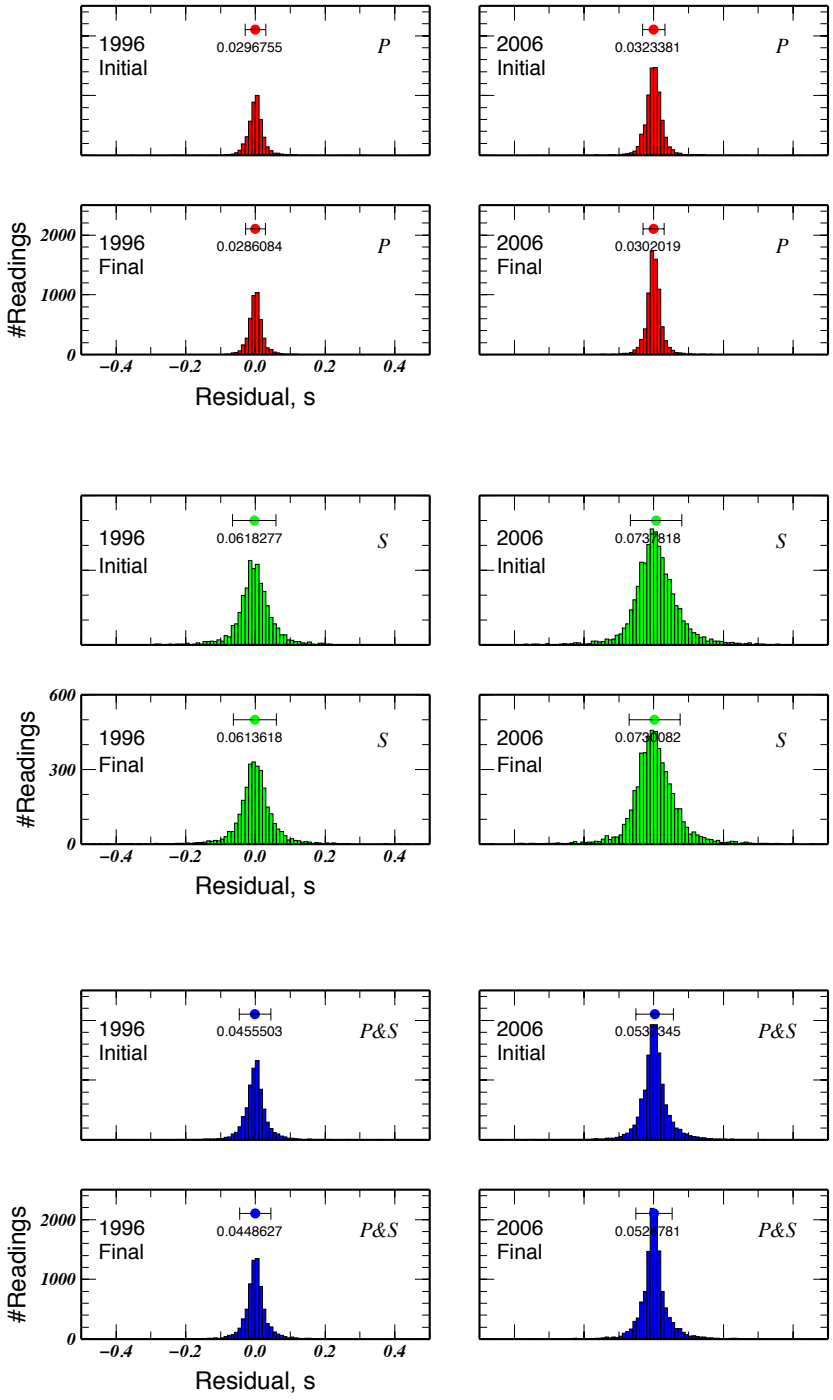

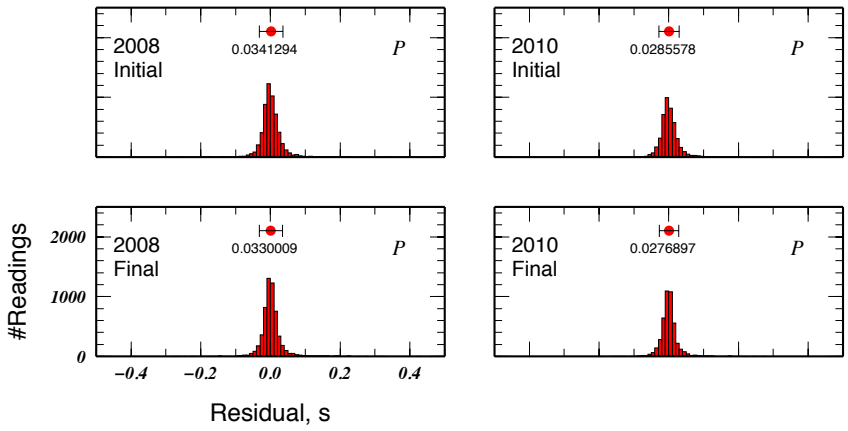
2008
Initial
0.0341294
P
2010
Initial
0.0285578
P
2008
Final
0.0330009
P
2010
Final
0.0276897
P
#Readings
2000
1000
0
−0.4
−0.2
0.0
0.2
0.4
Residual, s

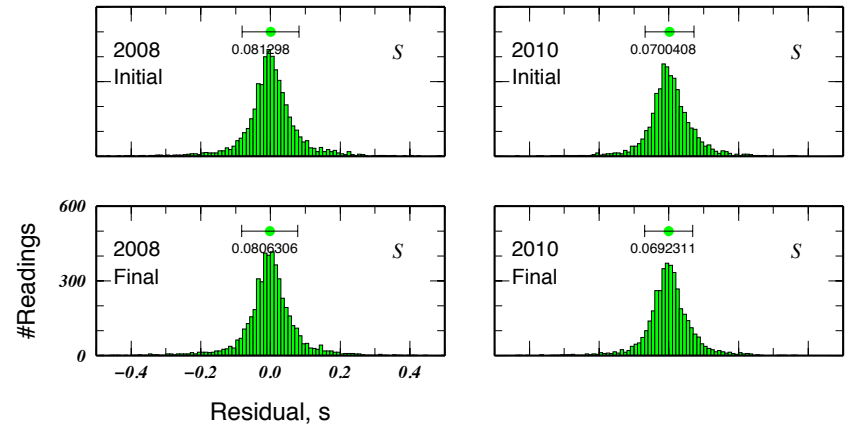
2008
Initial
0.081298
S
2010
Initial
0.0700408
S
2008
Final
0.0806306
S
2010
Final
0.0692311
S
#Readings
600
300
0
−0.4
−0.2
0.0
0.2
0.4
Residual, s

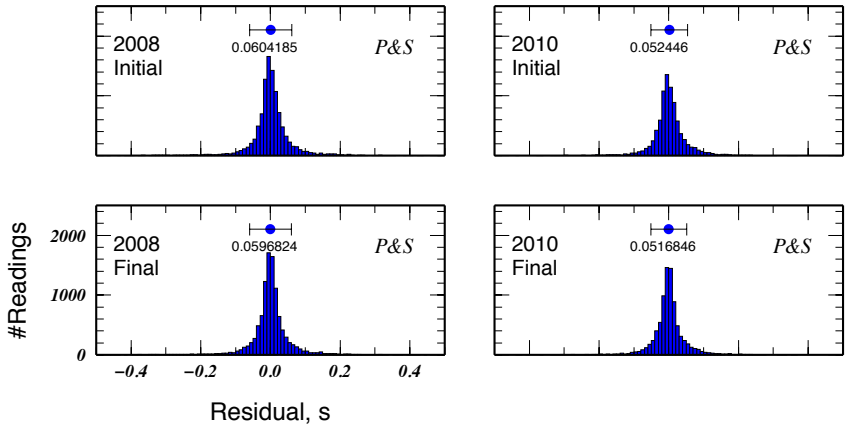
2008
Initial
0.0604185
P&S
2010
Initial
0.052446
P&S
2008
Final
0.0596824
P&S
2010
Final
0.0516846
P&S
#Readings
2000
1000
0
−0.4
−0.2
0.0
0.2
0.4
Residual, s

Appendix 21: Same as Appendix 20 but for inversions using *tomo4d*.

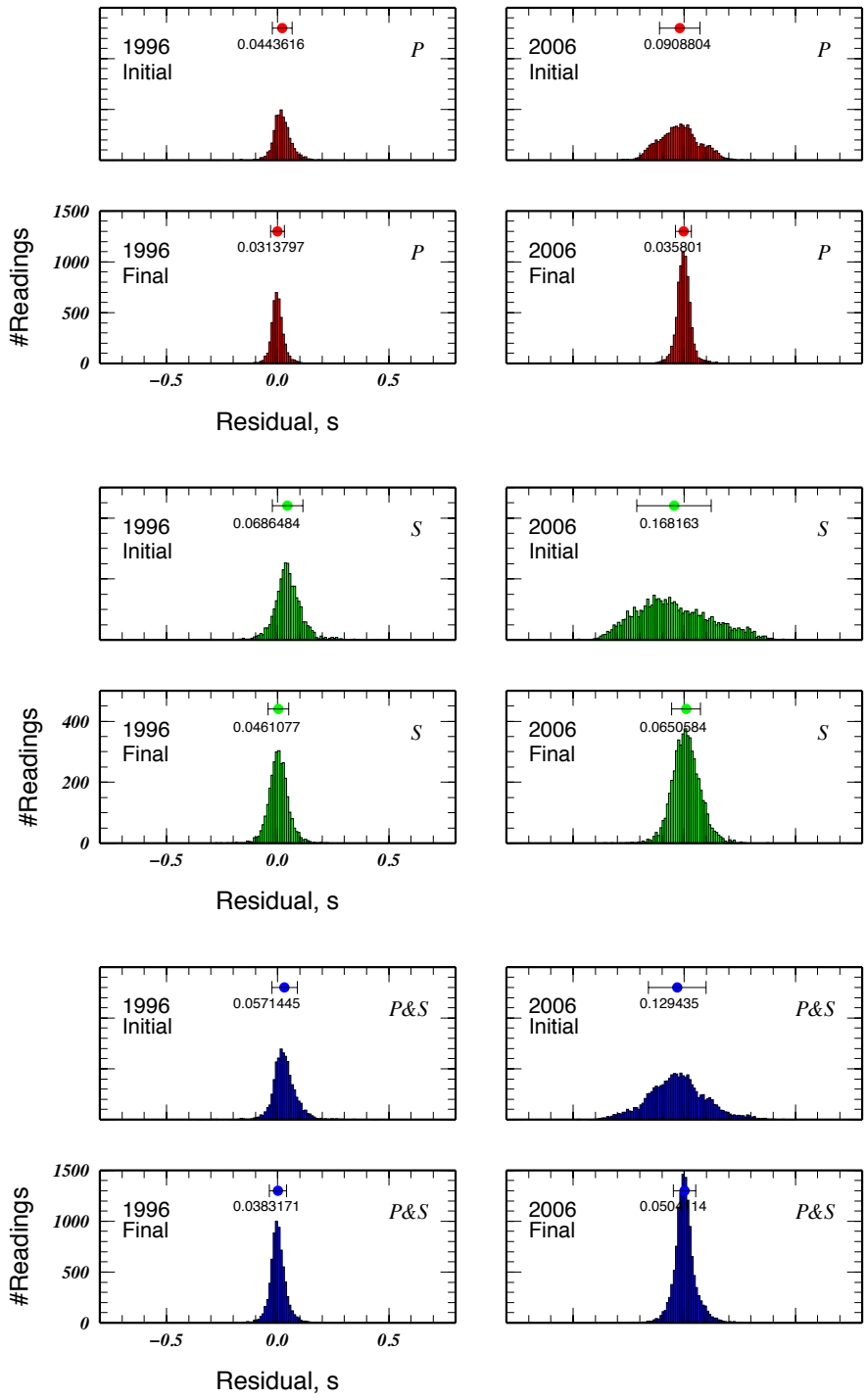

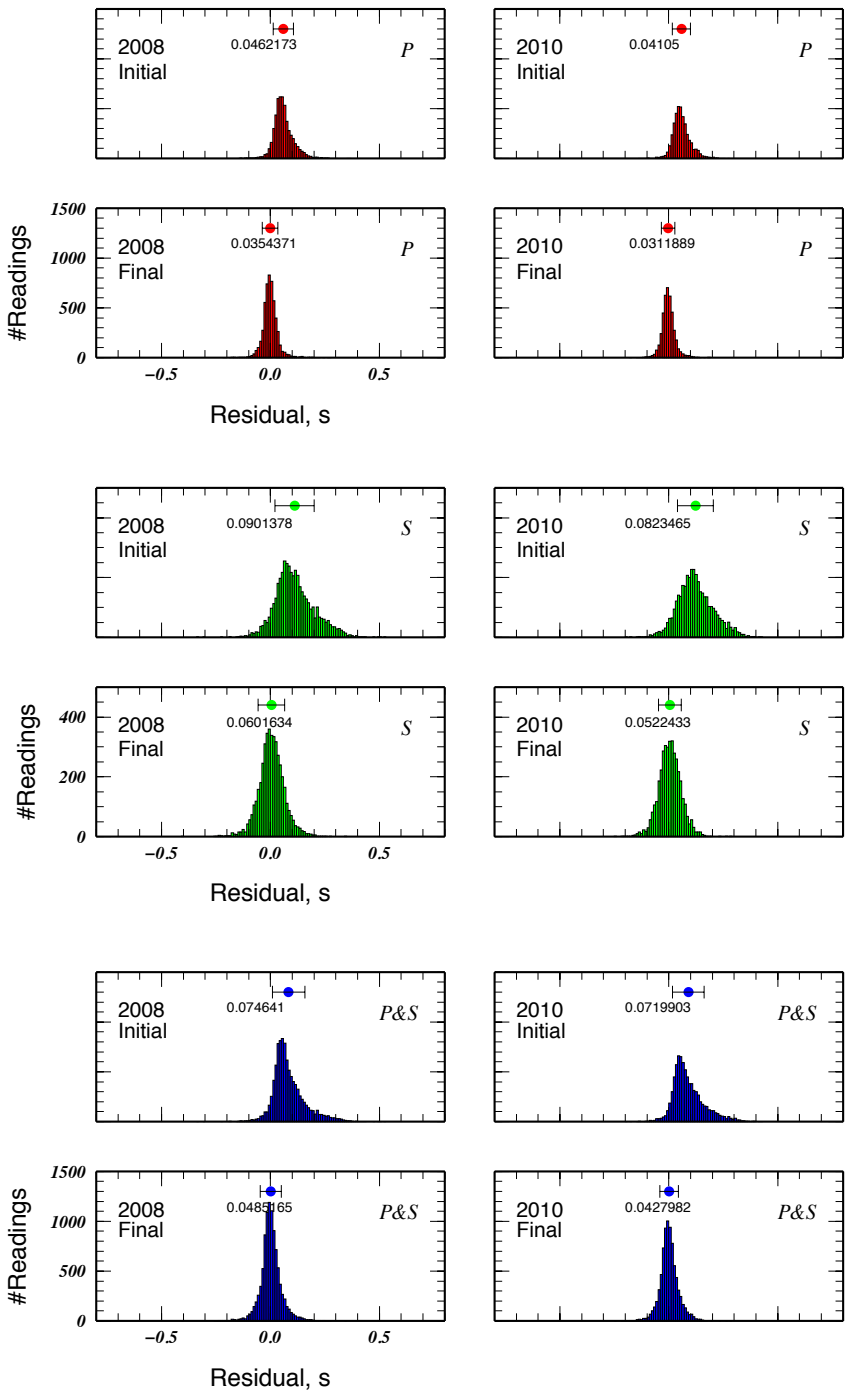
2008
Initial
0.0462173
P
2010
Initial
0.04105
P
2008
Final
0.0354371
P
2010
Final
0.0311889
P
#Readings
1500
1000
500
0
−0.5
0.0
0.5
Residual, s
2008
Initial
0.0901378
S
2010
Initial
0.0823465
S
2008
Final
0.0601634
S
2010
Final
0.0522433
S
#Readings
400
200
0
−0.5
0.0
0.5
Residual, s
2008
Initial
0.074641
P&S
2010
Initial
0.0719903
P&S
2008
Final
0.0485165
P&S
2010
Final
0.0427982
P&S
#Readings
1500
1000
500
0
−0.5
0.0
0.5
Residual, s

Appendix 22: Results from inversions using *simul2000A*, differencing pairs of years for the Coso geothermal area.

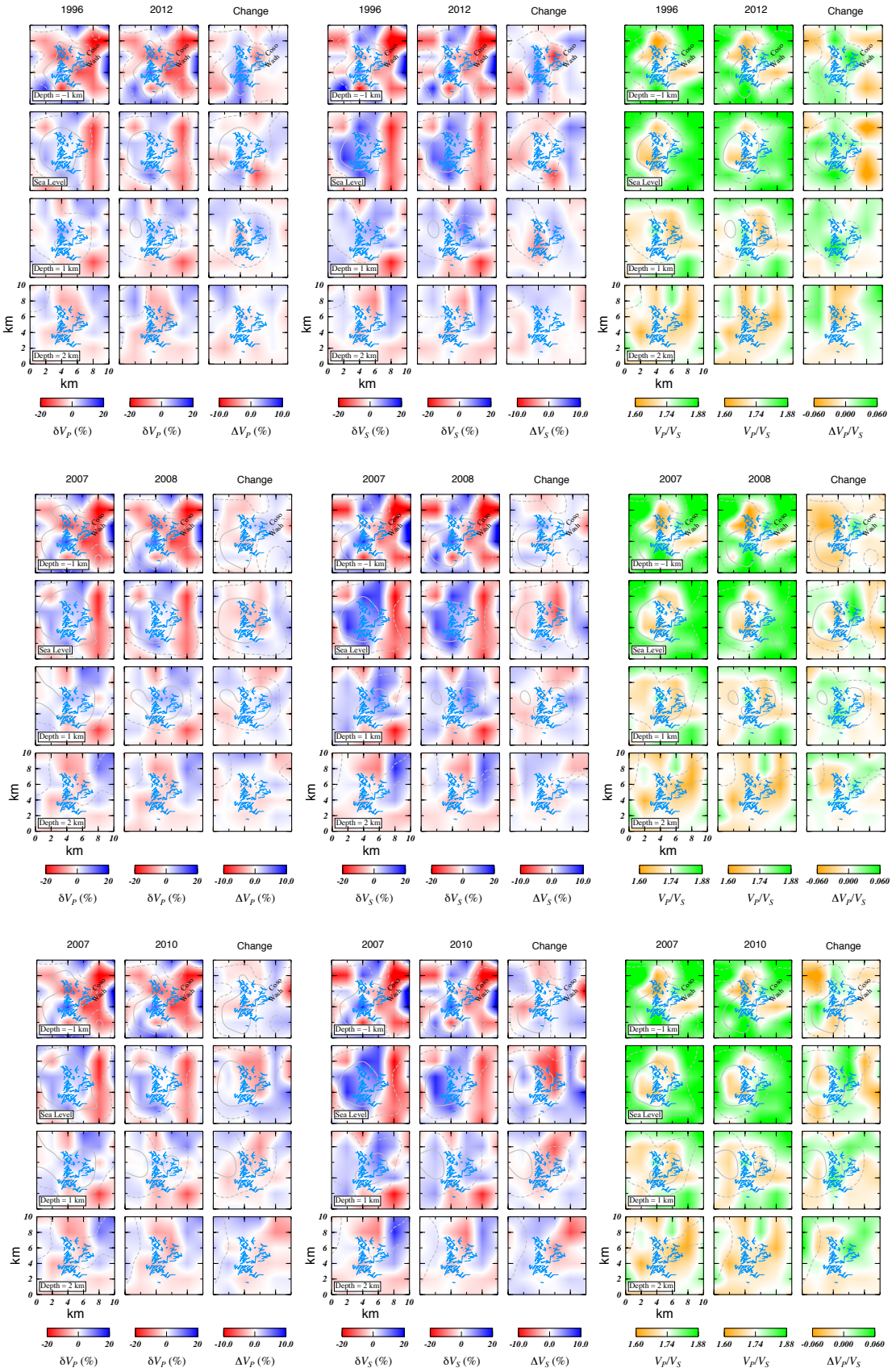

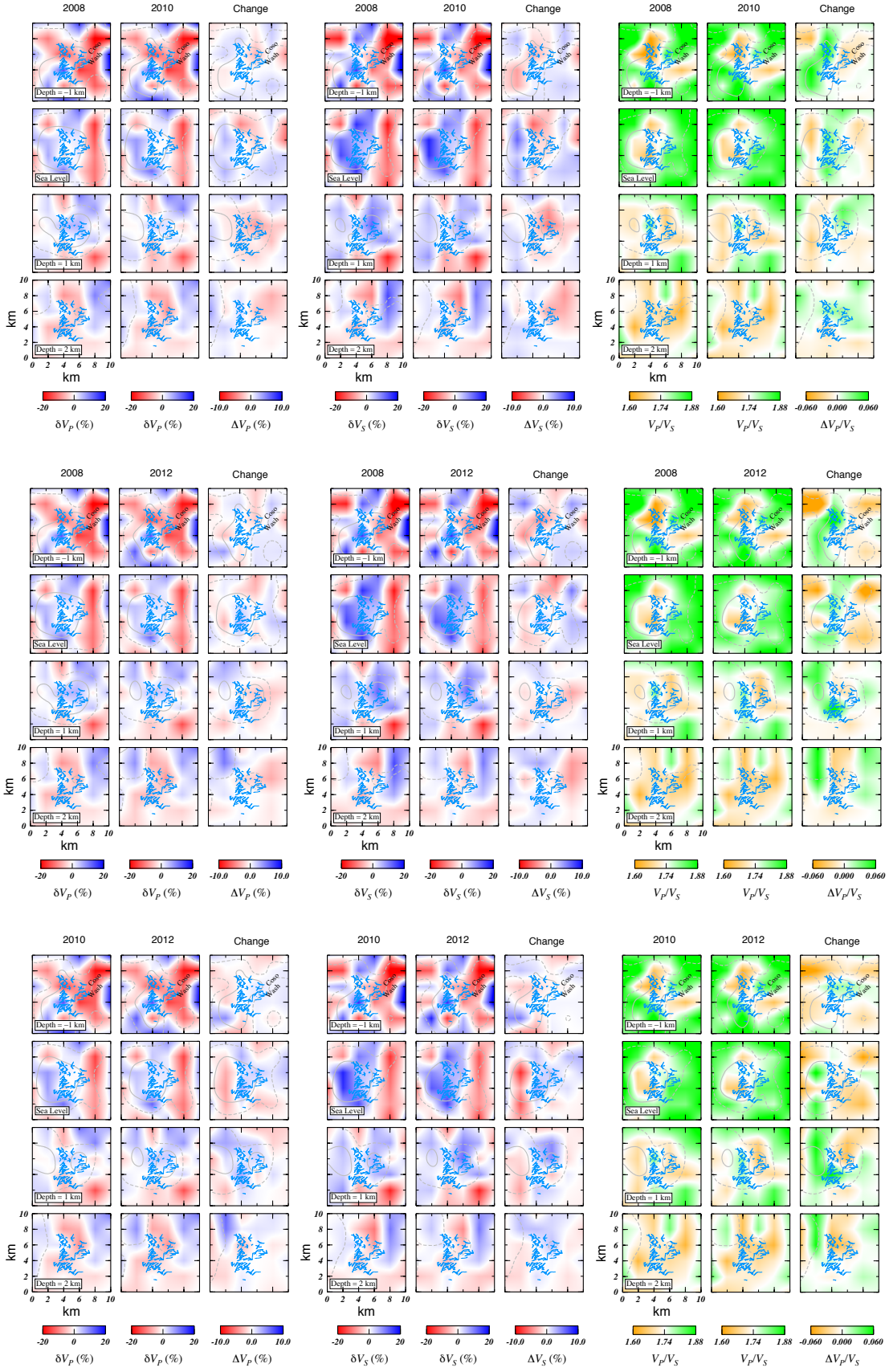
2008
2010
Change
Depth = −1 km
Sea Level
Depth = 1 km
Depth = 2 km
Coso Wash
km
δV_P (%)
δV_S (%)
ΔV_P (%)
ΔV_S (%)
V_P/V_S
ΔV_P/V_S
2008
2012
Change
2010
2012
Change

Appendix 23: Same as Appendix 22 but for inversions using *tomo4d*.

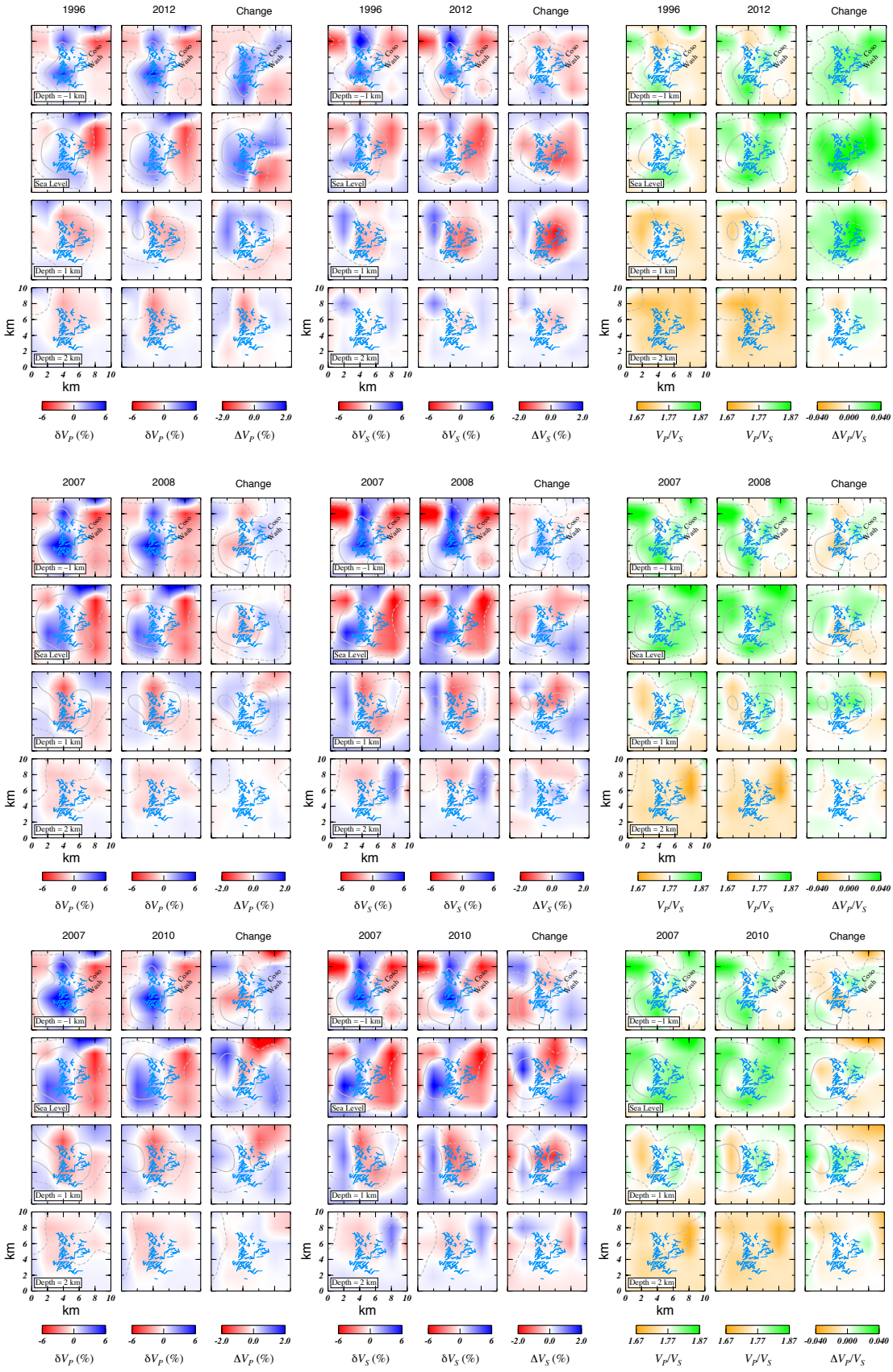

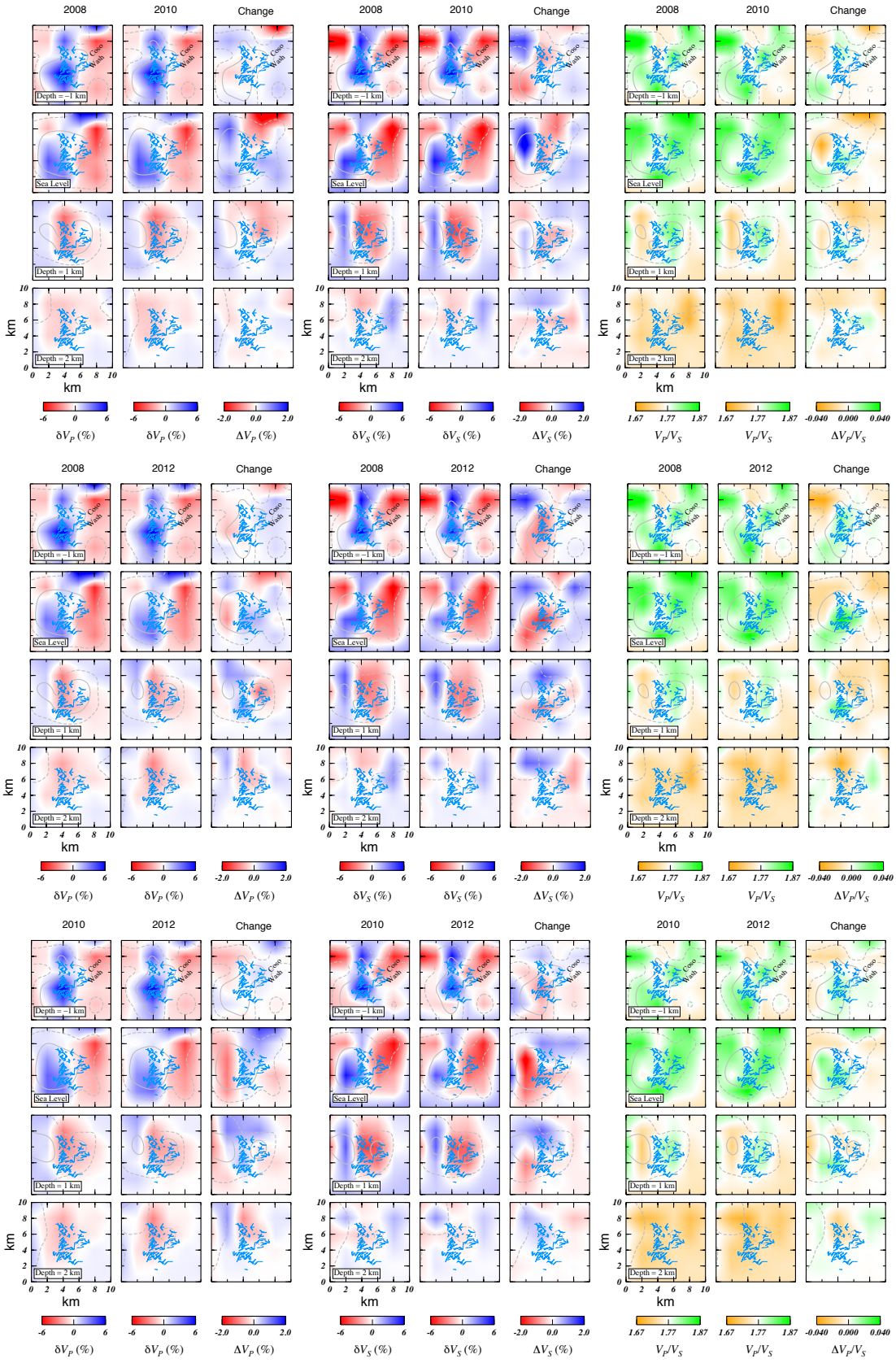
2008
2010
Change
Depth = −1 km
Sea Level
Depth = 1 km
Depth = 2 km
km
δV_P (%)
δV_S (%)
ΔV_P (%)
ΔV_S (%)
V_P/V_S
ΔV_P/V_S
2012